NONEQUILIBRIUM MANY-BODY EFFECTS IN MESOSCOPIC SYSTEMS

By

Mahmoud Tarek Khalaf Elewa

A DISSERTATION

Submitted to
Michigan State University
in partial fulfillment of the requirements
for the degree of

Physics—Doctor of Philosophy

2026

ABSTRACT

This dissertation investigates the dynamics of mesoscopic systems far from thermal equilibrium, with the primary goal to reveal novel coherent many-body effects, but also to understand how comparatively weak coupling in dissipative systems can lead to a strongly nonlinear behavior. It is organized into two parts. The first reveals nontrivial dynamical bulk signatures of the emergent topology in a parametrically driven spin-$1/2$ chain. The second concerns nonlinear collective dynamics in doped semiconductor mechanical resonators and in a low-dimensional Wigner crystal formed by electrons above superfluid helium.

In the spin-chain problem, a strong static magnetic field defines a large Larmor frequency, while a weak modulation of an anisotropic nearest-neighbor interaction at approximately twice this frequency resonantly creates spin excitations in pairs. In a frame rotating at half the modulation frequency, the driven spin chain maps, within the rotating-wave approximation, onto the Kitaev chain. The static exchange becomes fermion hopping, the modulation amplitude becomes p-wave pairing, and the frequency detuning becomes an effective chemical potential. Tuning the modulation frequency therefore moves the effective fermionic system into a topologically nontrivial regime. The central question is what are the observable consequences of the resonantly induced topology, whether they manifest in the bulk properties, and if so, what these manifestations are.

For a periodic chain, the response to the modulation switching exhibits bulk signatures of the nontrivial winding despite the absence of physical edges. Following a rapid turn-on, the continuous time-averaged magnetization change is independent of detuning throughout the topological regime, while the longitudinal spin correlations vanish in the thermodynamic limit. These results follow from the analytic structure of the same momentum-dependent angle that determines the winding number. In the weak-drive limit, the excitation density and the winding-number density become concentrated near the same momenta and are locally proportional.

A slow turn-on prepares a different state. Adiabaticity necessarily fails within shrinking momentum regions around the points at which the initial quasiparticle gap closes. Nevertheless, the time-averaged magnetization remains independent of detuning in the topological regime, while

the longitudinal correlations are strongly suppressed near resonance. Different amplitude-ramp and frequency-sweep protocols can reach the same final Hamiltonian but produce different mode occupations and correlations, giving rise to a preparation-dependent hysteresis.

The analysis is extended to finite open chains using a real-space Bogoliubov–de Gennes formulation. Depending on quasienergy and drive parameters, the bulk dispersion supports one or two propagating momentum channels. In the single-channel regime, the eigenmodes simultaneously have both a bulk sinusoidal-like part and a part localized at the edges, whereas in the two-channel regime, the boundaries select mixtures of two propagating momenta through their scattering matrices. Continuation of the same characteristic-root structure describes the separation of a state from the bulk band and its evolution into an exponentially localized edge mode with almost a mid-gap zero energy. In the two-channel regime, boundary-induced mixing between degenerate momentum channels affects an extensive set of bulk modes and can appreciably modify the bulk response after the boundary-dependent signal has propagated to the observation site. This effect is distinct from the direct contribution of a finite number of localized edge modes. The mixing can also change the time-averaged bulk response, while self-interference between amplitudes reflected from opposite boundaries produces later oscillatory features.

The second part first considers dispersive coupling between vibrational modes in p-doped semiconductor mechanical resonators. Such resonators are used as precision frequency references, often in a dual-mode architecture in which a weakly temperature-dependent clock mode is stabilized using a second mode as an in situ thermometer. Doping can compensate the temperature dependence of the clock-mode frequency, but the same electron–phonon coupling also modifies the nonlinear interaction between modes. We derive the hole-induced nonlinear elastic response from the strain-dependent free energy of the valence-band holes and apply the theory to the coupling between Lamé and torsional modes of a thin silicon plate. The doping-induced dispersive coupling can greatly exceed the intrinsic coupling of the undoped crystal and displays nonmonotonic dependence on hole density and, at sufficiently high densities, on temperature. Its magnitude also depends strongly on crystal orientation.

Finally, we study the nonlinear high-frequency conductivity of a Wigner crystal formed by electrons confined above the surface of superfluid helium. In the conventional quasistatic Bragg–Cherenkov effect, a steadily moving electron lattice coherently emits helium surface waves, or ripplons, whose wave vector matches its reciprocal-lattice vector, producing a frictional back-action and a saturated crystal velocity. Experiments in a microchannel reveal a strongly nonlinear, low-conductivity crystalline response at drive frequencies of the order of the ripplon frequency associated with the fundamental reciprocal-lattice shell, even when the oscillatory displacement is substantially smaller than the electron-lattice spacing. We extend the Bragg–Cherenkov theory to a rapidly oscillating Wigner solid and show that higher-order reciprocal-lattice vectors provide channels for resonant coupling to higher-frequency ripplons. The resulting dynamical friction provides a mechanism for high-frequency pinning.

Across these systems, the common theme is how the interplay of the coupling and strongly nonequilibrium dynamics in mesoscopic systems, including transient and resonant effects, can lead to nontrivial, sometimes counterintuitive consequences. The results open avenues for further studies of nonequilibrium mesoscopic dynamics.

Copyright by
MAHMOUD TAREK KHALAF ELEWA
2026

To Ayah, my parents, and my siblings, for their unwavering support.

ACKNOWLEDGEMENTS

Nearly five years ago, I left everything I knew behind in pursuit of science. I arrived in an unfamiliar world, naively expecting my greatest challenge to be the rigor of a PhD, wholly unaware that I was about to build a life from scratch. Suddenly, I found myself in a nonequilibrium phase that lacked control parameters or a familiar recipe for equilibration. Yet, like most systems eventually find their way to equilibrium, I found mine. Such equilibrium wasn't guaranteed to be kind, but I was lucky enough to find a version that was. I grew up not only as a scientist, but most importantly, as a human. Looking back, certain people were vital to shaping this journey, and I want to thank them as I complete the PhD that started it all.

First and foremost, I want to thank my advisor, Mark Dykman. His support has been beyond what I can describe in a few sentences. He cared deeply about my growth, not just as a scientist, but also as a person. He taught me how to approach complex problems and how to develop intuition through guided approximations. I learned so much from him, but also by watching him: his inspiring passion for physics, his deep commitment to science, his scientific integrity, and the unwavering care he invests in supporting those who work with him.

I want to also thank my PhD committee members: Prof. Carlo Piermarocchi, Prof. Johannes Pollanen, Prof. Mohammad Maghrebi, and Prof. Dean Lee. Their guidance and support in my research and beyond were invaluable to my scientific and personal growth.

I also want to honor the memory of Dr. Ahmed Zewail, who fought bureaucracy for thirteen years and continued his efforts even while battling cancer to establish a scientific institution where qualified students could learn regardless of their financial status. Without his vision and tireless efforts, I cannot imagine a path that would have led me to who I am today. I dedicate any success I may achieve to his soul.

Friendship has always been vital to my journey, and these past five years were certainly no exception. From long-distance old friends to new friends made along the way, their support carried me through the hardest phase of this transition and helped me find the kind of life I have today. I am indebted to my childhood friends, Al-Ashqiya, and my undergraduate friends. I am particularly

thankful for the friendships I made in Michigan: my physics friends who turned moments of struggle into joyful memories, and my Arab friends who helped bridge the cultural gap and made a once-unfamiliar environment feel like home. Whenever homesick, I was lucky that a four-hour drive could bring me to my Egyptian undergraduate friends in West Lafayette and Columbus, who always opened their doors to me when I needed a piece of home, which is, by the way, how I met my wonderful wife, Ayah.

Ayah was the last missing piece to finish building the new life that I started from scratch. Starting our journey together marked the moment I finally felt at home again. Her love and selflessness supported me at times when I most needed support, and through her, I was blessed not just with a partner, but with a family here in the US.

Finally, none of this would have been possible without the foundation laid by my family back home. Their sacrifices, unconditional love, and constant prayers across the miles have been the driving force behind everything I do. I am very thankful that I was born to this loving family. I am thankful to my parents, Tarek and Salwa, for all the sacrifices they made for me and for instilling in me love and strong moral values. I am thankful to my brother, Mohamed, for his guidance as I grew up, and to my sister, Hasnaa, for her emotional support. Family is and will always be everything.

TABLE OF CONTENTS

LIST OF TABLES xi

LIST OF FIGURES xii

LIST OF ABBREVIATIONS xvii

I Parametric Resonance and Dynamical Topology in a Spin-1/2 Chain 1

CHAPTER 1 INTRODUCTION: TOPOLOGY MADE VISIBLE THROUGH SPIN DYNAMICS 2
1.1 From Magnons to spinless fermions: a topological perspective 4
1.2 Periodically driven quantum systems 13
1.3 The Kitaev chain: bulk topology and Majorana edge modes 21
1.4 Bulk dynamical signatures in the driven spin chain 27
1.5 Organization of the dissertation 33

CHAPTER 2 FROM RESONANT SPIN DRIVING TO THE KITAEV CHAIN 36
2.1 Laboratory-frame spin Hamiltonian 36
2.2 Rotating frame and rotating-wave approximation 37
2.3 Jordan–Wigner transformation: Kitaev-chain mapping and boundary conditions 38
2.4 Bogoliubov–de Gennes representation 40
2.5 Preparation protocols, dynamical equations, and observables 46

CHAPTER 3 DYNAMICAL BULK TOPOLOGY IN THE PERIODIC CHAIN 53
3.1 Laboratory-frame manifestation of the anomalous response 53
3.2 Sudden turn-on of the modulation 58
3.3 Slow turn-on of the modulation 66
3.4 Preparation memory and hysteresis 70
3.5 General solution for a slowly turned-on drive 72
3.6 Summary and transition to open boundaries 82

CHAPTER 4 DYNAMICS OF A FINITE OPEN CHAINS 84
4.1 Why the open-chain modes are not simple standing waves 85
4.2 Solution of the boundary problem 86
4.3 How boundary mixing changes time-averaged observables 94
4.4 Real-space propagation and the spin observables 95
4.5 Covariance matrix and spin observables 99
4.6 Numerical results 102
4.7 Concluding remarks 112

II Nonlinear Dynamics in Mesoscopic Systems 114

CHAPTER 5 DISPERSIVE MODE COUPLING IN P-DOPED SEMICONDUCTOR NANOMECHANICAL RESONATORS . . . 115
5.1 Introduction . . . 115
5.2 Adiabatic backaction from the hole-vibrational coupling . . . 118
5.3 Estimates of the coupling-induced elasticity parameters . . . 120
5.4 The effect of dispersive coupling to high-frequency phonons . . . 122
5.5 Phase diffusion due to dispersive coupling . . . 124
5.6 Dispersive coupling of two low-frequency modes . . . 127
5.7 Three-band model and numerical procedure . . . 131
5.8 Temperature and density dependence of the dispersive frequency shifts . . . 133
5.9 Conclusion . . . 138

CHAPTER 6 HIGH-FREQUENCY NONLINEAR CONDUCTIVITY OF A WIGNER CRYSTAL . . . 140
6.1 Electrons, Wigner crystallization, and ripplons on liquid helium . . . 140
6.2 Quasistatic Bragg–Cherenkov transport . . . 147
6.3 High-frequency nonlinear transport of a Wigner crystal . . . 155

CHAPTER 7 CONCLUSIONS AND OUTLOOK . . . 163
7.1 Principal results and their physical implications . . . 163
7.2 Experimental tests of the spin-chain response . . . 168
7.3 Future directions . . . 170
7.4 Final perspective . . . 173

APPENDIX A MATRIX PRODUCT STATE SIMULATIONS . . . 174

BIBLIOGRAPHY . . . 179

LIST OF TABLES

Table 3.1 Dimensionless parameters characterizing the four laboratory-frame ramp protocols. Here $\tau_F = F_{\mathrm{fin}}/\eta_F$, $\omega_0 = 30J$, and $52J \le \omega_F \le 68J$. The time-dependent carrier-scale parameter used in the rotating-frame construction is $\max_\mu(\eta_F/\omega_F^2)$. The quantity $\chi_{\mathrm{ramp}} = F_{\mathrm{fin}}^2/\eta_F$ is an upper bound on the pair-rotation angle accumulated during the linear ramp in the RWA. The slow protocols are quasi-adiabatic away from the initial gap-closing momenta, but they are not globally adiabatic in the topological regime. 55

Table 5.1 List of Symbols 118

LIST OF FIGURES

Figure 2.1 Bulk dispersion relation Λ_k for a Kitaev chain with $J = 1$, $F = 0.5$, and $\mu = 0.5$. The horizontal dashed lines indicate representative energies in the single-channel (orange) and two-channel (green) regimes, with the corresponding momentum intersections marked explicitly. 43

Figure 3.1 Full laboratory-frame dynamics of a periodic chain of $N = 500$ spins with $\omega_0 = 30J$ and $J_{xx} = J_{yy} = J/2$. (a) Continuous time-averaged magnetization change $\overline{\Delta m_n^z} = 1 - \langle \sigma_n^z \rangle$. (b) Continuous time-averaged nearest-neighbor longitudinal correlation $Q^z(1) = \langle \sigma_n^z \sigma_{n+1}^z \rangle - \langle \sigma_n^z \rangle^2$. Blue and red curves correspond to $F_{\text{fin}}/J = 0.5$ and 0.7, respectively. Solid curves are obtained using the fast ramp $\eta_F = 3J^2$, while dashed curves correspond to the slow ramp $\eta_F = 10^{-2}J^2$. The dynamics of each $(k, -k)$ sector is propagated using 100 time steps per modulation period, and the observables are averaged over 1000 periods after the ramp. 57

Figure 3.2 Time-averaged magnetization change $1 - \langle \sigma_n^z \rangle$ and nearest-neighbor connected longitudinal correlation $Q^z(1)$ following a sudden turn-on of the RWA modulation, as functions of the scaled detuning μ/J. The final pairing amplitude is $F/J = 0.5$. The analytical curves refer to the thermodynamic limit. The dotted dashed curves are finite-chain MPS simulations of the RWA Hamiltonian with $N = 20$; the MPS method, averaging window, and finite-size analysis are described in Appendix A. The magnetization is independent of detuning and the longitudinal correlation vanishes throughout the topological interval $|\mu| < 2|J|$. 60

Figure 3.3 Momentum-resolved densities following a sudden turn-on at $F/J = 0.1$. Solid curves show the time-averaged fermion occupation $\langle c_k^\dagger c_k \rangle$, while dashed curves show the winding-number density $d\theta_k/dk$, multiplied by $F/2J$ to place the two quantities on the same scale. In the weak-drive regime, both quantities consist of two narrow Lorentzian peaks. Their centers $\pm k_\mu = \pm \arccos(\mu/2J)$ depend on detuning, whereas their shapes and integrated areas do not. 64

Figure 3.4 Time-averaged magnetization change $1 - \langle \sigma_n^z \rangle$ and nearest-neighbor connected longitudinal correlation $Q^z(1)$ for a slow linear turn-on of the RWA pairing amplitude. The final amplitude is $F_{\text{fin}}/J = 0.5$. The analytical curves use the adiabatic contractions in Eq. (3.34). The symbols are MPS simulations of the RWA Hamiltonian for $N = 40$ and a ramp time $\tau_{\text{sl}} = 10^3 J^{-1}$, followed by continuous time averaging at the final parameters. Numerical details are given in Appendix A. The magnetization remains independent of detuning in the topological interval, but $Q^z(1)$ is generally nonzero, in contrast to the sudden-turn-on result. 67

Figure 3.5 Magnitude of the time-averaged nearest-neighbor transverse correlator $|\langle\sigma_n^+\sigma_{n+1}^-\rangle|$ after sudden and slow turn-on, plotted as a function of μ/J for $F_{\rm fin}/J = 0.5$. The analytical results are obtained from Eqs. (3.21) and (3.34). The dashed dotted lines are MPS simulations of the RWA Hamiltonian with $N = 20$ for the sudden protocol and $N = 40$ for the slow protocol. The slow ramp uses $\tau_{\rm sl} = 10^3 J^{-1}$. Details are provided in Appendix A. 68

Figure 3.6 Time-averaged transverse correlation $|\langle\sigma_n^+\sigma_{n+1}^-\rangle|$ obtained along two slow preparation paths. Path 1 turns on the pairing amplitude directly at the displayed value of μ. Path 2 first turns on the amplitude to $F_{\rm fin} = 0.5J$ in the trivial regime and then sweeps the modulation frequency to the same final detuning. Lines show the adiabatic analytical results; dashed dotted lines are MPS simulations of the RWA Hamiltonian with $N = 40$ and $\tau_{\rm sl} = 10^3 J^{-1}$. Details are given in Appendix A. 70

Figure 3.7 Preparation-path dependence of the time-averaged magnetization change $1 - \langle\sigma_n^z\rangle$ (left) and the connected nearest-neighbor longitudinal correlation $Q^z(1)$ (right). Path 1 turns on the modulation at fixed detuning. Path 2 first establishes $F_{\rm fin}/J = 0.5$ in the trivial regime and then sweeps the frequency to the same final μ. Lines are obtained from Eqs. (3.34) and (3.39); dashed dotted lines are MPS simulations of the RWA Hamiltonian. The simulation protocol and convergence tests are described in Appendix A. 71

Figure 3.8 Momentum-resolved occupation $\langle c_k^\dagger c_k\rangle$ for a weak, finite-rate turn-on at $\mu/J = 1$, for which $k_\mu = \pi/3$. The solid curve is the Lorentzian nonadiabatic peak in Eq. (3.52), obtained when the inverse turn-on time exceeds the final pairing scale. The dashed curve is the adiabatic peak in Eq. (3.53). Both have a detuning-independent shape when expressed relative to k_μ, but their profiles differ. 74

Figure 3.9 Time-averaged momentum occupation for a linear turn-on at $\mu/J = 1$, $k_\mu = \pi/3$, and $F_{\rm fin}/J = 0.2$. The solid curve is the adiabatic expression in Eq. (3.34). Dashed curves are obtained by direct integration of the exact pair-amplitude equations and subsequent use of Eq. (3.47) for two ramp rates. The agreement becomes excellent once $F_{\rm fin}\tau_{\rm sl} \gg 1$, and remains qualitatively good even outside the asymptotic limit. 75

Figure 4.1 Standing-wave content of the exact open-chain modes for $N = 256$ and $F/J = 0.5$. The color represents $\log_{10}|C_{s\ell}|^2$, with the displayed scale restricted to $[-5, 0]$. Modes are ordered by increasing energy along the vertical axis. Left: $\mu/J = 0.5$, where part of the bulk spectrum has two propagating channels. Many modes have two separated packets of standing-wave weight. Right: $\mu/J = 1.7$, where the bulk spectrum has one propagating channel at each energy. The extended modes have one principal packet. The lowest, edge-localized mode has a broad standing-wave expansion. 86

Figure 4.2 Crossings and avoided crossings in the static spectrum of an open chain with $N = 50$. (a) Pairing sweep over $0 \le F/J \le 0.5$ at fixed $\mu/J = 1$. (b) Detuning sweep over $0 \le \mu/J \le 1$ at fixed $F/J = 0.5$. Solid blue curves show the numerical squared excitation energies Λ_s^2/J^2, obtained from the eigenvalues of $(A-B)(A+B)$. Dashed curves show the squared bulk dispersion $\Lambda^2(k_p)/J^2$ evaluated at all standing-wave momenta $k_p = p\pi/(N+1)$, with dark orange for even p and green for odd p. The displayed vertical windows are $0 \le \Lambda^2/J^2 \le 0.8$ in (a) and $0.9 \le \Lambda^2/J^2 \le 2.8$ in (b). For nonzero pairing, intersections of reference branches with the same index parity correspond to exact crossings, whereas intersections between opposite-parity branches are replaced by avoided crossings in the open-chain spectrum. 92

Figure 4.3 Strict infinite-time averages following the sudden turn-on from the polarized state. Top: $F/J = 0.5$. Bottom: $F/J = 0.7$. Open-chain sizes are $N = 128, 256, 512$. The magnetization is evaluated at a central site, $n = N/2$, and correlations on the central bond $(N/2, N/2+1)$. The finite-ring curve uses $N = 512$ and antiperiodic fermionic boundary conditions. The dotted curve is the thermodynamic result. From left to right: magnetization change, $Q^z_{n,n+1}(\infty)$, and the magnitude of the averaged transverse correlation. 102

Figure 4.4 Open-chain magnetization change for $N = 128$ minus the thermodynamic result for $F/J = 0.5$. Top row: $\mu/J = 0.5$. Bottom row: $\mu/J = 1.7$. Left column: instantaneous differences. Right column: differences between uniform running averages over $[0, T]$. Each panel has its own color scale. The boundary-dependent response develops first near the ends and subsequently reaches the interior. 104

Figure 4.5 Central-site dynamics at $\mu/J = F/J = 0.5$. Left: instantaneous magnetization change for an open chain with $N = 384$, compared with the thermodynamic bulk. The central site is $n = N/2 + 1$. Right: difference between the open and thermodynamic bulk running averages over the same interval $[0, T]$, for $N = 256, 384, 512$. The displayed range is $0 \le TJ/N \le 12$. The curves approach size-dependent plateaus with residual finite-time oscillations. 105

Figure 4.6 Threshold-defined central-site arrival times for $F/J = 0.5$, $\mu/J = 0.5, 1.7, 3$, and $N = 64, 96, 128, 192, 256, 384, 512$. The displayed thresholds are $\eta = 10^{-3}$ and 10^{-2}. Left: arrival times versus size. Right: the same times scaled as $t_{\text{arrival}} v_{\max}/(N/2)$. The denominator $N/2$ is the distance convention used in the numerical analysis; endpoint corrections are $O(1)$. 106

Figure 4.7 Size dependence of the early central-site boundary signal after a sudden quench from the fully polarized initial state, with $F/J = 0.5$. For an open chain of N sites, the observation site is $n = N/2 + 1$, and the instantaneous signal is $\delta_N(t) = \Delta m_n^{z,\mathrm{open}}(t) - \Delta m^{z,\mathrm{bulk}}(t)$, where the bulk reference is the infinite uniform chain with the same parameters and initial state. Each point gives $\max_{0.8 \le t/t_{\mathrm{boundary}} \le 1.2} |\delta_N(t)|$, with $t_{\mathrm{boundary}} = N/(2v_{\max})$ and $v_{\max}$ evaluated for the corresponding parameters. Blue: $\mu/J = 0.5$, where a two-channel interval exists. Orange and green: the single-channel controls $\mu/J = 1.7$ and 3, respectively. The computed sizes range from $N = 64$ to 4096. Both axes are logarithmic; lines connect the numerical points. 107

Figure 4.8 Zero-detuning symmetry and its sensitivity to chain length at $F/J = 0.5$. Left: strict central-site magnetization changes at exactly $\mu = 0$, with $n = \lfloor N/2 \rfloor + 1$. The displayed classes are $N \bmod 4 = 0, 1, 3$, extending through $N = 1025$. Dotted lines show the values in Eq. (4.75). The unplotted even class $N \bmod 4 = 2$ also gives one and was checked through $N = 1026$. Right: the small-detuning dependence for $N = 64, 128, 256, 512$. The sharp feature near zero becomes narrower with increasing size. 109

Figure 4.9 Convergence of uniform time averages over $[0, T]$ for open chains at $\mu/J = F/J = 0.5$. The observation site is $n = N/2 + 1$, and the sizes are $N = 64, 128, 256, 512, 1024$. Left: absolute difference between the running average and each chain's own strict infinite-time average, for durations $10^{-1} \le TJ \le 10^7$. Right: the running averages plotted against TJ/N, with displayed range $10^{-2} \le TJ/N \le 10^4$. Colors identify the same sizes in both panels. The dotted horizontal line is the bulk reference value $1/3$. 111

Figure 5.1 The coordinate system for a thin square plate with side length L_s and thickness h_s. For a plate cut out along the $\langle 100 \rangle$ crystalline axes, the coordinates (x_1, x_2, x_3) are parallel to the axes, as indicated by the black arrows. For a plate cut out in the plane along the $\langle 110 \rangle$ axes, the coordinates (x, y) are shown by the red arrows, while the z-coordinate is still normal to the plate and points along $\langle 100 \rangle$ axes 128

Figure 5.2 Mode profiles for (a) the in-plane second Lamé mode and (b) the considered torsional mode. The modes can be simultaneously activated in a thin square plate that is clamped through the middle points of its four sides. 130

Figure 5.3 Temperature dependence of the eigenfrequencies of the second Lamé and torsional modes, $\Delta_\alpha = [\omega_\alpha(T) - \omega_\alpha(T_0)]/\omega_\alpha(T_0)$ for a plate cut out along the $\langle 110 \rangle$ axes. The ratio of the thickness to later side of the plate is $h_s/L_s = 0.1$. We set $T_0 = 298$ K. Solid lines show the temperature dependence in the presence of doping, whereas the results for undoped crystals are shown by dashed lines. 134

Figure 5.4 Temperature dependence of the dispersive frequency shift $\aleph_{\mathrm{TL}}$ of the torsional mode scaled by the squared amplitude of the second Lamé mode sketched in Fig. 5.2. The parameter $\aleph_{\mathrm{TL}}$ is defined in Eq. (5.25). The results refer to a square single-crystal silicon plate with the ratio of the thickness to length $h_s/L_s = 0.1$. The panels show the results for the crystal orientations $\langle 100\rangle$ and $\langle 110\rangle$. The left and right panels refer to the hole density $n_{\mathrm{h}} = 2.0\times 10^{19}$ cm^{-3} and $n_{\mathrm{h}} = 1.0\times 10^{20}$ cm^{-3}, respectively. 135

Figure 5.5 Temperature dependence of the dispersive frequency shift $\aleph_{\mathrm{LT}}$ of the second Lamé mode scaled by the squared amplitude of the torsional mode. The modes are sketched in Fig. 5.2. The parameter $\aleph_{\mathrm{LT}}$ is defined in Eq. (5.24). The plots refer to a square single-crystal silicon plate with the ratio of the thickness to length $h_s/L_s = 0.1$. The panels show the results for the crystal orientations $\langle 100\rangle$ and $\langle 110\rangle$. The left and right panels refer to the hole density $n_{\mathrm{h}} = 2.0\times 10^{19}$ cm^{-3} and $n_{\mathrm{h}} = 1.0\times 10^{20}$ cm^{-3}, respectively. 136

Figure 5.6 Density dependence of the scaled dispersive nonlinear frequency shifts of the torsional (left panel) and the second Lamé (right panel) modes sketched in n Fig. 5.2. The shifts are defined in Eqs. (5.25) and (5.24), respectively. The plots refer to two crystalline orientations of a square single-crystal silicon plate with the ratio of the thickness to length $h_s/L_s = 0.1$. The temperature is $T = 300$ K. 137

Figure 6.1 Representative high-frequency transport measurements of the microchannel-confined electron system. (a) Compensation-line scheme used to suppress the parasitic capacitive background. (b) Channel current I_{ch} as a function of the central-channel voltage V_{ch} and the amplitude of the ac driving field $\mathbf{E}_{\mathrm{ac}}$ for drive frequencies 0.3, 25, and 150 MHz. The three transport regimes correspond to an empty channel, a high-conductivity electron state, and a low-conductivity Wigner-crystal state. 156

Figure A.1 The time-averaged correlator $Q^z(1)$ for a sudden turn-on of parametric modulation as a function of the scaled frequency detuning μ/J. The final modulation amplitude is $F/J = 0.5$. The analytical result (thermodynamic limit) is compared with MPS simulation results for a finite chain of $N = 20$. 177

Figure A.2 A log-log plot of the integrated error $E_N[Q^z(1)]$ versus the number of sites N. The linear fit (dashed line) has a slope of approximately -1, confirming that the finite-size corrections to the correlator scale as N^{-1}. 177

Figure A.3 The time-averaged correlators $1-\langle\sigma_z\rangle$ and $Q^z(1)$ obtained by slowly increasing the drive to $F(t_f)/J = 0.5$ for a fixed μ (line and circles 1) and by slowly turning on the drive to the same F/J in the trivial regime and then slowly changing the modulation frequency to arrive at the same μ (line and circles 2). The simulations refer to $N = 40$ and $F(t) = F(t_f)t/\tau_{\mathrm{sl}}$ with $\tau_{\mathrm{sl}} = 10^3/J$. 178

LIST OF ABBREVIATIONS

DMI Dzyaloshinskii–Moriya interaction

HPT Holstein–Primakoff transformation

JWT Jordan–Wigner transformation

RWA Rotating-Wave Approximation

BdG Bogoliubov–de Gennes

SVD Singular value decomposition

ED Exact Diagonalization

ETH Eigenstate Thermalization Hypothesis

GGE Generalized Gibbs Ensemble

HFB Hartree–Fock–Bogoliubov

MPS Matrix Product States

MPO Matrix Product Operator

TEBD Time-Evolving Block Decimation

Part I

Parametric Resonance and Dynamical Topology in a Spin-$1/2$ Chain

CHAPTER 1

INTRODUCTION: TOPOLOGY MADE VISIBLE THROUGH SPIN DYNAMICS

This dissertation is organized into two parts. Part I concerns parametric resonance and dynamical topology in a spin-$1/2$ chain, whereas Part II concerns nonlinear dynamics in nanomechanical resonators and a low-dimensional Wigner crystal. The present chapter introduces the physical and mathematical background needed for Part I; the background specific to the two projects in Part II is introduced in their respective chapters.

Topology is most familiar in condensed-matter physics as a property of a stationary band structure. A gapped bulk is assigned an integer or binary invariant, and a boundary between phases with different invariants supports states that cannot be removed without closing a gap or breaking a protecting symmetry [1–3]. This equilibrium language is powerful, but, as we show here, it does not exhaust the observable consequences of topology. A driven quantum system also carries information in how it responds, dephases, and remembers its preparation [4–6]. The central question of Part I is therefore dynamical: *can a weak resonant modulation lead to the onset of a nontrivial topology and can this topology be observed?*

A natural precedent comes from the long-standing theory of magnetic excitations. Since Bloch's introduction of spin waves in 1930 [7], small deviations from an ordered magnetic state have been described as bosonic quasiparticles, or magnons, whose Bloch modes form bands. In linear spin-wave theory, Dzyaloshinskii–Moriya interactions, noncollinear magnetic order, and dipolar couplings can endow these bands with Berry curvature and nontrivial invariants, producing Chern bands, Dirac and Weyl nodes, and topological boundary modes [8–13].

This literature established that a magnetic ground state which can be by itself topologically trivial may nevertheless support topological excitations at finite frequency. The observable consequences differ from those of electronic insulators. Because magnons are bosons, their bands are not filled up to a Fermi level and their topology does not generally yield a quantized Hall response. It is instead inferred from excitation spectra and boundary modes, or from thermal and spin-transport responses whose magnitude depends on the thermal or externally pumped magnon population [9, 13–17].

The spin-chain problem studied in Part I enters a different regime. Spin-$1/2$ quantum magnets can also host topological magnon or triplon bands [13, 18, 19], so the distinction is not the spin magnitude alone. This description, however, is limited to the single magnon sector due to the hardcore nature of spin-1/2. Here, however, we consider a one-dimensional geometry which allows this hard-core nature of spin flips to be retained exactly through the Jordan–Wigner transformation, which maps them to spinless fermions. We consider a spin-1/2 chain in a strong static magnetic field with anisotropic nearest-neighbor coupling, one component of which is modulated near twice the single-spin Larmor frequency. Although the modulation is weak compared with the Larmor frequency, it resonantly creates pairs of spin excitations. After moving to a rotating frame and retaining the resonant terms, the Jordan–Wigner fermions are governed by the Kitaev-chain Hamiltonian: the static exchange becomes fermion hopping, the modulation amplitude becomes p-wave pairing, and the frequency detuning becomes an effective chemical potential [20–22]. Changing the modulation frequency then drives a transition in the winding number of the effective fermion system.

This mapping creates an interesting experimental opportunity. Rather than inferring this topology from boundary modes or transverse transport, it can be detected from the bulk magnetization and spin correlations after the modulation is switched on in a closed (periodic) chain [22]. Moreover, the answer depends on the switching protocol. A sudden quench, a slow ramp, and a frequency sweep can end at the same rotating-frame Hamiltonian yet produce different time-averaged states. Opening the chain adds another layer: the boundary mixes propagating channels and generates localized edge solutions, and it changes how the long-time and thermodynamic limits are taken.

In this chapter, we present the physical and mathematical background needed to formulate and interpret the results of Part I. We begin with a brief overview of magnons and topological magnon bands, which provides context for the theoretical tractability and experimental accessibility of the spin model studied here. We then introduce the framework of periodically driven quantum systems, including Floquet theory and the rotating-wave approximation. Next, we review the physics of the Kitaev chain, whose bulk topology underlies the effective model realized by the driven spin system.

Finally, we summarize the principal results of Part I and outline the organization of the remaining chapters.

1.1 From Magnons to spinless fermions: a topological perspective

In this section, we first introduce the Holstein–Primakoff transformation and use it to describe magnons within linear spin-wave theory for large spin S. We then discuss two different mechanisms that could induce nontrivial topology in number-conserving magnon bands and bosonic Bogoliubov bands, and briefly examine how higher-order terms modify the noninteracting magnon picture. We next turn to spin-$1/2$ systems, where spin excitations obey a hard-core constraint. We identify the conditions under which the single-magnon sector can still be described by a quadratic hopping Hamiltonian and support topological bands, and discuss the limitations of this description at finite excitation density and under external driving. Finally, we introduce the Jordan–Wigner transformation, which maps a one-dimensional spin-$1/2$ chain onto spinless fermions and provides the framework used in the remainder of Part I.

1.1.1 Holstein–Primakoff transformation

Magnons are the quantized small-amplitude fluctuations about a magnetically ordered state. For definiteness, consider a field-polarized or ferromagnetically ordered state, and choose the local quantization axis such that $\langle S_n^z \rangle \simeq S$. A single magnon excitation lowers the spin projection along this axis by one unit. The spin operators can be represented in terms of canonical bosonic operators through the Holstein–Primakoff transformation (HPT) [23],

$$S_n^z = S - b_n^\dagger b_n, \qquad S_n^+ = \sqrt{2S}\sqrt{1 - \frac{b_n^\dagger b_n}{2S}}\, b_n, \qquad S_n^- = \sqrt{2S}\, b_n^\dagger \sqrt{1 - \frac{b_n^\dagger b_n}{2S}}. \tag{1.1}$$

Here, the operators b_n and $b_n^\dagger$ obey the canonical commutation relations $[b_n, b_m^\dagger] = \delta_{n,m}$. With the convention in (1.1), $b_n^\dagger$ creates a magnon and is therefore associated with the spin-lowering operator S_n^-. The transformation is exact provided that the bosonic Hilbert space is restricted to the physical subspace, i.e., $0 \le b_n^\dagger b_n \le 2S$. The upper bound is essential because the unrestricted bosonic Fock space contains states that have no counterpart in the original spin Hilbert space.

1.1.2 Magnons in large spin systems

The square roots in (1.1) make the exact representation difficult to use for a generic interacting spin system. In an ordered state with a low density of spin deviations, $\langle b_n^\dagger b_n\rangle/(2S) \ll 1$, they can be systematically expanded to give [13, 23, 24]

$$\begin{aligned} S_n^z &= S - b_n^\dagger b_n, \\ S_n^+ &= \sqrt{2S}\left[1 - \frac{b_n^\dagger b_n}{4S} - \frac{(b_n^\dagger b_n)^2}{32S^2} + \cdots\right] b_n, \\ S_n^- &= \sqrt{2S}\, b_n^\dagger \left[1 - \frac{b_n^\dagger b_n}{4S} - \frac{(b_n^\dagger b_n)^2}{32S^2} + \cdots\right]. \end{aligned} \tag{1.2}$$

Linear spin-wave theory retains the leading terms,

$$S_n^z = S - b_n^\dagger b_n, \qquad S_n^+ \simeq \sqrt{2S}\, b_n, \qquad S_n^- \simeq \sqrt{2S}\, b_n^\dagger. \tag{1.3}$$

The resulting Hamiltonians from this linear approximation are typically quadratic in the bosonic operators and describe noninteracting magnons. The higher-order terms in (1.2) generate interactions between these magnons. As an example, consider a general bilinear Hamiltonian for localized spins [13, 24],

$$H = \frac{1}{2}\sum_{ia,jb}\sum_{\alpha,\beta=x,y,z} J_{ia,jb}^{\alpha\beta} S_{ia}^\alpha S_{jb}^\beta - \sum_{ia} \boldsymbol{h}_{ia}\cdot\boldsymbol{S}_{ia}. \tag{1.4}$$

Here, i and j label magnetic unit cells, a and b label the magnetic sublattices within a unit cell, and $J_{ia,jb}^{\alpha\beta}$ includes isotropic and anisotropic exchange interactions. A local coordinate frame is chosen on each sublattice so that the local z axis is parallel to the classical ordered moment. Substitution of (1.2) into (1.4) produces an expansion of the form

$$H = E_{\mathrm{cl}} + H_1 + H_2 + H_3 + H_4 + \cdots. \tag{1.5}$$

The linear term H_1 vanishes when the reference spin configuration is a stationary point of the classical energy. The quadratic term H_2 defines linear spin-wave theory, while H_3, H_4, and the higher-order terms describe magnon–magnon interactions [24].

Introducing the Fourier transformation

$$b_{ia} = \frac{1}{\sqrt{N_c}} \sum_{\boldsymbol{k}} e^{i\boldsymbol{k}\cdot\boldsymbol{R}_i} b_{\boldsymbol{k}a}, \qquad b_{\boldsymbol{k}a} = \frac{1}{\sqrt{N_c}} \sum_{i} e^{-i\boldsymbol{k}\cdot\boldsymbol{R}_i} b_{ia}, \tag{1.6}$$

where $\boldsymbol{R}_i$ is the Bravais-lattice vector of the ith magnetic unit cell, N_c is the number of magnetic unit cells, and $a = 1, \ldots, N_s$ labels the N_s magnetic sublattices, or spin sites, within each unit cell. The total number of spin sites is therefore $N = N_c N_s$, the quadratic Hamiltonian can be written in bosonic Bogoliubov–de Gennes (BdG) form [10, 13, 25],

$$\begin{aligned} H_2 &= E_2 + \frac{1}{2} \sum_{\boldsymbol{k}} \Psi_{\boldsymbol{k}}^\dagger \mathcal{H}_{\mathrm{BdG}}(\boldsymbol{k}) \Psi_{\boldsymbol{k}}, \\ \Psi_{\boldsymbol{k}} &= \begin{pmatrix} b_{\boldsymbol{k}1} & \cdots & b_{\boldsymbol{k}N_s} & b_{-\boldsymbol{k}1}^\dagger & \cdots & b_{-\boldsymbol{k}N_s}^\dagger \end{pmatrix}^T, \\ \mathcal{H}_{\mathrm{BdG}}(\boldsymbol{k}) &= \begin{pmatrix} \mathcal{A}(\boldsymbol{k}) & \mathcal{B}(\boldsymbol{k}) \\ \mathcal{B}^*(-\boldsymbol{k}) & \mathcal{A}^*(-\boldsymbol{k}) \end{pmatrix}. \end{aligned} \tag{1.7}$$

The block $\mathcal{A}(\boldsymbol{k})$ contains the number-conserving terms $b_{\boldsymbol{k}a}^\dagger b_{\boldsymbol{k}b}$, including the magnon on-site energies and hopping amplitudes. The block $\mathcal{B}(\boldsymbol{k})$ contains anomalous terms that create or annihilate pairs of magnons,

$$H_2^{\mathrm{pair}} = \frac{1}{2} \sum_{\boldsymbol{k}} \sum_{a,b} \left[\mathcal{B}_{ab}(\boldsymbol{k}) b_{\boldsymbol{k}a}^\dagger b_{-\boldsymbol{k}b}^\dagger + \mathcal{B}_{ab}^*(\boldsymbol{k}) b_{-\boldsymbol{k}b} b_{\boldsymbol{k}a} \right]. \tag{1.8}$$

For the Hamiltonian in (1.4), the anomalous block contains the combination [13]

$$\mathcal{B}_{ab}(\boldsymbol{k}) = \frac{S}{2} \left[J_{ab}^{xx}(\boldsymbol{k}) - J_{ab}^{yy}(\boldsymbol{k}) - i J_{ab}^{xy}(\boldsymbol{k}) - i J_{ab}^{yx}(\boldsymbol{k}) \right]. \tag{1.9}$$

Equation (1.8) makes clear that the quadratic spin-wave Hamiltonian need not conserve magnon number. However, if the microscopic Hamiltonian has a continuous $U(1)$ spin-rotation symmetry about the ordered axis, then

$$J_{ab}^{xx}(\boldsymbol{k}) = J_{ab}^{yy}(\boldsymbol{k}), \qquad J_{ab}^{xy}(\boldsymbol{k}) = -J_{ab}^{yx}(\boldsymbol{k}), \tag{1.10}$$

and consequently $\mathcal{B}(\boldsymbol{k}) = 0$. In-plane exchange anisotropy, symmetric off-diagonal exchange, dipolar interactions, or a noncollinear choice of local spin frames can instead produce a nonzero anomalous block. The distinction between the number-conserving case $\mathcal{B}(\boldsymbol{k}) = 0$ and the anomalous case $\mathcal{B}(\boldsymbol{k}) \neq 0$ is important both physically and mathematically.

Number-conserving magnon bands. When $\mathcal{B}(\boldsymbol{k}) = 0$, the quadratic spin-wave Hamiltonian reduces to an ordinary bosonic hopping problem,

$$H_2 = E_2 + \sum_{\boldsymbol{k}} \boldsymbol{b}_{\boldsymbol{k}}^\dagger \mathcal{A}(\boldsymbol{k}) \boldsymbol{b}_{\boldsymbol{k}}, \qquad \boldsymbol{b}_{\boldsymbol{k}} = \begin{pmatrix} b_{\boldsymbol{k}1} & \cdots & b_{\boldsymbol{k}N_s} \end{pmatrix}^T. \tag{1.11}$$

The Hermitian matrix $\mathcal{A}(\boldsymbol{k})$ can then be diagonalized by an ordinary unitary transformation,

$$\mathcal{A}(\boldsymbol{k}) \left| u_{n\boldsymbol{k}} \right\rangle = \varepsilon_{n\boldsymbol{k}} \left| u_{n\boldsymbol{k}} \right\rangle, \qquad \left\langle u_{n\boldsymbol{k}} | u_{m\boldsymbol{k}} \right\rangle = \delta_{n,m}. \tag{1.12}$$

The sublattice structure of the magnetic unit cell produces multiple magnon bands, while spin–orbit interactions, noncollinear magnetic order, and dipolar couplings can make their Bloch eigenvectors vary nontrivially throughout the Brillouin zone [13].

A common microscopic mechanism for producing topological magnon bands is the Dzyaloshinskii–Moriya interaction (DMI) [8, 26]. Consider, for example, a bond between two moments in a collinear ferromagnet polarized along the unit vector $\hat{\boldsymbol{z}}$,

$$H_{ij} = -J_{ij} \boldsymbol{S}_i \cdot \boldsymbol{S}_j + \boldsymbol{D}_{ij} \cdot \left(\boldsymbol{S}_i \times \boldsymbol{S}_j \right). \tag{1.13}$$

The component $D_{ij}^{\parallel} = \boldsymbol{D}_{ij} \cdot \hat{\boldsymbol{z}}$ preserves spin rotations about the polarization axis and therefore conserves the magnon number. To quadratic order in the Holstein–Primakoff expansion, its contribution to (1.13) gives

$$\begin{aligned} H_{ij}^{(2)} = &- J_{ij} S^2 + J_{ij} S \left(b_i^\dagger b_i + b_j^\dagger b_j \right) \\ &- S \left[\left(J_{ij} + i D_{ij}^{\parallel} \right) b_i^\dagger b_j + \left(J_{ij} - i D_{ij}^{\parallel} \right) b_j^\dagger b_i \right]. \end{aligned} \tag{1.14}$$

The one-magnon hopping amplitude is therefore complex,

$$t_{ij} = S \left(J_{ij} + i D_{ij}^{\parallel} \right) = S \sqrt{J_{ij}^2 + \left(D_{ij}^{\parallel} \right)^2}\, e^{i\phi_{ij}}, \qquad \phi_{ij} = \tan^{-1}\left(\frac{D_{ij}^{\parallel}}{J_{ij}} \right). \tag{1.15}$$

Although the phase of an individual hopping amplitude depends on the choice of local bosonic basis, the phase accumulated around a closed lattice path C,

$$\Phi_C = \arg \left[\prod_{(ij) \in C} t_{ij} \right], \tag{1.16}$$

is invariant under the local transformation $b_i \to e^{i\chi_i} b_i$. A nontrivial loop phase acts as an effective orbital flux for the neutral magnons [9–11, 27]. On lattices with several sites in each unit cell, it can gap band crossings and generate nonzero Berry curvature. This is the magnonic analogue of the complex hopping responsible for electronic Chern bands. Importantly, in this collinear geometry the DMI modifies the number-conserving block $\mathcal{A}(\boldsymbol{k})$ rather than producing the pairing block $\mathcal{B}(\boldsymbol{k})$.

Bosonic Bogoliubov bands. When $\mathcal{B}(\boldsymbol{k}) \neq 0$, the Nambu doubling in (1.7) becomes essential. Although the resulting Hamiltonian resembles a superconducting BdG Hamiltonian, its diagonalization is fundamentally different because the quasiparticles are bosons. In particular, the Nambu spinor satisfies

$$\left[\Psi_{\boldsymbol{k},\lambda}, \Psi^{\dagger}_{\boldsymbol{k}',\lambda'}\right] = \delta_{\boldsymbol{k},\boldsymbol{k}'}\eta_{\lambda\lambda'}, \qquad \eta = \begin{pmatrix} I_{N_s} & 0 \\ 0 & -I_{N_s} \end{pmatrix}. \tag{1.17}$$

The Heisenberg equation of motion is consequently generated by the dynamical matrix $\eta\mathcal{H}_{\mathrm{BdG}}(\boldsymbol{k})$. The physical frequencies are obtained from the generalized eigenvalue problem

$$\eta\mathcal{H}_{\mathrm{BdG}}(\boldsymbol{k})\,|u_{n\boldsymbol{k}}\rangle = \varepsilon_{n\boldsymbol{k}}\,|u_{n\boldsymbol{k}}\rangle\,, \qquad \langle u_{n\boldsymbol{k}}|\,\eta\,|u_{m\boldsymbol{k}}\rangle = \delta_{n,m}, \tag{1.18}$$

where the normalization shown applies to the positive-frequency, positive-norm branches. The negative-frequency branches are redundant partners required by the Nambu representation.

A matrix $T(\boldsymbol{k})$ formed from the complete set of Bogoliubov eigenvectors must preserve the bosonic commutation relations and therefore satisfies

$$T^{\dagger}(\boldsymbol{k})\eta T(\boldsymbol{k}) = \eta, \qquad T^{-1}(\boldsymbol{k}) = \eta T^{\dagger}(\boldsymbol{k})\eta. \tag{1.19}$$

Such a transformation is paraunitary rather than unitary [10, 13, 25]. The Berry connection of a stable positive-frequency bosonic band must be defined using the same metric [10, 13],

$$\mathcal{A}_{n,\mu}(\boldsymbol{k}) = i\,\langle u_{n\boldsymbol{k}}|\,\eta\,\partial_{k_\mu}\,|u_{n\boldsymbol{k}}\rangle\,. \tag{1.20}$$

For a number-conserving Hamiltonian, the positive-frequency eigenvector has support only in the particle sector, and (1.20) reduces to the usual Bloch-band Berry connection. In two dimensions,

the corresponding Berry curvature and Chern number are

$$\Omega_n(\boldsymbol{k}) = \partial_{k_x}\mathcal{A}_{n,y}(\boldsymbol{k}) - \partial_{k_y}\mathcal{A}_{n,x}(\boldsymbol{k}),$$
$$C_n = \frac{1}{2\pi}\int_{\mathrm{BZ}} d^2\boldsymbol{k}\,\Omega_n(\boldsymbol{k}) \in \mathbb{Z}. \tag{1.21}$$

An individual-band Chern number is defined only if the band remains separated from the other positive-frequency bands throughout the Brillouin zone. Demptomg the minimum direct separation by Δ_n, one requires $\Delta_n > 0$. The Chern number cannot change under a smooth deformation that preserves this gap and the dynamical stability of the bosonic spectrum. In two dimensions, a nonzero C_n implies chiral magnon modes at an interface with a topologically trivial phase [10, 11].

Limits of the quadratic magnon-band description. The preceding classification applies directly to the quadratic Hamiltonian H_2. The higher-order terms H_3, H_4, and beyond in (1.5) generate magnon–magnon interactions [24, 28]. Large S organizes these corrections as an expansion in inverse powers of S, while a low magnon density further suppresses the probability of collisions. Nevertheless, interactions renormalize the magnon energies and can give the quasiparticles finite lifetimes.

At weak coupling, these effects can be expressed through the retarded one-magnon Green's function,

$$G_n^R(\boldsymbol{k},\omega) = \frac{1}{\omega - \varepsilon_{n\boldsymbol{k}} - \Sigma_n^R(\boldsymbol{k},\omega)}, \tag{1.22}$$

where Σ_n^R is the retarded self-energy. The renormalized energy and linewidth are approximately

$$\widetilde{\varepsilon}_{n\boldsymbol{k}} \simeq \varepsilon_{n\boldsymbol{k}} + \mathrm{Re}\,\Sigma_n^R\left(\boldsymbol{k},\varepsilon_{n\boldsymbol{k}}\right),$$
$$\Gamma_{n\boldsymbol{k}} \simeq -\,\mathrm{Im}\,\Sigma_n^R\left(\boldsymbol{k},\varepsilon_{n\boldsymbol{k}}\right). \tag{1.23}$$

For example, a cubic interaction permits a magnon in band n to decay into two magnons when the corresponding matrix element is nonzero and the energy–momentum condition, $\widetilde{\varepsilon}_{n\boldsymbol{k}} = \widetilde{\varepsilon}_{m\boldsymbol{q}} + \widetilde{\varepsilon}_{\ell,\boldsymbol{k}-\boldsymbol{q}}$, can be satisfied. The collection of two-magnon energies on the right-hand side forms a multiparticle continuum [13, 28].

Weak interactions do not automatically destroy the topology of a magnon band. Smooth energy renormalizations leave its Chern number unchanged provided that the renormalized bands remain stable and separated. However, a sharp topological quasiparticle interpretation additionally requires $\Gamma_{n\boldsymbol{k}} \ll \Delta_n$ throughout the relevant region of momentum space. If the linewidth becomes comparable to the band gap, neighboring bands and multi-magnon states can no longer be separated spectroscopically, and a nominal edge mode may strongly hybridize with the bulk continuum. The failure in this case is not necessarily an immediate change of the integer calculated from the quadratic Hamiltonian; rather, it is the loss of the coherent one-magnon band to which that integer was assigned [13, 29].

Finally, this topology characterizes finite-frequency bosonic excitations rather than a filled many-body ground-state band. The magnon vacuum may be topologically trivial even when the one-magnon bands have nonzero Chern numbers. Moreover, because magnon bands are not filled up to a Fermi energy, a nonzero Chern number does not generally fix a quantized bulk response. Spectroscopic, thermal, and spin-transport signals depend additionally on the magnon occupation, dispersion, lifetime, and coupling to the measurement apparatus [9, 13–15].

1.1.3 Magnons in spin-$1/2$ systems

For a spin-$1/2$ system, the physical occupation at each site is restricted to zero or one spin deviation. It is therefore useful to introduce hard-core boson operators d_n through the exact local mapping [30]

$$\begin{aligned} &S_n^z = \frac{1}{2} - d_n^\dagger d_n, \qquad S_n^+ = d_n, \qquad S_n^- = d_n^\dagger, \\ &d_n^2 = (d_n^\dagger)^2 = 0, \qquad \{d_n, d_n^\dagger\} = 1, \qquad [d_n, d_m] = [d_n, d_m^\dagger] = 0 \quad (n \neq m). \end{aligned} \tag{1.24}$$

Thus, hard-core bosons commute on different sites but satisfy a fermion-like on-site algebra. Equivalently, one may begin with canonical bosons β_n and impose the hard-core constraint by adding an infinite on-site repulsion [30],

$$H_U = \lim_{U\to\infty} \frac{U}{2} \sum_n \beta_n^\dagger \beta_n^\dagger \beta_n \beta_n. \tag{1.25}$$

The finite-energy sector of (1.25) contains only occupations zero and one. Hard-core bosons are therefore neither canonical bosons nor canonical fermions, which generally makes their many-body dynamics highly nontrivial.

A particularly important simplification occurs when the fully polarized state is an exact reference state and the Hamiltonian conserves the total spin projection,

$$\left[H, S^z_{\mathrm{tot}}\right] = 0, \qquad S^z_{\mathrm{tot}} = \sum_n S^z_n. \tag{1.26}$$

The Hilbert space then separates into sectors with fixed numbers of spin deviations. In the one-magnon sector, the total number of Holstein–Primakoff bosons is exactly one, so double occupation of a site is impossible and the local hard-core constraint can be ignored. Thus, a large value of S is not required for an exact one-magnon hopping description in this special setting.

This situation is realized approximately in the field-polarized kagome ferromagnet studied in Refs. [11, 18], where the microscopic magnetic moments have $S = 1/2$ but coherent one-magnon bands were resolved experimentally. The component of the DMI parallel to the polarization produces the same complex hopping mechanism as (1.15). Because the kagome unit cell contains three magnetic sites, the one-magnon sector contains three Bloch bands which are gapless in the absence of DMI. The DMI opens open all gap crossings and generates Berry curvature, with two of the three isolated bands carrying opposite nonzero Chern numbers. The spin-$1/2$ value does not produce the topology; it is the complex, direction-dependent hopping induced by the DMI that provides the essential topological ingredient.

As we discussed above, the controlled character of the one-magnon sector does not extend automatically to a finite-density state. Particularly, for spin-1/2 at nonzero temperature or under a drive that creates many spin excitations, the hard-core constraint generates strong effective interactions. Magnon–magnon scattering renormalizes the excitation bands, while couplings between one- and multi-magnon sectors can broaden or destroy the coherent states. In kagome ferromagnets, for example, components of the DMI perpendicular to the magnetization can generate cubic interaction vertices and strong decay into the two-magnon continuum. The resulting linewidth may become comparable to the topological band gap [13, 29].

This limitation is especially relevant for parametric excitation [31–33]. A drive that creates and annihilates spin deviations in pairs does not remain in the one-magnon sector. A canonical-boson approximation would then have to account explicitly for the hard-core repulsion, the excitation-dependent frequency shifts, and the processes that saturate bosonic parametric amplification. The measured response would depend on the nonuniversal occupation and lifetime of the magnon modes rather than only on their Chern numbers. Topological magnon bands are consequently most naturally manifested through finite-frequency spectroscopy, boundary propagation, and thermal or spin transport, provided that the corresponding quasiparticles remain sufficiently coherent and long lived.

In one dimension, the hard-core algebra can instead be represented exactly by canonical spinless fermions through the nonlocal Jordan–Wigner transformation (JWT) [34–36]. Using the Pauli-matrix convention $\sigma_n^\alpha = 2S_n^\alpha$ and $\sigma_n^\pm = (\sigma_n^x \pm i\sigma_n^y)/2$, the relation between spins and spinless fermions is

$$\sigma_n^z = 1 - 2c_n^\dagger c_n, \quad \sigma_n^+ = \left[\prod_{m=1}^{n-1}\left(2c_m^\dagger c_m - 1\right)\right] c_n. \tag{1.27}$$

The operators c_n and $c_n^\dagger$ satisfy the canonical anticommutation relations $\{c_n, c_m\} = \{c_n^\dagger, c_m^\dagger\} = 0$ and $\{a_n, a_m^\dagger\} = \delta_{n,m}$. The nonlocal string in (1.27) converts the commuting off-site algebra of the spin operators into fermionic anticommutation relations. The transformation itself is exact at arbitrary excitation density and does not rely on a dilute-magnon approximation. Whether the resulting fermionic Hamiltonian is noninteracting or interacting depends on the form of the original spin couplings. For a periodic spin chain, the coupling across the boundary acquires a dependence on the total fermion parity; after fixing a parity sector, the corresponding fermionic boundary condition is fixed as well [35, 36].

The JWT therefore provides a complementary route for studying the collective dynamics of a one-dimensional spin-$1/2$ system beyond the single-magnon sector. In the model considered in Part I, spin-exchange terms become fermion hopping, while pairwise spin flips become creation and annihilation of neighboring spinless fermions. Fermionic pair production is bounded by Pauli exclusion and consequently does not exhibit the unbounded mode occupation of an ideal

parametrically driven bosonic theory. Most importantly, the pair-flip term generated by resonant modulation maps onto the p-wave pairing interaction of the Kitaev chain [20–22].

1.2 Periodically driven quantum systems

The static mappings discussed in the previous section do not by themselves explain how an effective pairing interaction can be generated by an external field or how the quantum state responds to the protocol by which that field is applied. At the spin level, the pair-flip interaction $S_i^+ S_j^+ + S_i^- S_j^-$ is proportional to the transverse anisotropy $S_i^x S_j^x - S_i^y S_j^y$. Such an interaction, together with the number-conserving combination $S_i^x S_j^x + S_i^y S_j^y$, has been Floquet engineered experimentally in a chain of transmon qubits using periodic sideband drives [37].

A periodically driven Hamiltonian is described naturally in terms of quasienergies and time-periodic Floquet modes rather than stationary energy eigenstates. In this section, we first introduce the basic framework of Floquet theory. We then specialize to weak near-resonant modulation and show how a transformation to the rotating frame, followed by the rotating-wave approximation (RWA), produces the effective fermionic pairing Hamiltonian that forms the basis for the remainder of Part I.

1.2.1 Continuous and discrete translation symmetry

Symmetry provides one of the most economical routes from the equations of motion to physical predictions. If a continuous transformation leaves the dynamics invariant, Noether's theorem associates that transformation with a conserved quantity [38]. Continuous spatial-translation symmetry gives momentum conservation, while continuous time-translation symmetry gives energy conservation. In quantum mechanics the same connection appears algebraically: when the generator of a symmetry commutes with the Hamiltonian, the corresponding observable is constant in time. A time-independent Hamiltonian therefore has stationary states with a well-defined energy. Once the Hamiltonian depends explicitly on time, continuous time-translation symmetry and ordinary energy conservation are generally lost. Intuitively, the drive can supply energy to, or remove energy from, the system.

Discrete symmetries retain a closely related but slightly different structure. Rather than implying

a continuously generated conserved quantity, a discrete translation allows quantum states to be classified by the phase acquired under that translation. The most famous example is the Bloch theorem for a particle in a spatially periodic potential, $V(x + a) = V(x)$ [39]. Its Hamiltonian commutes with translation by one lattice period. Writing the action of this translation on a wavefunction as $\hat{\mathcal{T}}_a\psi(x) = \psi(x + a)$, the energy eigenstates can be chosen to obey

$$\hat{\mathcal{T}}_a\psi_k(x) = e^{ika}\psi_k(x). \tag{1.28}$$

It follows that $\psi_k(x) = e^{ikx}u_k(x)$ with $u_k(x + a) = u_k(x)$. Because the eigenvalue in (1.28) is unchanged under $k \longrightarrow k + 2\pi m/a$, the *quasimomentum* k is defined modulo a reciprocal lattice vector. Quasimomentum is thus the quantum number associated with discrete spatial-translation symmetry, even though the physical momentum need not be conserved in a lattice.

1.2.2 Floquet theory

Floquet theory is the temporal analogue of the construction above [4, 40–43]. Let $\hat{H}(t+T) = \hat{H}(t)$ and set $\hbar = 1$. Although translation by an arbitrary time is not a symmetry, translation by one drive period is. For a reference time t_0, we can define the one-period evolution operator as $\hat{U}_F(t_0) \equiv \hat{U}(t_0 + T, t_0)$. This unitary operator is the discrete time-translation operator acting on states at t_0. Its eigenvalues lie on the unit circle, so its eigenvectors may be written as

$$\hat{U}_F(t_0)\,|\phi_\alpha(t_0)\rangle = e^{-i\varepsilon_\alpha T}\,|\phi_\alpha(t_0)\rangle = e^{-i\hat{H}_F(t_0)T}\,|\phi_\alpha(t_0)\rangle\,, \tag{1.29}$$

where $\hat{H}_F(t_0) = (i/T)\log\hat{U}_F(t_0)$ is the Floquet Hamiltonian for a chosen branch of the logarithm. To see the consequence of this eigenvalue equation, evolve one such vector according to $|\Psi_\alpha(t)\rangle = \hat{U}(t, t_0)\,|\phi_\alpha(t_0)\rangle$. Periodicity of the Hamiltonian implies $\hat{U}(t + T, t_0 + T) = \hat{U}(t, t_0)$, and therefore

$$|\Psi_\alpha(t + T)\rangle = \hat{U}(t + T, t_0 + T)\hat{U}_F(t_0)\,|\phi_\alpha(t_0)\rangle = e^{-i\varepsilon_\alpha T}\,|\Psi_\alpha(t)\rangle\,. \tag{1.30}$$

Defining $|u_\alpha(t)\rangle = e^{i\varepsilon_\alpha t}\,|\Psi_\alpha(t)\rangle$ then gives the Floquet form

$$|\Psi_\alpha(t)\rangle = e^{-i\varepsilon_\alpha t}\,|u_\alpha(t)\rangle\,, \qquad |u_\alpha(t + T)\rangle = |u_\alpha(t)\rangle\,. \tag{1.31}$$

This implies that the time evolution can be separated into stroboscopic evolution generated by $\hat{H}_F(t_0)$ and a periodic micromotion within every drive cycle generated by $\hat{P}(t, t_0)$ [4, 44, 45]

$$\hat{U}(t, t_0) = \hat{P}(t, t_0) e^{-i\hat{H}_F(t_0)(t-t_0)}, \tag{1.32}$$

where $\hat{P}(t + T, t_0) = \hat{P}(t, t_0)$. Equivalently, using the Schrödinger equation, the periodic part satisfies the eigenvalue problem $\left[\hat{H}(t) - i\partial_t\right] |u_\alpha(t)\rangle = \varepsilon_\alpha |u_\alpha(t)\rangle$ [40, 41].

The parallel with Bloch's theorem is straightforward: e^{ika} is the eigenvalue of one spatial translation, whereas $e^{-i\varepsilon_\alpha T}$ is the eigenvalue of one temporal translation. Consequently, the quasienergy ε_α is defined modulo the drive frequency $\omega_F = 2\pi/T$. Indeed, $\varepsilon_\alpha \to \varepsilon_\alpha + m\omega_F$ accompanied by $|u_\alpha(t)\rangle \to e^{im\omega_F t} |u_\alpha(t)\rangle$ describes the same physical state. A periodic drive therefore does not restore ordinary energy conservation. Instead, quasienergy plays the role of crystal quasimomentum, and the system can exchange energy with the drive in integer multiples of ω_F.

The periodicity of quasienergy becomes especially important near a resonance. To see this, let

$$\hat{H}_0 |n\rangle = E_n |n\rangle, \qquad \hat{V}(t) = \sum_{\ell=-\infty}^{\infty} \hat{V}_\ell e^{i\ell\omega_F t}, \tag{1.33}$$

where $\hat{H}(t) = \hat{H}_0 + \hat{V}(t)$. In the extended Floquet space, the state $|n, m\rangle\rangle = |n\rangle e^{im\omega_F t}$ has the unperturbed quasienergy $E_n + m\omega_F$ [40, 41]. The matrix elements of the quasienergy operator are

$$\left\langle\langle n, m| \left[\hat{H}(t) - i\partial_t\right] |n', m'\rangle\right\rangle = (E_n + m\omega_F)\, \delta_{n,n'}\delta_{m,m'} + \langle n| \hat{V}_{m-m'} |n'\rangle . \tag{1.34}$$

Suppose that two undriven states satisfy $E_\beta - E_\alpha = \ell\omega_F + \delta$, where $|\delta| \ll \omega_F$. The Floquet replicas $|\beta, 0\rangle\rangle$ and $|\alpha, \ell\rangle\rangle$ are then nearly degenerate . A weak periodic perturbation can strongly mix these states because their relevant energy difference is the small detuning δ, rather than the much larger energies E_α and E_β. A rotating transformation removes the rapid phase associated with $\ell\omega_F$ and makes the resonant coupling slowly varying. The rotating-wave approximation consists of retaining this slow coupling while neglecting the remaining rapidly oscillating terms [4, 40].

1.2.3 Near-resonant driving and the rotating-wave approximation

The analysis of resonant driving is best done in a frame rotating with the drive [4, 44, 45]. Let $\hat{R}(t)$ be a time-dependent unitary transformation and define the rotating-frame state by

$|\widetilde{\Psi}(t)\rangle = \hat{R}^\dagger(t)\,|\Psi(t)\rangle$. Substitution into the Schrödinger equation gives

$$i\partial_t|\widetilde{\Psi}(t)\rangle = \widetilde{H}(t)|\widetilde{\Psi}(t)\rangle, \tag{1.35}$$

where the rotating-frame Hamiltonian is $\widetilde{H}(t) = \hat{R}^\dagger(t)\hat{H}(t)\hat{R}(t) - i\hat{R}^\dagger(t)\dot{\hat{R}}(t)$. The second term in $\widetilde{H}(t)$ shifts the energies by the rotation frequency and converts the original energy difference into the small detuning from resonance.

The laboratory- and rotating-frame evolution operators are related by

$$\widetilde{U}(t,t_0) = \mathcal{T}\exp\left[-i\int_{t_0}^{t} dt'\,\widetilde{H}(t')\right] = \hat{R}^\dagger(t)\hat{U}(t,t_0)\hat{R}(t_0). \tag{1.36}$$

For fixed drive parameters, the rotating-frame Hamiltonian can be separated into a time-independent resonant part and rapidly oscillating terms

$$\begin{aligned}
&\widetilde{H}(t) = \hat{H}_{\mathrm{RWA}} + \hat{V}_{\mathrm{fast}}(t),\\
&\hat{H}_{\mathrm{RWA}} = \frac{1}{T}\int_{t_0}^{t_0+T} dt\,\widetilde{H}(t), \qquad \frac{1}{T}\int_{t_0}^{t_0+T} dt\,\hat{V}_{\mathrm{fast}}(t) = 0.
\end{aligned} \tag{1.37}$$

The precise Fourier frequencies appearing in $\hat{V}_{\mathrm{fast}}(t)$ depend on the rotating transformation. They are typically ω_F or integer multiples of ω_F. These rapidly oscillating terms produce only a small net change during many drive cycles. For example, a constant Fourier component $\hat{V}_m e^{im\omega_F t}$ satisfies

$$\left\|\int_{t_0}^{t} dt'\,\hat{V}_m e^{im\omega_F t'}\right\| \le \frac{2\|\hat{V}_m\|}{|m|\omega_F}. \tag{1.38}$$

The contribution is suppressed by the ratio of the coupling strength to the fast oscillation frequency. In the interaction picture, the RWA neglects the contribution of the second factor in (1.37), i.e., $\mathcal{T}\exp\left[-i\int_{t_0}^{t} dt'\,\hat{V}_I(t')\right] \simeq I$, where $\hat{V}_I(t) = e^{i\hat{H}_{\mathrm{RWA}}(t-t_0)}\hat{V}_{\mathrm{fast}}(t)e^{-i\hat{H}_{\mathrm{RWA}}(t-t_0)}$, which gives [4, 45]

$$\begin{aligned}
&\widetilde{U}(t,t_0) \simeq e^{-i\hat{H}_{\mathrm{RWA}}(t-t_0)},\\
&\hat{U}(t,t_0) \simeq \hat{R}(t)e^{-i\hat{H}_{\mathrm{RWA}}(t-t_0)}\hat{R}^\dagger(t_0).
\end{aligned} \tag{1.39}$$

Thus, $\hat{H}_{\mathrm{RWA}}$ generates the slow evolution in the rotating frame, while $\hat{R}(t)$ restores the rapid rotation when the state is transformed back to the laboratory frame. Similar to (1.32), the exact rotating-frame

propagator can be written as

$$\widetilde{U}(t,t_0) = \widetilde{P}(t,t_0)e^{-i\widetilde{H}_F(t_0)(t-t_0)}, \tag{1.40}$$

where again $\widetilde{H}_F(t_0) = (i/T)\log\widetilde{U}_F(t_0)$ and $\widetilde{P}(t+T,t_0) = \widetilde{P}(t,t_0)$, with $\widetilde{U}_F(t_0) \equiv \widetilde{U}(t_0+T,t_0)$. Combining this expression with (1.36) gives the exact laboratory-frame evolution

$$\hat{U}(t,t_0) = \hat{R}(t)\widetilde{P}(t,t_0)e^{-i\widetilde{H}_F(t_0)(t-t_0)}\hat{R}^\dagger(t_0). \tag{1.41}$$

If $\hat{R}(t)$ is itself T-periodic, the laboratory-frame Floquet Hamiltonian and micromotion operator can be chosen as

$$\hat{H}_F(t_0) = \hat{R}(t_0)\widetilde{H}_F(t_0)\hat{R}^\dagger(t_0), \qquad \hat{P}(t,t_0) = \hat{R}(t)\widetilde{P}(t,t_0)\hat{R}^\dagger(t_0). \tag{1.42}$$

The relation between $\hat{H}_{\mathrm{RWA}}$ and $\widetilde{H}_F(t_0)$ can be made systematic using the Floquet–Magnus expansion in the rotating frame [44–46]. One writes $\widetilde{H}_F(t_0) = \widetilde{H}_F^{(0)} + \widetilde{H}_F^{(1)}(t_0) + \widetilde{H}_F^{(2)}(t_0) + \cdots$, where

$$\widetilde{H}_F^{(0)} = \frac{1}{T}\int_{t_0}^{t_0+T} dt\, \widetilde{H}(t) = \hat{H}_{\mathrm{RWA}}, \tag{1.43}$$

and the first correction is

$$\widetilde{H}_F^{(1)}(t_0) = \frac{1}{2iT}\int_{t_0}^{t_0+T} dt_1 \int_{t_0}^{t_1} dt_2\, \left[\widetilde{H}(t_1), \widetilde{H}(t_2)\right]. \tag{1.44}$$

Let Λ denote the largest characteristic local scale among the detuning, the resonant coupling, and the amplitudes of the remaining Fourier harmonics. If $\Lambda \ll \omega_F$, then the terms in the Floquet expansion scale as

$$\widetilde{H}_F^{(0)} = O(\Lambda), \qquad \widetilde{H}_F^{(1)} = O\left(\frac{\Lambda^2}{\omega_F}\right), \qquad \widetilde{H}_F^{(2)} = O\left(\frac{\Lambda^3}{\omega_F^2}\right). \tag{1.45}$$

Therefore,

$$\widetilde{H}_F(t_0) = \hat{H}_{\mathrm{RWA}} + O\left(\frac{\Lambda^2}{\omega_F}\right). \tag{1.46}$$

The RWA Hamiltonian is thus the zeroth-order Floquet Hamiltonian in the rotating frame. Its absolute correction is generically $O(\Lambda^2/\omega_F)$, while its relative correction is $O(\Lambda/\omega_F)$. The leading

correction includes effects such as drive-induced frequency shifts and corrections to the resonant couplings [4, 47]. Similarly, the residual micromotion satisfies

$$\widetilde{P}(t, t_0) = I + O\left(\frac{\Lambda}{\omega_F}\right). \tag{1.47}$$

Consequently, for a T-periodic rotating transformation,

$$\begin{aligned} \hat{H}_F(t_0) &= \hat{R}(t_0)\hat{H}_{\mathrm{RWA}}\hat{R}^\dagger(t_0) + O\left(\frac{\Lambda^2}{\omega_F}\right), \\ \hat{P}(t, t_0) &= \hat{R}(t)\hat{R}^\dagger(t_0) + O\left(\frac{\Lambda}{\omega_F}\right). \end{aligned} \tag{1.48}$$

The RWA therefore makes two approximations: it replaces the exact rotating-frame Floquet Hamiltonian by $\hat{H}_{\mathrm{RWA}}$, and it neglects the residual micromotion $\widetilde{P}(t, t_0)$.

Strict Floquet theory also assumes fixed periodic drive parameters. If the amplitude or frequency changes during the turn-on protocol, the Hamiltonian is not exactly periodic over the full preparation interval. A slowly varying rotating-frame description remains appropriate when the envelope and frequency vary little during one drive cycle, for example,

$$\frac{|\dot{F}|}{\omega_F^2} \ll 1, \qquad \frac{|\dot{\omega}_F|}{\omega_F^2} \ll 1. \tag{1.49}$$

The turn-on may nevertheless be sudden on the much longer RWA time scale Λ^{-1}. Once the parameters become constant, the usual Floquet Hamiltonian is again well defined.

Rotation at half the drive frequency and parity. Parametric excitation creates or annihilates excitations in pairs [21, 22, 31, 32]. Let $\hat{N}_{\mathrm{ex}}$ count the excitations and let $\hat{B}^\dagger$ create a pair, so that

$$\left[\hat{N}_{\mathrm{ex}}, \hat{B}^\dagger\right] = 2\hat{B}^\dagger, \qquad \left[\hat{N}_{\mathrm{ex}}, \hat{B}\right] = -2\hat{B}. \tag{1.50}$$

Consider a pair drive of the form

$$\hat{H}_{\mathrm{pair}}(t) = 2F\cos\left[\omega_F(t - t_0)\right]\left(\hat{B}^\dagger + \hat{B}\right). \tag{1.51}$$

The natural transformation rotates each individual excitation at $\omega_F/2$,

$$\hat{R}_{1/2}(t) = \exp\left[-i\frac{\omega_F}{2}(t - t_0)\hat{N}_{\mathrm{ex}}\right], \qquad \hat{R}_{1/2}(t_0) = I. \tag{1.52}$$

It follows that $\hat{R}^{\dagger}_{1/2}(t)\hat{B}^{\dagger}\hat{R}_{1/2}(t) = e^{i\omega_F(t-t_0)}\hat{B}^{\dagger}$. The transformed pair drive is therefore

$$\hat{R}^{\dagger}_{1/2}(t)\hat{H}_{\text{pair}}(t)\hat{R}_{1/2}(t) = F\left[\left(1+e^{2i\omega_F(t-t_0)}\right)\hat{B}^{\dagger} + \left(1+e^{-2i\omega_F(t-t_0)}\right)\hat{B}\right]. \tag{1.53}$$

The constant terms describe resonant pair creation and annihilation, whereas the terms oscillating at $2\omega_F$ are discarded in the RWA [31, 32]. The transformation also contributes

$$-i\hat{R}^{\dagger}_{1/2}(t)\dot{\hat{R}}_{1/2}(t) = -\frac{\omega_F}{2}\hat{N}_{\text{ex}}, \tag{1.54}$$

which converts the original excitation energy into the detuning from half the drive frequency. For a spin-1/2 chain,

$$\hat{N}_{\text{ex}} = \frac{1}{2}\sum_{n=1}^{N}\left(1-\sigma^z_n\right), \quad \hat{R}_{1/2}(t) = \exp\left[-i\frac{\omega_F}{2}(t-t_0)\hat{N}_{\text{ex}}\right], \tag{1.55}$$

which is the rotating transformation used for the parametrically modulated spin chain [21, 22].

The half-frequency rotation is not generally T-periodic as was assumed in (1.48). Instead,

$$\hat{R}_{1/2}(t+T) = \hat{R}_{1/2}(t)e^{-i\pi\hat{N}_{\text{ex}}} = \hat{R}_{1/2}(t)\hat{\Pi}, \qquad \hat{\Pi} = (-1)^{\hat{N}_{\text{ex}}}, \tag{1.56}$$

where $\hat{\Pi}$ is the excitation-parity operator. The transformation is strictly periodic only after two drive periods, i.e., $\hat{R}_{1/2}(t+2T) = \hat{R}_{1/2}(t)$. For a pair-driven system, parity is conserved, and we have $\left[\hat{\Pi}, \widetilde{H}(t)\right] = \left[\hat{\Pi}, \hat{H}_{\text{RWA}}\right] = 0$. Using $\hat{R}_{1/2}(t_0) = I$, the exact one-period propagator is related to the rotating-frame Floquet Hamiltonian by $\hat{U}_F(t_0) = \hat{\Pi}\exp\left(-i\widetilde{H}_F(t_0)T\right)$, and we can see that equation (1.48) now takes the new form

$$\begin{aligned}
\hat{H}_F(t_0) &= \hat{H}_{\text{RWA}} + \frac{\omega_F}{4}\left(I-\hat{\Pi}\right) + O\left(\frac{\Lambda^2}{\omega_F}\right) \mod \omega_F, \\
\hat{P}(t,t_0) &= \hat{R}_{1/2}(t)\exp\left[i\frac{\omega_F}{4}\left(I-\hat{\Pi}\right)(t-t_0)\right]\hat{R}^{\dagger}_{1/2}(t_0) + O\left(\frac{\Lambda}{\omega_F}\right).
\end{aligned} \tag{1.57}$$

The parity-dependent term in (1.57) shifts the quasienergies of the odd-parity sector by $\omega_F/2$, while leaving the even-parity sector unchanged. Equivalently, an odd-parity state acquires an additional phase of -1 after one drive period. The apparent $2T$ periodicity of the half-frequency rotation is therefore divided between the Floquet Hamiltonian and the micromotion operator, which

remains T periodic. Consequently, the use of a rotating frame at $\omega_F/2$ does not by itself imply a physical period-doubled response [48–50].

A period-doubled signal can arise when two Floquet states of opposite parity have quasienergies separated by one half of the Floquet zone,

$$\varepsilon_{\beta,-} - \varepsilon_{\alpha,+} = \frac{\omega_F}{2} \mod \omega_F, \tag{1.58}$$

and the initial state contains coherence between them. For an observable $\hat{O}_-$ that is odd under parity, $\hat{\Pi}\hat{O}_-\hat{\Pi} = -\hat{O}_-$, the corresponding interference term changes sign after one period,

$$\langle \hat{O}_-(t+T)\rangle = -\langle \hat{O}_-(t)\rangle, \qquad \langle \hat{O}_-(t+2T)\rangle = \langle \hat{O}_-(t)\rangle. \tag{1.59}$$

Such a response requires both the quasienergy relation in (1.58) and a state and observable that connect the two parity sectors. If the initial density matrix is diagonal in parity, or if the observable is parity even, the parity shift alone does not generate period doubling. In particular, the longitudinal magnetization and longitudinal spin correlations considered in Part I are parity-even observables [48–50].

Connection to long-time averages. The response of an isolated driven system contains information beyond a quasienergy spectrum. One must specify an initial state and a protocol. After a quench, different Floquet or quasiparticle components acquire different phases. Their interference can make the instantaneous expectation value oscillatory even after the drive parameters have become stationary. A reproducible long-time response is therefore often defined in the weak sense of a time average [5, 51],

$$\overline{A} = \lim_{\bar{T}\to\infty} \frac{1}{\bar{T}} \int_{t_f}^{t_f+\bar{T}} dt\ \langle \Psi_0|A(t)|\Psi_0\rangle\,, \tag{1.60}$$

where t_f is the time at which a ramp ends. In the Floquet basis, averaging suppresses off-diagonal contributions with nondegenerate quasienergy differences and also averages the periodic micromotion over the drive cycle. For the effective integrable model studied in Part I, the resulting value is fixed by conserved quasiparticle-mode occupations and is closely related to a diagonal or generalized Gibbs ensemble [5, 51–53].

Two features make this response especially revealing in the present problem. First, the resonant modulation opens gaps near selected momenta. The same momentum-space structure determines both the topological winding and the density of excitations created by a quench. Second, a gap closes when the modulation is initiated inside the topological interval. Consequently, the limit of an arbitrarily slow ramp is not uniform in momentum, and the resulting state remembers how the gap was opened [5, 22].

1.3 The Kitaev chain: bulk topology and Majorana edge modes

The preceding section established how a weak near-resonant modulation can be described by a time-independent Hamiltonian in the rotating-wave approximation. For the one-dimensional spin-$1/2$ system considered I, the Jordan–Wigner transformation converts the spin-exchange interaction into fermion hopping and converts pairwise spin flips into the creation and annihilation of neighboring spinless fermions. The resulting rotating-frame Hamiltonian map onto the Kitaev chain, a one-dimensional spinless p-wave superconductor [20, 54, 55]. Consequently, the topology of the driven spin system is inherited from the bulk topology of the Kitaev chain. We therefore review its bulk spectrum, winding number, and Majorana boundary modes before returning to the specific driven-spin realization.

1.3.1 Hamiltonian and Majorana representation

For an open chain of N sites, the Kitaev Hamiltonian is

$$\hat{H}_{\mathrm{K}} = -\mu \sum_{n=1}^{N} \left(c_n^\dagger c_n - \frac{1}{2} \right) + J \sum_{n=1}^{N-1} \left(c_n^\dagger c_{n+1} + c_{n+1}^\dagger c_n \right) + F \sum_{n=1}^{N-1} \left(c_n^\dagger c_{n+1}^\dagger + c_{n+1} c_n \right). \tag{1.61}$$

Here, μ is the chemical potential, J is the nearest-neighbor hopping amplitude, and F is the nearest-neighbor pairing amplitude. The operators c_n and $c_n^\dagger$ satisfy the canonical fermionic anticommutation relations.

When $F = 0$, the Hamiltonian conserves the total fermion number,

$$\hat{\mathcal{N}} = \sum_{n=1}^{N} c_n^\dagger c_n, \qquad \left[\hat{H}_{\mathrm{K}}, \hat{\mathcal{N}} \right] = 0. \tag{1.62}$$

The pairing term changes the fermion number by two and therefore breaks this continuous $U(1)$

symmetry. It nevertheless preserves the fermion parity [20, 54],

$$\hat{\Pi} = (-1)^{\hat{N}} = e^{i\pi\hat{N}}, \qquad \left[\hat{H}_{\mathrm{K}}, \hat{\Pi}\right] = 0. \tag{1.63}$$

The pairing is p-wave because it acts between identical spinless fermions on neighboring sites. The physical content of (1.61) becomes particularly transparent after decomposing each complex fermion into two Majorana operators,

$$\gamma_n^A = c_n^\dagger + c_n, \qquad \gamma_n^B = i\left(c_n^\dagger - c_n\right). \tag{1.64}$$

These operators are Hermitian and satisfy $\left(\gamma_n^\alpha\right)^\dagger = \gamma_n^\alpha$, and $\{\gamma_n^\alpha, \gamma_m^\beta\} = 2\delta_{n,m}\delta_{\alpha,\beta}$. Conversely,

$$c_n = \frac{1}{2}\left(\gamma_n^A + i\gamma_n^B\right), \qquad c_n^\dagger = \frac{1}{2}\left(\gamma_n^A - i\gamma_n^B\right). \tag{1.65}$$

Thus, each ordinary fermionic degree of freedom may be represented by two Majorana operators located on the same site. Substituting (1.65) into (1.61) gives

$$\hat{H}_{\mathrm{K}} = -\frac{i\mu}{2}\sum_{n=1}^{N}\gamma_n^A\gamma_n^B + \frac{i(J-F)}{2}\sum_{n=1}^{N-1}\gamma_n^A\gamma_{n+1}^B - \frac{i(J+F)}{2}\sum_{n=1}^{N-1}\gamma_n^B\gamma_{n+1}^A. \tag{1.66}$$

Two limiting cases illustrate the distinction between the trivial and topological regimes. First, consider $J = F = 0$. The Hamiltonian becomes

$$\hat{H}_{\mathrm{K}} = -\frac{i\mu}{2}\sum_{n=1}^{N}\gamma_n^A\gamma_n^B. \tag{1.67}$$

Each Majorana operator is coupled to the other Majorana on the same site. The two Majoranas therefore recombine locally into an ordinary fermion, and no unpaired boundary operators remain. A contrasting limit is $\mu = 0$ and $J = F$. In this case,

$$\hat{H}_{\mathrm{K}} = -iJ\sum_{n=1}^{N-1}\gamma_n^B\gamma_{n+1}^A. \tag{1.68}$$

The Majorana operator γ_n^B on one site is now coupled to γ_{n+1}^A on the neighboring site. The operators γ_1^A and γ_N^B do not appear in the Hamiltonian and therefore commute with it, i.e., $\left[\hat{H}_{\mathrm{K}}, \gamma_1^A\right] = \left[\hat{H}_{\mathrm{K}}, \gamma_N^B\right] = 0$. They can be combined into a nonlocal fermion,

$$f = \frac{1}{2}\left(\gamma_1^A + i\gamma_N^B\right), \qquad f^\dagger = \frac{1}{2}\left(\gamma_1^A - i\gamma_N^B\right). \tag{1.69}$$

Occupying this fermion changes the total parity but costs no energy in this limiting case. Because its two Majorana components are localized at opposite ends of the chain, a local parity-preserving perturbation cannot couple them directly. This spatial separation is the origin of the exponential protection of the corresponding parity doublet in a long, but finite, chain.

1.3.2 Bulk spectrum

To determine when the two limiting cases belong to distinct phases, we first remove the boundaries and examine the bulk Hamiltonian. For a periodic chain, introduce the Fourier transformation

$$c_n = \frac{e^{-i\pi/4}}{\sqrt{N}} \sum_k e^{ikn} c_k. \tag{1.70}$$

The phase $e^{-i\pi/4}$ is a convenient convention that makes the momentum-space pairing term real. In a Jordan–Wigner representation of a periodic spin chain, the allowed momenta depend on the fermion-parity sector [35, 36]. In the thermodynamic limit, this changes only the discrete momentum grid and does not affect the bulk spectrum or its topological classification.

Defining the Nambu spinor $\Psi_k = \begin{pmatrix} c_k & c_{-k}^\dagger \end{pmatrix}^T$, the Hamiltonian can be written as

$$\begin{aligned} \hat{H}_{\mathrm{K}} &= -\frac{1}{2} \sum_k \Psi_k^\dagger \mathcal{H}_{\mathrm{BdG}}(k) \Psi_k, \\ \mathcal{H}_{\mathrm{BdG}}(k) &= M_k \tau_z + F_k \tau_x, \qquad M_k = \mu - 2J\cos k, \qquad F_k = 2F \sin k, \end{aligned} \tag{1.71}$$

where τ_α are the Pauli matrices which act in Nambu space. The Bogoliubov spectrum is

$$\varepsilon_k = \sqrt{M_k^2 + F_k^2} = \sqrt{(\mu - 2J\cos k)^2 + 4F^2 \sin^2 k}. \tag{1.72}$$

A bulk gap closes when both components of the BdG Hamiltonian vanish, $M_k = F_k = 0$. For $F \neq 0$, the second condition requires $k = 0$ or $k = \pi$. The two phase boundaries are therefore $\mu = 2J$ at $k = 0$ or $\mu = -2J$ at $k = \pi$. When $F = 0$, the system is instead gapless throughout the interval $|\mu| \leq 2|J|$. A change of topological invariant must pass through one of these bulk gap closings.

1.3.3 Winding number

The BdG Hamiltonian obeys particle–hole symmetry,

$$\tau_x \mathcal{H}_{\mathrm{BdG}}^*(k) \tau_x = -\mathcal{H}_{\mathrm{BdG}}(-k). \tag{1.73}$$

For real μ, J, and F, it also contains only τ_x and τ_z and therefore anticommutes with τ_y,

$$\left\{\tau_y, \mathcal{H}_{\mathrm{BdG}}(k)\right\} = 0. \tag{1.74}$$

This chiral symmetry constrains the BdG vector to the (τ_x, τ_z) plane and places the real Kitaev chain in symmetry class BDI. The corresponding bulk classification is an integer winding number. Particle–hole symmetry alone would instead give the $\mathbb{Z}_2$ classification of symmetry class D [3, 56–58].

To define the winding number, we define the two-component vector $\boldsymbol{h}(k) = (M_k \quad F_k)^T$, and its polar angle $\theta_k = \arg\left[M_k + iF_k\right]$. Then, the winding number is [20, 58]

$$\nu = \frac{1}{2\pi}\int_{-\pi}^{\pi} dk\, \partial_k \theta_k. \tag{1.75}$$

As k traverses the Brillouin zone, $\boldsymbol{h}(k)$ traces an ellipse in the (F_k, M_k) plane. The Hamiltonian is topological precisely when this closed curve encloses the origin [20, 58]. The result is

$$\nu = \begin{cases} -\operatorname{sgn}(JF), & |\mu| < 2|J|, \quad F \neq 0, \\ 0, & |\mu| > 2|J|. \end{cases} \tag{1.76}$$

For the convention $J > 0$, this reduces to $\nu = \operatorname{sgn}(F)$ in the topological regime. The sign depends on the orientation convention for the Brillouin zone and the BdG vector, whereas $|\nu|$ determines the number of Majorana zero modes at each boundary. When fermionic hopping is allowed up to the n-th nearest neighbor, the winding number ranges from $-n$ to n [59].

The winding number is undefined at the gap-closing points. In particular, changing the sign of F within $|\mu| < 2|J|$ changes ν from $+1$ to -1 by passing through the gapless line $F = 0$. The two signs have the same number of boundary modes but exchange which Majorana component is localized at a given edge.

The integer invariant remains unchanged under any smooth deformation that preserves the bulk gap and the chiral symmetry. If chiral symmetry is broken while particle–hole symmetry and fermion parity remain, the integer classification reduces to a $\mathbb{Z}_2$ distinction between the trivial phase and a phase containing one Majorana mode per edge [3, 56, 57].

1.3.4 Majorana boundary modes

The bulk–boundary correspondence predicts one Majorana zero mode at each end of an open nearest-neighbor chain when $|\nu| = 1$ [20, 54]. This can also be seen directly by constructing the edge operators.

For definiteness, take $J > 0$ and $F > 0$ and consider a semi-infinite chain extending from $n = 1$. A left-edge Majorana operator may be written as

$$\Gamma_L = \sum_{n=1}^{\infty} u_n \gamma_n^A, \qquad \Gamma_L^\dagger = \Gamma_L. \tag{1.77}$$

Requiring $[\hat{H}_\mathrm{K}, \Gamma_L] = 0$ in the bulk gives the recurrence relation

$$(J - F)u_{n-1} - \mu u_n + (J + F)u_{n+1} = 0, \tag{1.78}$$

with the boundary condition $u_0 = 0$. Using the ansatz $u_n \propto \lambda^n$ gives

$$(J + F)\lambda^2 - \mu\lambda + (J - F) = 0, \tag{1.79}$$

whose roots are

$$\lambda_\pm = \frac{\mu \pm \sqrt{\mu^2 - 4\left(J^2 - F^2\right)}}{2(J + F)}. \tag{1.80}$$

For distinct roots, the amplitude has the form $u_n = \alpha_+\lambda_+^n + \alpha_-\lambda_-^n$, and the boundary condition $u_0 = 0$ gives $\alpha_+ + \alpha_- = 0$. A normalizable left-edge mode requires both independent solutions needed to satisfy the boundary condition to decay into the bulk, i.e., $|\lambda_\pm| < 1$. For $J > 0$ and $F > 0$, this occurs precisely when $|\mu| < 2J$. The localization length is controlled by the root of largest magnitude, $\xi^{-1} = -\ln\left[\max\left(|\lambda_+|, |\lambda_-|\right)\right]$. When the roots form a complex-conjugate pair, the edge wavefunction decays exponentially while oscillating in space.

For a finite chain, a corresponding right-edge operator is localized in the γ_n^B sector. Its amplitudes may be written in terms of the distance from the right boundary,

$$\Gamma_R = \sum_{n=1}^{N} v_n \gamma_n^B, \qquad v_n = \beta_+\lambda_+^{N+1-n} + \beta_-\lambda_-^{N+1-n}. \tag{1.81}$$

For $F < 0$, the localization pattern is exchanged: the left mode is constructed predominantly from γ_n^B, while the right mode is constructed predominantly from γ_n^A. This exchange is the boundary manifestation of the change $\nu \to -\nu$.

In the trivial regime $|\mu| > 2|J|$, the two decaying solutions required to satisfy the boundary condition are not available. A normalizable zero-energy edge operator therefore cannot be constructed. At $|\mu| = 2|J|$, one root reaches the unit circle, the localization length diverges, and the edge state merges with the bulk at the topological transition.

For a finite chain, the two edge wavefunctions overlap. The Majorana operators then commute with the Hamiltonian only up to an exponentially small correction,

$$\left[\hat{H}_{\mathrm{K}}, \Gamma_L\right], \left[\hat{H}_{\mathrm{K}}, \Gamma_R\right] = O\left(e^{-N/\xi}\right), \qquad \delta E = O\left(e^{-N/\xi}\right). \tag{1.82}$$

The exact zero-energy degeneracy is therefore recovered in the thermodynamic limit. Nevertheless, as long as the bulk remains gapped and fermion parity is preserved, local perturbations can couple the two ends only through their exponentially small overlap. This overlap was missing in the semi-infinite discussion of boundary modes. However, it becomes essential for a finite chain, as it allows the solution to satisfy the additional boundary conditions.

The bulk and boundary descriptions are thus equivalent:

$$\begin{aligned} \nu = 0 \quad &\Longleftrightarrow \quad \text{no Majorana boundary mode,} \\ |\nu| = 1 \quad &\Longleftrightarrow \quad \text{one Majorana mode at each boundary.} \end{aligned} \tag{1.83}$$

In the driven spin chain studied I, the detuning of the modulation from resonance acts as an effective chemical potential μ, the spin-exchange interaction provides the hopping amplitude J, and the resonantly generated pair-flip interaction provides the p-wave pairing amplitude F. Varying the modulation frequency therefore tunes the effective Kitaev chain through the phase boundaries $|\mu| = 2|J|$. For an open chain, this transition controls the emergence of Majorana boundary modes. Previous studies of open Ising and Kitaev chains showed that strong zero modes localized at the boundaries can produce anomalously long edge-spin coherence [60, 61]. Related noise-resilient strong edge modes were subsequently observed in a periodically driven chain of 47 superconducting

qubits [62]. By contrast, we first focus on bulk effects. We consider a periodic chain with no physical edges, for which the same bulk transition is characterized by the winding number in (1.75). We later show how these results are modified for a finite chain with open ends. The central question is therefore how this bulk topology is encoded in the magnetization, correlations, and preparation-dependent long-time response of the original spin system [22].

1.4 Bulk dynamical signatures in the driven spin chain

We now turn to the specific model studied in Part I. We begin with a brief overview of its physical ingredients and show how it connects to the Floquet and Kitaev-chain frameworks developed in the preceding sections. We then introduce the preparation protocols considered in our analysis and define the observables used to characterize the resulting dynamics. Finally, we summarize the principal results and their physical implications.

1.4.1 Physical setting and possible realizations

We consider a one-dimensional spin-$1/2$ chain in a strong static magnetic field. The field defines a large single-spin Larmor frequency and favors an initially polarized state. Neighboring spins are weakly coupled through an anisotropic transverse interaction, and one component of this interaction is modulated periodically at a frequency close to twice the Larmor frequency. This parametric modulation can therefore resonantly create or annihilate two neighboring spin excitations. For a translationally invariant chain, these excitations are created in pairs with opposite quasimomenta.

While the modulation amplitude is weak compared with the Larmor frequency, its resonant character still allows it to produce a substantial response. The system therefore satisfy the conditions used to obtain Eq. (1.39). Thus, in a frame rotating at half the modulation frequency, the rapidly oscillating nonresonant processes can be neglected within the rotating-wave approximation. The remaining number-conserving spin-exchange term maps onto fermion hopping under the Jordan–Wigner transformation (1.27), while the pair-flip term generated by the modulation maps onto nearest-neighbor p-wave pairing. The detuning of half the modulation frequency from the Larmor frequency acts as an effective chemical potential. The rotating frame physics of the driven spin

chain is consequently described by the Kitaev-chain Hamiltonian (1.61), with the correspondences

$$\text{detuning} \longleftrightarrow \mu, \qquad \text{static exchange} \longleftrightarrow J, \qquad \text{modulation amplitude} \longleftrightarrow F. \tag{1.84}$$

As we discussed in Sec. 1.3, the effective fermionic system is topologically nontrivial for $|\mu| < 2|J|$ and trivial for $|\mu| > 2|J|$. The modulation frequency therefore provides a direct external control parameter for moving the system across its topological phase boundaries [21, 22].

The local two-state constraint of a spin-$1/2$ system is important for the dynamics. Within a quadratic approximation, a bosonic parametric magnon mode can acquire an arbitrarily large occupation. This unlimited growth not only render the single-magnon band topology irrelevant to the overall dynamics, but also complicates the theoretical analysis, as these high occupation must ultimately be stabilized by damping or nonlinear interactions. By contrast, each Jordan–Wigner fermion mode can be occupied at most once. Parametric pair creation is therefore bounded by Pauli exclusion, allowing the ideal closed spin chain to display coherent and dephasing dynamics without a runaway instability.

One direct candidate for experimental realization of this model is superconducting-qubit. Floquet sideband driving has already been used to engineer both the pairing interaction $XX - YY$ and the number-conserving hopping interaction $XX + YY$ in a one-dimensional chain of six transmon qubits, with independent control of the effective XX and YY couplings [37]. Related experiments on substantially larger superconducting-qubit chains have resolved symmetry-protected strong edge dynamics [62]. More generally, the same effective model can arise in a field-polarized spin chain whenever an anisotropic exchange component can be modulated coherently near twice the spin transition frequency.

The periodic chain considered first I is an idealized geometry chosen to isolate the bulk response from boundary effects. In an experimental open chain, the corresponding bulk behavior can be probed sufficiently far from the ends. The changes introduced by finite open boundaries are treated explicitly in Chapter 4.

1.4.2 Preparation protocols and observables

We consider the dynamical bulk response of the spin chain after the parametric modulation is switched on. In the absence of the drive, the strong static magnetic field fully polarizes the spins, preparing the initial state of the system. This polarized state is both the vacuum of the Jordan–Wigner fermions and an eigenstate of the undriven Hamiltonian. Once the modulation is applied, however, it is no longer an eigenstate of the effective rotating-frame Hamiltonian, and pairs of spin excitations are created.

We consider several protocols for preparing the final driven state. In a sudden turn-on, the modulation is switched on rapidly with a fixed modulation frequency over a time short compared with the effective dynamical time scales J^{-1} and F^{-1}, while its envelope still varies slowly over the much shorter Larmor period so that the rotating-wave approximation remains valid (Eq. (1.49)). In a slow turn-on, the modulation amplitude is increased over a time much longer than the characteristic effective dynamical time. Nevertheless, when the drive is switched on at a frequency corresponding to the topological regime, a fully adiabatic preparation is not possible in the thermodynamic limit because the instantaneous gap closes at the beginning of the ramp. We also consider a frequency-sweep protocol in which the modulation is first established in the topologically trivial regime and its frequency is subsequently swept into the topological interval. These protocols can produce different states even when they all end at the same values of μ, J, and F. The final Hamiltonian alone therefore does not determine the observed response.

After the drive parameters have reached their final stationary values, we study continuous long-time averages of bulk spin observables, as in Eq. (1.60). The simplest of these is the longitudinal magnetization change, $\Delta m_z \equiv 1 - \overline{\langle \sigma_n^z \rangle}$, which directly determines the density of spin excitations through $\overline{\langle c_n^\dagger c_n \rangle} = m_z/2$. We also consider the connected longitudinal correlations $Q^z(m) = \overline{\langle \Delta\sigma_n^z \Delta\sigma_{n+m}^z \rangle}$, where $\Delta\sigma_n^z = \sigma_n^z - \left\langle \sigma_n^z \right\rangle$, and the magnitude of the nearest-neighbor transverse correlator $|\overline{\langle \sigma_n^+ \sigma_{n+1}^- \rangle}|$. These quantities involve only one- and two-spin measurements and are therefore considerably simpler to access than a complete reconstruction of the many-body state or its momentum-resolved Bogoliubov wavefunctions [22].

All observables considered here are even under the fermion-parity transformation and therefore commute with the parity operator $\hat{\Pi}$. Moreover, the fully polarized initial state has definite parity, and the pair-driven Hamiltonian preserves parity. The expectation value of any parity-odd operator consequently vanishes at all times for the preparation protocols considered here. More generally, if the initial state contains coherence between opposite-parity Floquet sectors, a parity-odd observable may contain a period-doubled contribution satisfying Eq. (1.59). Such a contribution changes sign after every drive period and therefore vanishes under a continuous long-time average over many periods.

1.4.3 Overview of the principal results

We now give a brief overview of the main results. For a sudden turn-on, the time-averaged magnetization exhibits a striking plateau throughout the topologically nontrivial interval. In the thermodynamic limit and for the ideal polarized initial state, the excitation density is

$$1 - m_z = \frac{1}{1 + |J/F|} \qquad |\mu| < 2|J|. \tag{1.85}$$

The response is therefore independent of the modulation frequency throughout the topological interval, even though changing the frequency changes the resonant momenta. Outside this interval, the response again has the conventional frequency dispersion and decreases as the modulation is moved away from resonance [22].

The origin of this plateau is most transparent for a weak modulation. From Eq. (1.75), we can define the winding number density as $(2\pi)^{-1}\partial_k\theta_k$. In the topological regime, the driven spectrum crosses zero at two opposite momenta in the zero drive limit. Non-zero modulation opens narrow gaps near these momenta. Both the winding number density and density of excitations $\langle c_k^\dagger c_k\rangle$ produced by a sudden turn-on become concentrated near the same two momentum regions. Changing the detuning moves these regions through the Brillouin zone but does not change their integrated weight. Away from the phase boundaries, we get

$$\langle c_k^\dagger c_k\rangle = -\frac{F}{2J}\frac{\partial\theta_k}{\partial k}, \qquad |F| \ll |J|. \tag{1.86}$$

Thus, to leading order, the integrated excitation density distinguishes the sectors with $|\nu| = 1$ and $\nu = 0$.

The plateau in (1.85) is not a quantized response: its height depends continuously on F/J. Its topological content lies instead in its absence of frequency dispersion, its restriction to the interval with nonzero winding number, and its weak-drive connection to the integral of the winding-number density. The drive effectively converts a momentum-space winding into a spatially averaged spin response.

The correlations contain complementary information. After a sudden turn-on, the connected longitudinal correlations vanish in the topological regime, whereas they are nonzero in the trivial regime. Transverse correlations remain finite and vary with the detuning inside the topological interval. The derivatives of the magnetization and correlations with respect to the modulation frequency are nonanalytic at $|\mu| = 2|J|$, where the quasiparticle gap closes and the winding number changes [22].

A slow turn-on preserves the frequency-independent magnetization plateau, but it does not produce the same state as a sudden turn-on. In particular, the longitudinal correlations generally remain nonzero, although they are strongly suppressed near resonance. A key difference in the analysis is that the slow-ramp limit is singular inside the topological interval. At the beginning of the ramp, the pairing amplitude vanishes and the instantaneous gap closes at the two resonant momenta. Consequently, there is always a shrinking momentum window in which adiabaticity fails, regardless of how slowly the modulation is applied. The size of this window determines the leading nonadiabatic correction.

Preparation history becomes even more explicit when the final state is reached by changing the modulation frequency. Turning on the drive inside the topological regime and turning it on in the trivial regime before sweeping its frequency through the transition can lead to different time-averaged correlations at the same final Hamiltonian. A frequency sweep through $|\mu| = 2|J|$ also introduces Kibble–Zurek-type critical dynamics. The resulting hysteresis is a memory of the path through parameter space rather than a property of the final spectrum alone [22].

The periodic, noninteracting chain provides the cleanest setting in which to expose these effects, but the later chapters of Part I test how they change when its simplifying assumptions are relaxed. Opening the chain removes exact momentum conservation, mixes degenerate bulk propagation channels at the boundaries, and permits localized edge solutions. Depending on the parameters, the spectrum splits into singe- and two- channel regions. Both regions generally participate in the dynamics, and the boundary conditions determine how they combine. This makes the finite open chain a genuinely different dynamical problem rather than merely a truncated version of the periodic system. It also makes the order of the long-time and thermodynamic limits physically important.

1.4.4 Physical significance

Topological invariants are nonlocal functions of the Bloch or Bogoliubov eigenstates and are not usually represented by a simple local order parameter. Earlier dynamical measurements have successfully extracted topological information by reconstructing momentum-space spin textures, dynamical vortices, linking numbers, or topological charges after a quench [63, 64]. The present system provides a complementary route. Resonant pair excitation supplies a momentum-selective weight whose integral is reflected in the ordinary bulk magnetization. As a result, topology can be inferred from a one-point observable and strengthened by measurements of low-order correlations, without requiring a physical edge, transverse transport, or complete momentum-space state tomography.

This feature suggests a relatively low-overhead diagnostic for analog quantum simulators. The hopping and pairing interactions can first be Floquet engineered and calibrated, after which scanning the modulation frequency tests whether the magnetization develops the predicted plateau and whether the correlation pattern changes at its endpoints. The same measurement can therefore probe the engineered pairing interaction, locate the effective topological phase boundaries, and test the validity of the rotating-wave description. The demonstrated control of $XX + YY$ and $XX - YY$ interactions in transmon arrays makes this use of the response experimentally concrete [37].

The preparation dependence adds a second type of information. Two protocols that realize the same final effective Hamiltonian need not produce the same time-averaged state. Comparing sudden

turn-on, slow amplitude-ramp, and frequency-sweep protocols therefore probes nonadiabaticity, dephasing, and the conserved mode occupations of the effective integrable system. The resulting hysteresis provides a controllable way to encode and read out the history of a nonequilibrium preparation.

More broadly, these results illustrate a mechanism by which resonant driving can make an abstract topological invariant visible in a bulk observable. The response is nonuniversal in magnitude, but its frequency dependence, correlation structure, and singular behavior at the transition are constrained by the topology of the effective Hamiltonian. This distinction between a quantized equilibrium response and a topology-organized nonequilibrium response is one of the central themes of Part I.

1.5 Organization of the dissertation

This dissertation is organized into two parts and seven chapters. The present chapter, Chapter 1, provides the conceptual introduction to Part I. It begins with topological magnon bands and the limitations of a dilute quasiparticle-band description, introduces the Floquet and rotating-wave frameworks for resonant modulation, reviews the bulk and boundary topology of the Kitaev chain, and concludes with the overview of the driven spin-chain problem given above.

Part I: Parametric Resonance and Dynamical Topology in a Spin-$1/2$ Chain. Chapter 2 develops the model in detail. It introduces the laboratory-frame spin Hamiltonian and derives the rotating-frame Hamiltonian within the rotating-wave approximation. The relation between this Hamiltonian and the targeted resonant sector of the full Floquet problem is then clarified. The Jordan–Wigner transformation is applied with careful attention to fermion parity and boundary conditions, after which the Bogoliubov–de Gennes representation, quasiparticle spectrum, and winding number are derived. The chapter then defines the initial state, the sudden and slow turn-on protocols, and the frequency-sweep protocol. It discusses continuous long-time averages and formulates the exact free-fermion dynamics in both the Schrödinger and Heisenberg pictures. The chapter concludes by expressing the spin observables used throughout Part I in the fermionic language and by collecting the notational conventions.

Chapter 3 studies the response of the periodic chain for both sudden and slow turn-on of the modulation. It first verifies directly that the anomalous response is present in the full laboratory-frame dynamics without invoking the rotating-wave approximation. The pair excitation of opposite-momentum fermionic modes is then derived within the RWA and related to the winding-number density. The chapter obtains the frequency-independent magnetization plateau in the topological regime, the vanishing connected longitudinal correlations after a sudden turn-on, and the contrasting behavior of transverse correlations. It also analyzes the singular behavior at the topological transition, finite-size corrections, initial thermal populations, and the interpretation of the results in spin and superconducting-qubit experiments.

The chapter then asks whether the sudden-turn-on results survive when the drive is applied gradually. It first explains why the nominal adiabatic limit is subtle: the instantaneous spectrum is gapless at selected momenta when the pairing amplitude starts from zero. Adiabatic evolution away from these momenta is combined with exact and asymptotic treatments of the nonadiabatic windows. The resulting magnetization and correlation functions are derived and connected to Kibble–Zurek scaling near the topological transition. The chapter also compares amplitude ramps with frequency sweeps, establishes the resulting path dependence and hysteresis, and follows the crossover from sudden to slow turn-on. We also provide an analytical solution to the finite-ramp problem using a combination of a *semi*-WKB solution and parabolic cylinder functions. Matrix-product-state simulations provide finite-size checks of the analytical results.

Chapter 4 studies the dynamics of a finite chain with free ends. The real-space Bogoliubov–de Gennes equations are used to formulate the boundary problem in terms of the characteristic roots of the bulk recurrence relation. The resulting solutions distinguish single-channel modes, which combine a propagating component with evanescent boundary components, from two-channel modes, in which the boundaries mix two distinct propagating momenta at the same quasienergy. The chapter derives the corresponding quantization conditions and discusses exact crossings, avoided crossings, and localized edge modes. Majorana propagators and the covariance matrix are then introduced to calculate the spin observables and connect their boundary dependence to propagation

and interference. Numerical calculations examine the spatial development of the boundary response, its arrival at the center, and its dependence on group velocity and system size. Particular attention is paid to distinguishing the contribution of localized edge modes from the modification of extended bulk states by boundary channel mixing.

Part II: Nonlinear Dynamics in Mesoscopic Systems. Chapter 5 concerns dispersive coupling between vibrational modes in p-doped semiconductor nanomechanical resonators [65]. Hole doping strongly enhances the coupling between modes of different frequencies and produces nonmonotonic density and temperature dependences. The analysis is applied to silicon resonators in which one mode serves as a temperature-compensated clock mode and a lower-frequency mode acts as a thermometer for frequency stabilization.

Chapter 6 concerns the nonlinear conductivity of a low-dimensional Wigner crystal formed by electrons above superfluid helium [66]. High-frequency transport measurements in a microchannel reveal a nonlinear response at drive frequencies comparable to or exceeding the first-shell ripplon frequency associated with the conventional Bragg–Cherenkov effect. The response is interpreted in terms of coupling to ripplons at higher-order Bragg vectors, which generates dynamical friction and a mechanism for high-frequency pinning. Together, the two projects broaden the dissertation from driven spin dynamics to nonlinear collective phenomena in nanomechanical and electronic mesoscopic systems.

Chapter 7 returns to the central question of how topology becomes visible through dynamics. It summarizes the bulk response of the periodic chain and the changes caused by boundaries. It then discusses an experimental program for testing the predictions, including frequency-dependent magnetization and correlation measurements in programmable qubit arrays. The chapter concludes with immediate directions for future work, including higher-winding and multi-band extensions, interactions, dissipation, and disorder.

CHAPTER 2

FROM RESONANT SPIN DRIVING TO THE KITAEV CHAIN

This chapter introduces the main system studied in Part I. After providing the laboratory-frame Hamiltonian, we show how the effective physics of resonant modulation maps onto the Kitaev chain. We then introduce the nonequilibrium preparation protocols considered here and outline the mathematical construction used to analyze a periodic chain and a finite chain with open ends. The derivations are given in some detail because several later results depend on signs, parity sectors, and the distinction between a ring and an open chain.

2.1 Laboratory-frame spin Hamiltonian

We consider a chain of N spin-$1/2$ degrees of freedom in a strong magnetic field along z, with nearest-neighbor XY coupling. Resonant parametric excitation comes from sinusoidally modulating the coupling at frequency ω_F close to twice the Larmor frequency ω_0. The laboratory-frame Hamiltonian of the chain is

$$\hat{H}_{\text{lab}} = -\frac{1}{2}\omega_0 \sum_{n=1}^{N} \sigma_n^z - J_{xx}(t) \sum_{n=1}^{\overline{N}} \sigma_n^x \sigma_{n+1}^x - J_{yy} \sum_{n}^{\overline{N}} \sigma_n^y \sigma_{n+1}^y,$$
$$J_{xx}(t) = J_{xx} + 2F(t)\cos\varphi_F(t), \quad \dot{\varphi}_F(t) = \omega_F(t), \qquad (\hbar = 1), \tag{2.1}$$

where σ_n^i are the Pauli matrices ($i = \{x, y, z\}$), F is the modulation amplitude, and $\overline{N} = N$ or $N - 1$ for a periodic or open chain, respectively. In the former case, we set $n + N \equiv n$. We assume that the coupling parameters and the modulation amplitude are small compared to ω_0. Furthermore, the time-dependent envelope of the modulation parameters is also assumed to be slow on the carrier scale, $|\dot{F}|, |\dot{\omega}_F| \ll \omega_F^2$.

The static exchange contains both spin-conserving and pair-flip terms. Using $\sigma^{\pm} = (\sigma^x \pm i\sigma^y)/2$,

$$\sigma_n^x \sigma_{n+1}^x + \sigma_n^y \sigma_{n+1}^y = 2\left(\sigma_n^+ \sigma_{n+1}^- + \sigma_{n+1}^+ \sigma_n^-\right),$$
$$\sigma_n^x \sigma_{n+1}^x - \sigma_n^y \sigma_{n+1}^y = 2\left(\sigma_n^+ \sigma_{n+1}^+ + \sigma_{n+1}^- \sigma_n^-\right). \tag{2.2}$$

The first line exchanges an excitation between adjacent sites. The second creates or annihilates two excitations. Near $\omega_F = 2\omega_0$, the modulation makes the second process resonant.

2.2 Rotating frame and rotating-wave approximation

It is convenient to analyze resonant parametric modulation by going to the rotating frame at frequency $\omega_F/2 \approx \omega_0$ using the transformation

$$\hat{U}(t) = \exp\left[\frac{i}{4}\varphi_F(t)\sum_{n=1}^{N}\sigma_n^z\right]. \tag{2.3}$$

Because $U^\dagger\sigma_n^\pm U = \mathrm{e}^{\mp i\varphi_F/2}\sigma_n^\pm$, spin-exchange terms are stationary whereas pair flips acquire phases $\mathrm{e}^{\mp i\varphi_F}$. Multiplying these phases by $\cos\varphi_F = (\mathrm{e}^{i\varphi_F} + \mathrm{e}^{-i\varphi_F})/2$ produces one stationary component and one component oscillating at approximately $2\omega_F$. The latter and the nonresonant static anisotropy average away on times long compared with ω_F^{-1}. Defining

$$\hat{Z} = \sum_{n=1}^{N}\sigma_n^z, \quad \hat{X} = \sum_{n=1}^{\overline{N}}(\sigma_n^+\sigma_{n+1}^- + \sigma_{n+1}^+\sigma_n^-), \quad \hat{P} = \sum_{n=1}^{\overline{N}}\sigma_n^+\sigma_{n+1}^+, \tag{2.4}$$

the transformed Hamiltonian of the system in the rotating frame $\hat{H}_{\mathrm{rot}} = U^\dagger\hat{H}_{\mathrm{lab}}U - iU^\dagger\dot{U}$ has the form

$$\begin{aligned}
&\hat{H}_{\mathrm{rot}} = \hat{H}_{\mathrm{RWA}} + \hat{V}(t), \qquad \hat{H}_{\mathrm{RWA}} = \frac{1}{2}\mu\hat{Z} - J\hat{X} - F(\hat{P} + \hat{P}^\dagger),\\
&\hat{V}(t) = -2F\cos\varphi_F(t)\hat{X} - \Delta\left(\mathrm{e}^{-i\varphi_F(t)}\hat{P} + \mathrm{e}^{i\varphi_F(t)}\hat{P}^\dagger\right) - F\left(\mathrm{e}^{-2i\varphi_F(t)}\hat{P} + \mathrm{e}^{2i\varphi_F(t)}\hat{P}^\dagger\right),
\end{aligned} \tag{2.5}$$

where $\mu = \omega_F/2 - \omega_0$, $J = J_{xx} + J_{yy}$, and $\Delta = J_{xx} - J_{yy}$. In the rotating-wave approximation (RWA), we discard the rapidly oscillating term $\hat{V}(t)$ and consider the dynamics governed by the effective Hamiltonian $\hat{H}_{\mathrm{RWA}}$, which is explicitly written in terms of the Pauli operators as

$$\hat{H}_{\mathrm{RWA}} = \frac{1}{2}\mu\sum_{n=1}^{N}\sigma_n^z - J\sum_{n=1}^{\overline{N}}(\sigma_n^+\sigma_{n+1}^- + \sigma_{n+1}^+\sigma_n^-) - F\sum_{n=1}^{\overline{N}}(\sigma_n^+\sigma_{n+1}^+ + \sigma_{n+1}^-\sigma_n^-). \tag{2.6}$$

The Hamiltonian $\hat{H}_{\mathrm{RWA}}$ clearly shows that resonant parametric excitation leads to birth or annihilation of pairs of magnons or, equivalently, to upward or downward flips of qubits in pairs. The sign of F depends on the phase chosen for the modulation. A shift of the time origin by π/ω_F changes $F \to -F$, so most scalar observables depend only on $|F|$.

The RWA is controlled by the hierarchy $|\mu|, |J_{xx}|, |J_{yy}|, |F| \ll \omega_0$, together with the requirement that the modulation envelope vary slowly on the scale ω_F^{-1}; it is not an exact replacement of the

driven problem as can be seen directly from Eq. (2.5). In the rotating frame, the discarded harmonics occur at ω_F and $2\omega_F$. For our discussion in Sec. 1.2.3, they generate bounded micromotion of order $(|F| + |\Delta|)/\omega_F$ and effective-Hamiltonian corrections of order $(F^2 + \Delta^2 + |F\Delta|)/\omega_F$, (see Eq. (1.38)). Consequently, for phase-resolved dynamics, the corresponding quasienergy corrections produce a secular phase error $\delta\epsilon_k t$. Thus, up to the bounded micromotion error, the uncorrected RWA trajectory remains phase accurate for $t \ll 1/\max_k |\delta\epsilon_k|$, generically of order $\omega_F/g_{\rm cr}^2$, where $g_{\rm cr} \equiv \max(|\Delta|, |F|)$ characterizes the counter-rotating terms. By contrast, in the continuously time-averaged observables considered in Part I (see Eq. (1.60)), these oscillatory phases are dephased rather than accumulated. The remaining discrepancy from the exact Floquet average arises from the bounded perturbative dressing of the Floquet modes, their occupations, and the observables, and can be systematically evaluated using a high-frequency expansion of the rotating-frame Hamiltonian. When the relevant slow energy scales are comparable, these corrections are of order $g_{\rm cr}/\omega_F$ and, unlike the phase error in an instantaneous trajectory, do not grow with the averaging time.

2.3 Jordan–Wigner transformation: Kitaev-chain mapping and boundary conditions

We now apply the Jordan–Wigner transformation (JWT) introduced in Eq. (1.27) to write the RWA Hamiltonian in (2.6) in terms of canonical spinless fermions. Although the JWT is inherently non-local due to the phase string in the $\sigma_n^{\pm}$ mapping, the nearest-neighbor structure of the RWA Hamiltonian simplifies this complexity. Because these strings cancel between adjacent spin operators, the Hamiltonian reduces to purely quadratic fermionic terms. For example, using the fermionic anti-commutation relations and $\left(2c_m^\dagger c_m - 1\right)^2 = 1$, we get

$$\begin{aligned}\sigma_n^+\sigma_{n+1}^- &= \left[\prod_{m=1}^{n-1}\left(2c_m^\dagger c_m - 1\right)\right] c_n c_{n+1}^\dagger \left[\prod_{m=1}^{n}\left(2c_m^\dagger c_m - 1\right)\right] \\ &= c_n c_{n+1}^\dagger \left(2c_n^\dagger c_n - 1\right) = -c_{n+1}^\dagger c_n, \end{aligned} \tag{2.7}$$

Similarly, we get $\sigma_n^-\sigma_{n+1}^+ = -c_n^\dagger c_{n+1}$, $\sigma_n^+\sigma_{n+1}^+ = c_n c_{n+1}$, and $\sigma_n^-\sigma_{n+1}^- = c_{n+1}^\dagger c_n^\dagger$. This is valid for any n such that $1 < n < N-1$. For a periodic chain, the Hamiltonain contains terms of the form $\sigma_N^\alpha\sigma_{N+1}^\beta \equiv \sigma_N^\alpha\sigma_1^\beta$. Now, since the spin on the first site does not contain any prefactors, the string contribution from the spin on the N-th site does not generally cancel out. Using

$\left(1-2c_N^\dagger c_N\right)c_N = c_N$, it can however be written as

$$\sigma_N^+\sigma_1^- = \left[\prod_{m=1}^{N-1}\left(2c_m^\dagger c_m - 1\right)\right]c_N c_1^\dagger = -\left[\prod_{m=1}^{N}\left(2c_m^\dagger c_m - 1\right)\right]c_N c_1^\dagger = \mathcal{P}c_1^\dagger c_N. \tag{2.8}$$

where $\mathcal{P} \equiv \left[\prod_{m=1}^{N}\left(2c_m^\dagger c_m - 1\right)\right]$ is the parity operator. We note that $[\hat{H}_{\rm lab}(t), \mathcal{P}] = [\hat{H}_{\rm RWA}, \mathcal{P}] = 0$. This is a consequence of spins flipped in pairs in resonant parametric excitation and, respectively, of the fermionic excitations being created or annihilated in pairs.

For any initial state $|\Psi_0\rangle = |\Psi_0^{(+)}\rangle + |\Psi_0^{(-)}\rangle$, where $\mathcal{P}|\Psi_0^{(\pm)}\rangle = \pm|\Psi_0^{(\pm)}\rangle$, the two parity sectors remain fully independent throughout the dynamics. Each sector evolve under a slightly different Hamiltonian. This can be seen by comparing Eqs. (2.7) and (2.8). We see that the periodic boundary conditions for the spins gives anti-periodic boundary conditions for the even parity sector, i.e., $c_{N+1}^\dagger = -c_1^\dagger$, whereas it gives periodic boundary conditions for the odd parity sector, i.e., $c_{N+1}^\dagger = c_1^\dagger$. More generally, a parity-changing operator connects the periodic and antiperiodic Jordan–Wigner sectors. Since the corresponding resulting sets of Fourier modes each form a complete basis, matrix elements between the two sectors can be evaluated through an explicit change of momentum basis [67].

Using Eq. (2.7) and the subsequent transformations, the RWA Hamiltonian (2.6) takes the form

$$\hat{H}_{\rm RWA} = -\mu\sum_{n=1}^{N}\left(c_n^\dagger c_n - \frac{1}{2}\right) + J\sum_{n=1}^{\overline{N}}\left(c_n^\dagger c_{n+1} + c_{n+1}^\dagger c_n\right) + F\sum_{n=1}^{\overline{N}}\left(c_n^\dagger c_{n+1}^\dagger + c_{n+1}c_n\right). \tag{2.9}$$

This is precisely the Kitaev-chain Hamiltonian introduced in Eq. (1.61) and discussed in detail in Sec. 1.3. In the thermodynamic limit, its bulk topology is characterized by the winding number, which is nonzero for $|\mu| < 2|J|$ and $F \neq 0$. In the limit of vanishing modulation, $F \to 0$, the effective pairing amplitude vanishes and the topological gap closes. The resulting number-conserving chain is gapless for $|\mu| < 2|J|$ and is gapped but topologically trivial for $|\mu| > 2|J|$. A nonzero periodic modulation generates the p-wave pairing required to gap the normal-state crossings and therefore produces a nontrivial effective RWA Hamiltonian when $|\mu| < 2|J|$.

Strictly speaking, in the complete absence of a periodic modulation $F = 0$, the frequency ω_F no longer defines a physically distinguished rotating frame, and the detuning μ should be understood

as the limit obtained as $F \to 0$ at fixed drive frequency. The drive therefore controls the effective spectrum through two distinct but simultaneous mechanisms: the detuning controls whether the normal particle and hole bands are inverted, while the modulation-induced pairing opens the topological gap.

This raises the central dynamical questions of Part I: can the topology of the effective Hamiltonian be inferred from the response following the turn-on of the modulation, and how do its observable signatures depend on the preparation protocol? We first address these questions for a periodic spin chain, where translational symmetry allows the dynamics to be resolved into independent momentum sectors. We then turn to a finite chain with open ends to determine how boundaries and the resulting loss of momentum conservation modify the response.

2.4 Bogoliubov–de Gennes representation

To prepare for the analysis of periodic and open chains, we next develop the Bogoliubov–de Gennes formulations of the Kitaev chain. We start with the simpler periodic chain formulation, and then discuss the finite open chain and the resulting boundary mixing.

2.4.1 BdG for a periodic chain

For a periodic Kitaev chain, the Hamiltonian in Eq. (1.71) decomposes into independent $(k, -k)$ sectors. Each sector can therefore be diagonalized by a 2×2 momentum-dependent Bogoliubov transformation. This decoupling follows directly from the discrete translational symmetry of the ring. For a finite chain with open ends, momentum is no longer an exact quantum number, and the corresponding real-space formulation is developed below. For the periodic chain, the $(k, -k)$ sector is diagonalized by a rotation about τ_y,

$$d_k = c_k \cos\frac{\theta_k}{2} + c_{-k}^\dagger \sin\frac{\theta_k}{2}, \qquad d_{-k}^\dagger = -c_k \sin\frac{\theta_k}{2} + c_{-k}^\dagger \cos\frac{\theta_k}{2}, \qquad \tan\theta_k = \frac{F_k}{M_k},$$
$$\varepsilon_k = \sqrt{M_k^2 + F_k^2}, \qquad M_k = \mu - 2J\cos(k), \qquad F_k = 2F\sin(k), \tag{2.10}$$

where the values of k are determined by the boundary conditions which depend on the parity sector as we discussed in Sec. 2.3. Below, the dynamics will be restricted to the even parity sector for which $k = \pi(2m-1)/N$, where $m = -(N/2)+1, -(N/2)+2, ..., N/2$ for even N. The odd-parity

sector is treated analogously using periodic fermionic boundary conditions. For even N, however, it also contains the self-conjugate momenta $k = 0$ and $k = \pi$, where $F_k = 0$; these unpaired modes must be handled separately. However, the results discussed below remain unchanged.

We note that θ_k is the same angle in the definition of the winding number in Eq. (1.75). Intuitively, the winding number represents how many times the BdG vector encircles the origin $\varepsilon_k = 0$. Thus, the winding cannot change without a gap closure as long as the chiral symmetry in Eq. (1.74) is not broken. For the nearest-neighbor model considered here, the winding number can only take the values 0 and ±1. In an extended Kitaev chain with hopping and pairing terms extending to the mth neighbor, phases with winding numbers satisfying $|\nu| \leq m$ can occur.

In terms of the quasiparticles in Eq. (2.10), the Hamiltonian in (1.71) takes the form

$$\hat{H} = \frac{1}{2} \sum_k \varepsilon_k [-\mathrm{sgn}(M_k \cos\theta_k)] \vec{d}_k^{\,\dagger} \tau^z \vec{d}_k, \qquad \vec{d}_k = \begin{pmatrix} d_k \\ d_{-k}^\dagger \end{pmatrix}. \tag{2.11}$$

A standard convention is that quasiparticles excited by the operators $\{d_k^\dagger\}$ have positive energies ε_k. This corresponds to the values θ_k such that $M_k \cos\theta_k < 0$. As k changes, function θ_k changes as well. However, the sign of $M_k \cos\theta_k < 0$ does not. As seen from Eq. (2.10), $\theta_{-k} = -\theta_k$.

The bulk–boundary correspondence relates the topological invariant of the translationally invariant bulk to the boundary spectrum of an open chain. For a noninteracting chain in symmetry class BDI, a bulk winding number ν implies $|\nu|$ Majorana zero modes at each end, provided that the boundary preserves the protecting chiral symmetry. For the nearest-neighbor model studied here, the nontrivial phases with $|\nu| = 1$ therefore support one Majorana mode at each end in the thermodynamic limit.

2.4.2 BdG for an open chain

In what follows, we study both the translationally invariant bulk dynamics of the periodic chain and the changes introduced by open boundaries. For an open chain, translational symmetry is broken and momentum no longer labels independent BdG sectors. The Hamiltonian nevertheless remains quadratic and can be diagonalized by a global Bogoliubov transformation in real space. We now develop this finite-chain formulation following the method of Lieb, Schultz, and Mattis [35]. For

the open chain, write

$$\hat{H} = \sum_{m,n=1}^{N} \left[c_m^\dagger A_{mn} c_n + \frac{1}{2} \left(c_m^\dagger B_{mn} c_n^\dagger + \text{H.c.} \right) \right] + \text{const}, \tag{2.12}$$

where the $N \times N$ matrices $\mathbf{A}$ and $\mathbf{B}$ are respectively symmetric and antisymmetric, with matrix elements

$$\begin{aligned} A_{mn} &= -\mu \delta_{mn} + J(\delta_{n,m+1} + \delta_{n,m-1}), \\ B_{mn} &= F(\delta_{n,m+1} - \delta_{n,m-1}). \end{aligned} \tag{2.13}$$

We define the Bogoliubov quasiparticle operators of the form

$$\eta_s^\dagger = \frac{1}{2} \sum_{n=1}^{N} \left[\phi_s(n) \gamma_n^A - i \psi_s(n) \gamma_n^B \right], \tag{2.14}$$

where $\gamma_n^A = c_n^\dagger + c_n$ and $\gamma_n^B = i(c_n^\dagger - c_n)$ are the Majorana operators introduced in Eq. (1.64). The mode amplitudes $\phi_s(n)$ and $\psi_s(n)$ can be chosen real, such that $[\hat{H}, \eta_s^\dagger] = \Lambda_s \eta_s^\dagger$, where $\Lambda_s \geq 0$, and, after appropriate normalization, $\{\eta_s, \eta_{s'}^\dagger\} = \delta_{ss'}$. This construction leads to the Bogoliubov–de Gennes (BdG) equations

$$(\mathbf{A} + \mathbf{B}) \boldsymbol{\phi}_s = \Lambda_s \boldsymbol{\psi}_s, \qquad (\mathbf{A} - \mathbf{B}) \boldsymbol{\psi}_s = \Lambda_s \boldsymbol{\phi}_s. \tag{2.15}$$

Decoupling the BdG equations gives

$$\begin{aligned} (\mathbf{A} - \mathbf{B})(\mathbf{A} + \mathbf{B}) \boldsymbol{\phi}_s &= \Lambda_s^2 \boldsymbol{\phi}_s, \\ (\mathbf{A} + \mathbf{B})(\mathbf{A} - \mathbf{B}) \boldsymbol{\psi}_s &= \Lambda_s^2 \boldsymbol{\psi}_s. \end{aligned} \tag{2.16}$$

Thus, the spectral problem reduces to diagonalizing $\mathbb{H} = (\mathbf{A} - \mathbf{B})(\mathbf{A} + \mathbf{B})$. For $\Lambda_s \neq 0$, once $\boldsymbol{\phi}_s$ is known, $\boldsymbol{\psi}_s$ follows directly from the coupled BdG equations (2.15). Away from the edges of the chain, $\mathbb{H}$ is translationally invariant. More precisely, for $3 \leq m \leq N-2$, its nonzero matrix elements take the bulk form

$$\mathbb{H}_{m,m} = \mu^2 + 2(J^2 + F^2), \qquad \mathbb{H}_{m,m\pm1} = -2\mu J, \qquad \mathbb{H}_{m,m\pm2} = J^2 - F^2. \tag{2.17}$$

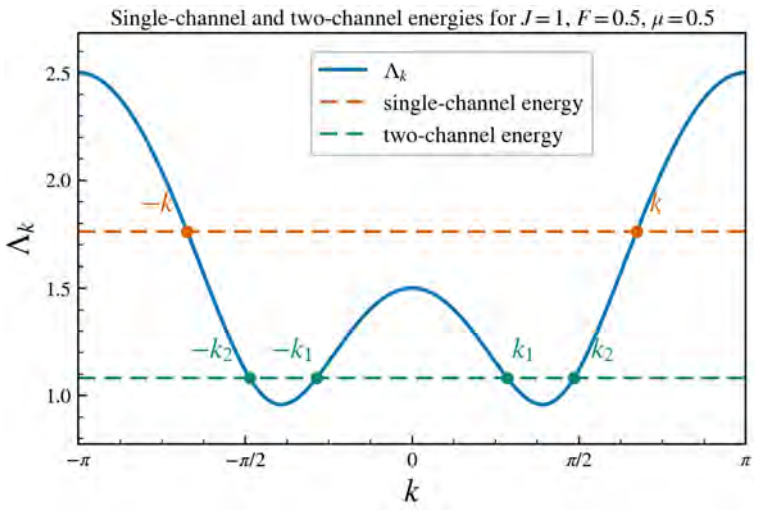


Figure 2.1 Bulk dispersion relation Λ_k for a Kitaev chain with $J = 1$, $F = 0.5$, and $\mu = 0.5$. The horizontal dashed lines indicate representative energies in the single-channel (orange) and two-channel (green) regimes, with the corresponding momentum intersections marked explicitly.

The rows $m = 2$ and $m = N - 1$ have the same diagonal and nearest-neighbor entries, but are missing one second-neighbor term because the chain terminates at $m = 1$ and $m = N$. In addition, the end-site diagonal elements differ from their bulk values and are given by

$$\mathbb{H}_{11} = \mu^2 + (J - F)^2, \qquad \mathbb{H}_{NN} = \mu^2 + (J + F)^2. \tag{2.18}$$

Except at the Ising points $J^2 = F^2$, this pentadiagonal structure is equivalent to a fourth-order finite-difference problem in the bulk, supplemented by two boundary conditions at each end. It is precisely this boundary structure that makes the finite open chain different from the periodic chain as it leads to the boundary-induced mixing of bulk modes as we discuss below.

Away from the ends of the chain, the eigenvalue equation for $\mathbb{H}$ is translationally invariant. In the bulk, we therefore seek plane-wave solutions of the form $\phi_k(m) = e^{ikm}$. Substituting this ansatz into the bulk equation obtained from Eq. (2.17) gives the familiar dispersion relation

$$\Lambda_k^2 = \varepsilon_k^2 = (\mu - 2J\cos k)^2 + (2F\sin k)^2. \tag{2.19}$$

For a given value of Λ within the bulk continuum, the equation $\Lambda_k^2 = \Lambda^2$ may have either one or two distinct positive solutions for $k \in (0, \pi)$. We refer to these cases as the single-channel and two-channel regimes, respectively.

The appearance of a two-channel region is controlled by the shape of the bulk dispersion. When Λ_k^2 develops extrema at momenta away from $k = 0$ and $k = \pi$, a finite interval of energies is intersected by four real momenta,$\{\pm k_1, \pm k_2\}$. This occurs when

$$|\mu J| < 2|J^2 - F^2|. \tag{2.20}$$

In the two-channel region, the open boundaries act not merely as phase-shifting reflectors, but as couplers between two distinct propagating bulk channels at the same energy. By contrast, outside this region only one propagating pair $\pm k$ exists at fixed Λ, and the remaining freedom needed to satisfy the open-boundary constraints must arise through boundary-induced mixing or, equivalently, through non-propagating components in an exact complex-k formulation.

This bulk distinction is illustrated schematically in Fig. 2.1. The distinction between the single-channel and two-channel regions will play a central role in the time-averaged bulk behavior discussed later, as it determines how the open boundaries constrain and mix the finite-chain eigenstates.

The bulk eigenvalue equation can be written as the fourth-order finite-difference equation

$$\begin{aligned}
&(J^2 - F^2)\big[\phi_s(m-2) + \phi_s(m+2)\big] \\
&\quad - 2\mu J\big[\phi_s(m-1) + \phi_s(m+1)\big] \\
&\quad + \big[\mu^2 + 2(J^2 + F^2) - \Lambda_s^2\big]\phi_s(m) = 0,
\end{aligned} \tag{2.21}$$

which is valid in the translationally invariant part of the chain. For $J^2 \neq F^2$, a convenient way to expose the boundary structure is to extend this equation formally to all sites $m = 1, \ldots, N$ by introducing four fictitious amplitudes:

$$\phi_s(-1), \quad \phi_s(0), \quad \phi_s(N+1), \quad \phi_s(N+2).$$

Comparing the extended bulk equation with the exact equations at $m = 1, 2, N-1, N$, one finds that the finite-chain problem is exactly equivalent to the uniform bulk equation (2.21) supplemented by the four boundary conditions

$$\phi_s(0) = 0, \qquad \phi_s(N+1) = 0, \tag{2.22}$$

and

$$(J - F)\phi_s(-1) + (J + F)\phi_s(1) = 0,$$
$$(J + F)\phi_s(N + 2) + (J - F)\phi_s(N) = 0. \tag{2.23}$$

The first pair has the familiar Dirichlet form and selects standing waves when $F = 0$. In the same limit, the second pair reduces to the corresponding odd continuation of the wavefunction beyond each boundary. For $F \neq 0$, the unequal coefficients $J - F$ and $J + F$ encode the additional boundary mixing introduced by pairing.

As we discuss in Chapter 4, this fictitious-site formulation is useful for two reasons. First, it provides a direct and compact route to the known solvable limits. Second, it makes the general open-chain problem conceptually transparent: the finite system is described by the same bulk difference equation at every site, while all boundary effects are isolated into four simple constraints on the fictitious amplitudes.

2.4.3 From BdG to SVD

It is also useful to note that the solution to the real space BdG problem in Eq. (2.15) can be obtained by finding the singular value decomposition (SVD) for the matrix $D = A + B$ given by

$$D = UEV^{\mathsf{T}}, \qquad E = \mathrm{diag}(\Lambda_1, \ldots, \Lambda_N), \tag{2.24}$$

where V and U are orthogonal matrices. If we set $\Phi = V$, and $\Psi = U$, we get

$$D\Phi = \Psi E, \qquad D^T\Psi = \Phi E, \tag{2.25}$$

which is the matrix version of Equation (2.15), where now the columns of Φ and Ψ are the corresponding modes. This implies that we can solve for the modes by obtaining the SVD. This has a numerical advantage since both partners ϕ_s and ψ_s are obtained simultaneously, and we never need to reconstruct one partner using$\Psi_s = D\Phi_s/\Lambda_s$, which can amplify errors when Λ_s is extremely small for the edge modes.

For the remainder of this chapter and the following chapter, we focus on the periodic chain. We return to the full solution of the finite open chain, and to the consequences of boundary-induced mode mixing for the bulk dynamics, in Chapter 4.

2.5 Preparation protocols, dynamical equations, and observables

Having established the BdG representations of the periodic and open chains, we now formulate the dynamical initial-value problems considered in Part I. We first specify the initial state and the protocols used to turn on the modulation. We then present two equivalent descriptions of the dynamics of the periodic chain: the Schrödinger-picture evolution of each $(k, -k)$ pair and the Heisenberg-picture evolution of the instantaneous Bogoliubov quasiparticles. Finally, we express the spin observables of interest in terms of Jordan–Wigner fermionic correlation functions. The solutions of these equations and their consequences for the bulk response are developed in the next chapter [22].

2.5.1 Initial state

Before the modulation is applied, the strong static magnetic field polarizes every spin along the positive z direction. Under the assumed hierarchy $\omega_0 \gg |J|$, the initial state is therefore

$$|\Psi_0\rangle = |\uparrow_1 \uparrow_2 \cdots \uparrow_N\rangle \,. \tag{2.26}$$

Using the Jordan–Wigner relation

$$\sigma_n^z = 1 - 2c_n^\dagger c_n, \tag{2.27}$$

the spin-up state at site n corresponds to an empty fermionic site. Consequently,

$$c_n \,|\Psi_0\rangle = 0, \qquad c_k \,|\Psi_0\rangle = 0, \qquad \hat{\mathcal{N}} \,|\Psi_0\rangle = 0, \tag{2.28}$$

where $\hat{\mathcal{N}} = \sum_n c_n^\dagger c_n$. The fully polarized spin state is therefore the vacuum of the Jordan–Wigner fermions. It has even fermion parity and, for the periodic spin chain with even N, belongs to the antiperiodic fermionic sector discussed in Sec. 2.3.

The static exchange term preserves this vacuum, whereas the modulation-induced pairing term does not. Once the modulation is switched on, pairs of Jordan–Wigner fermions with opposite momenta can be created from the initial state. Since both the RWA Hamiltonian and the lab Hamiltonian preserve fermion parity and total quasimomentum, the dynamics of the periodic chain remains restricted to the even-parity subspace of each $(k, -k)$ sector.

This initial state can be thought of as the zero-temperature state for the undriven system. However, we will show that the observations discuss in the next section will still be the same for an intial state at a finite temperature T given that $\omega_0 \gg k_B T \gg |J|$.

2.5.2 Turn-on and frequency-sweep protocols

The modulation envelope and frequency are assumed to vary slowly on the microscopic Larmor time scale. If τ_{env} denotes the characteristic time over which either quantity changes, we require $\omega_0 \tau_{\text{env}} \gg 1$. This condition ensures that the modulation remains narrowband near the parametric resonance and that the rotating-wave approximation remains applicable during the preparation. It does not imply adiabatic evolution with respect to the much smaller quasiparticle energies ε_k of the effective Hamiltonian.

We distinguish between protocols according to their speed on the effective dynamical scale. In an amplitude turn-on, the detuning μ is held fixed while the pairing amplitude changes from $F(0) = 0$ to $F(t_f) = F_{\text{fin}}$. The corresponding mode parameters are

$$M_k(t) = \mu(t) - 2J\cos k, \qquad F_k(t) = 2F(t)\sin k, \qquad \varepsilon_k(t) = \sqrt{M_k^2(t) + F_k^2(t)}. \tag{2.29}$$

A turn-on is sudden for a given mode when the state has insufficient time to follow the change in its instantaneous eigenbasis, $\tau_{\text{on}}\varepsilon_k \ll 1$. The experimentally relevant sudden-turn-on regime is therefore compatible with the RWA when

$$\omega_0^{-1} \ll \tau_{\text{on}} \ll \varepsilon_{\text{typ}}^{-1}, \tag{2.30}$$

where ε_{typ} denotes a characteristic quasiparticle scale of the modes that dominate the response.

In a slow turn-on, the modulation amplitude changes over a time long compared with the characteristic effective dynamical time. True adiabaticity is nevertheless a mode-dependent condition. Introducing the instantaneous Bogoliubov angle $\tan\theta_k(t) = F_k(t)/M_k(t)$, the instantaneous basis evolves adiabatically only when

$$\left|\dot{\theta}_k(t)\right| \ll \varepsilon_k(t). \tag{2.31}$$

When the modulation is switched on at a detuning in the topological interval, $|\mu| < 2|J|$, the initial spectrum at $F = 0$ contains momenta satisfying $M_k = 0$. The gap at these momenta closes at the

beginning of the ramp, so the condition in Eq. (2.31) cannot hold uniformly throughout the Brillouin zone. The consequences of this nonuniform adiabatic limit are analyzed in the next chapter.

We also consider a frequency-sweep protocol in which both the amplitude and the effective detuning are varied. A slow variation of the modulation frequency produces a time-dependent $M_k(t)$. The hysteresis protocol compares two paths that terminate at the same final Hamiltonian. In the direct protocol, the modulation is turned on at a final detuning μ_f inside the topological interval,

$$\mathcal{P}_{\mathrm{dir}}: \qquad (\mu_f, 0) \longrightarrow (\mu_f, F_{\mathrm{fin}}), \qquad |\mu_f| < 2|J|. \tag{2.32}$$

In the indirect protocol, the drive amplitude is first established in the trivial regime and the modulation frequency is then swept across the topological transition,

$$\mathcal{P}_{\mathrm{hys}}: \qquad (\mu_0, 0) \longrightarrow (\mu_0, F_{\mathrm{fin}}) \longrightarrow (\mu_f, F_{\mathrm{fin}}), \qquad |\mu_0| > 2|J|, \quad |\mu_f| < 2|J|. \tag{2.33}$$

The two protocols end at identical values of μ, J, and F, but they need not prepare the same many-body state. Comparing their long-time observables provides a direct test of the memory retained by the driven system.

2.5.3 Schrödinger-picture formulation

For the periodic chain, translational symmetry separates the Hamiltonian into independent $(k, -k)$ sectors. The many-body state can therefore be written as

$$|\Psi(t)\rangle = \prod_{k>0} \left[\sum_{m,n=0}^{1} A_{mn}(k,t)\, |m_{-k}, n_k\rangle \right], \tag{2.34}$$

where $|m_{-k}, n_k\rangle$ is the occupation-number basis of the two modes $-k$ and k. Since the initial state has even parity and the Hamiltonian creates and annihilates fermions only in pairs, and we get $A_{01}(k,t) = A_{10}(k,t) = 0$ for all times. The state therefore reduces to the BCS-like form

$$|\Psi(t)\rangle = \prod_{k>0} \left[A_{00}(k,t)\, |0_{-k}, 0_k\rangle + A_{11}(k,t)\, |1_{-k}, 1_k\rangle \right], \tag{2.35}$$

with $|A_{00}(k,t)|^2 + |A_{11}(k,t)|^2 = 1$. For a preparation that begins in the polarized state, the initial conditions $A_{00}(k,0) = 1$, and $A_{11}(k,0) = 0$.

In the even-parity subspace, the time-dependent Hamiltonian of a single momentum pair is

$$\mathcal{H}_k(t) = \begin{pmatrix} M_k(t) & -F_k(t) \\ -F_k(t) & -M_k(t) \end{pmatrix}. \tag{2.36}$$

The Schrödinger equation consequently gives

$$\begin{aligned} i\dot{A}_{00}(k,t) &= M_k(t)A_{00}(k,t) - F_k(t)A_{11}(k,t), \\ i\dot{A}_{11}(k,t) &= -M_k(t)A_{11}(k,t) - F_k(t)A_{00}(k,t). \end{aligned} \tag{2.37}$$

These two coupled equations define the mode-resolved dynamical problem for an arbitrary amplitude ramp, frequency sweep, or combination of the two.

The fermionic contractions needed below follow directly from the amplitudes,

$$\begin{aligned} \left\langle c_k^\dagger c_k \right\rangle_t &= \left\langle c_{-k}^\dagger c_{-k} \right\rangle_t = |A_{11}(k,t)|^2, \\ \left\langle c_k^\dagger c_{-k}^\dagger \right\rangle_t &= A_{11}^*(k,t)A_{00}(k,t). \end{aligned} \tag{2.38}$$

Thus, solving Eq. (2.37) for every positive momentum completely determines the state and all equal-time spin observables of the periodic chain.

2.5.4 Instantaneous-quasiparticle formulation

The same dynamics can be formulated in terms of instantaneous Bogoliubov quasiparticles. Let

$$\vec{c}_k = U(k,t)\vec{d}_k, \qquad \vec{d}_k = \begin{pmatrix} d_k \\ d_{-k}^\dagger \end{pmatrix}, \qquad U(k,t) = \exp\left[-i\frac{\theta_k(t)}{2}\tau^y\right]. \tag{2.39}$$

At every instant, this transformation diagonalizes the instantaneous BdG Hamiltonian. Because the basis itself changes during a ramp, the Heisenberg equation contains an additional geometric term,

$$\dot{\vec{d}}_k = -i\left[\vec{d}_k, \hat{H}_0(t)\right] - U^\dagger(k,t)\dot{U}(k,t)\vec{d}_k, \tag{2.40}$$

where $\hat{H}_0(t)$ is the instantaneous diagonal Hamiltonian.

For the positive-energy branch specified by $M_k(t)\cos\theta_k(t) < 0$, Eq. (2.40) becomes

$$\begin{aligned} \dot{d}_k &= -i\varepsilon_k(t)d_k + \frac{1}{2}\dot{\theta}_k(t)d_{-k}^\dagger, \\ \dot{d}_{-k}^\dagger &= i\varepsilon_k(t)d_{-k}^\dagger - \frac{1}{2}\dot{\theta}_k(t)d_k. \end{aligned} \tag{2.41}$$

The rate at which the instantaneous particle and hole branches are mixed is therefore controlled by $\dot{\theta}_k$. For the general protocol in which both F_k and M_k vary,

$$\dot{\theta}_k(t) = \frac{M_k(t)\dot{F}_k(t) - F_k(t)\dot{M}_k(t)}{\varepsilon_k^2(t)}. \tag{2.42}$$

Equation (2.42) treats amplitude ramps and frequency sweeps on the same footing. An amplitude ramp has $\dot{M}_k = 0$, whereas a frequency sweep has $\dot{M}_k = \dot{\mu}$. When the final parameters become stationary, we get $\dot{\theta}_k = 0$ and the instantaneous quasiparticles cease to mix.

The fixed-basis equations (2.37) and the instantaneous-basis equations (2.41) are equivalent. The former remain regular at an instantaneous gap closing and are convenient for exact evolution, whereas the latter isolate the nonadiabatic coupling and are useful for analyzing slow ramps.

2.5.5 Spin observables in fermionic form

After the preparation ends at time t_f, the drive parameters are held fixed and the system evolves under the final RWA Hamiltonian. We characterize the resulting state through continuous long-time averages,

$$\overline{\langle \hat{O} \rangle} = \lim_{\mathcal{T}\to\infty} \frac{1}{\mathcal{T}} \int_{t_f}^{t_f+\mathcal{T}} dt\, \langle \Psi(t)|\hat{O}|\Psi(t)\rangle. \tag{2.43}$$

The observables considered below are parity even and invariant under the global rotation at half the drive frequency. Their expectation values can therefore be evaluated directly in the rotating frame within the RWA.

The change of longitudinal magnetization due to modulation follows immediately from the Jordan–Wigner transformation,

$$1 - m_z(t) \equiv 1 - \left\langle \sigma_n^z \right\rangle_t = 2\left\langle c_n^\dagger c_n \right\rangle_t = \frac{2}{N}\sum_k \left\langle c_k^\dagger c_k \right\rangle_t = \frac{4}{N}\sum_{k>0} |A_{11}(k,t)|^2. \tag{2.44}$$

To express the spatial correlations compactly, define the normal and anomalous momentum-space contractions

$$\begin{aligned} q_1(m,t) &= \frac{2}{N}\sum_k \left\langle c_k^\dagger c_k \right\rangle_t e^{ikm} = \frac{2}{N}\sum_k |A_{11}(k,t)|^2 e^{ikm}, \\ q_2(m,t) &= -\frac{2i}{N}\sum_k \left\langle c_k^\dagger c_{-k}^\dagger \right\rangle_t e^{ikm} = -\frac{2i}{N}\sum_k A_{11}^*(k,t) A_{00}(k,t) e^{ikm} \end{aligned} \tag{2.45}$$

In particular, $1 - m_z(t) = q_1(0,t)$. The connected longitudinal correlation function is

$$\mathcal{Q}^z(m) = \left\langle \Delta\sigma_n^z \Delta\sigma_{n+m}^z \right\rangle_t = \frac{4}{N^2} \sum_{k_1,\ldots,k_4} \langle c_{k_1}^\dagger c_{k_2} c_{k_3}^\dagger c_{k_4} \rangle e^{i(k_1-k_2)m} \delta_{k_1-k_2,k_4-k_3}, \tag{2.46}$$

where $\Delta\sigma_n^z = \sigma_n^z - m_z(t)$, and $k_1 \neq k_2$ and $k_3 \neq k_4$. Since the time-evolved state remains Gaussian under the quadratic Hamiltonian, Wick's theorem gives, for $m \neq 0$,

$$\mathcal{Q}^z(m,t) = -|q_1(m,t)|^2 + |q_2(m,t)|^2. \tag{2.47}$$

The first term originates from normal fermionic correlations, while the second originates from the anomalous pair correlations generated by the modulation. Similarly, the three-site correlator $\langle \Delta\sigma_{n_1}^z \Delta\sigma_{n_2}^z \Delta\sigma_{n_3}^z \rangle_t$ is obtained by summing the product $\langle c_{k_1}^\dagger c_{k_2} c_{k_3}^\dagger c_{k_4} c_{k_5}^\dagger c_{k_6} \rangle$ with the weight $\prod_j \exp\left[-in_j(k_j - k_{j+1})\right]$. In turn, this comes to calculating 8 combinations where we take k_i so that the fermionic operators are paired into products with the total momentum transfer equal to zero, i.e., $c_{k_i}^\dagger c_{k_i}$, $c_{k_i}^\dagger c_{-k_i}^\dagger$, and $c_{k_i} c_{-k_i}$. This allows us to express the three-site correlator in terms of the functions $q_{1,2}(m,t)$ as

$$\begin{aligned} \langle \Delta\sigma_n^z \Delta\sigma_{n+m}^z \Delta\sigma_{n+l}^z \rangle_t = {} & 2q_1(m,t)q_1(l,t)q_1(m-l,t) - 2q_1(m,t)q_2(l,t)q_2(l-m,t) \\ & + 2q_1(l,t)q_2(m,t)q_2(l-m,t) - 2q_1(m-l,t)q_2(m,t)q_2(l,t), \end{aligned} \tag{2.48}$$

where $l > m > 0$. We also consider the nearest-neighbor transverse correlator. The Jordan–Wigner strings cancel between adjacent sites, giving

$$\left\langle \sigma_n^+ \sigma_{n+1}^- \right\rangle_t = -\left\langle c_{n+1}^\dagger c_n \right\rangle_t = -\frac{1}{N} \sum_k \left\langle c_k^\dagger c_k \right\rangle_t \cos k = -\frac{1}{2} q_1(1,t). \tag{2.49}$$

The quantities studied in the following chapters are the continuous long-time averages of Eqs. (2.44), (2.47), (2.48), and (2.49).

The preparation protocols, equations of motion, and observables defined above specify the dynamical problems addressed for the periodic chain. In the next chapter, we solve Eq. (2.37) for sudden and slow amplitude turn-ons and for the frequency-sweep protocol. We determine the momentum regions in which adiabaticity fails, derive the associated scaling laws, and evaluate the resulting time-averaged magnetization and spin correlations. This analysis will show how

the winding of the final effective Hamiltonian becomes encoded in bulk observables and how the observed response retains information about the path by which the driven state was prepared.

CHAPTER 3

DYNAMICAL BULK TOPOLOGY IN THE PERIODIC CHAIN

The preceding chapter established the mapping from the parametrically modulated spin chain to the Kitaev chain and formulated the resulting mode-resolved dynamical problem. In this chapter, we solve this problem for a periodic chain and determine how the topology of the effective rotating-frame Hamiltonian appears in time-averaged bulk observables. We first verify directly that the anomalous response is present in the full laboratory-frame dynamics, without invoking the rotating-wave approximation. We then use the RWA Hamiltonian to explain this response analytically for sudden and slow turn-on protocols. Particular attention is paid to the relation between the excitation density and the winding number, the disappearance or suppression of longitudinal correlations, the breakdown of adiabaticity near gap-closing momenta, and the memory associated with different paths through parameter space [22].

Throughout this chapter, the brackets

$$\langle \hat{O} \rangle \equiv \overline{\langle \hat{O} \rangle} \tag{3.1}$$

denote the continuous long-time average defined in Eq. (2.43). Unless otherwise stated, all analytical results refer to the thermodynamic limit. The symbols shown in the comparison figures are matrix-product-state simulations of the RWA Hamiltonian, not of the full laboratory-frame Hamiltonian. The details of these simulations and their convergence with system size, time step, and bond dimension are provided in Appendix A.

3.1 Laboratory-frame manifestation of the anomalous response

The analytical results developed in the remainder of this chapter rely on the RWA Hamiltonian in Eq. (2.6). Before turning to this description, we verify directly that the anomalous response is also present in the dynamics generated by the full laboratory-frame Hamiltonian in Eq. (2.1). For a spatially uniform periodic chain, the laboratory-frame Hamiltonian remains quadratic after the Jordan–Wigner transformation and decomposes into independent $(k, -k)$ sectors. Its time-dependent dynamics can therefore be obtained by numerically integrating a set of 2×2 Schrödinger equations

without discarding the counter-rotating terms in Eq. (2.5). Following the same steps used to obtain Eq. (2.37), the laboratory-frame evolution takes the form

$$
\begin{aligned}
i\dot{A}_{00}(k,t) &= M_{k,\mathrm{lab}}(t)A_{00}(k,t) - D_{k,\mathrm{lab}}(t)A_{11}(k,t),\\
i\dot{A}_{11}(k,t) &= -M_{k,\mathrm{lab}}(t)A_{11}(k,t) - D_{k,\mathrm{lab}}(t)A_{00}(k,t),\\
M_{k,\mathrm{lab}}(t) &= -\omega_0 - 2J(t)\cos k, \qquad D_{k,\mathrm{lab}}(t) = 2\Delta(t)\sin k,
\end{aligned}
\tag{3.2}
$$

where $J(t) \equiv J_{xx}(t) + J_{yy} = J + 2F(t)\cos\varphi_F(t)$, and $\Delta(t) \equiv J_{xx}(t) - J_{yy} = \Delta + 2F(t)\cos\varphi_F(t)$ with $J = J_{xx} + J_{yy}$ and $\Delta = J_{xx} - J_{yy}$. The polarized initial state still gives $A_{00}(k,0) = 1$, and $A_{11}(k,0) = 0$.

Equations (3.2) govern the evolution throughout both the linear ramp and the subsequent constant-envelope stage. Unlike Eq. (2.37), these equations retain the fast number-conserving modulation in $M_{k,\mathrm{lab}}(t)$ and the counter-rotating contribution to the pair coupling in $D_{k,\mathrm{lab}}(t)$.

We consider a periodic chain of $N = 500$ sites and choose $\omega_0 = 30J$, and $J_{xx} = J_{yy} = J/2$. The absence of static anisotropy $J_{xx} - J_{yy} = 0$ ensures that pair creation in the laboratory frame originates entirely from the periodically modulated part of $J_{xx}(t)$. The detuning is sampled over the interval $-4J \le \mu \le 4J$, using 61 equally spaced values of μ. For each value of μ, the modulation frequency $\omega_F = 2(\omega_0 + \mu)$ is held fixed during the time evolution; the horizontal axis in Fig. 3.1 therefore represents a collection of independent preparation protocols rather than a frequency sweep performed within a single realization. We choose the phase convention $\varphi_F(0) = 0$, so that the carrier is proportional to $\cos(\omega_F t)$ during the ramp. The modulation amplitude is increased linearly,

$$
F(t) = \begin{cases} \eta_F t, & 0 \le t \le \tau_F, \\ F_{\mathrm{fin}}, & t > \tau_F, \end{cases} \qquad \tau_F = \frac{F_{\mathrm{fin}}}{\eta_F}. \tag{3.3}
$$

We consider the two final amplitudes $F_{\mathrm{fin}} = 0.5J$ and $F_{\mathrm{fin}} = 0.7J$ each reached using the two ramp rates $\eta_F^{\mathrm{fast}} = 3J^2$ and $\eta_F^{\mathrm{slow}} = 10^{-2}J^2$.

To distinguish the laboratory-frame carrier scale from the effective many-body dynamical scale, it is useful to characterize each protocol by several dimensionless parameters. In addition to the

Table 3.1 Dimensionless parameters characterizing the four laboratory-frame ramp protocols. Here $\tau_F = F_{\mathrm{fin}}/\eta_F$, $\omega_0 = 30J$, and $52J \le \omega_F \le 68J$. The time-dependent carrier-scale parameter used in the rotating-frame construction is $\max_\mu(\eta_F/\omega_F^2)$. The quantity $\chi_{\mathrm{ramp}} = F_{\mathrm{fin}}^2/\eta_F$ is an upper bound on the pair-rotation angle accumulated during the linear ramp in the RWA. The slow protocols are quasi-adiabatic away from the initial gap-closing momenta, but they are not globally adiabatic in the topological regime.

F_{fin}/J	η_F/J^2	$J\tau_F$	$\max_\mu(\eta_F/\omega_F^2)$	χ_{ramp}	Protocol classification
0.5	3	0.167	1.11×10^{-3}	0.083	Fast, near-sudden
0.7	3	0.233	1.11×10^{-3}	0.163	Fast, near-sudden
0.5	10^{-2}	50	3.70×10^{-6}	25	Quasi-adiabatic away from $M_k = 0$
0.7	10^{-2}	70	3.70×10^{-6}	49	Quasi-adiabatic away from $M_k = 0$

weak-coupling hierarchy $|\mu|, |J|, |F_{\mathrm{fin}}| \ll \omega_F$, the rotating-frame construction assumes that the modulation envelope and instantaneous frequency satisfy $|\dot{F}|/\omega_F^2 \ll 1$, and $|\dot{\omega}_F|/\omega_F^2 \ll 1$. The frequency is fixed during each realization considered here, so that $\dot{\omega}_F = 0$, while the linear ramp in Eq. (3.3) has $|\dot{F}| = \eta_F$. Across all four protocols, $\eta_F/\omega_F^2 \le 1.1 \times 10^{-3}$, as summarized in Table 3.1. This carrier-scale condition is distinct from adiabaticity with respect to the effective RWA quasiparticle dynamics.

For the effective RWA problem, a useful measure of suddenness for the initial Jordan–Wigner vacuum and the linear fixed-frequency ramp is the maximum pair-rotation angle that can accumulate before the final amplitude is reached,

$$\chi_{\mathrm{ramp}} \equiv \max_k \left| \int_0^{\tau_F} F_k(t)\, dt \right| = \frac{F_{\mathrm{fin}}^2}{\eta_F}. \tag{3.4}$$

For the ramps with $\eta_F = 3J^2$, we get $\chi_{\mathrm{ramp}} = 0.083$ and $\chi_{\mathrm{ramp}} = 0.163$ for $F_{\mathrm{fin}}/J = 0.5$ and 0.7, respectively. Thus, these ramps approximate a sudden turn-on of the effective pairing interaction. In the topological regime, at a resonant momentum $k_\mu = \arccos(\mu/2J)$, where $M_{k_\mu} = 0$, the occupation created by the end of the linear ramp is $n_{k_\mu}(\tau_F) = \sin^2\left[\chi_{\mathrm{ramp}} \sin k_\mu\right] \le \sin^2 \chi_{\mathrm{ramp}}$. The upper bound is attained at $\mu = 0$, where $k_\mu = \pi/2$. For $F_{\mathrm{fin}}/J = 0.5$ and 0.7, the bounds are approximately 0.7% and 2.6%, respectively. The fast ramps therefore leave every resonant pair sector close to the initial fermionic vacuum when the final amplitude is reached and provide finite-time approximations to the ideal sudden turn-on.

By contrast, effective adiabaticity is mode dependent and requires

$$\frac{|\dot{\theta}_k(t)|}{\varepsilon_k(t)} = \frac{2\eta_F |M_k \sin k|}{\left[M_k^2 + 4F^2(t)\sin^2 k\right]^{3/2}} \ll 1. \tag{3.5}$$

Inside the topological regime, this condition cannot hold uniformly because the initial gap closes at $k = \pm k_\mu$. The two ramps with $\eta_F = 10^{-2}J^2$ are clearly not sudden as they both have $\chi_{\rm ramp} \gg 1$ (See Table 3.1). Their small values of η_F make the evolution adiabatic for modes whose initial gap $|M_k|$ is sufficiently large. Nevertheless, inside the topological interval the initial spectrum is gapless at $k = \pm k_\mu$, and a shrinking nonadiabatic momentum window remains for every finite ramp rate. The appropriate description of these protocols is therefore quasi-adiabatic rather than globally adiabatic. The scaling of this nonadiabatic region with the switching rate will be discussed later in this chapter. The parameters used in the simulations below as well as the relevant dimensionless parameters are summarized in Table 3.1.

For each momentum pair, the laboratory-frame time evolution is calculated with a unitary midpoint propagator constructed from Eqs. (3.2), using 100 time steps per modulation period. After the ramp reaches its final amplitude, the observables are continuously averaged over 1000 modulation periods. The resulting magnetization and connected nearest-neighbor longitudinal correlation are shown in Fig. 3.1. For $N = 500$, the discrete momentum grid produces negligible finite-size corrections away from the transition. Close to $\mu = \pm 2J$, however, the minimum quasiparticle energy becomes small, and the sharp features remain more sensitive to both the finite system size and the finite averaging interval.

The fast-ramp magnetization curves reproduce the principal prediction of the ideal sudden-turn-on RWA calculation. In the topological interval, the latter gives

$$1 - \langle \sigma_n^z \rangle_{\rm sudden} = \frac{|F_{\rm fin}|}{|J| + |F_{\rm fin}|} = \begin{cases} 1/3, & F_{\rm fin}/J = 0.5, \\ 7/17, & F_{\rm fin}/J = 0.7. \end{cases} \tag{3.6}$$

These are the plateau values approached by the solid blue and red curves in Fig. 3.1(a). The fast-ramp longitudinal correlation in panel (b) is also strongly suppressed throughout $|\mu| < 2|J|$, consistent

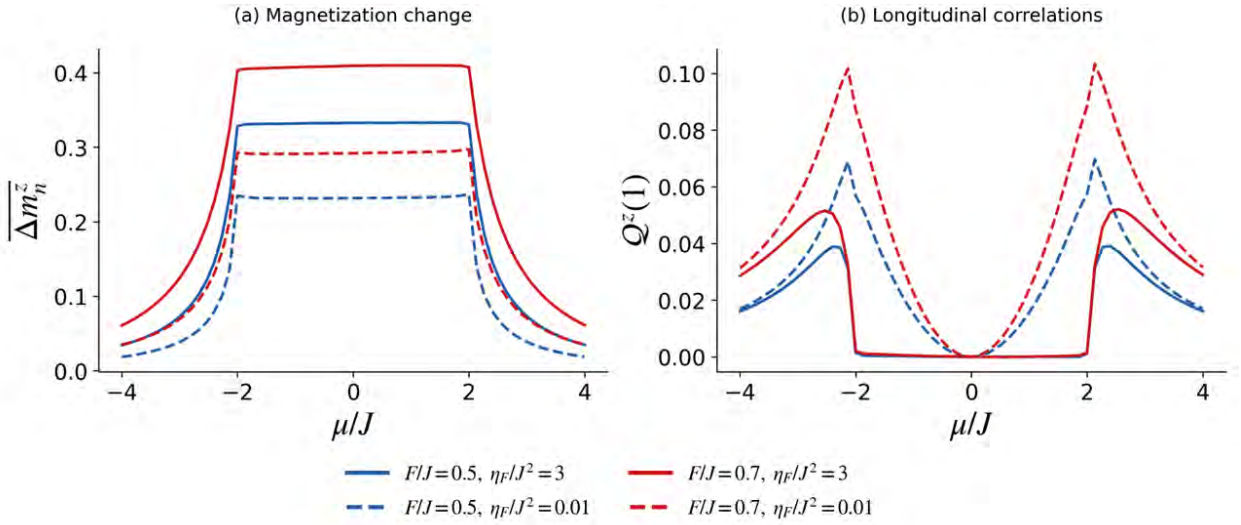


Figure 3.1 Full laboratory-frame dynamics of a periodic chain of $N = 500$ spins with $\omega_0 = 30J$ and $J_{xx} = J_{yy} = J/2$. (a) Continuous time-averaged magnetization change $\overline{\Delta m_n^z} = 1 - \langle \sigma_n^z \rangle$. (b) Continuous time-averaged nearest-neighbor longitudinal correlation $Q^z(1) = \langle \sigma_n^z \sigma_{n+1}^z \rangle - \langle \sigma_n^z \rangle^2$. Blue and red curves correspond to $F_{\text{fin}}/J = 0.5$ and 0.7, respectively. Solid curves are obtained using the fast ramp $\eta_F = 3J^2$, while dashed curves correspond to the slow ramp $\eta_F = 10^{-2}J^2$. The dynamics of each $(k, -k)$ sector is propagated using 100 time steps per modulation period, and the observables are averaged over 1000 periods after the ramp.

with the sudden-turn-on RWA prediction. The laboratory-frame calculation therefore reproduces the principal magnetization and correlation features obtained within the rotating-wave description.

The slow-ramp curves display a different prepared state. Their magnetization plateau has a smaller height, and the longitudinal correlation develops a strongly protocol-dependent structure, particularly near $\mu = \pm 2J$. This difference is not caused by a different final Hamiltonian: for fixed F_{fin} and μ, the fast and slow curves end at the same laboratory-frame Hamiltonian. It reflects the different occupations generated during the two ramps.

The laboratory-frame calculation demonstrates that the anomalous behavior is not an artifact of replacing the driven problem by $\hat{H}_{\text{RWA}}$. Its physical origin, however, is considerably more transparent in the rotating frame, where the band inversion, modulation-induced p-wave gap, and winding number appear explicitly. We therefore use the RWA Hamiltonian for the analytical discussion in the remainder of this chapter.

3.2 Sudden turn-on of the modulation

We first consider a modulation envelope that is turned on rapidly on the effective dynamical scale. In the ideal sudden limit, the pairing amplitude changes from zero to its final value F over a time δt satisfying

$$\omega_0^{-1} \ll \delta t \ll \varepsilon_k^{-1} \tag{3.7}$$

for the modes that dominate the response. The state therefore remains the Jordan–Wigner vacuum during the turn-on, but it is subsequently evolved by a Hamiltonian with nonzero pairing.

3.2.1 Mode-resolved dynamics and time averaging

The final RWA Hamiltonian is diagonalized by the Bogoliubov transformation in Eq. (2.10). After the modulation has reached its final value, the quasiparticle operators evolve as $d_k(t) = \exp(-i\varepsilon_k t) d_k(\delta t = +0) \equiv \exp(-i\varepsilon_k t) d_k$ for the positive-energy branch. Expressing the Jordan–Wigner occupation operator in terms of the final quasiparticles gives

$$c_k^\dagger(t) c_k(t) = d_k^\dagger d_k \cos^2 \frac{\theta_k}{2} + d_{-k} d_{-k}^\dagger \sin^2 \frac{\theta_k}{2} - \frac{1}{2} \sin\theta_k \left(d_k^\dagger d_{-k}^\dagger e^{2i\varepsilon_k t} + d_{-k} d_k e^{-2i\varepsilon_k t} \right). \tag{3.8}$$

For an averaging interval long compared with the inverse quasiparticle energies, the oscillatory terms dephase. Using the transformation (2.10) in Eq. (3.8) and taking the expectation value in the initial vacuum gives

$$\langle c_k^\dagger c_k \rangle = \frac{1}{2} \sin^2\theta_k = \frac{F_k^2}{2\varepsilon_k^2}. \tag{3.9}$$

Similarly, we get

$$\langle c_k^\dagger c_{-k}^\dagger \rangle = -\frac{1}{4} \sin 2\theta_k = -\frac{M_k F_k}{2\varepsilon_k^2}. \tag{3.10}$$

Equations (3.9) and (3.10), together with the observable relations in Sec. 2.5, determine all equal-time bulk spin correlations after a sudden turn-on.

3.2.2 Exact magnetization at finite drive

In the thermodynamic limit, using Eqs. (2.44) and (3.9), the magnetization change is

$$1 - \langle \sigma_n^z \rangle = \frac{1}{2\pi} \int_{-\pi}^{\pi} \sin^2\theta_k \, dk = \frac{1}{2\pi} \int_{-\pi}^{\pi} \left(\frac{F_k}{\varepsilon_k} \right)^2 dk. \tag{3.11}$$

This integral can be evaluated exactly by introducing $w = e^{ik}$ and converting the momentum integral into a contour integral over the unit circle. We obtain

$$1 - \langle \sigma_n^z \rangle = \frac{F}{2\pi} \operatorname{Im} \oint_{|w|=1} \frac{dw}{w} \frac{w^2 - 1}{P_1(w)}, \qquad P_1(w) = (F - J)w^2 + \mu w - (F + J). \tag{3.12}$$

The nonzero poles are located at

$$w_{\pm}^{(1)} = \frac{-\mu \pm \sqrt{\mu^2 - 4(J^2 - F^2)}}{2(F - J)}. \tag{3.13}$$

The distribution of these poles relative to the unit circle changes at $|\mu| = 2|J|$. In the topological regime, the two roots lie on the same side of the contour: both are inside for $FJ < 0$ and both are outside for $FJ > 0$. In the trivial regime, one root lies inside and the other lies outside. Evaluating the residues gives

$$1 - \langle \sigma_n^z \rangle = \begin{cases} \dfrac{F^2}{F^2 - J^2} \left[1 - \dfrac{|\mu|}{\sqrt{\mu^2 + 4(F^2 - J^2)}} \right], & |\mu| > 2|J|, \\ \dfrac{1}{1 + |J/F|} & |\mu| < 2|J|. \end{cases} \tag{3.14}$$

The first line describes the conventional decrease of the response as the modulation is detuned from resonance. The second line is the anomalous result: throughout the topological interval, the time-averaged excitation density is independent of the modulation frequency. Its magnitude is not quantized; it depends continuously on the ratio F/J. What is fixed by the topology is the absence of frequency dispersion within the interval bounded by the two gap closings.

Figure 3.2 compares the exact thermodynamic-limit result with finite-chain MPS simulations. The magnetization agrees well already for the simulated system size. Figure 3.2 also shows the connected longitudinal correlation. It has a larger finite-size correction. As we see below, longitudinal correlations contain a double sum of products of four fermionic operators which results in larger finite-size corrections. Appendix A shows that the integrated deviation decreases approximately as N^{-1}.

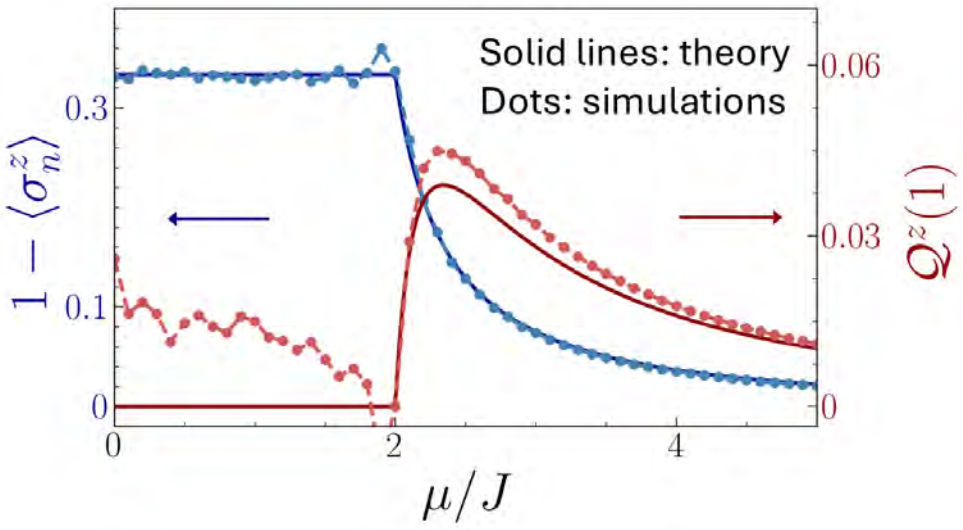


Figure 3.2 Time-averaged magnetization change $1-\langle\sigma_n^z\rangle$ and nearest-neighbor connected longitudinal correlation $Q^z(1)$ following a sudden turn-on of the RWA modulation, as functions of the scaled detuning μ/J. The final pairing amplitude is $F/J = 0.5$. The analytical curves refer to the thermodynamic limit. The dotted dashed curves are finite-chain MPS simulations of the RWA Hamiltonian with $N = 20$; the MPS method, averaging window, and finite-size analysis are described in Appendix A. The magnetization is independent of detuning and the longitudinal correlation vanishes throughout the topological interval $|\mu| < 2|J|$.

3.2.3 Longitudinal correlations

The connected longitudinal correlation is expressed through the normal and anomalous contractions defined in Eq. (2.45):

$$Q^z(m) = -|q_1(m)|^2 + |q_2(m)|^2. \tag{3.15}$$

For the sudden-turn-on contractions (3.9) and (3.10), the two functions can be written as

$$\begin{aligned} q_\alpha(m) &= \frac{F}{4\pi}\,\mathrm{Im}\oint_{|w|=1} dw\, w^{|m|-1}(w^2-1)\left[\frac{1}{P_1(w)} - \frac{(-1)^\alpha}{P_2(w)}\right], \\ P_\alpha(w) &= F(w^2-1) - (-1)^\alpha\left[\mu w - J(w^2+1)\right], \qquad \alpha = 1,2. \end{aligned} \tag{3.16}$$

The roots of $P_1(w)$ were given in Eq. (3.13) whereas the roots of the second polynomial are

$$w_\pm^{(2)} = \frac{\mu \pm \sqrt{\mu^2 - 4(J^2-F^2)}}{2(F+J)}. \tag{3.17}$$

In the topological regime, depending on $\mathrm{sgn}(JF)$, one of the two polynomials has no roots inside the unit circle. This gives $q_1(m) = -q_2(m)$ for $FJ > 0$, and $q_1(m) = q_2(m)$ for $FJ < 0$. It follows

immediately that

$$Q^z(m) = 0, \qquad |\mu| < 2|J|, \quad m \neq 0. \tag{3.18}$$

Thus, although the modulation creates a finite density of spin excitations, the time-averaged connected correlations of the longitudinal magnetization vanish for any pair of spins in the topological regime.

In the trivial regime, both P_1 and P_2 have one root inside the unit circle, and the two contributions no longer cancel. For the nearest-neighbor correlation,

$$Q^z(1) = \frac{2F^2(\mu^2 - 4J^2)}{r_\mu^2\left(\mu^2 - 2J^2 + 2F^2 + |\mu| r_\mu\right)}, \qquad |\mu| > 2|J|, \tag{3.19}$$

where $r_\mu = \sqrt{\mu^2 - 4J^2 + 4F^2}$. The correlation is continuous at $|\mu| = 2|J|$, but its derivative with respect to μ is discontinuous. It first increases after entering the trivial regime and subsequently decreases as μ^{-2} far from resonance.

The cancellation extends beyond the two-point function. For example, the connected three-site correlation introduced in Eq. (2.48) can be written as

$$\begin{aligned}\langle \Delta\sigma_n^z \Delta\sigma_{n+m}^z \Delta\sigma_{n+l}^z \rangle = {} & 2q_1(m)q_1(l)q_1(m-l) - 2q_1(m)q_2(l)q_2(l-m) \\ & + 2q_1(l)q_2(m)q_2(l-m) - 2q_1(m-l)q_2(m)q_2(l).\end{aligned} \tag{3.20}$$

Substituting $q_1 = \pm q_2$ shows that this correlator also vanishes in the topological regime. The same pairing structure causes the higher-order connected longitudinal correlations to vanish.

3.2.4 Transverse correlations

The nearest-neighbor transverse correlator is related to $q_1(1)$ by Eq. (2.49). Evaluating the same contour integrals gives

$$\langle \sigma_n^+ \sigma_{n+1}^- \rangle = \begin{cases} -\dfrac{\operatorname{sgn}(\mu) J F^2 (|\mu| - r_\mu)^2}{4 r_\mu (J^2 - F^2)^2}, & |\mu| > 2|J|, \\ -\operatorname{sgn}(FJ)\dfrac{\mu}{4F}\left(1 + |J/F|\right)^{-2}, & |\mu| < 2|J|. \end{cases} \tag{3.21}$$

Unlike the longitudinal connected correlations, the transverse correlator does not vanish in the topological regime. Instead, it varies linearly with the detuning. The analytical expressions for

the transverse correlations for both the fast and slow ramp is compared with MPS simulations in Figure 3.5. This difference provides complementary information: the magnetization identifies the plateau, the longitudinal correlations distinguish the cancellation characteristic of the sudden protocol, and the transverse correlator resolves the position inside the topological interval.

3.2.5 Finite-drive relation to the winding number

The contour calculation above is closely related to the explicit calculation of the winding number. Using the Bogoliubov angle defined in Sec. 2.4.1, one may write

$$\nu = \frac{1}{2\pi}\int_{-\pi}^{\pi} dk\, \frac{M_k \partial_k F_k - F_k \partial_k M_k}{\varepsilon_k^2}. \tag{3.22}$$

In terms of the same complex variable $w = e^{ik}$ and the polynomial $P_1(w)$ introduced in Eq. (3.12),

$$\nu = \frac{1}{2\pi}\,\mathrm{Im}\oint_{|w|=1} \frac{dw}{w}\frac{(F-J)w^2 + (F+J)}{P_1(w)}. \tag{3.23}$$

An equivalent representation follows by replacing $F \to -F$ and $P_1 \to P_2$. Clearly, the value of the winding number is determined by the structure of the poles of $P_1(w)$ and $P_2(w)$, which also determine the structure of the time-averaged spin observables we discussed above. To further see this, we assume $FJ > 0$. Then, we can write ν as

$$\nu = \frac{1}{2\pi}\mathrm{Im}\left\{(F-J)\oint dw \frac{w}{P_1(w)} + (F+J)\oint \frac{dw}{w}\frac{1}{P_1(w)}\right\}. \tag{3.24}$$

In the topological regime, the poles of $P_1(w)$ lie outside the unit circle, and therefore $\nu = (F+J)/P_1(0) = -1$. For $FJ < 0$, writing the integral in terms of P_2 and taking into account that P_2 does not have poles with $|w| < 1$ in the topological regime, we obtain $\nu = (J-F)/P_2(0) = 1$. A calculation for $|\mu/2J| > 1$ shows that $\nu = 0$ in this range. This is fully analogous to the calculations of the magnetization and the spin correlators above, revealing explicitly the relation of these calculations to the winding number.

3.2.6 Weak-drive limit

An insight into the anomalous behavior of the average magnetization and the correlators in the topologically nontrivial regime can be gained from the analysis of the effect of weak drive. In this regime, for $F = 0$ the gap in the dispersion law ε_k closes for two values of k in the Brillouin zone:

$\varepsilon_k = 0$ for $k = \pm k_\mu$, where $k_\mu = \arccos(\mu/2J)$. The drive opens the gap. For a weak drive the dispersion near the gap opening has a characteristic form

$$\varepsilon_k \approx |\sin k_\mu|[4J^2(|k| - |k_\mu|)^2 + 4F^2]^{1/2}, \qquad |F| \ll |J|, \quad |k| - |k_\mu| \ll \pi. \tag{3.25}$$

When the gap is small, excitations are created just near the two gap openings, i.e., for k close to k_μ or $-k_\mu$. From Eq. (3.9), the number of excitations with a given k is

$$\langle c_k^\dagger c_k \rangle = \frac{1}{2}\sin^2\theta_k = \frac{2F^2\sin^2 k}{\varepsilon_k^2} \approx \frac{2F^2}{4J^2(|k| - |k_\mu|)^2 + 4F^2}. \tag{3.26}$$

For small F, this expression as a function of k describes two narrow Lorentzian peaks at $k = \pm k_\mu$. The area of each peak is $\pi|F/2J|$. It is independent of μ. Therefore the magnetization change, which is given by $\int dk\, \langle c_k^\dagger c_k \rangle$, is also independent of μ. This is in spite the positions of the peaks being μ-dependent.

As $|F|$ increases, the peaks shift and are broadened, but still they do not overlap, since no excitations with $k = 0$ are created. As a result, the magnetization still remains independent of μ. To see this a calculation is required as we provided in Sec. 3.2.2. A formal insight is that the zeros of ε_k as a function of k go further into complex-k plane with the increasing $|F|$.

The correlator

$$\langle c_k^\dagger c_{-k}^\dagger \rangle = -\frac{1}{4}\sin 2\theta_k = -\frac{M_k F \sin k}{\varepsilon_k^2}$$

goes to zero at $k = \pm k_\mu$. Respectively, the correlator of the magnetization on different sites $Q^z(m)$ has no terms linear in F for $F \to 0$. The full calculation in Sec. 3.2.3 shows that it is equal to zero for any F in the topological regime.

In contrast, as seen from Eq. (3.26), in the topologically nontrivial regime the correlator of the off-diagonal spin components for small F is

$$\langle \sigma_n^+ \sigma_{n+1}^- \rangle = -N^{-1}\sum_k \langle c_k^\dagger c_k \rangle \cos k \approx -\frac{\mu}{4J}\,|F/J|.$$

This expression coincides with Eq. (3.21) for $|F/J| \ll 1$ and $|\mu/2J| < 1$. It shows that the correlator linearly increases with μ in the topological regime.

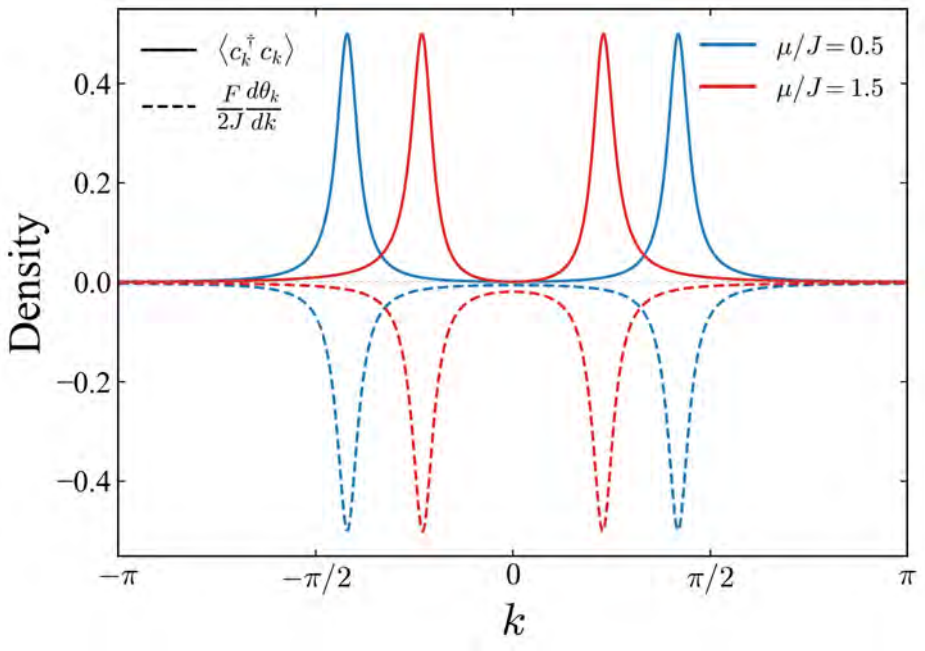


Figure 3.3 Momentum-resolved densities following a sudden turn-on at $F/J = 0.1$. Solid curves show the time-averaged fermion occupation $\langle c_k^\dagger c_k \rangle$, while dashed curves show the winding-number density $d\theta_k/dk$, multiplied by $F/2J$ to place the two quantities on the same scale. In the weak-drive regime, both quantities consist of two narrow Lorentzian peaks. Their centers $\pm k_\mu = \pm \arccos(\mu/2J)$ depend on detuning, whereas their shapes and integrated areas do not.

In the limit $F \to 0$ the winding number density in the topologically nontrivial becomes a set of two very narrow Lorentzians,

$$\frac{1}{2\pi}\frac{d\theta_k}{dk} = \frac{1}{2\pi}\frac{2FM_k\cos k - 2F_k J \sin k}{\varepsilon_k^2} \to -\frac{1}{2\pi}\frac{F/J}{(|k| - |k_\mu|)^2 + (F/J)^2} \tag{3.27}$$

The half-width of the Lorentzians is $|F/J| \ll 1$, their area (with the account taken of the factor $1/2\pi$) is $1/2$ independent of the scaled frequency detuning μ. The similarity of Eqs. (3.26) and (3.27) is obvious,

$$\langle c_k^\dagger c_k \rangle = -\frac{F}{2J}\frac{d\theta_k}{dk}.$$

The similarity of the densities $\langle c_k^\dagger c_k \rangle$ and $d\theta_k/dk$ is seen also from Fig. 3.3 that shows the full expressions for $\langle c_k^\dagger c_k \rangle$ and $d\theta_k/dk$.

3.2.7 Effect of an initial thermal population

We now discuss the effect of a nonzero temperature. The previous analysis refers to the case where, prior to the turn-on of the modulation, all spins are in the ground state, i.e., aligned along the

strong magnetic field. For a nonzero temperature some spins are flipped. For a low temperature compared to the Zeeman energy, $\beta\omega_0 \gg 1$, where $\beta = 1/T$ ($\hbar = k_B = 1$), the portion of flipped spins is exponentially small, $\propto \exp(-\beta\omega_0)$. This leads to a small correction to the effect of the modulation. We will consider this correction in the thermodynamic limit.

The density matrix of the spin system in the absence of modulation is

$$\rho_{\rm th} = Z^{-1}\exp\bigl(-\beta\hat{H}_T\bigr), \quad \hat{H}_T = -\frac{\omega_0}{2}\sum_{n=1}^{N}\sigma_n^z - J\sum_{n=1}^{N}(\sigma_n^+\sigma_{n+1}^- + \sigma_n^-\sigma_{n+1}^+), \tag{3.28}$$

where $J_{xx} = J_{yy} = J/2$ and $Z = \mathrm{Tr}[\exp\bigl(-\beta\hat{H}_T\bigr)]$ is the partition function. We can write the density matrix in terms of the Jordan-Wigner fermions in the momentum space, i.e., in terms of fermionic creation and annihilation operators $c_k^\dagger$ and c_k,

$$\rho_{\rm th} = \prod_k \exp\left[\beta\tilde{M}_k\left(c_k^\dagger c_k - \frac{1}{2}\right)\right]/2\cosh\bigl(\beta\tilde{M}_k/2\bigr), \quad \tilde{M}_k = -\omega_0 - 2J\cos k, \tag{3.29}$$

To the first order in $\exp(-\beta\omega_0)$ this gives

$$\langle\langle c_k^\dagger c_k\rangle\rangle \approx \exp\bigl(\beta\tilde{M}_k\bigr)$$

where $\langle\langle\hat{A}\rangle\rangle = \mathrm{Tr}\rho_{\rm th}\hat{A}$. Substituting this expression into Eq. (3.8), we obtain that, for a fast turn-on of the drive, the change $\Delta\langle c_k^\dagger c_k\rangle$ of the time-averaged fermion density is

$$\Delta\langle c_k^\dagger c_k\rangle \equiv \langle c_k^\dagger c_k\rangle - \langle\langle c_k^\dagger c_k\rangle\rangle = \frac{F_k^2}{2\varepsilon_k^2}[1 - 2\exp\bigl(\beta\tilde{M}_k\bigr)], \tag{3.30}$$

The corresponding change $\langle\langle\sigma_n^z\rangle\rangle - \langle\sigma_n^z\rangle$ of the magnetization is given by the integral of $\Delta\langle c_k^\dagger c_k\rangle$ over k. It is seen that the thermal correction is exponentially suppressed for $\exp(\omega_0/T) \gg 1$. Furthermore, its dependence on k becomes very weak if, while $\exp(\omega_0/T) \gg 1$, we have $T \gg |J|$, so that the factor $\tilde{M}_k$ is essentially independent of k.

A similar calculation gives for a fast turn-on

$$\langle c_k^\dagger c_{-k}^\dagger\rangle = -\frac{F_k M_k}{2\varepsilon_k^2}[1 - 2\exp\bigl(\beta\tilde{M}_k\bigr)].$$

It follows from these expressions and Eq. (2.45) that, for a fast turn-on and for $T \gg |J|$, the magnetization correlators $Q^z(m)$ remain equal to zero even where the terms $\sim \exp(-\beta\omega_0)$ are taken into account.

For later reference, for a slow turn-on of the drive in the adiabatic approximation, the time-averaged fermion density is

$$\Delta \langle c_k^\dagger c_k \rangle = \frac{\varepsilon_k - |M_k|}{2\varepsilon_k}[1 - 2\exp(\beta \tilde{M}_k)]. \tag{3.31}$$

In this case the thermal correction to the magnetization change is also independent of μ for $T \gg |J|$.

3.3 Slow turn-on of the modulation

We next consider an amplitude that increases monotonically $F(0) = 0$ to $F(t_f) = F_{\rm fin}$ and remains constant thereafter. The instantaneous quasiparticle equations were derived in Eq. (2.41). They separate the instantaneous phase accumulation, controlled by $\varepsilon_k(t)$, from transitions between the two branches, controlled by $\dot{\theta}_k(t)$.

We first neglect the nonadiabatic term and derive the adiabatic approximation. We then identify where and how this approximation fails. The general solution of the Schrödinger equation for all momenta under a general amplitude ramp is developed in Sec. 3.5 with a particular focus on linear ramp for which the dynamical equation maps on the Weber equation [68–71]. This ordering allows the physical consequences of the slow turn-on to be presented before the more detailed asymptotic analysis.

3.3.1 Adiabatic approximation

The mode evolution is adiabatic when $|\dot{\theta}_k| \ll \varepsilon_k$. Neglecting the off-diagonal term in Eq. (2.41) gives

$$d_k(t) = d_k(0) \exp\left[-i \int_0^t \varepsilon_k(t')dt'\right] \tag{3.32}$$

for the positive-energy branch. The value of $d_k(0)$ here is found from Eq. (2.10) by noting that $\theta_k(0)$ equals either 0 or π for $M_k \neq 0$ and $F \to 0$. In the considered case $M_k \cos\theta_k < 0$, we have $d_k(0) = c_k(0)$ for $M_k < 0$ and $d_k(0) = c_{-k}^\dagger(0)$ for $M_k > 0$. Then from equation $\vec{c}_k = U(k)\vec{d}_k$

$$c_k(t) = \begin{cases} c_k(0)e^{-i\Phi(t)} \cos[\theta_k(t)/2] - c_{-k}^\dagger(0)e^{i\Phi(t)} \sin[\theta_k(t)/2], & M_k < 0 \ [\theta_k(0) = 0] \\ c_{-k}^\dagger(0)e^{-i\Phi(t)} \cos[\theta_k(t)/2] - c_k(0)e^{i\Phi(t)} \sin[\theta_k(t)/2], & M_k > 0 \ [\theta_k(0) = \pi] \end{cases} \tag{3.33}$$

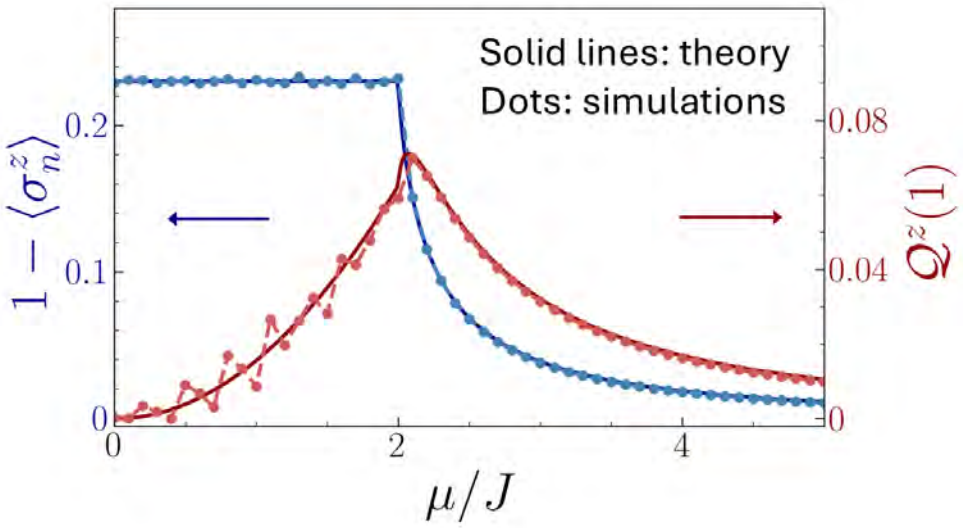


Figure 3.4 Time-averaged magnetization change $1-\langle\sigma_n^z\rangle$ and nearest-neighbor connected longitudinal correlation $Q^z(1)$ for a slow linear turn-on of the RWA pairing amplitude. The final amplitude is $F_{\rm fin}/J = 0.5$. The analytical curves use the adiabatic contractions in Eq. (3.34). The symbols are MPS simulations of the RWA Hamiltonian for $N = 40$ and a ramp time $\tau_{\rm sl} = 10^3 J^{-1}$, followed by continuous time averaging at the final parameters. Numerical details are given in Appendix A. The magnetization remains independent of detuning in the topological interval, but $Q^z(1)$ is generally nonzero, in contrast to the sudden-turn-on result.

where $\Phi(t) = \int_0^t dt' \varepsilon_k(t')$. Thus, the fermionic expectation values are given by

$$\begin{aligned}\langle c_k^\dagger(t) c_k(t)\rangle &= \frac{1}{2}(1 - |\cos\theta_k|) = \frac{\varepsilon_k - |M_k|}{2\varepsilon_k},\\ \langle c_k^\dagger(t) c_{-k}^\dagger(t)\rangle &= \frac{-1}{2}\sin\theta_k = -\frac{F_k}{2\varepsilon_k}\,\mathrm{sgn}\ M_k.\end{aligned} \tag{3.34}$$

Here and below, the quantities on the right-hand side are evaluated at the final drive amplitude. From Eq. (2.45), the corresponding functions that determine the spin observables are

$$\begin{aligned}q_1(m) &= \delta_{m,0} - \frac{1}{N}\sum_k \frac{|M_k|}{\varepsilon_k}\cos(mk),\\ q_2(m) &= -\frac{1}{N}\sum_k \sin\theta_k \sin(mk).\end{aligned} \tag{3.35}$$

In the thermodynamic limit, these expressions become contour integrals whose singularities are branching points associated with the zeros of $P_1(w)P_2(w)$. As in the sudden problem, their analytic structure changes when $|\mu|$ crosses $2|J|$. In the topological regime, the resulting magnetization remains independent of μ , the transverse correlations increases linearly with μ, whereas the longitudinal correlations no longer vanish identically (See Figures 3.4 and 3.5).

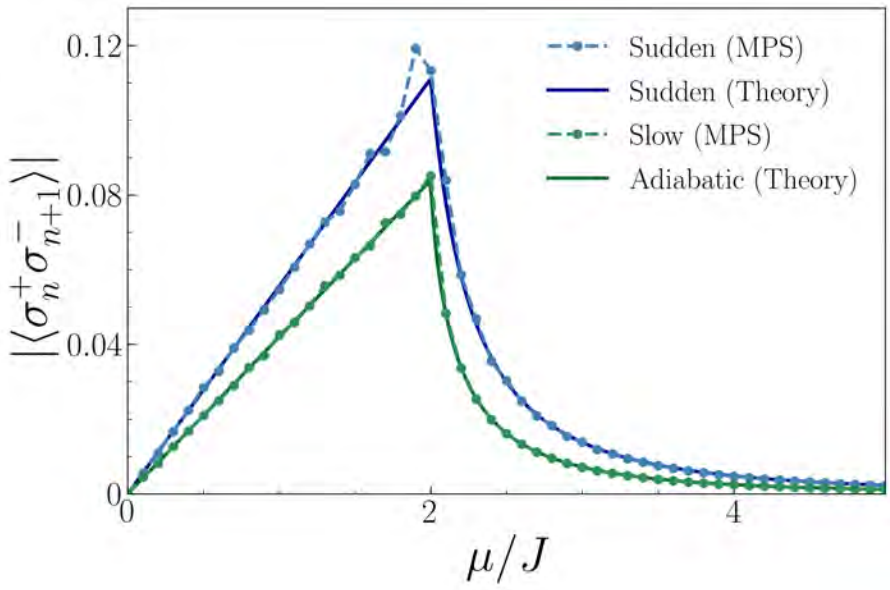


Figure 3.5 Magnitude of the time-averaged nearest-neighbor transverse correlator $|\langle\sigma_n^+\sigma_{n+1}^-\rangle|$ after sudden and slow turn-on, plotted as a function of μ/J for $F_{\text{fin}}/J = 0.5$. The analytical results are obtained from Eqs. (3.21) and (3.34). The dashed dotted lines are MPS simulations of the RWA Hamiltonian with $N = 20$ for the sudden protocol and $N = 40$ for the slow protocol. The slow ramp uses $\tau_{\text{sl}} = 10^3 J^{-1}$. Details are provided in Appendix A.

The difference between the sudden and slow protocols is particularly clear in the longitudinal correlations. The final Hamiltonian is identical, but the mode occupations retained after dephasing are different. The magnetization plateau is therefore not tied to one special quench state; it persists for both protocols. The cancellation of the longitudinal correlations, however, is specific to the sudden preparation.

Both the sudden and adiabatic expressions are nonanalytic at $|\mu| = 2|J|$. The observables themselves remain continuous, but their derivatives with respect to the modulation frequency are discontinuous in the thermodynamic limit. This nonanalyticity follows from the closing of the quasiparticle gap and the simultaneous change of the winding number.

3.3.2 Breakdown of adiabaticity

The adiabaticity condition $|\dot{\theta}_k| \ll \varepsilon_k$ breaks down where the energy gap is small. Inside the topological regime, $|\mu/2J| < 1$, the gap closes for $F(t = 0) = 0$ and $k = \pm k_\mu$, where

$$k_\mu = \arccos(\mu/2J).$$

Therefore, the adiabatic approximation does not apply for small $|F|$ and $\Big||k|-|k_\mu|\Big|$. For an amplitude ramp at fixed μ,

$$\dot{\theta}_k = \frac{2\dot{F}\sin k\, M_k}{\varepsilon_k^2}. \tag{3.36}$$

Thus, the region of k, where $\varepsilon_k \lesssim |\dot{\theta}_k|$ is limited to

$$\Big||k|-|k_\mu|\Big| \lesssim |\dot{F}/(J^2\sin k_\mu)|^{1/2}. \tag{3.37}$$

The analysis of the contribution of this region and the corrections to the adiabatic approximation are discussed in Sec. 3.5. These corrections strongly depend on the relation between the size of the gap $|2F_k|$ after it has been opened and the bandwidth J. They also depend on the interrelation between $|2F_k|$ and the characteristic time $\tau_{\rm sl}$ it took the system to reach the stationary state or, equivalently, the rate at which the drive amplitude is increased. The limit $|F_k|\tau_{\rm sl} \ll 1$ is discussed in Sec. 3.5.1. The above estimate of the smallness of the region of k where the adiabaticity is broken refers to the opposite limit. See Sec.3.5.2 for more details.

The energy gap closes also at the boundary of the topological regime, for $\mu/2J = 1$ and $k = 0$, and for $\mu/2J = -1$ and $k = \pi$. For $|\mu/2J| = 1$, the range of k where the quasi-adiabaticity is broken scales as $|\dot{F}/J^2|^{1/3}$.

We note that the dynamical equations can be solved in the explicit form where the gap is closed, i.e., $M_k = 0$. In this case, from the Heisenberg equations for the fermionic operators $c_k(t)$ we find

$$c_k(t) = \cos\left(\int_0^t F_k(t')dt'\right)c_k(0) + i\sin\left(\int_0^t F_k(t')dt'\right)c^\dagger_{-k}(0), \quad k = \pm k_\mu. \tag{3.38}$$

The time evolution of $c_k(t)$ as described by Eq. (3.38) is reminiscent of Rabi oscillations. Oscillations of $c_k(t)$ persist away from the points $\varepsilon_k = 0$. In the quasi-adiabatic regime they have frequency $\varepsilon_k(t)$ and are superposed on the smooth quasi-adiabatic evolution; they lead to oscillations of the spin variables. Of primary interest for the experiment are time-averaged spin correlators that we calculate. The simulation results shown in the main text also refer to time-averaged spin correlators, as we discuss in Appendix. A. Interestingly, it follows from Eq, (3.38) that $\langle c_k^\dagger c_k\rangle = 1/2$ for $k = \pm k_\mu$, which is the same value that follows form the adiabatic expression (3.34).

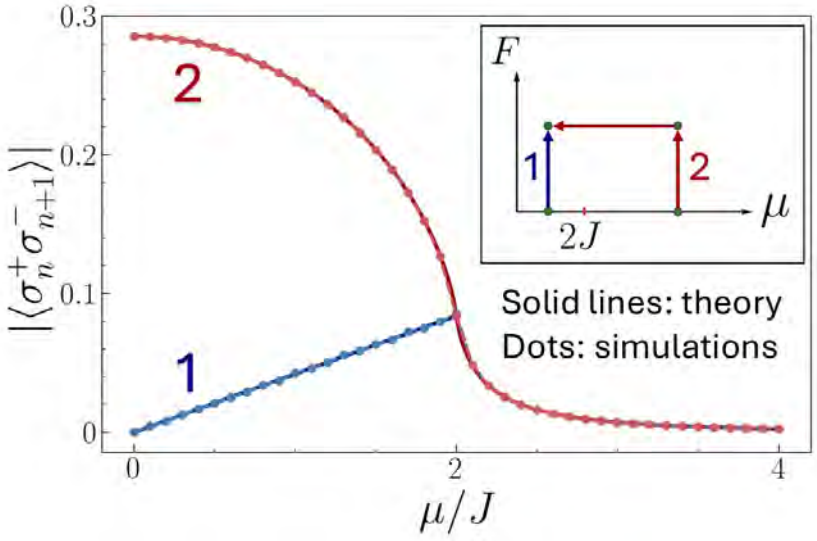


Figure 3.6 Time-averaged transverse correlation $|\langle\sigma_n^+\sigma_{n+1}^-\rangle|$ obtained along two slow preparation paths. Path 1 turns on the pairing amplitude directly at the displayed value of μ. Path 2 first turns on the amplitude to $F_{\rm fin} = 0.5J$ in the trivial regime and then sweeps the modulation frequency to the same final detuning. Lines show the adiabatic analytical results; dashed dotted lines are MPS simulations of the RWA Hamiltonian with $N = 40$ and $\tau_{\rm sl} = 10^3 J^{-1}$. Details are given in Appendix A.

3.4 Preparation memory and hysteresis

The distinction between the trivial and topological regimes permits two different slow preparation paths to terminate at the same final Hamiltonian. These paths were defined in Eqs. (2.32) and (2.33).

For the direct path, the drive amplitude is turned on at a fixed final detuning μ_f inside the topological interval. The adiabatic contractions are those in Eq. (3.34). For the indirect path, the amplitude is first turned on in the trivial regime at μ_0, where $\operatorname{sgn} M_k = \operatorname{sgn}\mu_0$ for all k, and the detuning is then swept into the topological interval. Neglecting the narrow nonadiabatic region generated while crossing the phase boundary, the final contractions are

$$\begin{aligned}\langle c_k^\dagger c_k\rangle_{\rm hys} &= \frac{\varepsilon_k - M_k \operatorname{sgn}\mu_0}{2\varepsilon_k},\\ \langle c_k^\dagger c_{-k}^\dagger\rangle_{\rm hys} &= -\frac{F_k}{2\varepsilon_k}\operatorname{sgn}\mu_0.\end{aligned} \tag{3.39}$$

These differ from Eq. (3.34), even though the final values of μ, J, and F are identical. The difference is retained in the conserved occupations of the final quasiparticle modes and therefore remains after dephasing.

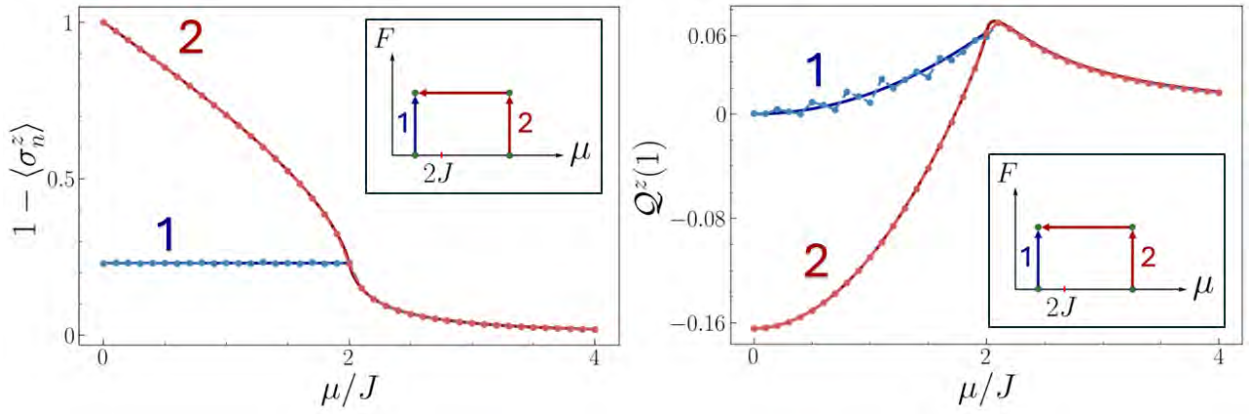


Figure 3.7 Preparation-path dependence of the time-averaged magnetization change $1-\langle\sigma_n^z\rangle$ (left) and the connected nearest-neighbor longitudinal correlation $\mathcal{Q}^z(1)$ (right). Path 1 turns on the modulation at fixed detuning. Path 2 first establishes $F_{\rm fin}/J = 0.5$ in the trivial regime and then sweeps the frequency to the same final μ. Lines are obtained from Eqs. (3.34) and (3.39); dashed dotted lines are MPS simulations of the RWA Hamiltonian. The simulation protocol and convergence tests are described in Appendix A.

The frequency sweep necessarily crosses one of the topological phase boundaries. Suppose, for example, that $\mu(t)$ crosses $2J$ at time t_c, and define $v_\mu = \dot{\mu}(t_c)$. For small k,

$$M_k(t) \approx v_\mu(t-t_c) + Jk^2, \qquad F_k \approx 2Fk. \tag{3.40}$$

After shifting the time origin separately for each momentum, the two-level problem reduces locally to a Landau–Zener crossing. With the normalization of the pair Hamiltonian in Eq. (2.36), the excitation probability is

$$p_k^{\rm KZ} \approx \exp\left[-\frac{\pi(2Fk)^2}{|v_\mu|}\right]. \tag{3.41}$$

The nonadiabatic excitations are therefore confined to a momentum window of width

$$k_{\rm KZ} \sim \frac{|v_\mu|^{1/2}}{2|F|}. \tag{3.42}$$

An analogous expression applies near $k=\pi$ when the sweep crosses $\mu=-2J$. The corrections to spatially averaged observables scale with the width of this window and vanish for an asymptotically slow sweep. This is the Kibble–Zurek mechanism for the present BdG problem [5, 70, 71].

The large difference between the two curves in Figs. 3.6 and 3.7 does not originate from these small Kibble–Zurek corrections. It is instead the memory of whether the mode occupations were

established by opening the pairing gap inside the topological regime or by first preparing the trivial phase. The hysteresis is therefore a property of the nonequilibrium state, not of the final Hamiltonian alone.

3.5 General solution for a slowly turned-on drive

The adiabatic treatment gives the dominant response away from the gap-closing momenta, while Eqs. (3.37)–(3.38) describe the scale and the center of the nonadiabatic region. We now solve the Schrödinger equation introduced in Sec. 2.5 to interpolate between these limits.

For any ramp, the state in each even-parity momentum sector is

$$|\psi_k(t)\rangle = A_{00}(k,t)\,|0_{-k},0_k\rangle + A_{11}(k,t)\,|1_{-k},1_k\rangle\,, \tag{3.43}$$

and the amplitudes obey Eq. (2.37). Once the parameters have reached their stationary final values, the amplitudes can be decomposed as

$$A_{mm}(k,t) = A^{+}_{mm}(k)e^{i\varepsilon_k t} + A^{-}_{mm}(k)e^{-i\varepsilon_k t}, \qquad m = 0,1. \tag{3.44}$$

The coefficients satisfy

$$A^{+}_{11}(k) = \frac{F_k A^{+}_{00}(k)}{\varepsilon_k - M_k}, \qquad A^{-}_{11}(k) = -\frac{F_k A^{-}_{00}(k)}{\varepsilon_k + M_k}. \tag{3.45}$$

In terms of the amplitudes at the end of the ramp,

$$A^{\pm}_{11}(k) = \frac{(\varepsilon_k \pm M_k)A_{11}(k,t_f) \pm F_k A_{00}(k,t_f)}{2\varepsilon_k}. \tag{3.46}$$

The continuous time averages are then

$$\begin{aligned}\langle c^{\dagger}_k c_k\rangle &= |A^{+}_{11}(k)|^2 + |A^{-}_{11}(k)|^2,\\ \langle c^{\dagger}_k c^{\dagger}_{-k}\rangle &= \frac{\varepsilon_k - M_k}{F_k}|A^{+}_{11}(k)|^2 - \frac{\varepsilon_k + M_k}{F_k}|A^{-}_{11}(k)|^2.\end{aligned} \tag{3.47}$$

Equations (3.46) and (3.47) apply to any turn-on protocol once the two amplitudes at t_f are known. They also provide the direct route used for the numerical integration of the mode equations.

3.5.1 Weak-drive limit for a finite turn-on rate

Near the gap-closing momenta, the dynamics involves three small scales: $|M_k|$, the instantaneous pairing amplitude $|F_k(t)|$, and the ramp rate. Two useful model envelopes are an exponential turn-on,

$$F(t) = F_{\rm fin} e^{\delta_{\rm on} t}, \qquad -\infty < t \le 0, \qquad 0 < \delta_{\rm on} \ll |J|, \tag{3.48}$$

and a linear turn-on,

$$F(t) = \eta(t + \tau_{\rm sl}), \qquad -\tau_{\rm sl} \le t \le 0, \qquad F_{\rm fin} = \eta\tau_{\rm sl}, \qquad |\eta| \ll J^2. \tag{3.49}$$

The time origin has been chosen so that the ramp ends at $t = 0$.

For the exponential protocol in the regime $|F_{\rm fin}| \ll \delta_{\rm on} \ll |J|$, one may neglect the feedback of A_{11} on A_{00} during the turn-on by disregarding the term $F_k A_{11}$ in Eq. (2.37) for A_{00} . To first order in the pairing amplitude,

$$A_{11}(k,t) \approx \int_{-\infty}^{t} dt'\, e^{iM_k t - 2iM_k t'} F_k(t'). \tag{3.50}$$

After the amplitude becomes stationary, this gives

$$\langle c_k^\dagger c_k \rangle \approx \frac{2F_{\rm fin}^2 \sin^2 k}{\varepsilon_k^2 \left(4M_k^2 + \delta_{\rm on}^2\right)} \left(\varepsilon_k^2 + M_k^2 + \delta_{\rm on}^2\right). \tag{3.51}$$

Near $\pm k_\mu$, the result reduces to

$$\langle c_k^\dagger c_k \rangle \approx \frac{|F_{\rm fin}|}{2|J|} \frac{|F_{\rm fin}/J|}{\left(|k| - |k_\mu|\right)^2 + |F_{\rm fin}/J|^2}. \tag{3.52}$$

The peak area is $\pi|F_{\rm fin}/2J|$ and is independent of μ. In the model (3.49), the perturbation theory in $F_{\rm fin} = \eta\tau_{\rm sl}$ applies for $|F_{\rm fin}| \ll |J|, \tau_{\rm sl}^{-1}$, and $|\eta| \ll J^2$. Then

$$A_{11}(t) \approx i\frac{F_k}{\varepsilon_k} \sin \varepsilon_k t + \frac{A_{11}(0)}{2\varepsilon_k} \left[(\varepsilon_k + M_k)e^{i\varepsilon_k t} + (\varepsilon_k - M_k)e^{-i\varepsilon_k t}\right],$$
$$A_{11}(0) = -\frac{F_k}{2M_k} + i\frac{F_k}{4M_k^2\tau_{\rm sl}} \left(1 - e^{2iM_k\tau_{\rm sl}}\right)$$

Here, too, of particular interest is the range $|M_k|\tau_{\rm sl} \ll 1$, where we have $A_{11}(0) \approx iF_k\tau_{\rm sl}/2$ and the correlator $\langle c_k^\dagger(t) c_k(t)\rangle$ shows two Lorentzian peaks, which are given by Eq. (3.52). For $|k|$ further away from $|k_\mu|$, the correlator is small.

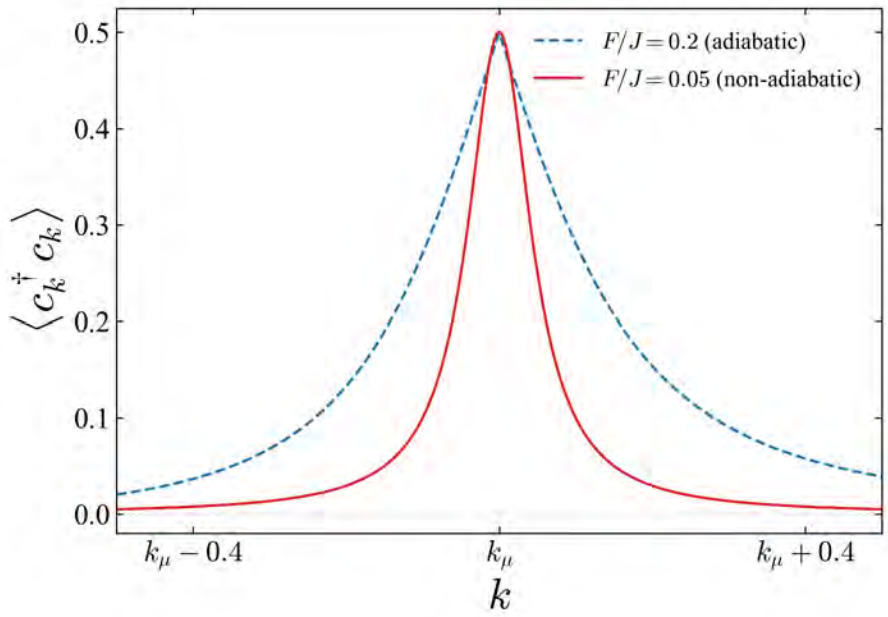


Figure 3.8 Momentum-resolved occupation $\langle c_k^\dagger c_k \rangle$ for a weak, finite-rate turn-on at $\mu/J = 1$, for which $k_\mu = \pi/3$. The solid curve is the Lorentzian nonadiabatic peak in Eq. (3.52), obtained when the inverse turn-on time exceeds the final pairing scale. The dashed curve is the adiabatic peak in Eq. (3.53). Both have a detuning-independent shape when expressed relative to k_μ, but their profiles differ.

These results show that the linear in $F_{\rm fin}$ terms are not described by the adiabatic theory: one has to assume that the turn-on is faster than the final value of the drive amplitude. However, in the topologically nontrivial regime, the magnetization is independent of the scaled frequency detuning μ. We note that the halfwidths of the peaks (3.52) are $|F_{\rm fin}/J|$, they are much smaller than what one might expect from the finite duration of the turn-on, $\delta_{on}/J, J\tau_{\rm sl}^{-1}$.

It is instructive to compare this result with Eq. (3.34), which is obtained in the adiabatic approximation, i.e., disregarding the adiabaticity breaking near the gap closing. There, for small F/J, the correlator $\langle c_k^\dagger(t) c_k(t) \rangle$ also displays sharp peaks for small $|k| - |k_\mu|$,

$$\langle c_k^\dagger(t) c_k(t) \rangle \approx \frac{1}{2} \frac{\left[(|k| - |k_\mu|)^2 + F^2/J^2\right]^{1/2} - \left||k| - |k_\mu|\right|}{\left[(|k| - |k_\mu|)^2 + F^2/J^2\right]^{1/2}} \qquad (F \equiv F_{\rm fin}). \tag{3.53}$$

The peaks are independent of μ, and so is $\int dk\ \langle c_k^\dagger(t) c_k(t) \rangle \propto |F/J|$, which explains the independence of the magnetization of μ in the topologically nontrivial regime. Interestingly, they have the same height $1/2$ as the peaks (3.52), but have a different shape.

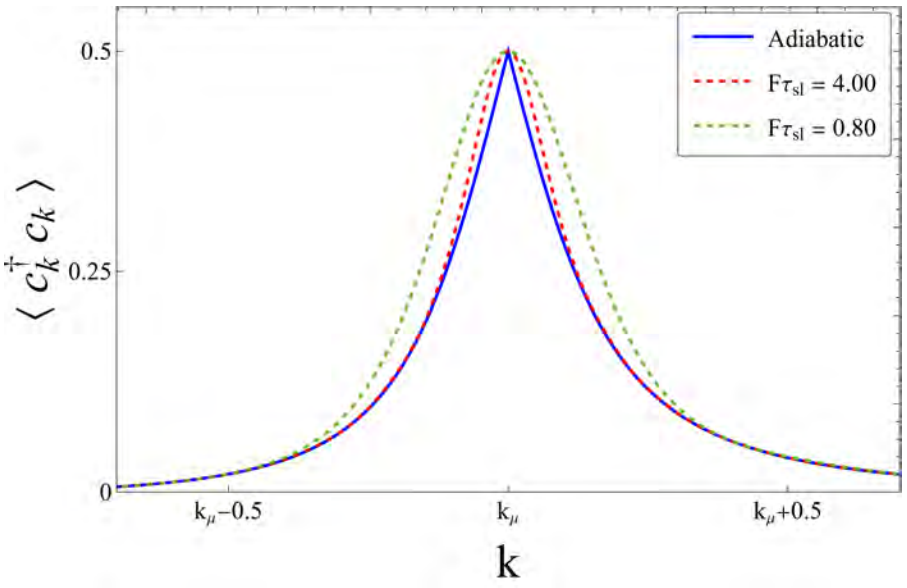


Figure 3.9 Time-averaged momentum occupation for a linear turn-on at $\mu/J = 1$, $k_\mu = \pi/3$, and $F_{\rm fin}/J = 0.2$. The solid curve is the adiabatic expression in Eq. (3.34). Dashed curves are obtained by direct integration of the exact pair-amplitude equations and subsequent use of Eq. (3.47) for two ramp rates. The agreement becomes excellent once $F_{\rm fin}\tau_{\rm sl} \gg 1$, and remains qualitatively good even outside the asymptotic limit.

3.5.2 Finite-rate correction to the adiabatic result

For a general linear ramp, the amplitudes at the end of the ramp can be found by numerically integrating Eq. (2.37) and then using Eq. (3.47). The results are compared with the adiabatic expression in Fig. 3.9. The agreement is very good already for $F \equiv F_{\rm fin} = 4\tau_{\rm sl}^{-1}$. Moreover even relatively far from the adiabatic limit, where $F \equiv F_{\rm fin} = 0.8\tau_{\rm sl}^{-1}$ the results are close. This provides justification to using the adiabatic approximation to describe the magnetization. We checked that a close agreement holds also for spin correlators.

Generally speaking, the nonadiabatic corrections scale with the width of the nonadiabatic quasimomentum region. As we already discussed, near this region where the adiabaticity condition $|\dot\theta_k| \ll \varepsilon_k$ breaks down, excitations are unavoidably generated as F is turned on. We showed above that the outcome depends on the relation between the final value of $F \equiv F_{\rm fin}$ and the rate at which it is reached, where the independence of $\langle\sigma_n^z\rangle$ on μ persists even where $F_{\rm fin}$ is smaller than this rate.

If $|\dot F| \ll F_{\rm fin}^2 \ll J^2$, the adiabatic approximation still does not apply for $\Big||k| - |k_\mu|\Big| \lesssim |\dot F/G_\mu|^{1/2}$, where $G_\mu = J(4J^2 - \mu^2)^{1/2}$. However, nonadiabatic corrections to the spin correlators and $\langle\sigma_n^z\rangle$

are small, as they are proportional to the size of the corresponding range of k and thus scale as $|\dot{F}/G_\mu|^{1/2}$. They increase as the system approaches the critical value of the modulation frequency where $|\mu/2J| = 1$. Near this value the width of the nonadiabatic region scales as $(|\dot{F}|/J^2)^{1/3}$.

Finally, it is important to note that the energy gap closing at $|\mu/2J| = 1$ and $k = 0$ or $k = \pi$ or all $F(t)$ also affects the time averaging. In particular, in the sudden turn-on approximation, we disregarded the time-averaged matrix elements $[d_k(t)d_{-k}(t) + \text{H.c.}]$, which are $\propto \sin(2\varepsilon_k T)/2\varepsilon_k T$. At $\mu = 2J$, since $\varepsilon_k \approx 2|F_{\text{fin}}k|$ for $|k| \ll 1$, the resulting correction is $\sim 1/F_{\text{fin}}T$. The smallness of this correction is determined by the restriction on T imposed by spin relaxation due to the coupling to a thermal reservoir and the $\sigma_n^z\sigma_m^z$-coupling, which leads to pre-thermalization of excitations.

3.5.3 WKB solution

Equations (2.37) for $A_{00} \equiv A_{00}(k,t), A_{11} \equiv A_{11}(k,t)$ can be written as

$$\ddot{A}_{00} = \frac{-i\dot{F}_k}{F_k}\left(i\dot{A}_{00} - M_k A_{00}\right) - \varepsilon_k^2 A_{00} - i\dot{M}_k A_{00}, \qquad A_{11} = -(i\dot{A}_{00} - M_k A_{00})/F_k(t) \tag{3.54}$$

We will seek the solution of these equations in the WKB approximation. This approximation relies on the slowness of the variation of F_k and M_k. The small parameter of the theory is $|\dot{\varepsilon}_k|/\varepsilon_k^2$. For simplicity, we present the results for the case of time-independent M_k, although they immediately extend to a slowly varying in time M_k.

The structure of Eq. (3.54) for A_{00} is different from the more conventional structure of the equations solved in the WKB approximation, where there are no terms with first derivatives. These terms can be eliminated (see below), but it is more convenient to seek the solution as a sum of an eikonal and non-eikonal terms. To the first order in $|\dot{\varepsilon}_k|/\varepsilon_k^2 \ll 1$ the eikonal term is

$$\begin{aligned} &A_{00}(k,t) = A_1(k,t) + A_2(k,t); \quad A_1(k,t) = C_{k1}\exp[iS(t)], \quad S(t) \approx S^{(0)}(t) + S^{(1)}(t), \\ &S^{(0)}(t) = -\int_0^t \varepsilon_k(t')dt' \,(\text{sgn } M_k), \qquad S^{(1)}(t) = \frac{i}{2}\left(\log\frac{\varepsilon_k(t)}{\varepsilon_k(0)} - \log\frac{\varepsilon_k(t) + |M_k|}{\varepsilon_k(0) + |M_k|}\right), \end{aligned} \tag{3.55}$$

where C_{k1} is a constant to be determined by the initial conditions. The WKB approximation implies that $|\dot{S}^{(0)}| \gg |\dot{S}^{(1)}|$, which can be shown to be equivalent to the condition $|\dot{\varepsilon}_k|/\varepsilon_k^2 \ll 1$.

The second solution is given by the method of parameter variations,

$$A_2(k,t)(t) = C_{k2}\exp[iS(t)]\int_0^t dt' F_k(t')\exp[-2iS(t')]. \tag{3.56}$$

The constants C_{k1} and C_{k2} can be found if the inequality $|\dot{\varepsilon}_k| \ll \varepsilon_k^2$ holds in the whole time interval during which the drive is turned on. For $F_k(t) \to 0$ for $t \to 0$, for the values of we obtain from $A_{00}(k, t = 0) = 1$

$$C_{k1} = 1, \quad C_{k2} = 0, \quad A_{11}(k,t) \approx -\,\mathrm{sgn}\; M_k \,\frac{F_k(t)}{\varepsilon_k(t) + |M_k|}\exp[iS(t)]. \tag{3.57}$$

It is easy to see that, for $\Big||k| - |k_\mu|\Big| \gg |\dot{F}/J\sin k_\mu|^{1/2}$, Eqs. (3.55) and (3.57) give the quasi-adiabatic results of Eq. (3.33). In particular,

$$\begin{aligned}
&\langle c_k^\dagger(t)c_k(t)\rangle = |A_{11}(k,t)|^2 \to \frac{\varepsilon_k - |M_k|}{2\varepsilon_k},\\
&\langle c_k^\dagger(t)c_{-k}^\dagger(t)\rangle = A_{11}^*(k,t)A_{00}(k,t) \to -\frac{F_k(t)\;\mathrm{sgn}\; M_k}{2\varepsilon_k(t)}.
\end{aligned} \tag{3.58}$$

On the other hand, for $M_k = 0$, where $\varepsilon_k(t) = F_k(t)$, to obtain the nonquasi-adiabatic solution, one needs to take the limit $M_k \to 0$ before the limit $t \to 0^+$. In this case, we get $C_{k2} = i$ which gives the results obtained in Eq. (3.38). This concludes that the solution developed here captures both the quasi-adiabatic and the fully nonquasi-adiabatic solutions discussed in earlier sections.

In the topological regime, the WKB condition $\dot{\varepsilon}_k \ll \varepsilon_k^2$ breaks down for small, but non-zero, $|M_k|$, i.e., for $|k|$ close to the gap-closing value $|k_\mu| = |\arccos(\mu/2J)|$, which is determined by the condition $\varepsilon_{k_\mu} = 0$ for $F_k = 0$. Formally, for a nonzero M_k, we have $\dot{\varepsilon}_k \propto F_k\dot{F}_k/M_k \to 0$ for $t \to 0$, since $F_k(t) \to 0$ for $t \to 0$. However, already for a small nonzero time, we can have $|M_k| \lesssim |F_k|$ for small $|M_k|$. Then the WKB appoximation requires that $|\dot{\varepsilon}_k| \approx |\dot{F}_k|$ be small compared to $\varepsilon_k^2 \approx F_k^2$; this condition breaks down for small F_k, and thus for a small nonzero time, even if F_k is varying slowly.

For later times, as F_k increases, the condition $|\dot{F}_k| \ll F_k^2$ can be met. Therefore, for small $|M_k|$, the WKB approximation becomes valid for not too small times, when

$$F_k^2(t) \gg |\dot{F}_k(t)|. \tag{3.59}$$

The corresponding WKB solution cannot be extended to $t = 0$, and therefore the constants $C_{k1,2}$ in $A_{11}(k,t)$ are undetermined.

The analysis is simplified if one takes into account that, in the large-time limit, one can expand in Eq. (3.56) $S(t') \approx S(t) + (t'-t)\dot{S}$, which gives

$$A_2(k,t) \approx -iC_{k2}(\text{sgn } M_k)\frac{F_k(t)}{2\varepsilon_k(t)}\exp[-iS(t)], \tag{3.60}$$

and

$$\begin{aligned} A_{11}(k,t) \approx &-\frac{C_{k1}\exp[iS(t)]}{\varepsilon_k + |M_k|}\left[F_k(t)\ \text{sgn}\ M_k - i\frac{\dot{F}_k|M_k|}{2\varepsilon_k^2}\right] \\ &- i\frac{C_{k2}\exp[-iS(t)]}{2\varepsilon_k}\left[\varepsilon_k + |M_k| - \frac{F_k\dot{F}_k|M_k|}{\varepsilon_k^2(\varepsilon_k + |M_k|)}\right] \end{aligned} \tag{3.61}$$

In what follows we disregard the terms $\propto \dot{F}_k$ in $A_{11}(k,t)$. We remind that $A_{00}(k,t) = A_1(k,t) + A_2(k,t)$, with $A_{1,2}$ given by Eqs. (3.55) and (3.60).

The parameters $C_{k1,2}$ can be found by noticing that, quite generally, $F_k(t) \propto t$ for a time that is small, but on the other hand, is sufficiently long, so that $F_k(t)$ becomes large compared to M_k and the above asymptotic expressions for A_{11}, A_{22} apply. We will use this below to obtain the full WKB solution by matching these expressions to the explicit solution of the Schrödinger equation (2.37) for $F_k(t) \propto t$ in terms of the parabolic cylinder functions.

For $F_k(t) = \eta_k t$ and $|\eta_k|t \gg |M_k|$, the condition of the applicability of the WKB approximation $\dot{\varepsilon}_k \ll \varepsilon_k^2$ is reduced to the inequality $|\eta_k| \ll (\eta_k t)^2$. The asymptotic expressions for $A_{00}(k,t)$, $A_{11}(k,t)$ strongly simplify in this case. We have in these expressions

$$\begin{aligned} &S^{(0)}(t) \approx -\frac{1}{2}|\eta_k|(\text{sgn } M_k)\left\{t^2 + \frac{M_k^2}{2\eta_k^2}\left[\log\left(4\eta_k^2 t^2/M_k^2\right) + 1\right]\right\}, \\ &S^{(1)}(t) \approx i\frac{1}{2}\log 2 - i\frac{|M_k|}{2|\eta_k|t}, \quad \varepsilon_k(t) \approx |\eta_k|t\left(1 + \frac{M_k^2}{2\eta_k^2 t^2}\right). \end{aligned} \tag{3.62}$$

Respectively, the expressions for A_{00} and A_{11} take the form

$$\begin{aligned} A_{00}(k,t) &\approx \frac{C_{k1}}{\sqrt{2}}\left(1 + \frac{|M_k|}{2|\eta_k|t}\right)e^{iS^{(0)}(t)} - i\frac{C_{k2}}{\sqrt{2}}\left(\text{sgn}(M_k\eta_k) - \frac{M_k}{2\eta_k t}\right)e^{-iS^{(0)}(t)}, \\ A_{11}(k,t) &\approx -\frac{C_{k1}}{\sqrt{2}}\left(\text{sgn}(M_k\eta_k) - \frac{M_k}{2\eta_k t}\right)e^{iS^{(0)}(t)} - i\frac{C_{k2}}{\sqrt{2}}\left(1 + \frac{|M_k|}{2|\eta_k|t}\right)e^{-iS^{(0)}(t)}. \end{aligned} \tag{3.63}$$

To set up the expressions for the matching with the expansion of the parabolic cylinder functions for $|\eta_k t| \gg |M_k|$, it is convenient to introduce functions $A_\pm = (A_{00} \pm A_{11})/\sqrt{2}$. In particular,

$$A_-(k,t) = \begin{cases} C_{k1}\exp\left(iS^{(0)}\right) + iC_{k2}(M_k/2\eta_k t)\exp\left(-iS^{(0)}\right), & \mathrm{sgn}(M_k\eta_k) = +1 \\ -C_{k1}(M_k/2\eta_k t)\exp\left(iS^{(0)}\right) + iC_{k2}\exp\left(-iS^{(0)}\right), & \mathrm{sgn}(M_k\eta_k) = -1. \end{cases} \tag{3.64}$$

whereas

$$A_+(k,t) = \begin{cases} C_{k1}(M_k/2\eta_k t)\exp\left(iS^{(0)}\right) - iC_{k2}\exp\left(-iS^{(0)}\right), & \mathrm{sgn}(M_k\eta_k) = +1 \\ C_{k1}\exp\left(iS^{(0)}\right) + iC_{k2}(M_k/2\eta_k t)\exp\left(-iS^{(0)}\right), & \mathrm{sgn}(M_k\eta_k) = -1. \end{cases} \tag{3.65}$$

Here $S^{(0)} \equiv S^{(0)}(t)$ is given by Eq. (3.62).

The parameters $C_{k1,2}$ depend on the ratio M_k^2/η_k. They are found by matching to the parabolic cylinder functions. One can then find A_{00}, A_{11} in the stationary regime, i.e., where $F_k(t)$ has reached its stationary value and no longer varies in time, $\dot{F}_k = 0$. To the first order in M_k/F_k

$$\begin{aligned} A_{00}(k,t) &= \frac{C_{k1}}{\sqrt{2}}e^{iS^{(0)}(t)}\left(1 + \frac{|M_k|}{2|F_k|}\right) - i\frac{C_{k2}}{\sqrt{2}}\,\mathrm{sgn}(M_k\eta_k)e^{-iS^{(0)}(t)}\left(1 - \frac{|M_k|}{2|F_k|}\right), \\ A_{11}(k,t) &= -\frac{C_{k1}}{\sqrt{2}}\,\mathrm{sgn}(M_k\eta_k)e^{iS^{(0)}(t)}\left(1 - \frac{|M_k|}{2|F_k|}\right) - i\frac{C_{k2}}{\sqrt{2}}e^{-iS^{(0)}(t)}\left(1 + \frac{|M_k|}{2|F_k|}\right), \end{aligned} \tag{3.66}$$

The factors $\exp\left[\pm iS^{(0)}(t)\right]$ in these expressions are fast oscillating, and therefore they drop out from the time-averaged parameters

$$\begin{aligned} \langle|A_{11}(k,t)|^2\rangle &\approx \frac{1}{2}|C_{k1}|^2\left(1 - \frac{|M_k|}{|F_k|}\right) + \frac{1}{2}|C_{k2}|^2\left(1 + \frac{|M_k|}{|F_k|}\right), \\ \langle A_{11}^*(k,t)A_{00}(k,t)\rangle &\approx \frac{1}{2}\left(|C_{k2}|^2 - |C_{k1}|^2\right) \end{aligned} \tag{3.67}$$

These parameters give the correlators we are interested in, cf. Eq. (3.58).

3.5.4 Solution in terms of the parabolic cylinder functions

For a linear turn-on of the drive, $F_k(t) = \eta_k t$, Eq. (2.37) can be solved using the parabolic cylinder functions. Indeed, from Eq. (2.37), we obtain the equation for $A_\pm(t)$, which has the form

$$\frac{d^2A_\pm}{dz_k^2} + \left(s_k \mp \frac{1}{2} - \frac{z_k^2}{4}\right)A_\pm = 0, \quad z_k = e^{i(\pi/4)\,\mathrm{sgn}\,\eta_k}(2|\eta_k|)^{1/2}t, \quad s_k = -i\frac{M_k^2}{2\eta_k}, \tag{3.68}$$

with

$$A_+ = ie^{i(\pi/4)\,\mathrm{sgn}\,\eta_k}\,\mathrm{sgn}\,M_k\left(\frac{dA_-}{dz_k}+\frac{1}{2}z_kA_-\right)/|s_k|^{1/2}.$$

Equation (3.68) is the Weber equation. Its general solution can be expressed in terms of the parabolic cylinder functions $D_\nu(z)$ [68, 69],

$$\begin{aligned}A_- &= \alpha_k D_{-s_k-1}(-iz_k)+\beta_k D_{-s_k-1}(iz_k),\\ A_+ &= \frac{e^{i(\pi/4)\,\mathrm{sgn}\,\eta_k}\,\mathrm{sgn}\,M_k}{\sqrt{|s_k|}}\left(-\alpha_k D_{-s_k}(-iz_k)+\beta_k D_{-s_k}(iz_k)\right),\end{aligned} \tag{3.69}$$

we consider $\pm iz_k \equiv \exp(\pm i\pi/2)z_k$. The factors α_k and β_k are determined by the initial conditions, which give

$$\begin{aligned}\alpha_k &= \frac{2^{s_k/2}}{\sqrt{4\pi}}\left[\Gamma\left(1+\frac{s_k}{2}\right)-e^{-i(\pi/4)\,\mathrm{sgn}\,\eta_k}\,\mathrm{sgn}\,M_k\sqrt{\frac{|s_k|}{2}}\Gamma\left(\frac{1}{2}+\frac{s_k}{2}\right)\right],\\ \beta_k &= \frac{2^{s_k/2}}{\sqrt{4\pi}}\left[\Gamma\left(1+\frac{s_k}{2}\right)+e^{-i(\pi/4)\,\mathrm{sgn}\,\eta_k}\,\mathrm{sgn}\,M_k\sqrt{\frac{|s_k|}{2}}\Gamma\left(\frac{1}{2}+\frac{s_k}{2}\right)\right],\end{aligned} \tag{3.70}$$

where $\Gamma(z)$ is the Gamma function.

Equations (3.69) and (3.70) provide a general solution of the problem of turning on the drive linearly in time at an arbitrary rate η_k for an arbitrary M_k. The solution depends on $z \propto \eta_k t$ and the dimensionless parameter $s_k \propto M_k^2/\eta_k$. It allows us to find the coefficients C_{k1} and C_{k2}, and thus to obtain the full WKB solution of the problem of the two-spin dynamics in the case where the drive is initially turned on linearly in time. This can be done by matching the asymptotic expansion of the solution (3.69) in the range $|\eta_k|^{1/2}t \gg 1$ with Eqs. (3.64) and (3.65) in the same time range. For completeness, we provide the leading-order terms of the expansion of the parabolic cylinder function $D_\nu(z)$ for $|z| \gg 1, |\nu|$ [68]:

$$D_\nu(z) \approx \begin{cases} e^{-z^2/4}z^\nu, & |\arg(z)| < 3\pi/4 \\ e^{-z^2/4}z^\nu - \frac{\sqrt{2\pi}}{\Gamma(-\nu)}e^{i\nu\pi}e^{z^2/4}z^{-\nu-1}, & \pi/4 < \arg(z) < 5\pi/4 \\ e^{-z^2/4}z^\nu - \frac{\sqrt{2\pi}}{\Gamma(-\nu)}e^{-i\nu\pi}e^{z^2/4}z^{-\nu-1}, & -5\pi/4 < \arg(z) < -\pi/4. \end{cases} \tag{3.71}$$

We will use that, from Eqs. (3.62) and (3.68), in the large-t limit

$$e^{iS_0(t)} \approx e^{-(z_k^2/4)\,\mathrm{sgn}(M_k\eta_k)} z^{s_k\ \mathrm{sgn}(M_k\eta_k)} \exp\left[\frac{1}{2}s_k\ \mathrm{sgn}(M_k\eta_k)\left(-i\frac{\pi}{2}\,\mathrm{sgn}\ \eta_k - \log|s_k| + 1\right)\right]$$

whereas

$$\frac{M_k}{2\eta_k t} = \mathrm{sgn}(M_k\eta_k)\frac{\sqrt{|s_k|}}{z_k} e^{i(\pi/4)\,\mathrm{sgn}\ \eta_k}$$

To express the parameters of the WKB solution C_{k1}, C_{k2} in terms of the coefficients α_k, β_k of the solution of the equations of motion in terms of the parabolic cylinder functions, it is convenient to introduce auxiliary parameters

$$\begin{aligned} J_k &= \frac{\sqrt{2\pi}}{\Gamma(s_k+1)}|s_k|^{s_k/2}\exp\left(-\frac{s_k}{2} - \frac{\pi|s_k|}{4}\right), \\ L_k &= |s_k|^{-(s_k+1)/2}\exp\left(\frac{i\pi}{4}\,\mathrm{sgn}\ \eta_k + \frac{s_k}{2} + \frac{\pi|s_k|}{4}\right). \end{aligned} \tag{3.72}$$

In terms of these parameters, from Eqs. (3.64), (3.65), and (3.69) we find that, for $M_k > 0$ and $\eta_k > 0$

$$C_{k1} = \beta_k J_k, \quad C_{k2} = -i\left(\alpha_k - \beta_k e^{-\pi|s_k|}\right) L_k. \tag{3.73}$$

For $M_k < 0$ and $\eta_k < 0$, on the other hand,

$$C_{k1} = \alpha_k J_k, \quad C_{k2} = -i\left(\beta_k - \alpha_k e^{-\pi|s_k|}\right) L_k. \tag{3.74}$$

For $M_k < 0, \eta_k > 0$ we find

$$C_{k1} = \left(\alpha_k - \beta_k e^{-\pi|s_k|}\right) L_k, \quad C_{k2} = -i\beta_k J_k. \tag{3.75}$$

For $M_k > 0, \eta_k < 0$ we find

$$C_{k1} = \left(\beta_k - \alpha_k e^{-\pi|s_k|}\right) L_k, \quad C_{k2} = -i\alpha_k J_k. \tag{3.76}$$

Equations (3.72) - (3.76), together with the expressions (3.70) for the parameters α_k, β_k provide a complete solution of the problem of the slow turn-on of the drive in the range of zero energy gap in the absence of the drive. For each k, the solution depends on a single parameter, the ratio of the squared gap M_k^2 to the rate of the increment of the drive η_k. We note that it is advantageous to express the coefficients C_{k1}, C_{k2} in terms of α_k, β_k, as this allows one to extend the WKB results to different initial conditions.

3.6 Summary and transition to open boundaries

The periodic chain provides an exactly solvable setting in which the bulk dynamical consequences of the effective Kitaev topology can be isolated from boundary and interaction effects. The full laboratory-frame calculation confirms that the anomalous response is present before making the RWA. The rotating-frame description then reveals its origin.

For a sudden turn-on, the exact finite-drive solution gives a frequency-independent magnetization plateau throughout the topological interval and vanishing connected longitudinal correlations at every nonzero separation. In the weak-drive limit, the excitation density becomes locally proportional to the winding-number density. The modulation frequency moves the relevant peaks through momentum space without changing their integrated weight.

For a slow turn-on, the magnetization remains independent of detuning inside the topological interval, but the longitudinal correlations no longer vanish. Perfect adiabaticity is impossible because the initial pairing gap closes at $\pm k_\mu$. Nevertheless, the nonadiabatic momentum window shrinks with decreasing ramp rate, and the adiabatic approximation accurately describes integrated observables over a broad parameter range. Matching the asymptotic limit of the WKB solution with the exact parabolic-cylinder solution due to a linear ramp provides the interpolation through the remaining nonadiabatic region.

Finally, the hysteresis protocol demonstrates that the final Hamiltonian does not uniquely determine the long-time state. Different paths to the same topological Hamiltonian retain different mode occupations and therefore different bulk correlations. The periodic chain thus converts the topology of the effective Hamiltonian into a protocol-dependent bulk response.

The central observables require no reconstruction of a fermionic wave function. Site-resolved z readout gives the excitation density, repeated measurements give $Q^z(m)$, and basis rotations before readout give transverse correlations. Qubit chains provide direct control of the required pair-flip Hamiltonian and readout [62, 72]; magnetic-resonance platforms provide ensemble access to the polarization [73]. To further connect these results to experimental setups, To further connect these results to experimental setups, the following chapter examines how opening the chain

modifies the response. In Chapter 4, we open the chain and determine how boundary scattering, propagating-channel mixing, and localized Majorana modes modify the nominally bulk response.

CHAPTER 4

DYNAMICS OF A FINITE OPEN CHAINS

In this chapter, we will consider the dynamics of a chain with free ends. The periodic chain assumption was essential to decouple the spin chain dynamics into the dynamics of $N/2$ independent 2×2 Schrödinger equations. For ab open chain, translational symmetry is broken. This introduces a new spectral problem even though the Hamiltonian remains quadratic. One might initially expect that the traveling waves of the periodic chain are simply replaced by standing waves. However, as we showed in Sec. 2.4.2, the real-space BdG equations impose two boundary conditions at each end. A single sine wave generally cannot satisfy all four conditions. The boundaries therefore change both the quantization of the bulk modes and their composition.

In this chapter, we will focus on the sudden turn-on of the modulation from the fully polarized initial state and assume $J > F > 0$ for simplicity. The dependence on $\mathrm{sgn}(JF)$ is the same as the periodic chain. We also assume $J^2 \neq F^2$, which would correspond to the Ising limit. The effect of open boundaries discussed below depends on the existence of the two-channel regions, which is absent for $J^2 = F^2$. The analysis of this limit is also simpler and was discussed in the literature [36].

In this chapter, we will first revisit the finite chain formulation discussed in Section. 2.4.2 to highlight the difference between the solution in the single- and two-channel regions. We will derive the analytical expressions for the Majorana amplitudes $\phi_s(n)$ for a long chain. We will show that the structure of the solution in the single channel region is a phase shifted standing-wave with size independent evanescent components that are essential to satisfy the boundary conditions. For two-channel region, boundaries admix two phase shifted standing waves to produce the finite chain eigenstates. From scattering matrix perspective, this boundary mixing propagates through the chain at some group velocity, which may affect time-averaged bulk observables after some propagation time. To explain this effect, we intoruces the Majorana covariance matrix, which we later use to obtain the numerical results that demonstrate how two-channel boundary mixing change time-averaged bulk observables.

4.1 Why the open-chain modes are not simple standing waves

We showed in Section. 2.4.2 that the finite chain Hamiltonian can be solved by solving the coupled real-space BdG equations,

$$D\boldsymbol{\phi}_s = \Lambda_s \boldsymbol{\psi}_s, \qquad D^{\mathsf{T}}\boldsymbol{\psi}_s = \Lambda_s \boldsymbol{\phi}_s, \qquad D = A + B, \tag{4.1}$$

where A and B are defined in Eq. (2.13). Eliminating $\boldsymbol{\psi}_s$ gives the fourth-order bulk recurrence in Eq. (2.21). With $L = N + 1$, the four boundary conditions are

$$\begin{gathered}\phi(0) = \phi(L) = 0, \\ (J - F)\phi(-1) + (J + F)\phi(1) = (J + F)\phi(L + 1) + (J - F)\phi(L - 1) = 0.\end{gathered} \tag{4.2}$$

Now, if we consider the usual standing wave $\phi(n) = \mathbb{C}\sin(kn)$ with $k = \pi\ell/L$ and $\mathbb{C} = (2/L)^{1/2}$, we see that it only satisfies the first line of Eq. (4.2). At the left boundary, however, we get

$$(J - F)\sin(-k) + (J + F)\sin k = 2F \sin k. \tag{4.3}$$

For $F \neq 0$ and $0 < k < \pi$, this expression is nonzero. Thus, the pairing term changes the boundary condition in a way that cannot be accommodated by unshifted sine waves.

The distinction is visible directly by expanding the exact modes in the orthonormal sine basis,

$$u_\ell(n) = \mathbb{C}\sin\left(\frac{\pi\ell n}{L}\right), \qquad \phi_s(n) = \sum_{\ell=1}^{N} C_{s\ell} u_\ell(n). \tag{4.4}$$

Here s labels the exact open-chain mode, whereas ℓ labels a basis function. In the single-channel part of the spectrum, the weight is concentrated around one momentum. Several neighboring sine functions can still be needed because, as we show below, reflection also produces a phase shift. In the two-channel part, an exact mode has appreciable weight around two different standing-wave momenta. The difference between the single- and two-channel regions is illustrated in Fig. 4.1.

The broad standing-wave content of the lowest mode has a different origin. In the topological regime, a topologically-protected edge mode localized near the boundary of the chain split from the bulk with zero energy in the long chain limit. This localization in real space requires a broad momentum distribution, which is shown in Fig. 4.1 near $s/N \approx 0$, particularly at $s = 1$ as the lowest energy mode.

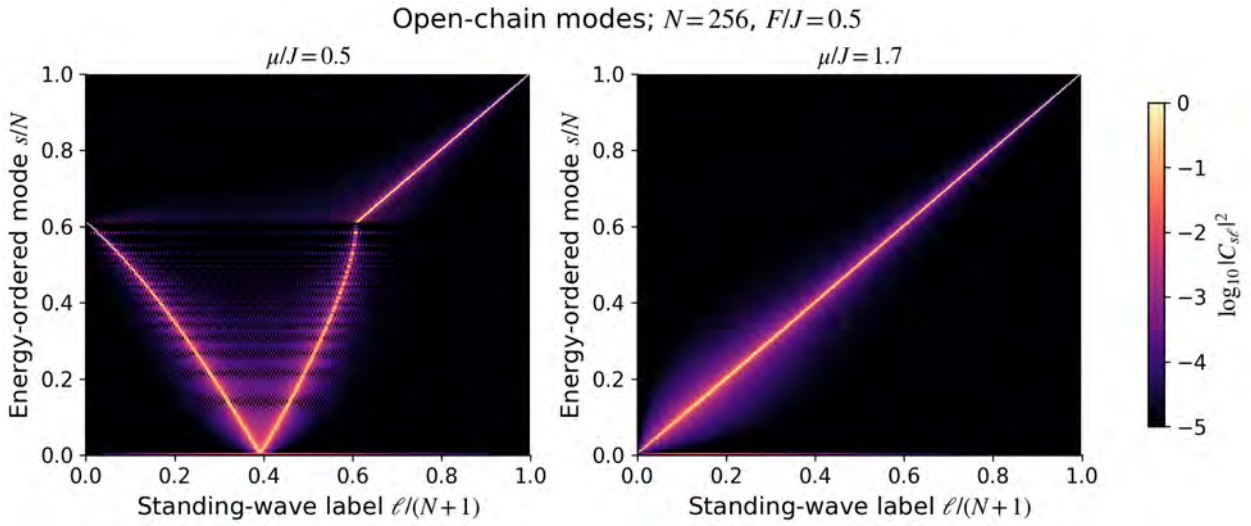


Figure 4.1 Standing-wave content of the exact open-chain modes for $N = 256$ and $F/J = 0.5$. The color represents $\log_{10}|C_{s\ell}|^2$, with the displayed scale restricted to $[-5, 0]$. Modes are ordered by increasing energy along the vertical axis. Left: $\mu/J = 0.5$, where part of the bulk spectrum has two propagating channels. Many modes have two separated packets of standing-wave weight. Right: $\mu/J = 1.7$, where the bulk spectrum has one propagating channel at each energy. The extended modes have one principal packet. The lowest, edge-localized mode has a broad standing-wave expansion.

4.2 Solution of the boundary problem

4.2.1 Bulk roots and the number of propagating channels

We saw in Subsection 2.4.2 that substituting $\phi_k(m) \propto e^{ikm}$ into the bulk recurrence gives

$$\Lambda^2(k) = (\mu - 2J\cos k)^2 + 4F^2\sin^2 k. \tag{4.5}$$

Writing $x = \cos k$ and $a_0 = J^2 - F^2 > 0$, we obtain

$$\Lambda^2 = 4a_0x^2 - 4\mu Jx + \mu^2 + 4F^2. \tag{4.6}$$

If one root is $x = \cos k$, the other is

$$X_k = \frac{\mu J}{a_0} - \cos k. \tag{4.7}$$

For $|X_k| > 1$, the second root does not correspond to a real momentum. The characteristic equation then has one propagating pair and one evanescent pair. This is the single-channel sector.

For $|X_k| < 1$, we can define a second real momentum $q \in (0, \pi)$ through

$$\cos q = X_k, \qquad \cos k + \cos q = \frac{\mu J}{a_0}. \tag{4.8}$$

The four roots are then $e^{\pm ik}$ and $e^{\pm iq}$. This is the two-channel sector. We note that $|X_k|$ can be smaller than one if and only if $|\mu J| < 2a_0$ which is the same condition obtained in Eq. (2.20) by requiring dispersion relation to have a minimum that lies inside $0 < k < \pi$. This minima corresponds to the energy $\Lambda_{\min} = 2F\sqrt{1 - \frac{\mu^2}{4a_0}}$, and the two-channel interval is $\Lambda_{\min} < \Lambda < 2J - |\mu|$. At higher energies there is only one propagating channel.

This energy-dependent classification is different from the topological classification. In the present parameter range, the topological interval is $|\mu| < 2J$, whereas a two-channel interval requires the stronger condition in Eq. (2.20). For example, at $F/J = 0.5$, two-channel energies exist for $|\mu|/J < 1.5$. The point $\mu/J = 1.7$ is therefore topological but has a single-channel bulk spectrum.

4.2.2 Single-channel modes: reflection phases and evanescent components

The single-channel part corresponds to $|X_k| > 1$. We therefore define

$$w_k = X_k - \mathrm{sgn}(X_k)\sqrt{X_k^2 - 1}, \qquad |w_k| < 1. \tag{4.9}$$

The second evanescent root is w_k^{-1}. A negative w_k describes a decaying component whose sign alternates between neighboring sites.

Near the left edge, by taking account of $\phi_k(0) = 0$, we can write the solution as

$$\phi_L(n) = \sin(kn - \eta_L) + \sin\eta_L\, w_k^n, \tag{4.10}$$

where the phase shift η_L is obtained from second boundary condition near the left edge as

$$\tan\eta_L = \frac{2F\sin k}{2J\cos k - (J-F)w_k^{-1} - (J+F)w_k}. \tag{4.11}$$

The evanescent term is necessary to satisfy the boundary conditions. It makes $\phi_L(0) = 0$ without forcing the propagating component to have zero phase.

Similarly, a solution near the right boundary satisfying the condition $\phi_k(L) = 0$ takes the form

$$\phi_R(n) = \sin[k(L-n) - \eta_R] + \sin\eta_R\, w_k^{L-n}, \tag{4.12}$$

where the phase shift near the right boundary is also obtained from the second boundary condition near this boundary as

$$\tan\eta_R = \frac{-2F\sin k}{2J\cos k - (J+F)w_k^{-1} - (J-F)w_k}. \tag{4.13}$$

Let $\kappa_k = -\ln|w_k|$. When $\kappa_k L \gg 1$, the evanescent components from the two ends have exponentially small overlap. Matching the propagating parts then gives

$$kL = \pi p + \eta_L(k) + \eta_R(k) + O(e^{-\kappa_k L}), \tag{4.14}$$

where p is an integer that follows the chosen continuous phase branch. The corresponding mode is

$$\phi_p(n) \simeq \mathcal{N}_p\big[\sin(kn - \eta_L) + \sin\eta_L\, w_k^n + (-1)^{p+1}\sin\eta_R\, w_k^{L-n}\big]. \tag{4.15}$$

This expression has exponentially small boundary errors. It is an asymptotic finite-chain formula; the exact finite-chain solution retains the overlap of the two evanescent components. Considering this overlap is mathematically involved [74]. It hides the physical structure illustrated by Equation. (4.15).

Although the momentum shift from the standing wave momenta is small,

$$k \approx \frac{\pi p}{L} + \frac{\eta_L(\pi p/L) + \eta_R(\pi p/L)}{L}, \tag{4.16}$$

its effect on the spatial phase need not be small. At a site with n/L finite, multiplying the $O(L^{-1})$ momentum correction by n gives an $O(1)$ phase correction. Dropping this correction can therefore give a poor wavefunction throughout a substantial fraction of the chain.

This also explains why a single-channel mode need not approach one particular standing wave vector. For a bulk mode p, the leading standing-wave coefficient in Eq. (4.4) of the solution in Eq. (4.15) is

$$C_{p,p+r} = \frac{\sin\eta_L + (-1)^r \sin\eta_R}{\eta_L + \eta_R - \pi r} + O(L^{-1}), \tag{4.17}$$

where r is an integer. Several neighboring labels can retain finite coefficients even though their momentum separation vanishes as L^{-1}. This is consistent with the single narrow momentum packet in Fig. 4.1.

The phases in Eqs. (4.11) and (4.13) must be followed continuously. Using the principal value of an ordinary arctangent independently at each parameter value can introduce artificial jumps by π. These jumps change the integer used to label a mode. They do not change the physical eigenstate. The exact spectral problem fixes the state counting, including the mode that becomes localized at the boundary.

Finally, the approximation $\kappa_k L \gg 1$ is not uniform near $|X_k| = 1$. There the evanescent length grows, and the full boundary determinant should be used.

4.2.3 Two-channel modes and exact quantization

When both k and q are real, the bulk solution takes the form

$$\phi(n) = a_k e^{ikn} + b_k e^{-ikn} + a_q e^{iqn} + b_q e^{-iqn}. \tag{4.18}$$

All four terms are propagating. The extra boundary conditions are now satisfied by mixing two bulk channels. For a compact notation, we define

$$\begin{aligned} &z_1 = e^{ik}, \quad z_2 = e^{-ik}, \quad z_3 = e^{iq}, \quad z_4 = e^{-iq}, \\ &\ell(z) = (J - F)z^{-1} + (J + F)z, \quad r(z) = (J + F)z + (J - F)z^{-1}. \end{aligned} \tag{4.19}$$

The four boundary conditions in Eq. (4.2) give $\mathcal{B}\boldsymbol{a} = 0$ where $\boldsymbol{a} = (a_k, b_k, a_q, b_q)^T$ and

$$\mathcal{B} = \begin{pmatrix} 1 & 1 & 1 & 1 \\ z_1^L & z_2^L & z_3^L & z_4^L \\ \ell(z_1) & \ell(z_2) & \ell(z_3) & \ell(z_4) \\ z_1^L r(z_1) & z_2^L r(z_2) & z_3^L r(z_3) & z_4^L r(z_4) \end{pmatrix}. \tag{4.20}$$

Thus the allowed energies satisfy

$$\det \mathcal{B} = 0. \tag{4.21}$$

This construction is consistent with the exact finite-chain solutions discussed in Ref. [74]. Using Eq. (4.8) and $J^2 \neq F^2$, the determinant condition can be reduced to

$$\begin{aligned} &f(k + q) = f(k - q), \\ &f(\chi) = \sin^2\!\left(\frac{L\chi}{2}\right)\left[1 + \frac{F^2}{J^2}\cot^2\!\left(\frac{\chi}{2}\right)\right]. \end{aligned} \tag{4.22}$$

As a consistency check, setting $F = 0$ in Eq. (4.22) gives $\sin(kL)\sin(qL) = 0$. The two channels then reduce to independent standing-wave solutions.

For each allowed pair (k, q), the real eigenstate can be expressed as a superposition of two phase-shifted standing waves,

$$\phi(n) = \mathcal{N}\left[A_k \sin(kn - \eta_k) + A_q \sin\!\big(qn - \eta_q\big)\right]. \tag{4.23}$$

The phases and relative amplitudes are fixed by the boundary conditions. In particular, $\phi(0) = 0$ requires

$$A_k \sin \eta_k = -A_q \sin \eta_q \equiv \beta. \tag{4.24}$$

Introducing $\alpha_k = A_k \cos \eta_k$ and $\alpha_q = A_q \cos \eta_q$, the remaining left boundary condition and $\phi(L) = 0$ become

$$\begin{aligned} F \sin k\, \alpha_k + F \sin q\, \alpha_q - J(\cos k - \cos q)\beta = 0, \\ \sin(kL)\alpha_k + \sin(qL)\alpha_q - [\cos(kL) - \cos(qL)]\beta = 0. \end{aligned} \tag{4.25}$$

These two homogeneous equations determine $(\alpha_k, \alpha_q, \beta)$ up to an overall factor, which is absorbed into the normalization factor $\mathcal{N}$. Defining $\Delta_c = \cos k - \cos q$, and $\Delta_C = \cos(kL) - \cos(qL)$, one convenient choice is

$$\begin{aligned} \alpha_k &= J\Delta_c \sin(qL) - F \sin q\, \Delta_C, \\ \alpha_q &= F \sin k\, \Delta_C - J\Delta_c \sin(kL), \\ \beta &= F\big[\sin k \sin(qL) - \sin q \sin(kL)\big]. \end{aligned} \tag{4.26}$$

The amplitudes and phases in Eq. (4.23) are therefore

$$\begin{aligned} A_k &= \sqrt{\alpha_k^2 + \beta^2}, & \eta_k &= \mathrm{atan2}(\beta, \alpha_k), \\ A_q &= \sqrt{\alpha_q^2 + \beta^2}, & \eta_q &= \mathrm{atan2}(-\beta, \alpha_q). \end{aligned} \tag{4.27}$$

The final right boundary condition is satisfied when (k, q) obeys Eq. (4.22). Thus, the bulk dispersion determines which two momenta can coexist at the same energy, while the boundaries select their relative amplitude and spatial phases. For momenta separated by a finite amount, their leading bulk weights are proportional to A_k^2 and A_q^2. Both weights can remain appreciable as the chain becomes long, producing the two separated momentum packets in Fig. 4.1. At a same-parity crossing, $\sin(kL) = \sin(qL) = \Delta_C = 0$, therefore, this construction does not apply at these points. These points will provide energy crossings that are discussed next.

4.2.4 Exact crossings and avoided crossings

An equal-energy pair of bulk momenta should be distinguished from a degeneracy between two exact finite-chain eigenstates. The former is present throughout the two-channel energy interval. The latter occurs only at particular parameter values when the dimension of the null space of the boundary matrix in Eq. (4.20) is bigger than one. This is only possible when both k and q take a standing wave value with the same parity.

In general, the set of pairs (k, q) are determined by the degeneracy condition in Eq. (4.8) and the quantization condition in Eq. (4.22). To identify points with exact crossings, we take two standing-wave momenta

$$k = k_p = \frac{\pi p}{L}, \qquad q = k_l = \frac{\pi l}{L}, \tag{4.28}$$

with $p \neq l$ and assume that $\Lambda(k_p) = \Lambda(k_l)$. For these standing wave momenta, the parameters z_j^L for $j \in \{1, 2, 3, 4\}$ in equation (4.20) are either $+1$ for even integers or -1 for odd integers. If $p + l$ is odd, the four rows of (4.20) are distinct and its null space dimension is zero. Thus, the crossing of these two unperturbed standing-wave energies is generally replaced by an avoided crossing in the open-chain spectrum. On the other hand, if $p + l$ is even, the second and fourth rows of (4.20) will be proportional to the first and third rows, respectively. This implies that the null space is two-dimensional and the finite chain will have a crossing. It is also easy to see that the boundary condition in Eq. (4.22) is satisfied for even $p + l$. This spectral behavior of corrssings and avoided crossings is illustrated in Fig. 4.2.

The eigenstates in this degenerate space can be constructed directly. For example, defining $s_p = \sin k_p$, $s_l = \sin k_l$, $S = s_p^2 + s_l^2$, and $\Delta = \cos k_p - \cos k_l$. An orthonormal basis is

$$\begin{aligned}
\phi^{(1)}(n) &= \mathcal{N}_1 \left[s_l \sin\big(k_p n\big) - s_p \sin(k_l n) \right], \\
\phi^{(2)}(n) &= \mathcal{N}_2 \Big[J\Delta\big(s_p \sin\big(k_p n\big) + s_l \sin(k_l n)\big) - FS\big(\cos\big(k_p n\big) - \cos(k_l n)\big) \Big],
\end{aligned} \tag{4.29}$$

where

$$\mathcal{N}_1 = \sqrt{\frac{2}{LS}}, \qquad \mathcal{N}_2 = \sqrt{\frac{2}{LS(J^2\Delta^2 + 2F^2S)}}. \tag{4.30}$$

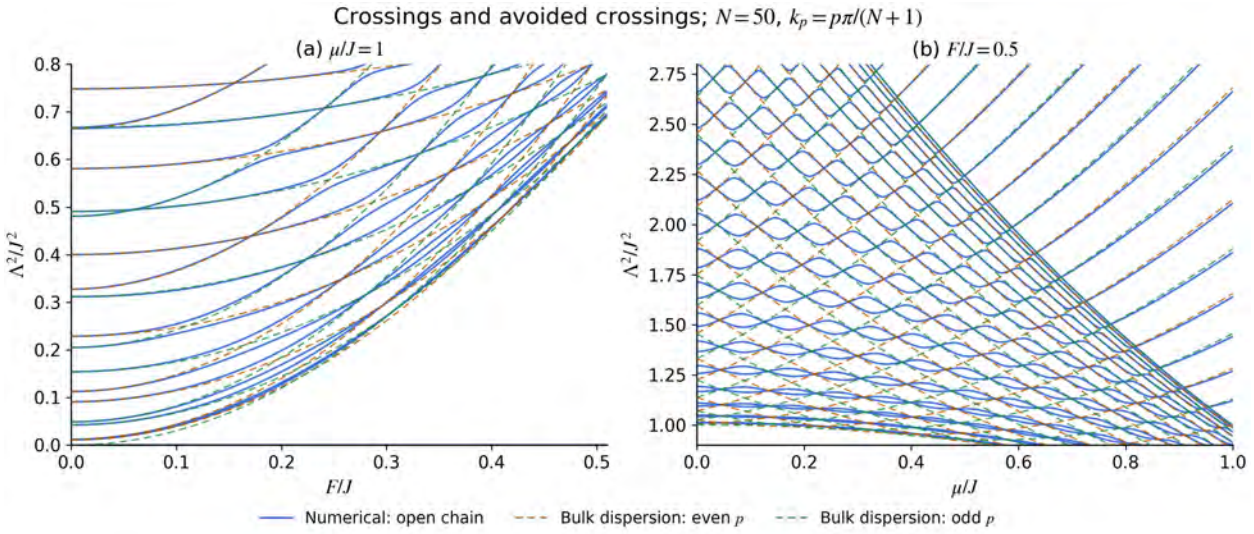


Figure 4.2 Crossings and avoided crossings in the static spectrum of an open chain with $N = 50$. (a) Pairing sweep over $0 \le F/J \le 0.5$ at fixed $\mu/J = 1$. (b) Detuning sweep over $0 \le \mu/J \le 1$ at fixed $F/J = 0.5$. Solid blue curves show the numerical squared excitation energies Λ_s^2/J^2, obtained from the eigenvalues of $(A - B)(A + B)$. Dashed curves show the squared bulk dispersion $\Lambda^2(k_p)/J^2$ evaluated at all standing-wave momenta $k_p = p\pi/(N + 1)$, with dark orange for even p and green for odd p. The displayed vertical windows are $0 \le \Lambda^2/J^2 \le 0.8$ in (a) and $0.9 \le \Lambda^2/J^2 \le 2.8$ in (b). For nonzero pairing, intersections of reference branches with the same index parity correspond to exact crossings, whereas intersections between opposite-parity branches are replaced by avoided crossings in the open-chain spectrum.

At an exact crossing, the individual eigenvectors are not unique. Any simultaneous orthogonal rotation of the two ϕ modes and their ψ partners describes the same physical eigenspace. Observable averages must therefore depend on the full degenerate subspace.

4.2.5 The edge mode and spectral ordering

The localized mode is obtained from the same boundary problem. On a semi-infinite chain, a zero-energy solution of $D\boldsymbol{\phi} = 0$ has characteristic roots

$$z_\pm = \frac{\mu \pm \sqrt{\mu^2 - 4(J^2 - F^2)}}{2(J + F)}. \tag{4.31}$$

A combination proportional to $z_+^n - z_-^n$ satisfies the left termination condition. In the topological interval, the roots support a normalizable boundary solution. The finite chain combines the two boundary Majoranas into a fermionic mode whose energy is generically exponentially small in N, with possible oscillatory zeros at special parameter values.

This mode contributes only one state to the spectrum. Its direct contribution to an observable

deep inside a long chain is suppressed by localization. It cannot by itself explain a change that involves an extensive set of extended modes.

4.2.6 Boundary scattering and propagation times

The same boundary problem can also be viewed as reflection and conversion of propagating bulk waves. This interpretation gives the same eigenstates and quantization condition, while making the time required for a boundary-dependent signal to reach the interior explicit.

The propagation direction is determined by the group velocity,

$$v(p) = \frac{d\Lambda(p)}{dp} = \frac{2\sin p\left[\mu J - 2(J^2 - F^2)\cos p\right]}{\Lambda(p)}, \qquad v_{\max} = \max_p |v(p)|. \tag{4.32}$$

In the two-channel interval, the positive roots lie on opposite sides of the dispersion minimum:

$$k < k_0 < q, \qquad k_0 = \arccos\left(\frac{\mu J}{2(J^2 - F^2)}\right). \tag{4.33}$$

Consequently, $v(k) < 0$ and $v(q) > 0$. At the left boundary, Eq. (4.18) can be understood as incoming waves with momenta $(k, -q)$ and amplitudes (a_k, b_q), and outgoing waves with momenta $(-k, q)$ and amplitudes (b_k, a_q). Writing $h_p = J\cos p + iF\sin p$, the two left boundary conditions give

$$\begin{pmatrix} b_k \\ a_q \end{pmatrix} = S_L^{(\phi)} \begin{pmatrix} a_k \\ b_q \end{pmatrix}, \qquad S_L^{(\phi)} = -\frac{1}{h_q - h_k^*} \begin{pmatrix} h_q - h_k & h_q - h_q^* \\ h_k - h_k^* & h_q^* - h_k^* \end{pmatrix}. \tag{4.34}$$

For the finite chain, an outgoing wave propagates to the opposite boundary, is reflected there, and returns. Requiring its amplitudes to reproduce themselves after this round trip gives the same four boundary equations as $\mathcal{B}\boldsymbol{a} = 0$, and hence the quantization condition in Eq. (4.22). The scattering description therefore gives the solution already obtained as expected.

The dynamical significance of boundary scattering follows by superposing the scattering states into a wave packet. Suppose an incoming narrow-band packet reaches the left boundary at time t_b. Its outgoing component in channel b at distance d is

$$\mathcal{A}_b(d,t) = \sum_a \int dE\, f_a(E)\big(S_L^{(\phi)}\big)_{ba}(E) e^{ip_b(E)d - iE(t-t_b)}, \qquad p_1 = -k(E), \quad p_2 = q(E). \tag{4.35}$$

Here $f_a(E)$ specifies the ordinary incoming wave amplitude per unit energy. The reflection coefficients determine the outgoing channel weights and phases, while the factors $e^{ip_b(E)d}$ describe

propagation from the boundary to the observation point. Thus, the energy derivative of the propagation phase is $d/|v_b|$ gives the travel time from the boundary to the observation point at distance d where $v_b = \left(\frac{dp_b}{dE}\right)^{-1}$.

For a packet centered at E_0, stationary phase gives its propagation delay:

$$t_{\text{arrival}} - t_b = \frac{d}{|v_b(E_0)|} + \frac{\partial}{\partial E} \arg\left(S_L^{(\phi)}\right)_{ba}(E)\Big|_{E_0}. \tag{4.36}$$

The second term is the reflection phase delay. At fixed energy away from thresholds and zeros of the relevant amplitude, it does not grow with chain length. The propagation term does: reaching a central site requires $d = N/2 + O(1)$.

Equation (4.36) describes the center of a wave packet, rather than an exactly sharp onset. The appearance and magnitude of a boundary correction in a spin observable additionally depend on which scattering contributions are populated and how they interfere. We establish that connection below.

4.3 How boundary mixing changes time-averaged observables

Boundary scattering fixes the channel composition of the finite-chain eigenstates. To determine its effect on the spin dynamics, it is useful to collect the normalized BdG amplitudes into the matrices

$$\Phi_{ns} = \phi_s(n), \qquad \Psi_{ns} = \psi_s(n), \qquad \mathsf{O} = \Phi^{\mathsf{T}}\Psi. \tag{4.37}$$

These are the same matricies that were introduced in the SVD of the matrix $D = A + B$ in Eq. (2.24). The matrix O describes the overlap between the two BdG partners. It generally has nonzero off-diagonal elements which may contribute to the time-dependence of different observables. For example, for the initially polarized state, the exact longitudinal magnetization change after a sudden modulation switching is

$$\Delta m_n^z(t) = 1 - \frac{1}{2}\sum_{s,r} \phi_s(n)\psi_r(n)\Big[(\mathsf{O}_{sr} + \mathsf{O}_{rs})\cos\big((\Lambda_s - \Lambda_r)t\big) + (\mathsf{O}_{sr} - \mathsf{O}_{rs})\cos\big((\Lambda_s + \Lambda_r)t\big)\Big], \tag{4.38}$$

where $\Delta m_n^z(t) = 1 - \langle\sigma_n^z(t)\rangle$. The mode profiles and the overlap matrix O are fixed by the post-quench Hamiltonian and do not evolve with time. Their contributions to Eq. (4.38), however, interfere

through the time-dependent cosine factors. At $t = 0$, completeness ensures that their sum reproduces the initially polarized state, giving $\Delta m_n^z(0) = 0$ for any boundary condition.

The wave-packet calculation in Sec. 4.2.6 identifies the time needed for a propagating amplitude to travel from a boundary to the observation site. To connect this result to Eq. (4.38), we must identify how these amplitudes enter the magnetization. As we show below, the magnetization is bilinear in the real-space propagation amplitudes. Their products are evaluated at the same time, so forming the observable does not require an additional propagation interval. The relative weights and interference of these products determine whether the earliest boundary contribution is visible.

This connection is more transparent in real space than in the double sum over energies. The real space amplitudes $\phi_s(n)$ and $\psi_s(n)$ were originally constructed as the Majorana amplitudes of the quasiparticles (See Eq. (2.14)). We therefore introduce the Majorana propagator of the same quadratic Hamiltonian, and then collect its two-point expectation values into the covariance matrix used later for the numerical calculations.

4.4 Real-space propagation and the spin observables

4.4.1 Majorana operators and their propagator

The Majorana operators were introduced in Chapter 2 as $\gamma_n^A = c_n^\dagger + c_n$ and $\gamma_n^B = i(c_n^\dagger - c_n)$. Writing $\boldsymbol{\gamma}^A = (\gamma_1^A, \ldots, \gamma_N^A)^\mathsf{T}$ and similarly for $\boldsymbol{\gamma}^B$, the quadratic Hamiltonian in Eq. (2.12) takes the form

$$\hat{H} = \frac{i}{2}(\boldsymbol{\gamma}^A)^\mathsf{T} D^\mathsf{T} \boldsymbol{\gamma}^B + \text{const.} \tag{4.39}$$

The Heisenberg equations are therefore linear:

$$\frac{d}{dt}\begin{pmatrix}\boldsymbol{\gamma}^A \\ \boldsymbol{\gamma}^B\end{pmatrix} = K\begin{pmatrix}\boldsymbol{\gamma}^A \\ \boldsymbol{\gamma}^B\end{pmatrix}, \qquad K = \begin{pmatrix}0 & D^\mathsf{T} \\ -D & 0\end{pmatrix}. \tag{4.40}$$

Defining $\tilde{\boldsymbol{\gamma}}^A = \Phi^T \boldsymbol{\gamma}^A$ and $\tilde{\boldsymbol{\gamma}}^B = \Psi^T \boldsymbol{\gamma}^B$ where the matrices Φ and Ψ were introduced in Eq.(2.25), the above equation becomes

$$\frac{d}{dt}\begin{pmatrix}\tilde{\boldsymbol{\gamma}}^A \\ \tilde{\boldsymbol{\gamma}}^B\end{pmatrix} = \tilde{K}\begin{pmatrix}\tilde{\boldsymbol{\gamma}}^A \\ \tilde{\boldsymbol{\gamma}}^B\end{pmatrix}, \qquad \tilde{K} = \begin{pmatrix}0 & E \\ -E & 0\end{pmatrix}, \qquad E = \text{diag}(\Lambda_1, \ldots, \Lambda_N). \tag{4.41}$$

Thus, each pair of Majorana amplitudes in this basis rotates at frequency Λ_s. Transforming back and defining $\boldsymbol{\gamma} = \left(\boldsymbol{\gamma}^A \ \boldsymbol{\gamma}^B\right)^T$, the full Heisenberg time evolution is given by

$$\boldsymbol{\gamma}(t) = R(t)\boldsymbol{\gamma}(0), \qquad R(t) = e^{Kt} = \begin{pmatrix} \Phi\cos(Et)\Phi^{\mathsf{T}} & \Phi\sin(Et)\Psi^{\mathsf{T}} \\ -\Psi\sin(Et)\Phi^{\mathsf{T}} & \Psi\cos(Et)\Psi^{\mathsf{T}} \end{pmatrix}. \tag{4.42}$$

We denote these four blocks by $R^{AA}, R^{AB}, R^{BA}, R^{BB}$. We note that $R(t)$ is an orthogoanal matrix.

An entry $R^{\alpha\beta}_{nm}(t)$ gives the coefficient of the initial operator $\gamma^{\beta}_{m}(0)$ in $\gamma^{\alpha}_{n}(t)$. Each block contains the same mode profiles and time factors $e^{\pm i\Lambda_s t}$ that underlie the wave-packet construction. The propagating bulk components therefore have the group velocities in Eq. (4.32). This directly determines how the boundaries affect spin observables. For instance, the longitudinal spin operator is

$$\sigma^z_n = -i\gamma^A_n\gamma^B_n. \tag{4.43}$$

Thus, the magnetization requires the expectation value of a product of two Majorana operators at the observation site.

4.4.2 How propagation enters the magnetization

For the initial fermion vacuum, the required contractions are

$$\langle\gamma^A_m\gamma^A_l\rangle_0 = \langle\gamma^B_m\gamma^B_l\rangle_0 = \delta_{ml}, \qquad \langle\gamma^A_m\gamma^B_l\rangle_0 = i\delta_{ml}. \tag{4.44}$$

Substituting the propagated operators into Eq. (4.43) gives

$$\Delta m^z_n(t) = 1 - \sum_{m=1}^{N}\left[R^{AA}_{nm}(t)R^{BB}_{nm}(t) - R^{AB}_{nm}(t)R^{BA}_{nm}(t)\right]. \tag{4.45}$$

Here we used $\sum_m (R^{AA}_{nm}R^{BA}_{nm} + R^{AB}_{nm}R^{BB}_{nm}) = 0$, which follows directly from the orthogonality of the propagator $R(t)$. Inserting Eq. (4.42) into this expression reproduces Eq. (4.38).

Equation (4.45) connects propagation to the observable. It combines two amplitudes arriving at site n from the same initial site m, with the relative signs fixed by the initial fermionic contractions. Both amplitudes evolve during the same interval t. The requirement of a common initial site is important for distinguishing a response associated with either boundary separately from interference involving both boundaries.

A global quench acts throughout the chain, including near its ends. Boundary-dependent contributions can therefore originate near an end and propagate toward the center. For example, using the reference boundary positions 0 and $L = N + 1$, a direct path from m to n has length $|n - m|$, while a path reflected from the left boundary has length $n + m$. For initial sites $m = O(1)$ near that boundary, both lengths are $n + O(1)$. Their contributions to Eq. (4.45) can therefore become appreciable after a propagation time of order $n/v_{\max}$. They do not require a packet to travel from the observation site to the boundary and then return.

Writing $d_n = \min(n, L - n)$, the earliest bulk ballistic scale associated with the nearest boundary is consequently

$$t_{\text{boundary}} \sim \frac{d_n}{v_{\max}} \sim \frac{N}{2v_{\max}} \tag{4.46}$$

for a central site. As in the wave-packet discussion of Sec. 4.2.6, this is a propagation scale rather than an exactly sharp onset. Packet spreading and reflection phases broaden and shift the response, and its observable weight can be small.

Another distinct boundary effect arise due to the effect of both boundaries. Its contribution can be understood as self-interference: two amplitudes originating at the same initial site propagate toward opposite boundaries, are reflected, and interfere at the observation site. For an initial site m, their propagation lengths are $\ell_{\text{L}} = n + m$ and $\ell_{\text{R}} = 2L - n - m$. These are the paths $m \to 0 \to n$ and $m \to L \to n$. For a common propagation speed $v_{\max}$, the time it takes for both amplitudes to arrive at the same site is

$$t_{\text{joint}} \sim \frac{\ell_{\text{L}} + \ell_{\text{R}}}{2v_{\max}} \sim \frac{N}{v_{\max}}. \tag{4.47}$$

This effect is independent of the site location and is expected to produce boundary corrections at times close to t_{joint} visible for all spins. Focusing on a spin n near the center, the common source for this interference $m = L - n$ is also near the center. Each of these two amplitudes then travels from the central region to one boundary and back. This differs from the earlier response, which can originate near a boundary and travel only toward the center. The two scales therefore give

$$\frac{t_{\text{boundary}} v_{\max}}{N/2} \sim 1, \qquad \frac{t_{\text{joint}} v_{\max}}{N/2} \sim 2. \tag{4.48}$$

Disturbances originating near opposite ends can already reach the center on the earlier scale. Their simultaneous arrival does not by itself produce the interference described above: the initial contractions in Eq. (4.44) require the two amplitudes in a product to originate at the same site. Contributions from different initial sites instead enter the sum over m separately. The finite-chain response can therefore contain the sum of two individual boundary corrections before the additional contribution involving both ends becomes appreciable.

These propagation mechanisms are available in both the single-channel and two-channel regions. Their relative importance is determined by the weights and interference in Eq. (4.45). As shown below, for the parameters studied here, two-channel boundary mixing is associated with a substantially stronger early response, which eventually alter the time-averaged response. In the single-channel controls, the early correction is weaker and the later contribution involving both ends is more prominent. This interference, however, is oscillatory in nature and has a weaker effect on the time-averaged response. A numerical arrival threshold can consequently select a feature near either of the scales in Eq. (4.48). The distinction concerns which contribution is detectable, rather than a different propagation rule in the two spectral regions. It is therefore necessary to distinguish these scales when defining an arrival time and assessing their effect on a time average.

4.4.3 Arrival and time averaging

To study this boundary effect, we define the instantaneous open–bulk difference by

$$\delta_n(t) = \Delta m^z_{n,\mathrm{open}}(t) - \Delta m^z_{n,\mathrm{bulk}}(t). \tag{4.49}$$

For running averages over the same interval $[0, T]$,

$$\overline{\Delta m^z_{n,\mathrm{open}}}_T - \overline{\Delta m^z_{n,\mathrm{bulk}}}_T = \frac{1}{T}\int_0^T \delta_n(t)\, dt. \tag{4.50}$$

Thus, an averaging interval ending before an appreciable boundary response arrives also has a small boundary correction. Once the response arrives, it contributes to the integral, initially diluted by the earlier portion of the averaging window.

Convergence to the strict average is a separate issue. Uniform averaging replaces each cosine in

Eq. (4.38) by

$$\mathcal{K}_T(\omega) = \frac{1}{T}\int_0^T \cos(\omega t)\, dt = \frac{\sin(\omega T)}{\omega T}, \qquad \mathcal{K}_T(0) = 1. \tag{4.51}$$

A nonzero frequency is suppressed only when $|\omega|T \gg 1$. Away from stationary points of the dispersion, neighboring momenta typically have spacings of order π/N, giving

$$\Delta\Lambda \sim \frac{\pi|v(p)|}{N}. \tag{4.52}$$

Near a band extremum, the leading spacing can instead be $O(N^{-2})$. Consequently, the response can reach the center well before its running average has converged. The strict average of the magnetization in Eq. (4.38) retains the complete equal-energy blocks:

$$\overline{m^z_{n\infty}} = \frac{1}{2}\sum_{\Lambda_s=\Lambda_r} \phi_s(n)\psi_r(n)(\mathsf{O}_{sr} + \mathsf{O}_{rs}). \tag{4.53}$$

For a nondegenerate spectrum, this reduces to

$$\overline{m^z_{n\infty}} = \sum_s \phi_s(n)\psi_s(n)\mathsf{O}_{ss}. \tag{4.54}$$

Exact zero modes are treated by retaining every zero-frequency term in the full expression (4.38). At exact degeneracies, the off-diagonal contributions within the degenerate subspace must remain.

The boundaries change the mode profiles and overlaps entering these averages. Each extended mode has local weight of order $1/N$, but changes involving an extensive number of modes can give a finite total contribution. The propagation time explains when such a contribution can become visible locally; frequency resolution determines how long its time average takes to converge.

4.5 Covariance matrix and spin observables

4.5.1 Exact covariance evolution

The magnetization calculation above used products of propagated Majoranas and the initial contractions explicitly. To organize the same calculation for all observables, define the covariance matrix

$$C_{ab}(t) = -\frac{i}{2}\left\langle [\gamma_a(t), \gamma_b(t)] \right\rangle. \tag{4.55}$$

The indices a, b run over all $2N$ Majoranas. This matrix is real and antisymmetric. For distinct indices, $C_{ab} = -i\langle\gamma_a\gamma_b\rangle$, while $C_{aa} = 0$.

In particular,

$$C_{A_nB_n}(t) = \langle \sigma_n^z(t) \rangle, \qquad \Delta m_n^z(t) = 1 - C_{A_nB_n}(t). \tag{4.56}$$

The initial contractions in Eq. (4.44) become

$$C_0 = \begin{pmatrix} 0 & I \\ -I & 0 \end{pmatrix}. \tag{4.57}$$

Since both Majorana operators evolve with $R(t)$ (See Eq. (4.42)),

$$C(t) = R(t) C_0 R^{\mathsf{T}}(t). \tag{4.58}$$

This compact matrix equation contains the real-space magnetization formula (4.45). For example, its AB block is

$$C_{AB}(t) = \Phi \left[\cos(Et) \mathsf{O} \cos(Et) + \sin(Et) \mathsf{O}^{\mathsf{T}} \sin(Et) \right] \Psi^{\mathsf{T}}. \tag{4.59}$$

Taking its diagonal and applying the product-to-sum identities gives the magnetization change in Eq. (4.38). The evolution preserves $C^{\mathsf{T}} = -C$, and $C^2 = -I$ for the present pure Gaussian initial state. Together with $R^{\mathsf{T}} R = I$ and the coupled equations (2.25), these provide numerical consistency checks. The mode construction also includes zero or very small excitation energies without reconstructing either BdG partner through division by Λ_s.

4.5.2 Magnetization and transverse correlators

The same covariance matrix determines the spin correlations. For two distinct sites n and m, the longitudinal spin product contains four Majorana operators. Wick's theorem gives

$$\left\langle \sigma_n^z \sigma_m^z \right\rangle_t = C_{A_nB_n}(t) C_{A_mB_m}(t) - C_{A_nA_m}(t) C_{B_nB_m}(t) + C_{A_nB_m}(t) C_{B_nA_m}(t). \tag{4.60}$$

The first term is the product of the local magnetizations. The remaining terms involve contractions connecting the two sites.

For comparison with the analytical periodic-chain correlator, we use the same prescription of first averaging the two-point contractions and then forming their products. Define

$$\overline{C}_{ab}^{(T)} = \frac{1}{T} \int_0^T C_{ab}(t)\, dt = \left[\frac{1}{T} \int_0^T R(t) C_0 R^{\mathsf{T}}(t)\, dt \right]_{ab}. \tag{4.61}$$

Applying the pairing structure in Eq. (4.60) to these averaged contractions and subtracting the product of the averaged magnetizations defines the magnetization correlator

$$Q^z_{nm}(T) \equiv -\overline{C}^{(T)}_{A_nA_m}\overline{C}^{(T)}_{B_nB_m} + \overline{C}^{(T)}_{A_nB_m}\overline{C}^{(T)}_{B_nA_m}. \tag{4.62}$$

The nearest-neighbor transverse correlator requires only two-point contractions because the Jordan–Wigner strings cancel. With the convention of Chapter 2, its time average is

$$\overline{\left\langle \sigma^+_n \sigma^-_{n+1} \right\rangle}_T = \frac{1}{4}\left[\overline{C}^{(T)}_{A_nB_{n+1}} - \overline{C}^{(T)}_{B_nA_{n+1}} + i\left(\overline{C}^{(T)}_{A_nA_{n+1}} + \overline{C}^{(T)}_{B_nB_{n+1}}\right)\right]. \tag{4.63}$$

All entries of $C(t)$ follow from Eq. (4.42) and contain sine and cosine terms at frequencies $\Lambda_s \pm \Lambda_r$. Their averages can therefore be evaluated analytically. The cosine terms use the kernel in Eq. (4.51); the corresponding sine integral is

$$\frac{1}{T}\int_0^T \sin(\omega t)\, dt = \begin{cases} \dfrac{1-\cos(\omega T)}{\omega T}, & \omega \neq 0, \\ 0, & \omega = 0. \end{cases} \tag{4.64}$$

Consequently, constructing the averaged covariance does not require numerical time quadrature. In the strict averaging limit, the complete zero-frequency contributions are retained, including those within degenerate eigenspaces.

For the real Hamiltonian and initial state considered here, the AA and BB covariance blocks contain only sine terms. Their strict averages therefore vanish:

$$\overline{C}^{(\infty)}_{AA} = \overline{C}^{(\infty)}_{BB} = 0. \tag{4.65}$$

This remains true at exact degeneracies, since a zero-frequency sine is identically zero. Using the antisymmetry of C, the two correlators then simplify to

$$Q^z_{nm}(\infty) = -\overline{C}^{(\infty)}_{A_nB_m}\overline{C}^{(\infty)}_{A_mB_n}, \tag{4.66}$$

$$\overline{\left\langle \sigma^+_n \sigma^-_{n+1} \right\rangle}_\infty = \frac{1}{4}\left[\overline{C}^{(\infty)}_{A_nB_{n+1}} + \overline{C}^{(\infty)}_{A_{n+1}B_n}\right]. \tag{4.67}$$

The averaged AB block therefore organizes all three quantities: its diagonal gives the magnetization, while its off-diagonal entries determine the magnetization and transverse correlators. We now turn to the numerical results to examine how boundary scattering changes these quantities and how the changes depend on chain length and averaging time.

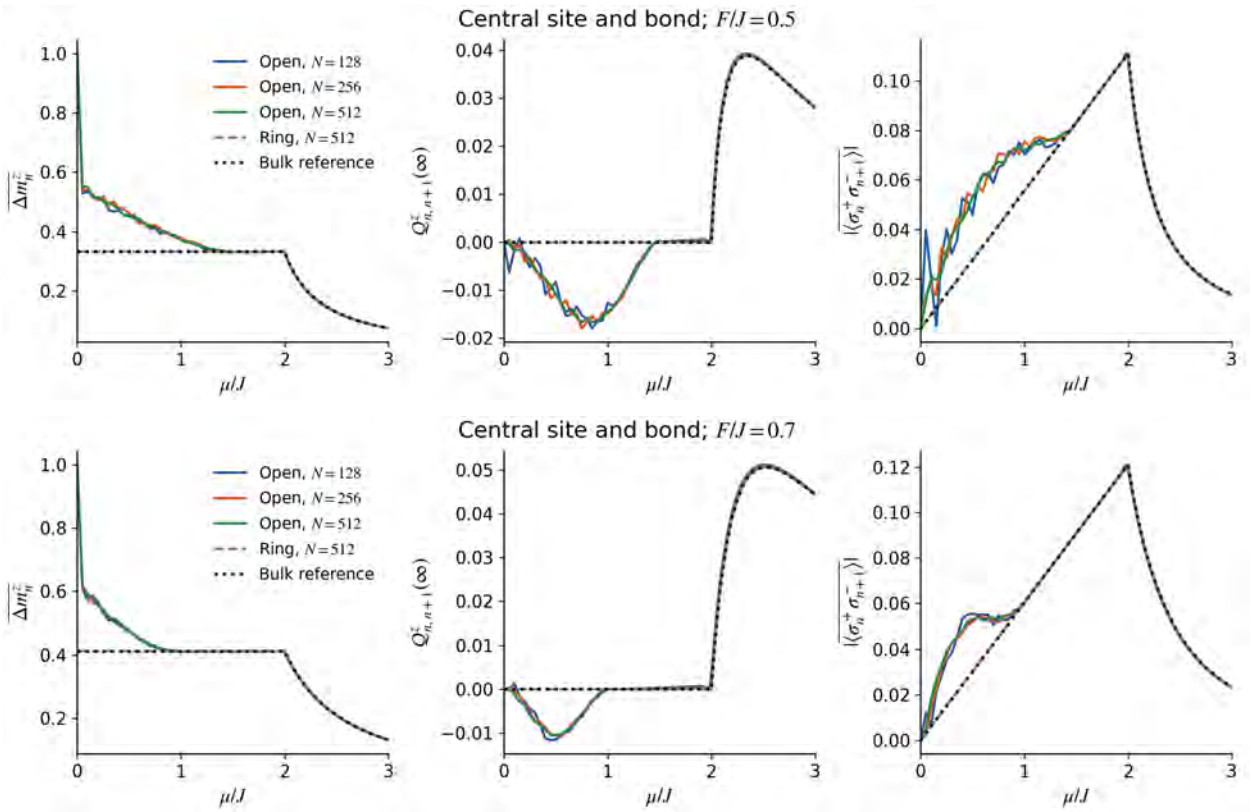


Figure 4.3 Strict infinite-time averages following the sudden turn-on from the polarized state. Top: $F/J = 0.5$. Bottom: $F/J = 0.7$. Open-chain sizes are $N = 128, 256, 512$. The magnetization is evaluated at a central site, $n = N/2$, and correlations on the central bond $(N/2, N/2 + 1)$. The finite-ring curve uses $N = 512$ and antiperiodic fermionic boundary conditions. The dotted curve is the thermodynamic result. From left to right: magnetization change, $Q^z_{n,n+1}(\infty)$, and the magnitude of the averaged transverse correlation.

4.6 Numerical results

4.6.1 Detuning dependence and the two-channel interval

We first compare strict time averages in Eq. (4.67) at the center of an open chain with the finite spin ring and the thermodynamic results. The initial state has even fermion parity. Accordingly, the finite spin ring is represented using antiperiodic Jordan–Wigner fermions. This parity convention is included explicitly in the comparison.

The numerical results is shown in Fig. 4.3 for $F/J = 0.5$ (upper panel) and $F/J = 0.7$ (lower panel). For $F/J = 0.5$, the principal open-chain departure occurs in the interval $|\mu|/J < 1.5$, where the spectrum contains two-channel energies. In the topological single-channel interval $1.5 < |\mu|/J < 2$, the central magnetization approaches the periodic plateau. For $|\mu|/J > 2$, the

chain is topologically trivial and the open and periodic results again approach one another. For $F/J = 0.7$, the two-channel threshold moves to $|\mu|/J < 1.02$. The corresponding change in the detuning dependence supports the connection to the bulk channel structure.

The distinction between these thresholds is useful physically. A topological edge mode is present on both sides of the two-channel threshold within $|\mu| < 2J$. The large bulk deviation instead follows the region where boundary reflection can mix two propagating channels. The arrival time scaling below will further establish this result.

The exactly zero-detuning point is singular and will be examined separately below. A narrow feature near $\mu = 0$ should not be interpreted as a smooth continuation of generic-detuning size scaling.

4.6.2 Spatial propagation and the central-site time evolution

For $F/J = 0.5$, figure 4.4 resolves where the difference in the magnetization between an open chain and thermodynamic bulk develops for $\mu/J = 0.5$ (upper panel), corresponding to a spectrum that supports two-channel, and $\mu/J = 1.7$ (lower panel) corresponding to single-channel spectrum. The instantaneous time evolution is shown on the left. At early times, the interior for both cases follows the bulk periodic dynamics. The boundary-dependent signal propagates inward from the ends, producing a stronger response for the two-channel case. This corresponds to the single boundary propagation with the estimate in Eq. (4.46). At later times, we observe a developing oscillating signal that arise uniformly across all sites. This corresponds to the two-boundary interference with the estimate in Eq. (4.47).

The running-average panels on the right contain the accumulated response over the entire interval $[0, T]$. They therefore have a different appearance from the instantaneous panels. In particular, a late boundary contribution is initially diluted by the earlier part of the averaging window during which the center followed the bulk dynamics. The results shows that the time-average difference in the upper panel eventually develops an appreciable central correction, whereas the single-channel correction remains much smaller. This supports the claim that boundary channel mixing is responsible for the time-averaged bulk sensitivity to the boundaries.

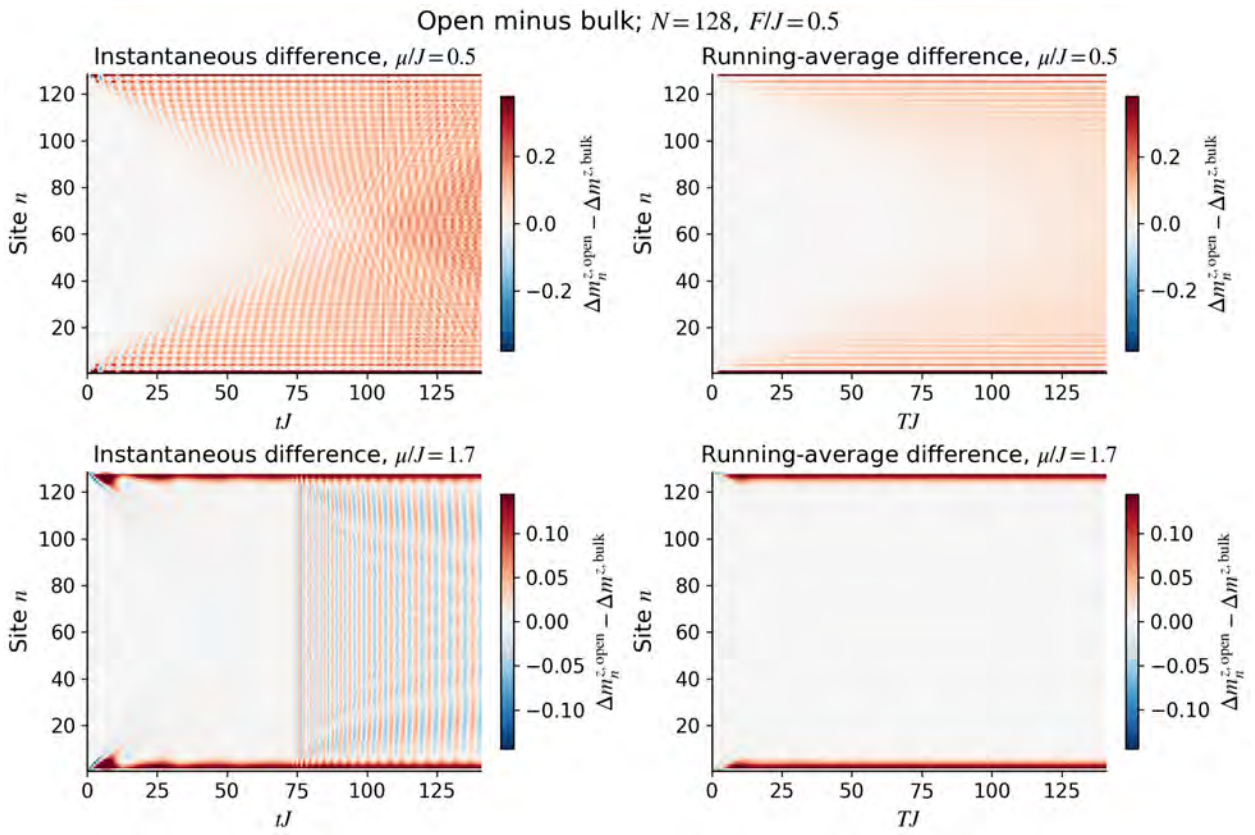


Figure 4.4 Open-chain magnetization change for $N = 128$ minus the thermodynamic result for $F/J = 0.5$. Top row: $\mu/J = 0.5$. Bottom row: $\mu/J = 1.7$. Left column: instantaneous differences. Right column: differences between uniform running averages over $[0, T]$. Each panel has its own color scale. The boundary-dependent response develops first near the ends and subsequently reaches the interior.

Focusing on the central cite, the left panel of Fig. 4.5 shows that the open center initially follows the thermodynamic bulk trace. A substantial difference appears only after a time proportional to the distance from the boundaries. This proportionality is illustrated in the right panel which uses the scaled duration TJ/N. The comparable evolution of different sizes on this axis is consistent with a ballistic boundary time proportional to N. The displayed curves approach a difference of order 0.12, while retaining finite-time oscillations. While this establish the scaling with N it does not establish the physical mechanism; it does not identify whether the arrival time scales as Eq. (4.46) or Eq. (4.47) corresponding to boundary propagation or two-boundary interference, respectively. The heatmap in Fig. 4.4, however, indicates that it arises due to the former. We next establish this correspondence.

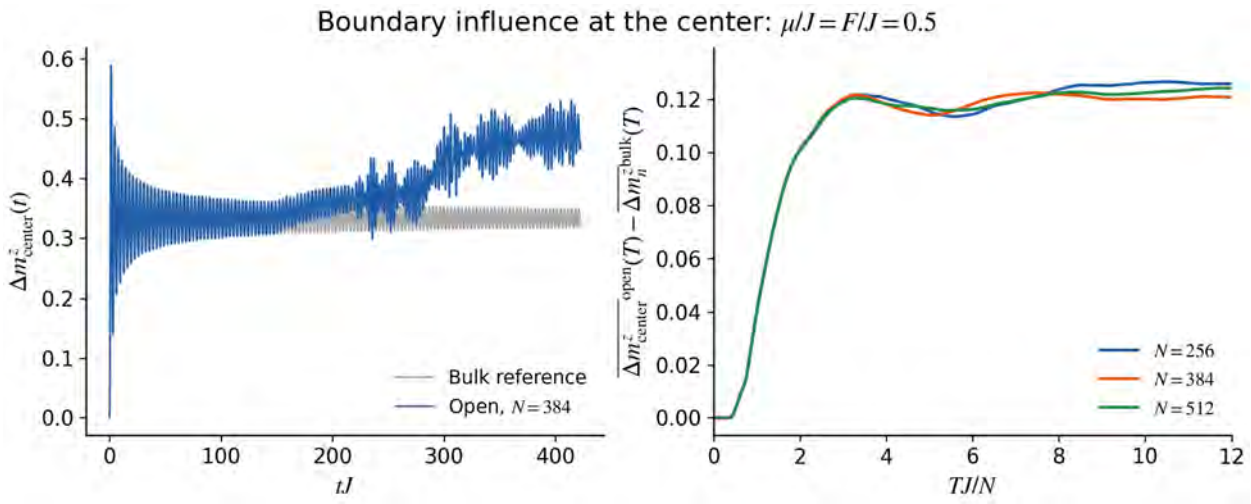


Figure 4.5 Central-site dynamics at $\mu/J = F/J = 0.5$. Left: instantaneous magnetization change for an open chain with $N = 384$, compared with the thermodynamic bulk. The central site is $n = N/2 + 1$. Right: difference between the open and thermodynamic bulk running averages over the same interval $[0, T]$, for $N = 256, 384, 512$. The displayed range is $0 \le TJ/N \le 12$. The curves approach size-dependent plateaus with residual finite-time oscillations.

4.6.3 Operational arrival times and their velocity scaling

The arrival time used in the simulations is defined from the instantaneous central-site difference, $\delta_N(t) = \Delta m^z_{\mathrm{center,open}}(t) - \Delta m^z_{\mathrm{bulk},\infty}(t)$, through

$$t_{\mathrm{arrival}}(N;\eta) = \min\{t_j : |\delta_N(t_j)| > \eta\}. \tag{4.68}$$

Here t_j are sampled times and η is a specified threshold. The main sampling interval is $\Delta t\, J = 0.25$.

For the three detunings, the maximum velocities are

$$\frac{v_{\max}}{J} \simeq \begin{cases} 1.26772, & \mu/J = 0.5, \\ 1.72393, & \mu/J = 1.7, \\ 1.90898, & \mu/J = 3. \end{cases} \tag{4.69}$$

Thus, dividing by the distance and multiplying by $v_{\max}$ tests whether the propagation scale derived from the bulk dispersion agree with the boundary scattering or interference estimates in Eq. (4.48). In Fig. 4.6, we used the two thresholds $\eta = 10^{-3}$ and 10^{-2}. At $\mu/J = 0.5$, both displayed thresholds give a scaled arrival close to one. This shows that an appreciable central response appears on the scale needed for a bulk wave packet to propagate from an end to the center.

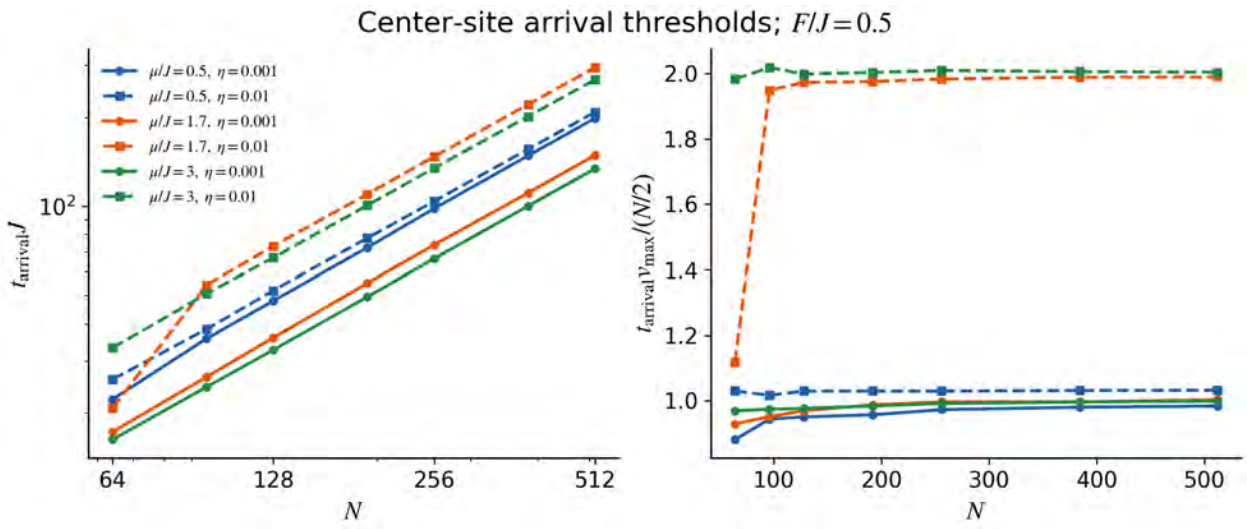


Figure 4.6 Threshold-defined central-site arrival times for $F/J = 0.5$, $\mu/J = 0.5, 1.7, 3$, and $N = 64, 96, 128, 192, 256, 384, 512$. The displayed thresholds are $\eta = 10^{-3}$ and 10^{-2}. Left: arrival times versus size. Right: the same times scaled as $t_{\mathrm{arrival}} v_{\mathrm{max}}/(N/2)$. The denominator $N/2$ is the distance convention used in the numerical analysis; endpoint corrections are $O(1)$.

The single-channel controls require a qualification. Their ratio is close to two at the larger threshold, but close to one at the smaller threshold. For example, at $N = 512$,

μ/J	$\eta = 10^{-3}$	$\eta = 10^{-2}$
0.5	0.9842	1.0325
1.7	1.0034	1.9899
3.0	0.9992	2.0041

(4.70)

where the listed values corresponds to $t_{\mathrm{arrival}} v_{\mathrm{max}}/(N/2)$. Consequently, the data do not establish a universal rule assigning propagation time $N/(2v_{\mathrm{max}})$ to two-channel spectra and N/v_{max} to single-channel spectra. The controls already have a weaker signal on the earlier scale. The larger threshold selects a later, stronger feature.

Although both responses propagate on the scale $t_{\mathrm{boundary}} = N/(2v_{\mathrm{max}})$, their amplitudes have different size dependence. Figure 4.7 illustrates this by plotting the maximum absolute boundary signal $|\delta_N(t)|$ over the interval $0.8 \le t/t_{\mathrm{boundary}} \le 1.2$. For the parameters studied, the single-channel boundary transients weaken with increasing chain length, whereas the two-channel response becomes nearly independent of size over the larger chains and remains appreciable up to $N = 4096$.

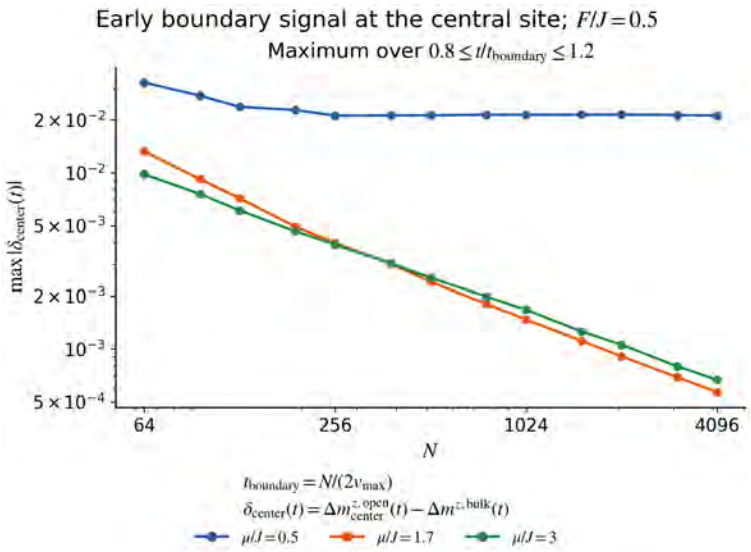


Figure 4.7 Size dependence of the early central-site boundary signal after a sudden quench from the fully polarized initial state, with $F/J = 0.5$. For an open chain of N sites, the observation site is $n = N/2 + 1$, and the instantaneous signal is $\delta_N(t) = \Delta m_n^{z,\mathrm{open}}(t) - \Delta m^{z,\mathrm{bulk}}(t)$, where the bulk reference is the infinite uniform chain with the same parameters and initial state. Each point gives $\max_{0.8\le t/t_{\mathrm{boundary}}\le 1.2} |\delta_N(t)|$, with $t_{\mathrm{boundary}} = N/(2v_{\max})$ and $v_{\max}$ evaluated for the corresponding parameters. Blue: $\mu/J = 0.5$, where a two-channel interval exists. Orange and green: the single-channel controls $\mu/J = 1.7$ and 3, respectively. The computed sizes range from $N = 64$ to 4096. Both axes are logarithmic; lines connect the numerical points.

The distinction therefore concerns the observable weight of the response, rather than a different propagation rule.

The robust conclusion is that the first detectable boundary response follows a ballistic distance-over-velocity scale for all regimes. The amplitude and subsequent structure of that response depend on the channel content, reflection amplitudes, and observable weights. The ratio near one supports a boundary-propagation interpretation, but it does not by itself isolate channel conversion at a given threshold. That interpretation also uses the mode composition in Fig. 4.1 and the detuning dependence in Fig. 4.3, and is also supported by the observation of a decaying single channel signal with system size around t_{boundary}.

4.6.4 Zero detuning: sublattice symmetry and size parity

The exactly zero-detuning point requires a separate discussion. At $\mu = 0$, the diagonal entries of D vanish, and D connects only opposite site sublattices. Consequently, $D^{\mathsf{T}}D$ preserves the even and odd sublattices. This additional structure imposes constraints on the time-averaged magnetization

that are absent at generic detuning.

Consider first an even chain, $N = 2M$, with $0 < F < J$, and define $a_\pm = J \pm F$. The two sublattice blocks of $D^\mathsf{T}D$ are tridiagonal. After reversing the site order in one block, their first diagonal entries are a_-^2 and a_+^2, respectively. All remaining diagonal entries are $a_+^2 + a_-^2$, and the off-diagonal entries are a_+a_-. Thus, the blocks differ by a positive change of $4JF$ in one endpoint diagonal entry. Since their off-diagonal entries are nonzero, their eigenvalues strictly interlace. In particular, the two blocks have no common eigenvalue.

Each nondegenerate eigenvector ϕ_s therefore occupies only one sublattice. Its partner,

$$\psi_s = \frac{D\phi_s}{\Lambda_s}, \tag{4.71}$$

occupies the opposite sublattice. Their product consequently vanishes at every site:

$$\phi_s(n)\psi_s(n) = 0. \tag{4.72}$$

Substitution into Eq. (4.54) gives the exact result

$$\overline{m^z_{n\infty}} = 0, \qquad \overline{\Delta m^z_{n\infty}} = 1, \qquad \mu = 0, \quad N \text{ even}. \tag{4.73}$$

This holds at every site, including the center. It follows from the sublattice structure of the complete mode spectrum. For comparison, the uniform bulk reference at zero detuning is

$$\overline{\Delta m^z}_{\infty,\mathrm{bulk}} = \int_0^\pi \frac{dk}{\pi} \frac{F^2 \sin^2 k}{J^2 \cos^2 k + F^2 \sin^2 k} = \frac{F}{J+F}. \tag{4.74}$$

At $F/J = 0.5$, this gives $1/3$, compared with the exact open-chain value of one for even N.

Odd chains have a different degeneracy structure. The two sublattices now contain different numbers of sites, and the corresponding rectangular blocks of D have identical nonzero singular spectra. The nonzero excitation energies therefore occur in exact doublets. The off-diagonal contributions within these doublets must be retained in Eq. (4.53); applying the nondegenerate formula would incorrectly remove them.

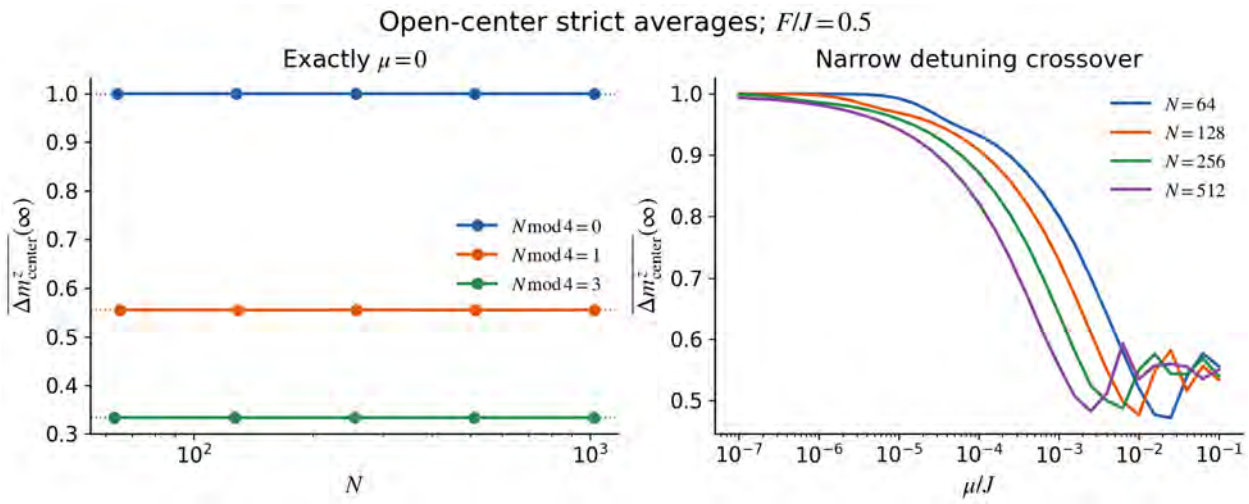


Figure 4.8 Zero-detuning symmetry and its sensitivity to chain length at $F/J = 0.5$. Left: strict central-site magnetization changes at exactly $\mu = 0$, with $n = \lfloor N/2 \rfloor + 1$. The displayed classes are $N \bmod 4 = 0, 1, 3$, extending through $N = 1025$. Dotted lines show the values in Eq. (4.75). The unplotted even class $N \bmod 4 = 2$ also gives one and was checked through $N = 1026$. Right: the small-detuning dependence for $N = 64, 128, 256, 512$. The sharp feature near zero becomes narrower with increasing size.

Evaluating the complete degenerate blocks gives the following central-site values for long chains:

$$\overline{\Delta m^z_{\text{center}\infty}} \simeq \begin{cases} 1, & N \text{ even}, \\ 1 - \dfrac{J^2}{(J+F)^2}, & N = 4r+1, \qquad \mu = 0. \\ \dfrac{F}{J+F}, & N = 4r+3, \end{cases} \tag{4.75}$$

The even-chain result is exact at finite size; the odd-chain expressions are the large-size values. Here the central site is defined as $n = \lfloor N/2 \rfloor + 1$. For odd chains, this site belongs to the odd sublattice when $N = 4r + 1$ and to the even sublattice when $N = 4r + 3$. This explains why changing the odd length by two changes the central-site result. At $F/J = 0.5$, the three values are 1, $5/9$, and $1/3$, respectively.

Figure 4.8 demonstrates this parity dependence and resolves the narrow feature near $\mu = 0$. A nonzero detuning introduces diagonal entries into D and removes the sublattice separation used above. The displayed even chains approach the exact zero-detuning value continuously, but the detuning interval over which this value is approached becomes narrower as the size increases. Thus, the singular zero-detuning behavior should not be interpreted as a discontinuity of these finite-chain

curves or as a smooth continuation of the generic-detuning size dependence.

This feature is also distinct from a topological transition. At $\mu = 0$ and $0 < F < J$, the bulk excitation gap is $2F$, which remains nonzero. The exceptional response instead follows from the additional sublattice symmetry and its consequences for the mode overlaps and degeneracies.

4.6.5 Convergence of finite-window averages

The propagation results establish when a boundary-dependent response becomes visible. We next check whether the averaging durations are sufficient to determine its long-time contribution. This requires comparing the running average with the strict average of the same finite chain.

Grouping the terms in Eq. (4.38) by their nonzero frequencies gives

$$\Delta m_n^z(t) = \overline{\Delta m_{n\infty}^z} + \sum_{\omega>0} a_{n,\omega} \cos(\omega t). \tag{4.76}$$

Here $a_{n,\omega}$ collects all contributions at frequency ω, including those originating from the difference and sum frequencies $\Lambda_s - \Lambda_r$ and $\Lambda_s + \Lambda_r$. All exactly zero-frequency contributions are included in the strict average.

Using the uniform averaging kernel in Eq. (4.51), the remaining finite-duration contribution is exactly

$$\overline{\Delta m_{nT}^z} - \overline{\Delta m_{n\infty}^z} = \sum_{\omega>0} a_{n,\omega} \frac{\sin(\omega T)}{\omega T}. \tag{4.77}$$

Since $|\sin x| \leq \min(|x|, 1)$, this gives the conservative bound

$$\left| \overline{\Delta m_{nT}^z} - \overline{\Delta m_{n\infty}^z} \right| \leq \sum_{\omega>0} |a_{n,\omega}| \min\left(1, \frac{1}{\omega T}\right). \tag{4.78}$$

The bound allows no cancellation between different frequencies and is therefore generally larger than the actual error.

These expressions clarify why arrival and convergence need not occur on the same time scale. Arrival depends on the distance from the boundary and the velocities of the propagating contributions. Convergence additionally requires $\omega T \gg 1$ for the nonzero frequencies carrying appreciable weight. Closely spaced energies can therefore produce slowly decaying contributions to the running average after the boundary response has already reached the center.

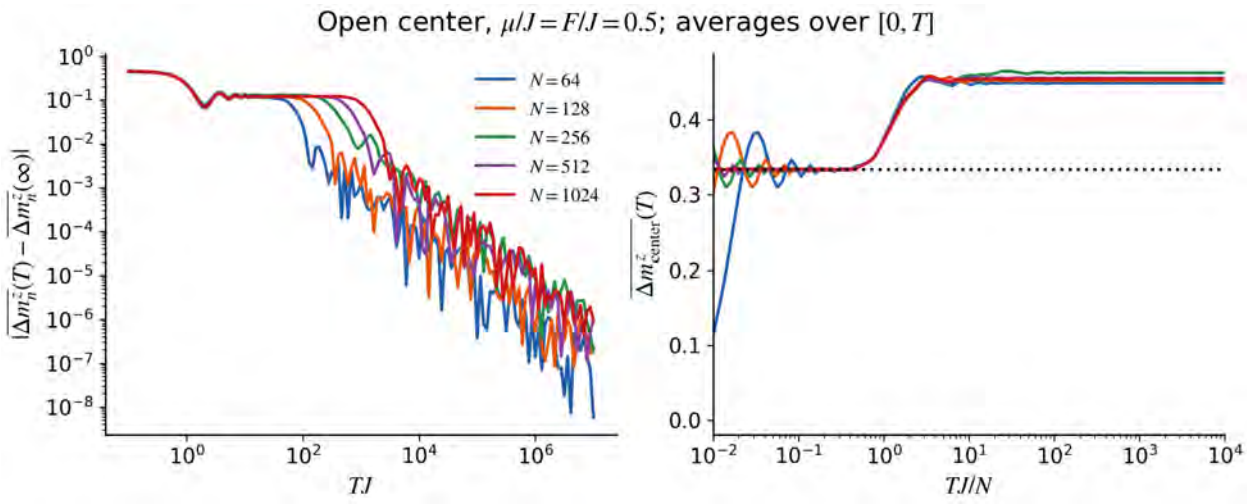


Figure 4.9 Convergence of uniform time averages over $[0, T]$ for open chains at $\mu/J = F/J = 0.5$. The observation site is $n = N/2 + 1$, and the sizes are $N = 64, 128, 256, 512, 1024$. Left: absolute difference between the running average and each chain's own strict infinite-time average, for durations $10^{-1} \leq TJ \leq 10^{7}$. Right: the running averages plotted against TJ/N, with displayed range $10^{-2} \leq TJ/N \leq 10^{4}$. Colors identify the same sizes in both panels. The dotted horizontal line is the bulk reference value $1/3$.

Figure 4.9 checks this convergence for the two-channel parameters $\mu/J = F/J = 0.5$. The reference value used in the left panel is obtained directly by retaining the complete zero-frequency blocks, as in Eq. (4.53). It is not estimated from the running average. The finite-window values are evaluated using the exact frequency kernels, so the comparison does not require a numerical time-integration step.

The error oscillates as the averaging duration increases because the different sinc contributions change sign and interfere. Nevertheless, its overall magnitude decreases. At $TJ = 10^{7}$, the largest absolute error among the displayed sizes is approximately 9.98×10^{-7}. The largest corresponding bound from Eq. (4.78) is approximately 1.51×10^{-5}. These bounds concern the finite-duration contribution for the calculated frequencies and coefficients; they do not estimate errors in the spectral calculation itself.

The right panel shows how this convergence relates to the earlier propagation results. Scaling the duration by N brings the initial development of the boundary-dependent average onto a comparable scale for different lengths. The averages subsequently settle near their respective finite-chain values, with residual oscillations and some size dependence. Their convergence need not collapse onto a

single function of TJ/N, since the contributing frequency spacings and weights also depend on size.

For example, the strict central-site averages are approximately 0.44918 for $N = 64$ and 0.45472 for $N = 1024$, compared with the bulk value $1/3$. Their separation from the bulk reference is therefore much larger than the remaining finite-window error at the longest averaging duration. For these sizes and parameters, the observed boundary-dependent average cannot be attributed to terminating the time average before convergence.

4.7 Concluding remarks

In this chapter, we extended the analysis of the driven spin chain to a finite chain with free ends. Opening the chain changes both the quantization and the composition of its eigenstates. In the single-channel region, the propagating part is accompanied by evanescent components needed to satisfy the boundary conditions. In the two-channel region, the boundaries mix two distinct propagating momenta at the same quasienergy. This mixing involves extended states and provides a mechanism for modifying bulk observables that is distinct from the direct contribution of localized edge modes.

The observable consequences develop through propagation and interference. Following the sudden turn-on of the modulation, the central spins initially follow the uniform bulk dynamics. An appreciable boundary-dependent response can appear after a time set by the distance from the ends and the bulk group velocities. This propagation scale applies in both channel regimes, while the strength of the arriving signal depends on the mode composition and observable weights. For the parameters studied, the two-channel response remains appreciable over the largest evaluated sizes, whereas the early single-channel transients weaken with increasing length. The finite-window calculations also demonstrate convergence to boundary-dependent time averages, establishing that their separation from the bulk reference is not explained by an insufficient averaging duration.

These results complete Part I. Together with the periodic-chain analysis, they show how the response to resonant modulation depends on the excitation spectrum, the preparation protocol, and the boundary conditions. In Part II, we turn to nonlinear dynamics in mesoscopic systems. Chapter 5 examines how the strain response of valence-band holes produces dispersive coupling between

vibrational modes of semiconductor resonators, leading to amplitude-dependent frequency shifts and frequency fluctuations. Chapter 6 considers a Wigner crystal of electrons above liquid helium, where the weak coupling between the driven electron lattice and helium surface waves produces a strong nonlinear transport. In these systems, we investigate how coupling between different degrees of freedom determines the measured dynamical response.

Part II

Nonlinear Dynamics in Mesoscopic Systems

CHAPTER 5

DISPERSIVE MODE COUPLING IN P-DOPED SEMICONDUCTOR NANOMECHANICAL RESONATORS

5.1 Introduction

Micro- and nanoelectromechanical systems (MEMS and NEMS) are broadly used for precision timing, inertial sensing, and frequency control. Semiconductor-based mechanical resonators are especially attractive, because they are small, have a high quality factor Q, and are compatible with standard micro-scale electronics. These systems have been extensively studied both in physics and in engineering [75–80]. They are mesoscopic: their low-frequency eigenmodes are well-separated in frequency and can be individually accessed. At the same time, the dynamical properties are well described by macroscopic characteristics such as density and strain and stress tensors, for example.

For frequency-reference applications, in particular those that require long-term stability, the clock-mode frequency of a resonator must remain stable against comparatively slow fluctuations in the environment, including temperature and pressure fluctuations. Another factor to keep controlled is the vibration amplitude: because of the inherent nonlinearity of mechanical resonators, an amplitude change leads to a change of the vibration frequency. Whereas pressure control can be accomplished by sealing the resonator, control of temperature is often beyond direct control. Even if the eigenfrequency of a chosen vibrational mode weakly depends on temperature, it may be insufficient for the required stability.

An efficient approach to frequency stabilization is based on a dual-mode architecture. Here, two mechanical modes of the same resonator are operated simultaneously. One mode serves as the frequency reference, while the other serves as an in situ thermometer [81–87]. The clock mode is chosen for its weak temperature dependence, whereas the auxiliary mode is chosen to have a larger temperature coefficient. Monitoring the auxiliary-mode frequency then provides a direct measure of the resonator temperature, which can be used to control it even where the temperature of the environment changes.

An important factor to be taken into account in the analysis of multi-mode mesoscopic vibrational

system is the dispersive, or cross-Kerr, nonlinear mode-mode coupling, i.e., a nonresonant coupling between modes with incommensurate frequencies. Such coupling leads to the dependence of the mode frequency on the amplitudes of the modes it is coupled to. In particular, the clock-mode frequency depends on the amplitude of the auxiliary mode, but also on the amplitudes of other modes. To the lowest order, the corresponding coupling comes from the terms in the energy of nonresonant modes, which are bilinear in the squared modes coordinates Q_α, where α enumerates the mode. Phenomenologically, the corresponding energy is $\propto Q_\alpha^2 Q_{\alpha'}^2$, with $\alpha \neq \alpha'$.

Dispersive coupling has been well known in the physics of solids, cf. [88, 89]. More recently it has attracted attention in the physics of nanomechanical systems, cf. [90–95]; in particular, it has been used as a sensitive probe of modal occupation [96–98]. It plays an important role in optomechanics [99]. Dispersive coupling of a nanomechanical modes and a qubit provides a means to measure quantum states of the mode [100]. In a slightly different form, dispersive coupling underlies a commonly used way of measuring the states of superconducting qubits [72]. Generally, dispersive coupling is a major mechanism of frequency fluctuations of various mesoscopic systems, including fluctuations that come from thermal fluctuations of the amplitudes of the modes dispersively coupled to the system of interest [80].

For all relevant applications, it is necessary to understand the strength of the dispersive coupling. In two-mode based clocks, in particular, it puts a constraint on how strongly the auxiliary mode can be driven before the frequency of the clock mode significantly changes, and thus on sensing capability of the auxiliary mode.

Dynamical properties of semiconductor-based resonators can be efficiently modified using doping and thus changing the free carrier density. This is a consequence of the typically strong electron-phonon coupling. The relevant aspect of the coupling is that the vibration-induced strain changes the electronic band structure, leading to a redistribution of the carriers within and between energy bands. The redistribution adds strain-induced terms to the carrier free energy and thus to the free energy of the crystal as whole. In turn, this changes the elasticity parameters, as they are determined by the derivatives of the free energy over strain. This is a mechanism of the

electrons-mediated backaction on the vibrations. This mechanism was first proposed by Keyes [101] and has since been analyzed in several types of semiconductors [102–111]. In silicon resonators, the carrier-mediated elastic response has been shown experimentally to significantly modify the temperature dependence of the elastic constants, reducing the temperature dependence of the frequencies of certain modes [112, 113] or even making it nonmonotonic [114].

In this chapter, we present the theoretical results of the study of the dispersive (cross-Kerr) nonlinearity in a doped semiconductor resonator [65]. We develop a general approach that allows us to find the strength of the coupling between low-frequency modes as a function of hole density and temperature. We also study the effect of the coupling to high-frequency modes and the frequency fluctuations that come from this coupling. The results refer to p-doped diamond or zinc-blende semiconductors such as Si or GaAs, which are typically used as mechanical resonators. The branches of light and heavy holes of such semiconductors are degenerate at the center of the Brillouin zone. This makes them sensitive to strain, which lifts the degeneracy and thus significantly distorts the band structure. We extend to multi-mode nonlinear coupling the analysis of the effect of electron-phonon coupling on the self-nonlinearity of a mode [111], which was done in a single-mode approximation. This extension includes, in particular, determining the appropriate components of the fourth-order nonlinear elasticity tensor and calculating their dependence on the hole density and temperature for both degenerate and nondegenerate hole gas.

The explicit results refer to the system of coupled modes in silicon resonators. As an example, we consider the modes studied in the experiments [82, 83, 86, 87]. In these and in a number of other experiments [115–118], the resonator is a thin plate, and the clock mode is a Lamé mode. This is a shear mode, and therefore it has reduced sensitivity to thermal expansion. It also displays a high quality factor and a low phase noise [119, 120]. As an auxiliary temperature-sensing mode in [82], an out-of-plane torsional mode was used. This allowed achieving parts-per-trillion-level frequency stability of the clock mode [86, 87].

In Sec. 5.2 we formulate a general approach to the problem by introducing normal modes and showing how the backaction of the phonon-hole coupling modifies the elastic part of the free energy

Table 5.1 List of Symbols

$\boldsymbol{u}^{(\alpha)}(\boldsymbol{r})$	Dimensionless spatial displacement profile of mode α
$\varepsilon^{(\alpha)}(\boldsymbol{r})$	Dimensional spatial strain profile of mode α determined by $\boldsymbol{u}^{(\alpha)}(\boldsymbol{r})$
Q_α	Dynamical coordinate of mode α
ω_α	Eigenfrequency of mode α
$\hat{C}^{(n)}$	nth-order intrinsic elasticity tensor
$\hat{\Lambda}^{(n)}$	Doping-induced corrections to the nth-order elasticity tensor
$\eta_\alpha = A_\alpha/L_s$	Amplitude A_α of mode α scaled by the side length of the plate L_s
$\aleph_{\alpha\beta} = \delta\omega_\alpha/\omega_\alpha\eta_\beta^2$	Scaled frequency shift $\delta\omega_\alpha$ of mode α due to coupling to mode β

of the crystal. We also provide Table 5.1 that shows major symbols used in the chapter. In Sec. 5.3 we provide estimates of the hole-induced parameters of linear and nonlinear elasticity. Section 5.4 provides a brief discussion of the effect of dispersive coupling of mesoscopic low-frequency modes to high-frequency phonons. Section 5.5 contains a discussion of phase diffusion of low-frequency modes due to dispersive mode-mode coupling. Section 5.6 describes the Lamé and torsional modes and the expressions for the effect of their dispersive coupling on the amplitude-dependent frequency shifts in terms of the nonlinearity parameters. Section 5.7 describes the numerical procedure of calculating the hole-induced contribution to the nonlinear elasticity tensor for a three-band model of the hole dispersion. Section 5.8 is the central part of the chapter. It provides numerical results on the temperature and density dependence of the frequency shifts of dispersively coupled Lamé and torsional modes in Si. Section 5.9 summarizes the results.

5.2 Adiabatic backaction from the hole-vibrational coupling

We consider a single-crystal semiconductor resonator and enumerate its vibrational modes by α. The displacement field is

$$\boldsymbol{u}(\boldsymbol{r},t) = \sum_\alpha Q_\alpha(t)\boldsymbol{u}^{(\alpha)}(\boldsymbol{r}), \tag{5.1}$$

where Q_α is the dynamical coordinate of the mode and $\boldsymbol{u}_\alpha$ is dimensionless mode profile normalized to the resonator volume V, i.e., $\int \boldsymbol{u}^{(\alpha_1)} \cdot \boldsymbol{u}^{(\alpha_2)} d\boldsymbol{r} = V\delta_{\alpha_1\alpha_2}$. The corresponding strain tensor is

$$\hat{\varepsilon}(\boldsymbol{r},t) = \sum_\alpha Q_\alpha(t)\varepsilon^{(\alpha)}(\boldsymbol{r}), \quad \varepsilon_{ij}^{(\alpha)} = \left(\partial_j u_i^{(\alpha)} + \partial_i u_j^{(\alpha)}\right), \tag{5.2}$$

where subscripts i, j enumerate the axes x, y, z, cf. [121]; we have disregarded quadratic in $\boldsymbol{u}^{(\alpha)}$ terms in $\varepsilon^{(\alpha)}$; their contribution is much smaller than the contribution from the nonlinear terms coming from the strong electron-phonon coupling, cf. [110]. In what follows we use Voigt notation,

$$\varepsilon_1^{(\alpha)} = \varepsilon_{xx}^{(\alpha)}, \quad \varepsilon_2^{(\alpha)} = \varepsilon_{yy}^{(\alpha)}, \quad \varepsilon_3^{(\alpha)} = \varepsilon_{zz}^{(\alpha)},$$
$$\varepsilon_4^{(\alpha)} = 2\varepsilon_{yz}^{(\alpha)}, \quad \varepsilon_5^{(\alpha)} = 2\varepsilon_{xz}^{(\alpha)}, \quad \varepsilon_6^{(\alpha)} = 2\varepsilon_{xy}^{(\alpha)}.$$

The Hamiltonian H of the modes can be written as a sum of a harmonic part and nonlinear parts, $H = H_{\text{lin}} + H_{\text{nl}}$. For modes with inversion symmetry, H_{nl} contains only even powers of the coordinates, so that

$$H_{\text{lin}} = \frac{1}{2}\sum_{\alpha}\left(\frac{P_\alpha^2}{M} + M\omega_\alpha^2 Q_\alpha^2\right)$$
$$H_{\text{nl}} = \frac{1}{4!}\sum_{\alpha_1,\alpha_2,\alpha_3,\alpha_4} \gamma^{(\alpha_1\alpha_2\alpha_3\alpha_4)} Q_{\alpha_1} Q_{\alpha_2} Q_{\alpha_3} Q_{\alpha_4} + \ldots, \tag{5.3}$$

where M is the mass of the resonator, ω_α is the eigenfrequency of mode α, and $\hat{\gamma}$ is the tensor of the 4th order nonlinearity. Here and below we imply summation over repeated indices. The dispersive coupling of modes α_1 and α_2 is described by the term $(1/4)\gamma^{(\alpha_1\alpha_1\alpha_2\alpha_2)} Q_{\alpha_1}^2 Q_{\alpha_2}^2$ in H_{nl}. The manifestation of this coupling in the mode dynamics is discussed in Sec. 5.5 below.

We will be interested in the effect of doping on the modes with frequencies ω_α in the range of $2\pi \times 10^6 - 2\pi \times 10^9$ s^{-1}. This range covers the typical frequencies of nano- and micro-mechanical resonators.

The analysis below directly extends to the modes with no inversion symmetry. For such modes, one has to take into account terms which are cubic in Q_α. As we show below, the doping-induced contribution from these terms to the dispersive coupling parameters is small.

5.2.1 The contribution of the hole-phonon coupling to the elastic free energy: general formulation

For diamond- and zinc-blend semiconductors, the valence band is formed by p-orbital atomic states, and the analysis should take into account three branches of the valence band. They correspond to heavy and light holes and the band, which is split off by the spin-orbit coupling.

To describe the effect of the hole-vibrational coupling we note that, for the hole densities and mode frequencies of interest, the hole thermalization time is much shorter than the reciprocal frequencies. The hole subsystem can be then described in the adiabatic approximation, as it remains in local quasiequilibrium for a given instantaneous strain field [111]. The density of the holes n_h is determined by the acceptor density. If this density is high and the temperature is not too low, all acceptors are ionized and the hole density is equal to the density of the acceptors. For Si, for example, this happens in the range where the acceptor densities are above 10^{18} cm^{-3} and $T \gtrsim 100$ K.

In the adiabatic approximation, the hole grand canonical potential density is

$$\Omega = -2k_BT \sum_\nu \int \frac{d^3\boldsymbol{k}}{(2\pi)^3} \ln\left[1 + \exp\left(\frac{\mu - E_\nu(\boldsymbol{k}, \hat{\varepsilon})}{k_BT}\right)\right], \tag{5.4}$$

where the factor of two accounts for the Kramers degeneracy, ν labels the energy branches of the valence band, and $E_\nu(\boldsymbol{k}, \hat{\varepsilon})$ is the hole energy. It can be found for a given strain $\hat{\varepsilon}$ by diagonalizing the Luttinger–Kohn–Bir–Pikus Hamiltonian [122–124]. The hole free energy density is $\mathcal{F}_\mathrm{h} = \Omega + \mu n_\mathrm{h}$, where $\mu \equiv \mu(\hat{\varepsilon})$ is the chemical potential.

The strain-induced term in the hole free-energy density $\Delta\mathcal{F}$ can be expanded in a power series in the strain,

$$\Delta\mathcal{F} = \frac{1}{2}\Lambda^{(2)}_{ij}\varepsilon_i\varepsilon_j + \frac{1}{3!}\Lambda^{(3)}_{ijk}\varepsilon_i\varepsilon_j\varepsilon_k + \frac{1}{4!}\Lambda^{(4)}_{ijkl}\varepsilon_i\varepsilon_j\varepsilon_k\varepsilon_l + \cdots, \tag{5.5}$$

where ε_i are the components of the strain tensor $\hat{\varepsilon}$ in the Voigt notations.

The term $\propto \Lambda^{(2)}$ in Eq. (5.5) has the same form as the elastic part of the free energy of the host crystal in the harmonic approximation. It directly gives the changes of the modes' eigenfrequencies. These changes depend on temperature, as seen from Eq. (5.4). The term $\propto \Lambda^{(4)}$ taken to the first order determines the parameters $\gamma^{(\alpha_1\ldots\alpha_4)}$ of the quartic nonlinearity in H_nl.

5.3 Estimates of the coupling-induced elasticity parameters

Prior to analyzing the effects of dispersive coupling on the dynamics of low-frequency modes and comparing the effects of doping and the intrinsic nonlinearity of the host crystal, we need to estimate the magnitude of the doping-induced terms in the elastic free energy. It follows from

Eqs. (5.4) and (5.5) that the nth-order hole-induced elastic coefficients scale as

$$\|\hat{\Lambda}^{(n)}\| \sim n_{\rm h} \frac{\mathcal{D}^n}{E_{\rm kin}^{n-1}}, \qquad n \geq 2, \tag{5.6}$$

cf. Ref. [111]. Here $\mathcal{D}$ is the typical value of the deformation potential parameter of the material and

$$E_{\rm kin} = \max(k_B T, \mu). \tag{5.7}$$

is the characteristic carrier kinetic energy, which crosses over from $k_B T$ in the nondegenerate regime to μ in the strongly degenerate regime. For semiconductors, $\mathcal{D}$ is typically of the order of a few electron-volts, whereas $E_{\rm kin}$ is $\sim 10^{-2}$–10^{-1} eV in the relevant range of temperatures and hole densities. Thus $\mathcal{D}/E_{\rm kin} \gg 1$.

Even though $\mathcal{D}/E_{\rm kin}$ is large, the quadratic in $\hat{\varepsilon}$ term in $\Delta\mathcal{F}$ is small compared with the quadratic in $\hat{\varepsilon}$ term in the free energy of the host crystal. The latter term has the form $\frac{1}{2} C_{ij}^{(2)} \varepsilon_i \varepsilon_j$. The parameters of the "acoustic part" of the intrinsic linear elasticity tensor $\hat{C}^{(2)}$, including the Young modulus, are $\|\hat{C}^{(2)}\| \sim \rho v_s^2$, where ρ is the crystal density and v_s is the sound velocity. The parameter ratio that characterizes the relative magnitude of the quadratic in $\hat{\varepsilon}$ term in $\Delta\mathcal{F}$ is

$$\frac{\|\hat{\Lambda}^{(2)}\|}{\|\hat{C}^{(2)}\|} \sim \frac{n_{\rm h} \mathcal{D}^2}{E_{\rm kin} \rho v_s^2}. \tag{5.8}$$

For typical values $\mathcal{D} \sim 3$ eV, $n_{\rm h} \sim 10^{19}$ cm^{-3}, $E_{\rm kin} \sim 0.03$ eV, $\rho \sim 2.3$ g cm^{-3}, and $v_s \sim 5 \times 10^5$ cm s^{-1}, it is $\sim 10^{-2}$.

An extra small factor that affects the ratio of the hole-induced elasticity to the intrinsic one comes from the fact that the adiabatic description of the hole-vibrational coupling used in Eq, (5.5) applies to vibrations with frequencies small compared to the reciprocal hole thermalization time. If the thermalization time is $t_{\rm h} \sim 10^{-12}$ s, the wave vectors of the relevant acoustic modes are $\lesssim q_{\max} \sim (v_s t_{\rm h})^{-1} \sim 2 \times 10^6$ cm^{-1}. This value is small compared to the wave vector of thermal phonons $q_T \sim k_B T/\hbar v_s \gtrsim 3 \times 10^7$ cm^{-1} for $T > 100$ K.

In contrast to the quadratic in $\hat{\varepsilon}$ part of $\Delta\mathcal{F}$, because of the large value of $\mathcal{D}/E_{\rm kin}$, the quartic in $\hat{\varepsilon}$ terms are typically large compared to the corresponding intrinsic terms for the modes with

frequencies smaller than $1/t_{\rm h}$. This makes it important to calculate them and to find their dependence on the hole density and temperature.

5.3.1 Convergence of the free energy expansion in strain

The expansion (5.5) is justified if the terms of higher order in $\hat{\varepsilon}$ are smaller than the lower-order terms. It is convenient to compare the quartic and quadratic terms in Eq. (5.5) by comparing their thermal averages integrated over the volume. Decoupling $\langle \hat{\varepsilon} \otimes \hat{\varepsilon} \otimes \hat{\varepsilon} \otimes \hat{\varepsilon} \rangle \sim \langle \hat{\varepsilon} \otimes \hat{\varepsilon} \rangle \langle \hat{\varepsilon} \otimes \hat{\varepsilon} \rangle$, we obtain, to the order of magnitude,

$$R = \frac{\int d\boldsymbol{r} \hat{\Lambda}^{(4)} \langle \hat{\varepsilon} \otimes \hat{\varepsilon} \otimes \hat{\varepsilon} \otimes \hat{\varepsilon} \rangle}{\int d\boldsymbol{r} \hat{\Lambda}^{(2)} \langle \hat{\varepsilon} \otimes \hat{\varepsilon} \rangle} \sim V^{-1} \frac{\|\hat{\Lambda}^{(4)}\|}{\|\hat{\Lambda}^{(2)}\|^2} \int d\boldsymbol{r} \hat{\Lambda}^{(2)} \langle \hat{\varepsilon} \otimes \hat{\varepsilon} \rangle$$
$$\sim (V n_{\rm h} E_{\rm kin})^{-1} \int d\boldsymbol{r} \hat{\Lambda}^{(2)} \langle \hat{\varepsilon} \otimes \hat{\varepsilon} \rangle \,, \tag{5.9}$$

where V is the volume of the system. Thermal average of the squared strain tensor can be estimated using the standard expansion for $\hat{\varepsilon}$ in terms of normal vibrational modes, cf. [125]. For classical vibrations, $k_B T \gg \hbar v_s q_{\rm max}$, this gives

$$\int d\boldsymbol{r} \langle \hat{\varepsilon} \otimes \hat{\varepsilon} \rangle \sim \frac{k_B T V}{\pi^2 \rho v_s^2} q_{\rm max}^3.$$

In turn, for the ratio (5.9), this gives

$$R \sim \frac{\|\hat{\Lambda}^{(2)}\| k_B T}{\pi^2 \rho v_s^2 E_{\rm kin} n_{\rm h}} q_{\rm max}^3 \lesssim 10^{-3}. \tag{5.10}$$

Similar estimates can be made for higher-order terms in the expansion (5.5) of the adiabatic part of the hole-induced terms in the elastic free energy. They justify the perturbation theory in $\hat{\varepsilon}$ used to obtain Eq. (5.5).

5.4 The effect of dispersive coupling to high-frequency phonons

We now estimate the contributions to the temperature dependence of the eigenfrequencies of low-frequency eigenmodes of a mechanical resonator. They come from both intrinsic elastic properties of the crystal and the effect of p-doping. They also come from phonons with different frequencies. In this section we will separate and estimate relative magnitude of different contributions. The starting point is that, in the harmonic approximation, the squared eigenfrequency of the mode α is

determined by the sum of the linear elasticity components with and without doping,

$$\omega_\alpha^2 = M^{-1} \int d\boldsymbol{r} \left(C_{ij}^{(2)} + \Lambda_{ij}^{(2)} \right) \varepsilon_i^{(\alpha)} \varepsilon_j^{(\alpha)}. \tag{5.11}$$

In the absence of doping, the temperature dependence of eigenfrequencies comes from the intrinsic vibration nonlinearity. The free energy density of the vibrations of the host crystal has the form of the series (5.5), with $\hat{\Lambda}^{(n)}$ replaced by the intrinsic elasticity tensors $\hat{C}^{(n)}$ with $n = 2, 3, 4, ...$ The tensors $\hat{C}^{(n)}$ come from the expansion of the potential energy of the interatomic coupling in a crystal. Generally, their major components are of the same order of magnitude, at least for not too large n [126] (however, a numerical approach [127] predicted $\hat{C}^{(n)}$ with the components that increase with n, with $\|\hat{C}^{(4)}\|/\|\hat{C}^{(2)}\| \gtrsim 10$ for Si, in particular; the physical origin of this increase was not specified). For our estimate we will use $\|\hat{C}^{(2)}\| \sim \|\hat{C}^{(3)}\| \sim \|\hat{C}^{(4)}\|$.

To the second order in $\hat{C}^{(3)}$ and to the first order in $\hat{C}^{(4)}$, the linear elasticity parameters of $\hat{C}^{(2)}$ in Eq. (5.11) acquire temperature-dependent corrections $\sim (\|\hat{C}^{(3)}\|^2/\|\hat{C}^{(2)}\|) \langle \hat{\varepsilon} \otimes \hat{\varepsilon} \rangle$, $\|\hat{C}^{(4)}\| \langle \hat{\varepsilon} \otimes \hat{\varepsilon} \rangle$, cf. [88, 89, 128, 129] (see also Sec. 5.5 below). For room temperatures, these corrections are determined primarily by short-wavelength thermal phonons, as these phonons have a large density of states. The relative magnitude of the corrections is

$$\left(\frac{\|\hat{C}^{(4)}\| \langle \hat{\varepsilon} \otimes \hat{\varepsilon} \rangle}{\|\hat{C}^{(2)}\|} \right)_{\text{intrinsic}} \sim \frac{k_B T q_T^3}{\pi^2 \rho v_s^2} \lesssim 10^{-2}. \tag{5.12}$$

Here $q_T = k_B T/\hbar v_s$ is the thermal wave number. This estimate gives $|d \ln \omega_\alpha^2 / d \ln T|_{\text{intrinsic}} \sim 10^{-2}$. For silicon, in particular, such estimate agrees with the results of various studies, cf. [104, 130–132].

Because of doping, the frequency becomes temperature-dependent even in the harmonic approximation (5.11). It follows from Eqs. (5.6) – (5.8) that the temperature dependence of the doping-induced correction to the frequency in the linear-elasticity approximation is

$$\left| \frac{d \ln \omega_\alpha^2}{d \ln T} \right|_{\text{doping}} \sim \|\hat{C}^{(2)}\|^{-1} \frac{d\|\hat{\Lambda}^{(2)}\|}{d \ln T} \sim 10^{-2}\text{–}10^{-3}. \tag{5.13}$$

It is comparable to the intrinsic temperature dependence of the frequency, which explains the success of using doping to compensate the intrinsic effect.

Even though $\|\hat{\Lambda}^{(2)}\| \ll \|\hat{C}^{(2)}\|$, the estimate of the hole-induced nonlinearity (5.6) gives

$$\frac{\|\hat{\Lambda}^{(4)}\|}{\|\hat{C}^{(4)}\|} \sim \frac{n_h \mathcal{D}^4/E_{\rm kin}^3}{\rho v_s^2} \gtrsim 10^2.$$

This shows that the doping-induced nonlinearity is much stronger than the intrinsic nonlinearity of a crystalline resonator.

However, the density of states of thermal phonons admixed to low-frequency modes by the intrinsic nonlinearity is much larger than the density of states of phonons admixed by the adiabatic hole-phonon coupling. The thermal wave number $q_T = k_B T/\hbar v_s$ in the expression (5.12) for the intrinsic temperature-dependent frequency correction is much larger than the wave number $q_{\max} \sim (v_s t_{\rm h})^{-1}$. As a result, even though $\|\hat{\Lambda}^{(4)}\| \gg \|\hat{C}^{(4)}\|$ for the coupling to phonons with $q \lesssim q_{\max}$, the temperature-dependent correction to ω_α due to the doping-induced nonlinearity is much smaller than that due to the intrinsic nonlinearity. It is also much smaller than the correction to the temperature dependence from the doping-induced terms in the linear elasticity, cf. Sec. 5.8. We note that T-dependent frequency shift comes in the second order of the perturbation theory from the cubic in ε terms in the free energy. Again, for $q_T \gg q_{\max}$, the main contribution to the shift comes from the intrinsic nonlinearity of the crystal.

5.5 Phase diffusion due to dispersive coupling

Since the doping-induced nonlinear coupling between low-frequency modes is much stronger than the intrinsic coupling, to describe this coupling we can approximate the quartic nonlinearity parameters in Eq. (5.3) by keeping only the doping-induced term. The quartic-nonlinearity term has the form

$$\gamma^{(\alpha_1\alpha_2\alpha_3\alpha_4)} = \int d\boldsymbol{r}\, \Lambda^{(4)}_{ijkl} \varepsilon_i^{(\alpha_1)} \varepsilon_j^{(\alpha_2)} \varepsilon_k^{(\alpha_3)} \varepsilon_l^{(\alpha_4)}. \tag{5.14}$$

The term in the nonlinear Hamiltonian $H_{\rm nl}$, Eq. (5.3), that describes dispersive coupling of modes α and β is bi-quadratic in the mode coordinates,

$$H_{\rm nl}^{(\alpha\beta)} = \frac{1}{4}\gamma^{(\alpha\alpha\beta\beta)} Q_\alpha^2 Q_\beta^2.$$

This term leads to a frequency shift of mode α that is proportional to the squared amplitude of mode β, and vice versa. Assuming that each of these modes is sinusoidally modulated in time,

$Q_\alpha(t) = A_\alpha \cos(\omega_\alpha t + \phi_\alpha)$, we find from the equations of motion $\ddot{Q}_\alpha = -\omega_\alpha^2 Q_\alpha - M^{-1}\partial_{Q_\alpha} H_{\rm nl}$ that the dispersive frequency shifts are, respectively

$$\delta\omega_\alpha = \frac{\gamma^{(\alpha\alpha\beta\beta)}}{8M\omega_\alpha} A_\beta^2, \quad \beta \neq \alpha. \tag{5.15}$$

Equation (5.15) immediately extends to the coupling of a low-frequency mode to thermal phonons,

$$\delta\omega_\alpha = \frac{1}{8M\omega_\alpha} \sum_\varkappa \gamma^{(\alpha\alpha\varkappa\varkappa)} A_\varkappa^2, \tag{5.16}$$

where $\varkappa$ enumerates thermal phonons and $A_\varkappa$ is the vibration amplitude of phonon $\varkappa$. To describe the coupling to short-wavelength phonons, which are not adiabatically followed by the hole gas, the expression for $\hat{\gamma}$ in Eq. (5.16) should include contributions from both intrinsic and doping-induced quartic nonlinearity. This means that, in Eq. (5.14), one should replace $\hat{\Lambda}^{(4)} \to \hat{\Lambda}^{(4)} + \hat{C}^{(4)}$ (the parameters $\hat{\Lambda}^{(4)}$ and $\hat{C}^{(4)}$ are renormalized by the cubic nonlinearity parameters, in this case).

Equation (5.16) for the thermal-averaged frequency shift $\langle\delta\omega_\alpha\rangle$ describes the thermal shift of the mode frequency due to phonon nonlinearity, with $\langle A_\varkappa^2\rangle = 2k_BT/M\omega_\varkappa^2$ for thermal vibrations. Note the scaling with the volume of the system V: with the chosen normalization, $\gamma^{(\alpha\alpha\varkappa\varkappa)}$ scales as V, whereas the squared amplitude of thermal phonons $A_\varkappa^2 \propto 1/M \propto 1/V$. To allow for quantum effects, one should replace $A_\varkappa^2 \to (2\hbar/M\omega_\varkappa)\hat{n}_\varkappa$, with $\hat{n}_\varkappa$ being the occupation number operator of phonon $\varkappa$. The $T = 0$-part of the energy of nonlinearly coupled vibrations is standardly incorporated into the mode eigenfrequencies, cf. [133].

The amplitudes $A_\varkappa$ in Eq. (5.16) are random. Therefore, along with the T-dependent shift $\langle\delta\omega_\alpha\rangle$, there occur frequency fluctuations. For a mode α that performs self-sustained vibrations, it is convenient to describe the effect of these fluctuations by looking at the dispersive-coupling induced diffusion of the vibration phase ϕ_α. In turn, this comes to calculating the phase variance that accumulates over time t,

$$\langle\Delta\phi_\alpha^2(t)\rangle = \Big\langle\Big[\int_0^t dt'\big(\delta\omega_\alpha(t') - \langle\delta\omega_\alpha\rangle\big)\Big]^2\Big\rangle\,. \tag{5.17}$$

Since $\delta\omega_\alpha$ is a sum over the modes $\varkappa$, as seen from Eq. (5.16), the phase variance $\langle\Delta\phi_\alpha^2(t)\rangle$ is given by a double sum over $\varkappa, \varkappa'$. The modes $\varkappa$ and $\varkappa'$ with different $\varkappa$ and $\varkappa'$ are statistically independent. Therefore, the calculation comes to evaluating the averages

$$\begin{aligned}&\Big\langle \iint_0^t dt_1\, dt_2 [A_\varkappa^2(t_1)A_\varkappa^2(t_2) - \langle A_\varkappa^2\rangle^2]\Big\rangle \\ &= 2\int_0^t dt_1 \int_0^{t_1} dt_2\, \langle A_\varkappa^2(t_1)[A_\varkappa^2(t_2) - \langle A_\varkappa^2\rangle]\rangle\,.\end{aligned}$$

Decay of the phonon amplitudes is typically exponential [134], and given the Boltzmann distribution of the squared amplitudes, we obtain

$$\langle A_\varkappa^2(t_1)[A_\varkappa^2(t_2) - \langle A_\varkappa^2\rangle]\rangle = \langle A_\varkappa^2\rangle^2 \exp(-|t_1 - t_2|/\tau_\varkappa),$$

where $\tau_\varkappa^{-1}$ is the decay rate of mode $\varkappa$. This gives, for t much larger than the phonon relaxation times,

$$\langle\Delta\phi_\alpha^2(t)\rangle \approx 2D_\alpha^{\rm ph} t, \quad D_\alpha^{\rm ph} = \sum_\varkappa \left(\frac{\gamma^{(\alpha\alpha\varkappa\varkappa)} k_B T}{4M^2\omega_\alpha\omega_\varkappa^2}\right)^2 \tau_\varkappa. \tag{5.18}$$

The dispersive-coupling induced phase diffusion (5.18) is a mesoscopic effect. Since $M = \rho V$, whereas summation over $\varkappa$ gives only a factor $\propto V$, the diffusion coefficient $D_\alpha^{\rm ph}$ goes to zero in the thermodynamic limit $V \to \infty$. An estimate of the contribution of thermal phonons shows that it is extremely small in micromechanical systems with volumes $\gtrsim 10^{-4}$ cm^3. However, it becomes larger for nanoscale systems.

We note that, if decay of thermal phonons was disregarded and one just calculated $\langle(\delta\omega_\alpha)^2\rangle - \langle\delta\omega_\alpha\rangle^2$, one would obtain a fairly strong constraint on the frequency stability of microelectromechanical systems.

The frequency shift $\delta\omega_\alpha$ of a low-frequency mode α, as given by Eq. (5.16), becomes much larger if the mode β is excited and performs forced vibrations with amplitude A_β much larger than the typical thermal amplitude $(k_B T/M\omega_\beta^2)^{1/2}$. This is why it is interesting and important to calculate the dispersive coupling parameters.

5.5.1 Renormalization of the quartic nonlinearity parameters for low-frequency modes

Generally, the parameters $\gamma^{(\alpha_1\ldots\alpha_4)}$ are renormalized by the cubic in $\hat{\varepsilon}$ terms in the free energy density. The corresponding hole-induced contribution to these terms has the form

$$\Delta\mathcal{F}^{(3)} = \frac{1}{3!}\sum \beta^{(\alpha_1\alpha_2\alpha_3)} Q_{\alpha_1} Q_{\alpha_2} Q_{\alpha_3},$$
$$\beta^{(\alpha_1\alpha_2\alpha_3)} = \int d\boldsymbol{r}\, \Lambda^{(3)}_{ijk} \varepsilon_i^{(\alpha_1)} \varepsilon_j^{(\alpha_2)} \varepsilon_k^{(\alpha_3)}.$$

General expression for the renormalization of the parameters $\gamma^{(\alpha_1\ldots\alpha_4)}$ that define the intrinsic and hole-induced mode nonlinearity by the parameters $\beta^{(\alpha_1\ldots\alpha_3)}$ is given in Refs. [110, 135]. The change of $\|\hat{\gamma}\|$ is $\propto \|\hat{\beta}\|^2$. To obtain an estimate, we note that, for acoustic modes with typical wavelength λ, and thus with frequencies $\sim v_s/\lambda$, we have $\|\hat{\gamma}\| \sim \|\hat{\Lambda}^{(4)}\| V/\lambda^4$ and $\|\hat{\beta}\| \sim \|\hat{\Lambda}^{(3)}\| V/\lambda^3$. Then the ratio of the renormalization $\|\delta\hat{\gamma}\|$ to $\|\hat{\gamma}\|$ is

$$\frac{\|\delta\hat{\gamma}\|}{\|\hat{\gamma}\|} \sim \frac{\|\hat{\beta}\|^2}{M(v_s/\lambda)^2\|\hat{\gamma}\|} \sim \frac{\|\hat{\Lambda}^{(3)}\|^2}{\|\hat{\Lambda}^{(4)}\|\rho v_s^2} \sim \frac{n_h\mathcal{D}^2}{E_{\mathrm{kin}}\rho v_s^2} \ll 1.$$

In what follows, the renormalization $\delta\hat{\gamma}$ is disregarded. The above estimate refers to $\hat{\gamma}, \hat{\beta}$ for $\{\alpha_i\}$ enumerating long-wavelength acoustic modes, but it applies also to the torsional mode considered below.

5.6 Dispersive coupling of two low-frequency modes

We now apply the general results to dispersive coupling between the modes with wavelengths of the order of the crystal size. Numerical results will refer to thin square plates of lateral size L_s in the range $10 - 500$ μm and thickness h_s in the range $10 - 100$ μm, although the general analysis is not limited to this size range. The typical wavelengths of the modes will be $\sim L_s$. In doped micromechanical systems, such modes have frequencies much smaller than the hole relaxation/thermalization rates $1/t_{\mathrm{h}}$, and the mechanical vibrations are adiabatically followed by the holes.

The modes we consider are mesoscopic: they are described by continuum elasticity, but their frequencies are well-separated. It is convenient to scale their amplitudes A_α and introduce a dimensionless parameters $\eta_\alpha = A_\alpha/L_s$. The strength of the mode dispersive coupling is characterized

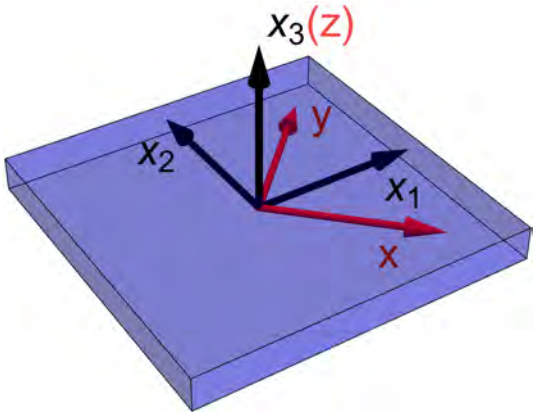


Figure 5.1 The coordinate system for a thin square plate with side length L_s and thickness h_s. For a plate cut out along the $\langle 100 \rangle$ crystalline axes, the coordinates (x_1, x_2, x_3) are parallel to the axes, as indicated by the black arrows. For a plate cut out in the plane along the $\langle 110 \rangle$ axes, the coordinates (x, y) are shown by the red arrows, while the z-coordinate is still normal to the plate and points along $\langle 100 \rangle$ axes

.

by the dimensionless parameters

$$\aleph_{\alpha\beta} = \frac{\delta\omega_\alpha}{\omega_\alpha \eta_\beta^2} \quad (\alpha \neq \beta), \quad \eta_\alpha = A_\alpha / L_s. \tag{5.19}$$

Equation (5.19) shows that, although the dispersive interaction itself is reciprocal, $\gamma^{(\alpha\alpha\beta\beta)} = \gamma^{(\beta\beta\alpha\alpha)}$, the observable fractional frequency shifts are not equal even for equal mode amplitudes. This should not be confused with the nonreciprocity in systems away from thermal equilibrium.

Of primary interest is the dependence of the dispersive coupling parameters on the temperature and hole density for different semiconducting systems. In the remainder of the chapter, we specialize the general two-mode framework to the mode pair studied in the experiment [82, 86, 87]. The clock mode α is the second Lamé mode and the mode β is the torsional mode of a square p-doped silicon plate.

5.6.1 Lamé and torsional mode profiles

We consider a thin silicon square plate of side length L_s and thickness $h_s \ll L_s$. We assume that the plate is cut out either along $\langle 100 \rangle$ or $\langle 110 \rangle$ axes. The coordinate system is shown in Fig. 5.1. Two coordinates [(x, y) or (x_1, x_2), depending on the axes orientation] lie in the midplane of the plate, whereas the third coordinate, x_3, is normal to the plate. The origin is chosen at the center of the plate.

The second Lamé mode is an isochoric in-plane mode. In the thin-plate limit, its displacement field with components (u_1, u_2, u_3) is independent of x_3 and is given by [136]

$$u_1^{(\mathrm{L})}(x_1, x_2) = \sqrt{2}\cos\left(\frac{2\pi x_1}{L_s}\right)\sin\left(\frac{2\pi x_2}{L_s}\right),$$
$$u_2^{(\mathrm{L})}(x_1, x_2) = -\sqrt{2}\sin\left(\frac{2\pi x_1}{L_s}\right)\cos\left(\frac{2\pi x_2}{L_s}\right) \tag{5.20}$$

with $u_3^{(\mathrm{L})} = 0$. This displacement field satisfies $\partial_{x_1} u_1^{(\mathrm{L})} + \partial_{x_2} u_2^{(\mathrm{L})} = 0$, so that the corresponding linear strain is traceless.

The torsional mode is described within the Kirchhoff–Love plate theory by a transverse displacement $w^{(\mathrm{T})}(x_1, x_2)$ of the midplane and the accompanying in-plane bending displacements (see also Ref. [121]),

$$u_1^{(\mathrm{T})}(x_1, x_2, x_3) = -x_3\,\partial_{x_1} w^{(\mathrm{T})}(x_1, x_2),$$
$$u_2^{(\mathrm{T})}(x_1, x_2, x_3) = -x_3\,\partial_{x_2} w^{(\mathrm{T})}(x_1, x_2),$$
$$u_3^{(\mathrm{T})}(x_1, x_2, x_3) = w^{(\mathrm{T})}(x_1, x_2). \tag{5.21}$$

For the square plate geometry considered here, the leading-order torsional mode shape may be written as [137]

$$w^{(\mathrm{T})}(x_1, x_2) = \frac{12}{\sqrt{1 + 2h_s^2/L_s^2}}\left(\frac{x_1 x_2}{L_s^2}\right). \tag{5.22}$$

With the prefactors chosen in Eqs. (5.20) and (5.22), both profiles satisfy the normalization condition

$$\frac{1}{V}\int d\boldsymbol{r}\,|\boldsymbol{u}^{(\mathrm{L})}|^2 = \frac{1}{V}\int d\boldsymbol{r}\,|\boldsymbol{u}^{(\mathrm{T})}|^2 = 1.$$

The displacement profiles for the modes are sketched in Fig. 5.2.

5.6.1.1 Mode displacement in the $\langle 100\rangle$-basis

The elastic tensor components of single-crystal silicon are conventionally expressed in the coordinate system where the axes (x, y, z) are pointing along the $\langle 100\rangle$-axes. Therefore, if the square plate is cut out so that its edges are along the $\langle 100\rangle$ directions, the strain tensor can be computed directly from the displacement fields in Eqs. (5.20) and (5.21).

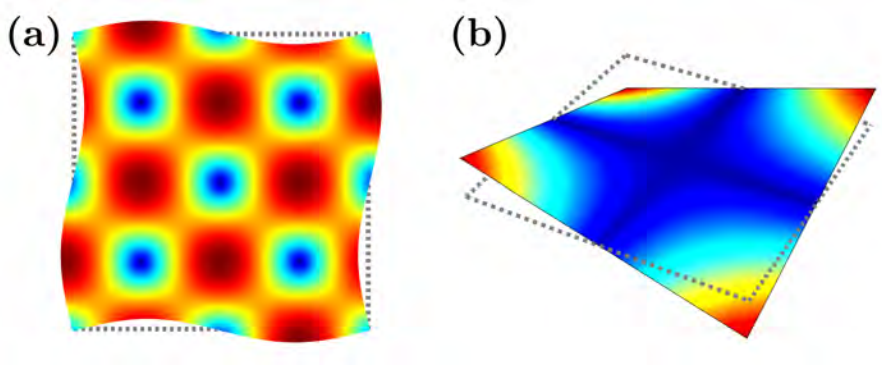


Figure 5.2 Mode profiles for (a) the in-plane second Lamé mode and (b) the considered torsional mode. The modes can be simultaneously activated in a thin square plate that is clamped through the middle points of its four sides.

For a different in-plane crystal orientation, it is convenient to rotate the displacements to the $\langle 100 \rangle$ axes. If the plate edges are aligned with the in-plane $\langle 110 \rangle$ directions, the coordinate system (x_1, x_2, x_3) has to be rotated by $\pi/4$, as shown in Fig. 5.1,

$$x_1 = \frac{x+y}{\sqrt{2}}, \quad x_2 = -\frac{x-y}{\sqrt{2}}, \quad x_3 = z.$$

Respectively, the displacement components become

$$u_x = \frac{u_1 - u_2}{\sqrt{2}}, \quad u_y = \frac{u_1 + u_2}{\sqrt{2}}, \quad u_z = u_3. \tag{5.23}$$

For both plate orientations, the strain tensor in the $\langle 100 \rangle$-axes has the form of Eq. (5.2).

5.6.2 Dispersive frequency shifts for the coupled Lamé and torsional modes

For the Lamé and torsional mode displacement fields, the overlap integrals in Eq. (5.14) can be evaluated analytically. If we disregard the much smaller intrinsic fourth-order elasticity parameters, the scaled frequency shift in Eq. (5.19) for the Lamé mode induced by the torsional mode becomes

$$\aleph_{\mathrm{LT}}^{\langle 100 \rangle} \approx \left(\frac{h_s}{L_s}\right)^2 \frac{6\Lambda_{\mathrm{LT}}}{C_{11} - C_{12}}, \tag{5.24a}$$

$$\aleph_{\mathrm{LT}}^{\langle 110 \rangle} \approx \left(\frac{h_s}{L_s}\right)^2 \frac{3\Lambda_{\mathrm{LT}}}{C_{44}}, \quad \Lambda_{\mathrm{LT}} \equiv \Lambda_{1166}^{(4)} - \Lambda_{1266}^{(4)}, \tag{5.24b}$$

where the superscript is to identify the crystal cut.. The torsional-mode shift induced by the Lamé mode is

$$\aleph_{\mathrm{TL}}^{\langle 100\rangle} = \frac{\pi^2 \Lambda_{\mathrm{LT}}}{2C_{44}}, \tag{5.25a}$$

$$\aleph_{\mathrm{TL}}^{\langle 110\rangle} = \frac{\pi^2 \Lambda_{\mathrm{LT}}}{C_{11} - C_{12}}. \tag{5.25b}$$

In these equations, $C_{ij} = C_{ij}^{(2)} + \Lambda_{ij}^{(2)}$ are the components of the full linear elasticity tensor.

Equations (5.24) and (5.25) show that the nonlinear frequency shifts of both modes are controlled by the same hole-induced dispersive-coupling coefficient Λ_{LT}. The shift magnitudes differ because this coefficient is divided by different mode stiffness. In the thin-plate limit, the shift of the Lamé mode frequency is suppressed by the factor $(h_s/L_s)^2$, which reflects the different geometries of the modes. This gives partial protection of the Lamé mode against vibrations of the torsional mode. At the same time, the torsional mode frequency is responsive to vibrations of the Lamé mode. Note, however, that we scale the torsional mode amplitude by the plate length, not thickness.

To realize a highly stable clock, it is important to understand the magnitude and the dependence of the dispersive shift of the both modes on temperature and hole density. They are determined by the coupling parameter Λ_{LT}.

5.7 Three-band model and numerical procedure

To determine the temperature and hole-density dependence of the dispersive mode frequency shifts, we use the same microscopic model, material parameters, and numerical procedure as in Ref. [111], generalized from the single-mode self-Kerr problem to the problem of the Lamé–torsional quartic coupling. We treat the valence-band holes within the full three-band Luttinger–Kohn–Bir–Pikus framework appropriate for p-doped silicon, where the relatively small spin-orbit splitting makes the split-off band relevant in the temperature and density range of interest. The hole Hamiltonian is written as

$$H_{\mathrm{h}}(\boldsymbol{k}, \hat{\varepsilon}) = H_{\mathrm{LK}}(\boldsymbol{k}) + H_{\mathrm{BP}}(\hat{\varepsilon}), \tag{5.26}$$

where H_{LK} describes the heavy-hole, light-hole, and split-off valence bands in the absence of strain, and H_{BP} is the Bir–Pikus strain Hamiltonian, which is linear in the strain tensor. The explicit

expressions for H_{LK} and H_{BP} can be found in the literature; see, e.g., Refs. [122–124]. We assume the strain to be a smooth function of coordinates. Therefore, for each wave vector $\boldsymbol{k}$, we locally diagonalize the full Hamiltonian, Eq. (5.26), and find three doubly degenerate strain-dependent branches $E_\nu(\boldsymbol{k}, \hat{\varepsilon})$, with $\nu = \{\mathrm{hh}, \mathrm{lh}, \mathrm{so}\}$ corresponding to heavy-hole, light-hole, and split-off bands, respectively.

The diagonalization gives a strain-dependent hole energy. For the temperatures and hole densities of interest, the dominant contribution to the grand canonical potential Ω comes from the wave vectors $\boldsymbol{k}$ where the strain-induced correction to the energy is small. Therefore, we expand the energy in a series in $\hat{\varepsilon}$ as

$$E_\nu(\boldsymbol{k}, \hat{\varepsilon}) = E_\nu^{(0)} + \sum_{n=1} E_\nu^{(n)}(\boldsymbol{k}, \hat{\varepsilon}), \tag{5.27}$$

where the terms $E_\nu^{(n)}$ are proportional to the convolutions of n tensors $\hat{\varepsilon}$, that is, to $\|\hat{\varepsilon}\|^n$.

For each value of the control parameters T and n_{h}, the chemical potential μ is determined from the condition that the total hole density remains equal to the prescribed value $n_{\mathrm{h}} = -\partial\Omega/\partial\mu$. Therefore μ is also strain-dependent. Similarly to $E_\nu(\boldsymbol{k}, \hat{\varepsilon})$ this dependence can be described by a series in $\hat{\varepsilon}$,

$$\mu = \mu^{(0)} + \mathcal{M}_i^{(1)}\varepsilon_i + \frac{1}{2}\mathcal{M}_{ij}^{(2)}\varepsilon_i\varepsilon_j + \cdots, \tag{5.28}$$

where $\mu^{(0)}$ is the chemical potential in the absence of strain.

The hole contribution to the elastic part of the free energy density $\Delta\mathcal{F}$ is then obtained order by order by expanding Ω in Eq. (5.4) using Eqs. (5.27) and (5.28). This gives the tensors $\hat{\Lambda}^{(2)}$ and $\hat{\Lambda}^{(4)}$ in terms of $E_\nu^{(n)}$. The explicit expressions are cumbersome, cf. Ref. [111]. The only change relative to the self-Kerr calculation of Ref. [111] is that we retain the quartic in $\hat{\varepsilon}$ terms associated with the combined strain field in Eq. (5.2) rather than the pure quartic term of a single mode. In particular, we calculate the quantity that enters the closed-form expressions for the shifts of Sec. 5.6, $\Lambda_{\mathrm{LT}} = \Lambda_{1166}^{(4)} - \Lambda_{1266}^{(4)}$, which gives the factor multiplying the product of the squared coordinates of the considered modes $Q_{\mathrm{L}}^2 Q_{\mathrm{T}}^2$ in the free energy.

Following the approach of Ref. [111], the integration over $\boldsymbol{k}$ in Eq. (5.4) and in the free-energy expansion is replaced by a summation over a uniform three-dimensional mesh in $\boldsymbol{k}$ space for each value of $\hat{\varepsilon}$, i.e., locally for each $\boldsymbol{r}$, which is appropriate given that the wavelengths of the modes of interest are much larger than the hole mean free path. Because the integrands decay exponentially at large $|\boldsymbol{k}|$, the integration domain can be truncated; convergence with respect to both the cutoff and the mesh spacing is checked.

For each mesh point, we diagonalize Eq. (5.26) for a discrete set of strain values determined by the mode pattern. To obtain $E_v^{(n)}$ in Eq. (5.27), the resulting band energies are then expanded in the strain using standard finite-difference formulas. These procedures give the same results as a direct perturbation theory, to high accuracy. They allow one to extract the strain expansion of the free energy efficiently without the need of high-order perturbation theory calculations of the eigenvectors.

Once the tensors $\hat{\Lambda}^{(2)}$ and $\hat{\Lambda}^{(4)}$ are calculated, the results are combined with the analytic mode profiles of Sec. 5.6 to evaluate the change of the mode frequencies ω_α, the Duffing (self-Kerr) nonlinearity coefficients $\gamma^{(\alpha\alpha\alpha\alpha)}$, and the dispersive coupling coefficient $\gamma^{(\alpha\alpha\beta\beta)}$. All silicon band and deformation potential parameters are taken from Ref. [124], while the temperature dependence of the elastic constants for pure silicon is taken from the data in Ref. [131]. This choice of parameters has been shown to be in excellent agreement with the experimental data on the temperature dependence of the first Lamé eigenmode of a silicon plate and with the extension eigenmode of a silicon beam, see Ref. [111]. For the results presented below, we use the aspect ratio $h_s/L_s = 0.1$, as in the experiment [82]. We also consider the temperature and hole density range where the acceptors are fully ionized, so that n_h is a temperature-independent parameter.

5.8 Temperature and density dependence of the dispersive frequency shifts

We first show in Fig. 5.3 the temperature dependence of the frequencies of the second Lamé and torsional modes. The results refer to a square p-doped silicon plate. The temperature dependence of the eigenfrequencies of the both modes is strongly reduced compared to the undoped case. For the hole density $n_\mathrm{h} = 10^{20}$ cm^{-3}, the Lamé mode frequency becomes almost fully independent

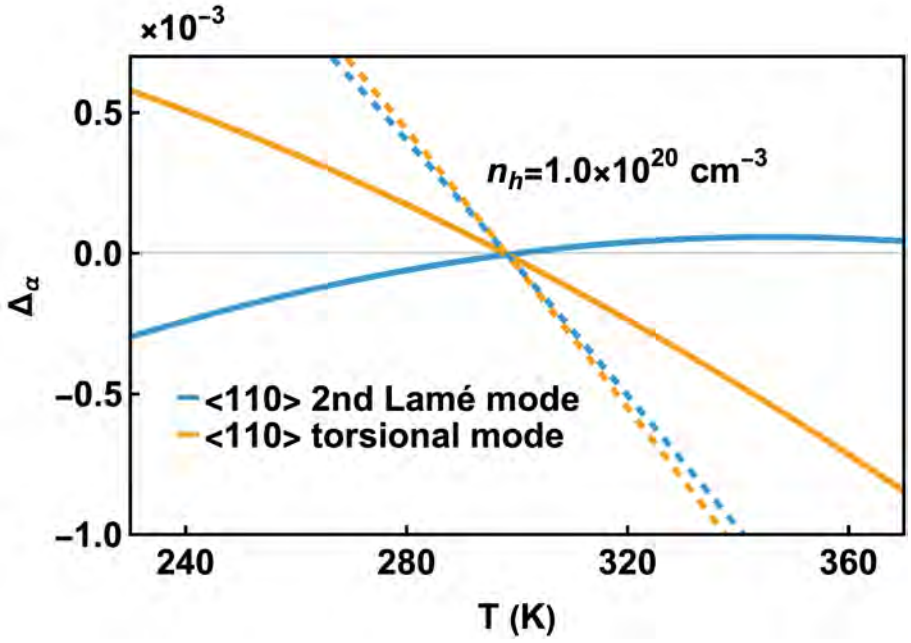


Figure 5.3 Temperature dependence of the eigenfrequencies of the second Lamé and torsional modes, $\Delta_\alpha = [\omega_\alpha(T) - \omega_\alpha(T_0)]/\omega_\alpha(T_0)$ for a plate cut out along the $\langle 110 \rangle$ axes. The ratio of the thickness to later side of the plate is $h_s/L_s = 0.1$. We set $T_0 = 298$ K. Solid lines show the temperature dependence in the presence of doping, whereas the results for undoped crystals are shown by dashed lines.

of temperature in a broad temperature range above 300 K. In contrast, the eigenfrequency of the torsional mode remains strongly temperature-dependent. This underlies the possibility of using this mode as a "thermometer" in doped MEMS.

We now present results on the hole-mediated dispersive frequency shifts $\aleph_{\alpha\beta}$, Eqs. (5.24) and (5.25), for the Lamé and torsional modes of the same system. The main qualitative features of the numerical results can be understood from the analytic expressions (5.24) and (5.25). For both modes, the shifts are controlled by the same hole-induced fourth-order elastic coefficient $\Lambda_{\rm LT}$. Therefore the dependencies of $\aleph_{\rm TL}$ and $\aleph_{\rm LT}$ on temperature are similar. They can be inferred from the estimate (5.6) of $\hat{\Lambda}^{(4)}$. In the nondegenerate regime, i.e., for high temperature, the hole kinetic energy is $E_{\rm kin} \sim k_B T$, while in the degenerate regime $E_{\rm kin} = \mu$. Consequently, $\|\hat{\Lambda}^{(4)}\|$, and in particular $\Lambda_{\rm LT}$, decrease with the increasing temperature in the nondegenerate regime. However, $\|\hat{\Lambda}^{(4)}\|$ can become nonmonotonic as a function of temperature close to degeneracy, since the chemical potential of a degenerate gas decreases with the increasing temperature.

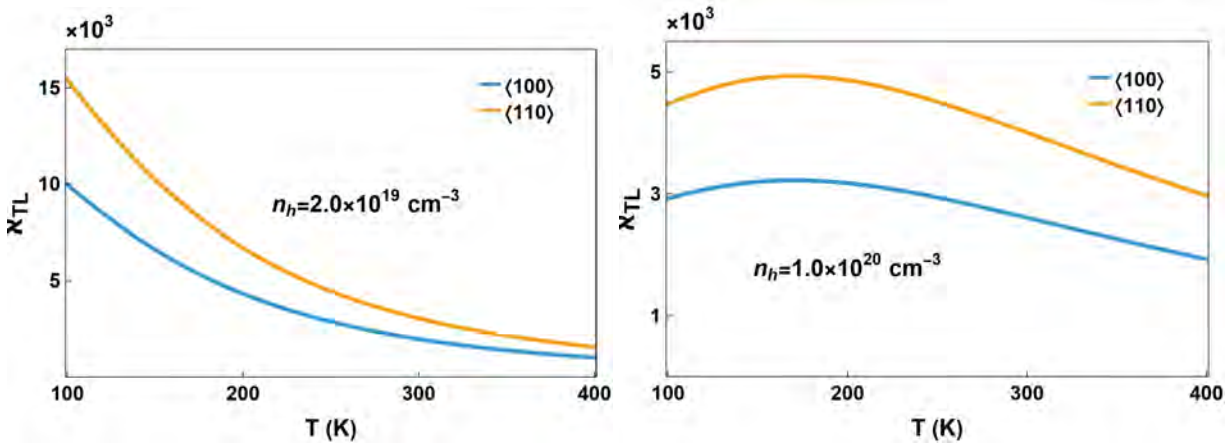


Figure 5.4 Temperature dependence of the dispersive frequency shift $\aleph_{\mathrm{TL}}$ of the torsional mode scaled by the squared amplitude of the second Lamé mode sketched in Fig. 5.2. The parameter $\aleph_{\mathrm{TL}}$ is defined in Eq. (5.25). The results refer to a square single-crystal silicon plate with the ratio of the thickness to length $h_s/L_s = 0.1$. The panels show the results for the crystal orientations $\langle 100\rangle$ and $\langle 110\rangle$. The left and right panels refer to the hole density $n_{\mathrm{h}} = 2.0 \times 10^{19}$ cm^{-3} and $n_{\mathrm{h}} = 1.0 \times 10^{20}$ cm^{-3}, respectively.

If the temperature is fixed, increasing n_{h} from small values increases the hole-induced nonlinearity, because more holes are coupled to the modes. However, at sufficiently high densities, the hole gas becomes degenerate and the increasing chemical potential suppresses the nonlinear response. For the quartic-nonlinearity parameters we have $\|\hat{\Lambda}^{(4)}\| \propto n_{\mathrm{h}}/\mu^3 \propto n_{\mathrm{h}}^{-1}$ in the strongly degenerate limit. This leads to a nonmonotonic density dependence of Λ_{LT} and ultimately of $\aleph_{\mathrm{LT}}$ and $\aleph_{\mathrm{TL}}$.

5.8.1 Dispersive frequency shifts for fixed hole density

Figure 5.4 shows the temperature dependence of the shift of the torsional mode frequency induced by the Lamé mode. At low hole density, $n_{\mathrm{h}} = 2 \times 10^{19}$ cm^{-3}, the scaled shift decreases monotonically with the increasing temperature, consistent with the estimate $\|\hat{\Lambda}^{(4)}\| \propto n_{\mathrm{h}}/(k_B T)^3$ for a nondegenerate hole gas. Physically, thermal motion broadens the hole distribution, resulting in a reduced sensitivity to the strain-induced change of the hole energy bands.

At higher densities, $n_{\mathrm{h}} = 1 \times 10^{20}$ cm^{-3}, the temperature dependence becomes nonmonotonic. In this regime, the hole gas is degenerate at low temperature. Since $\mu = E_{\mathrm{kin}}$ decreases with the increasing temperature, Λ_{LT} initially increases with the increasing T, as seen from Eq. (5.6). As the gas becomes nondegenerate for higher T, Λ_{LT} start decreasing. As a result, $\aleph_{\mathrm{TL}} \propto \Lambda_{\mathrm{LT}}$ displays a

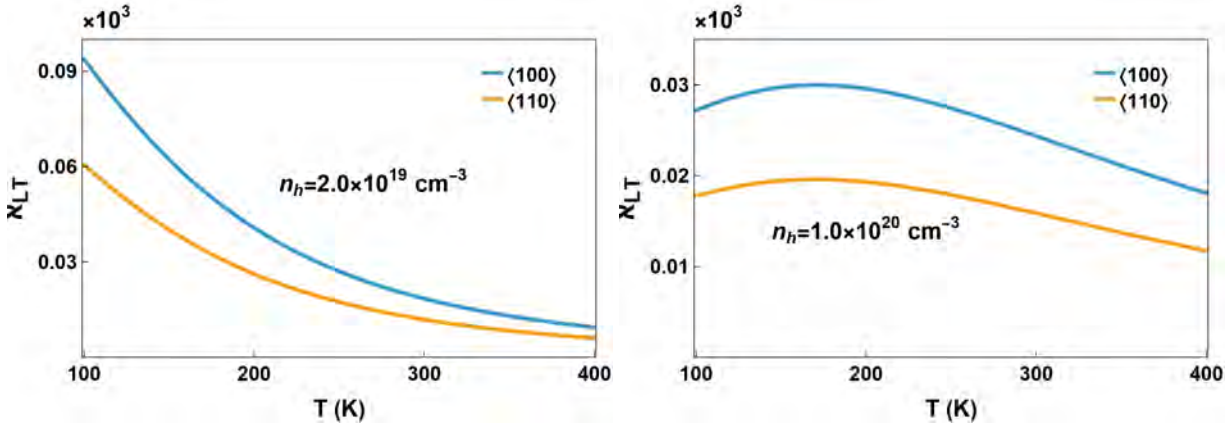


Figure 5.5 Temperature dependence of the dispersive frequency shift $\aleph_{\mathrm{LT}}$ of the second Lamé mode scaled by the squared amplitude of the torsional mode. The modes are sketched in Fig. 5.2. The parameter $\aleph_{\mathrm{LT}}$ is defined in Eq. (5.24). The plots refer to a square single-crystal silicon plate with the ratio of the thickness to length $h_s/L_s = 0.1$. The panels show the results for the crystal orientations $\langle 100\rangle$ and $\langle 110\rangle$. The left and right panels refer to the hole density $n_{\mathrm{h}} = 2.0 \times 10^{19}$ cm^{-3} and $n_{\mathrm{h}} = 1.0 \times 10^{20}$ cm^{-3}, respectively.

maximum as a function of T. The magnitude of $\aleph_{\mathrm{TL}}$ is large, reaching values $\gtrsim 10^3$ in the considered parameter range. This indicates strong sensitivity of the torsional mode to the Lamé mode amplitude.

The frequency shift for the studied Lamé mode is shown in Fig. 5.5. Its temperature dependence follows the same trends as in the case of the torsional mode. However, $\aleph_{\mathrm{LT}}$ is smaller than $\aleph_{\mathrm{TL}}$ roughly by two orders of magnitude. This has a geometric origin, as seen from Eq. (5.24): the factor $(h_s/L_s)^2$ in this equation is 0.01 for the considered geometry. The torsional mode strain is odd in the direction normal to the plate, and its contribution to the Lamé mode frequency shift is small, for a thin-plate limit.

5.8.2 Density dependence at fixed temperature

Figure 5.6 shows the density dependence of the dispersive frequency shifts at $T = 300$ K for the torsional and second Lamé modes. Both modes exhibit a strongly nonmonotonic dependence on the hole density n_{h} for both crystal orientations we studied. The overall behavior is in agreement with what is expected from the qualitative arguments presented above. At low density, where the hole gas is nondegenerate, the shifts grow proportional to the hole density. At large density, they

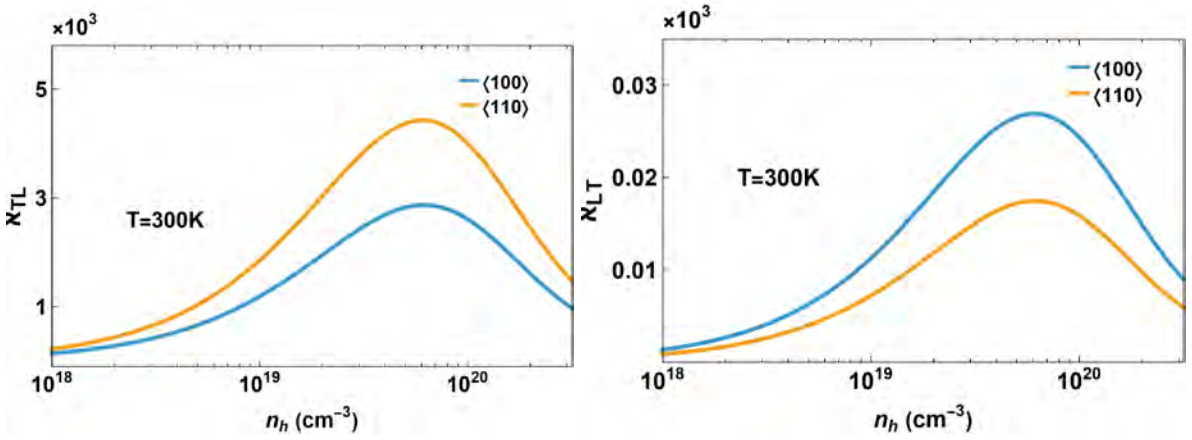


Figure 5.6 Density dependence of the scaled dispersive nonlinear frequency shifts of the torsional (left panel) and the second Lamé (right panel) modes sketched in n Fig. 5.2. The shifts are defined in Eqs. (5.25) and (5.24), respectively. The plots refer to two crystalline orientations of a square single-crystal silicon plate with the ratio of the thickness to length $h_s/L_s = 0.1$. The temperature is $T = 300$ K.

fall off as $n_{\rm h}^{-1}$, asymptotically. The maxima in Fig. 5.6 therefore mark the crossover between the nondegenerate and degenerate regimes. We observed the nonmonotonic behavior for all relevant temperatures. The peak moves toward smaller density as temperature decreases, indicating stronger degeneracy-induced suppression of the dispersive frequency shift.

5.8.3 Effect of the crystal orientation

Figures 5.4 – 5.6 show the opposite effect of the nonlinear coupling on the studied two modes: $\aleph_{\rm LT}$ is larger for the crystal orientation $\langle 100\rangle$ than for the orientation $\langle 110\rangle$, opposite to the dependence of $\aleph_{\rm TL}$ on the crystal orientation. This is a consequence of the difference between the elasticity components $C_{11} - C_{12}$ and C_{44} in Eqs. (5.24) and (5.25) which, in turn, is due to the different structure of the strain. For a plate whose edges are aligned with the $\langle 100\rangle$ axes, in the crystallographic frame, the non-zero strain elements for the Lamé mode are $\varepsilon_{xx}^{(\rm L)}$ and $\varepsilon_{yy}^{(\rm L)} = -\varepsilon_{xx}^{(\rm L)}$, whereas the non-zero strain element for the torsional mode is $\varepsilon_{xy}^{(\rm T)}$. In the plate cut along the $\langle 110\rangle$ directions, the strain components are effectively interchanged: $\varepsilon_{xx} - \varepsilon_{yy}$ goes over into shear strain component $2\varepsilon_{xy}$ and vice versa.

The orientation dependence has direct implications for dual-mode frequency references. By choosing the plate cut, one can reduce the sensitivity of the frequencies of the torsional and Lamé

modes to the vibration amplitudes of the Lamé and torsional modes, respectively.

5.9 Conclusion

This chappter explores the effect of p-type doping of semiconductor micromechanical resonators on the dispersive coupling of their vibrational eigenmodes. We show that doping makes this coupling much stronger than in undoped crystals. This provides an important means of controlling frequencies of one modes by driving other modes. Detailed numerical results refer to a system extensively studied in the experiment, a thin Si plate. Both analytical and numerical results demonstrate that the coupling displays a nonmonotonic dependence on the hole density and, for not too low densities, on the temperature.

The numerical data refers to the coupling of the second Lamé mode and the torsional mode with compatible clamping in a Si plate. This system has a record-high frequency stability [87]. The primary goal of doping in clock applications is to reduce the temperature dependence of the frequency of the mode that has to be stable and is called a clock mode. Usually this is a Lamé mode. The torsional mode is used as a "thermometer", as its frequency is much more sensitive to the temperature variations in the presence of doping. We show that, even though this sensitivity is reduced by doping, it remains sufficiently high in the relevant range of acceptor densities and temperatures. This is in spite of the temperature dependence of the Lamé mode frequency being fully compensated in a broad temperature range.

Besides a comparatively strong coupling of low-frequency eigenmodes of a resonator to each other, doping leads to three-wave and four-wave processes in which there participate both low-frequency eigenmodes and short-wavelength phonons of the crystal, including dispersive coupling to short-wavelenth phonons. Such doping-induced processses are effectively limited to the phonons with frequencies small compared to the hole relaxation/thermalization rate. For such phonons, it is stronger than the intrinsic coupling in the host crystal. Still its effect on the eigenfrequencies of low-frequency modes and their temperature dependence is small in a broad temperature range centered at room temperatures. This is because the intrinsic nonlinearity couples low-frequency modes to phonons with thermal wavelengths, which have a much higher density of states than the

phonons with frequencies limited by the hole relaxation rate.

An important mesoscopic effect is fluctuations of the eigenfrequencies of low-frequency modes. Because of thermal fluctuations of the amplitudes (occupation numbers) of high-frequency phonons, dispersive coupling to such phonons leads to fluctuations of the frequencies of low-frequency modes. As we show, these fluctuations lead to a very slow phase diffusion in micromechanical systems. However, they may become important for nanoscale systems.

We note in conclusion that, besides changing the elasticity parameters, doping affects the decay rates of low-frequency eigenmodes in micro- and nano-mechanical resonators. A major decay mechanism of such modes in a broad temperature range is the Akhiezer relaxation. Typically, the frequencies ω_α of the low-frequency modes are small compared to the decay rates of thermal phonons $\Gamma_{\rm ph}$. Then the Akhiezer relaxation rate is $\propto \omega_\alpha/\Gamma_{\rm ph}$. This suggests [111] that, increasing doping, and thus increasing $\Gamma_{\rm ph}$, may unexpectedly lower the Akhiezer damping rate. It would be interesting to explore this effect in the experiment.

CHAPTER 6

HIGH-FREQUENCY NONLINEAR CONDUCTIVITY OF A WIGNER CRYSTAL

Electrons bound above the surface of liquid helium provide an exceptionally clean realization of a two-dimensional electron system. Their motion perpendicular to the surface is quantized, whereas their motion parallel to an ideally flat surface is free. At sufficiently low temperature, the Coulomb interaction between the electrons becomes much larger than their thermal kinetic energy, and the electrons form a two-dimensional Wigner crystal. The helium surface is not merely a passive substrate: the electrons exert a normal force on the liquid and couple to capillary surface waves, or ripplons. When the electron system is crystalline, this coupling becomes coherent at reciprocal-lattice wave vectors and gives rise to strongly nonlinear Bragg–Cherenkov transport.

This chapter first introduces the surface-bound electron states, the classical Wigner crystal, and the ripplon modes of the helium surface. We then review the quasistatic Bragg–Cherenkov effect and the origin of the associated nonlinear conductivity. The final section turns to the high-frequency regime studied in this dissertation.

6.1 Electrons, Wigner crystallization, and ripplons on liquid helium

6.1.1 Image-potential confinement and the effective two-dimensional system

Let the equilibrium helium surface lie in the plane $\zeta = 0$, with $\zeta > 0$ denoting the vacuum above the liquid. Liquid ^{4}He has a dielectric constant only slightly larger than unity, $\varepsilon_{\mathrm{He}} \simeq 1.057$. An electron of charge $-e$ located a distance ζ above the surface polarizes the helium. In the vacuum region, the resulting electrostatic potential can be represented by an image charge of opposite sign,

$$q_{\mathrm{im}} = e\alpha_{\mathrm{He}}, \qquad \alpha_{\mathrm{He}} = \frac{\varepsilon_{\mathrm{He}} - 1}{\varepsilon_{\mathrm{He}} + 1}. \tag{6.1}$$

The corresponding image potential is

$$V_{\mathrm{im}}(\zeta) = -\frac{\Lambda}{\zeta}, \qquad \Lambda = \frac{\alpha_{\mathrm{He}} e^2}{16\pi\epsilon_0}. \tag{6.2}$$

The image potential attracts the electron toward the helium surface. Low-energy electrons cannot penetrate the liquid because helium atoms have closed $1s^2$ electronic shells. As the external

electron approaches the surface and its wave function begins to overlap with those of the helium electrons, the Pauli exclusion principle produces a strong short-range repulsive barrier. This barrier is of order an electron volt, which is much larger than the other electron energy scales considered here. The electron therefore remains on the vacuum side of the surface [138–140].

An electric field is commonly applied perpendicular to the surface. We take $E_\perp > 0$ to denote the magnitude of the field that presses an electron toward the helium. The potential energy of the electron then increases as it moves away from the surface. A simple model for the vertical potential is

$$V_\perp(\zeta) = \begin{cases} V_0, & \zeta < 0, \\ -\dfrac{\Lambda}{\zeta} + eE_\perp\zeta, & \zeta > 0, \end{cases} \tag{6.3}$$

where V_0 represents the short-range helium barrier. In the limit $V_0 \to \infty$, the vertical wave function satisfies $\psi_n(0) = 0$, and the corresponding Schrödinger equation is

$$\left[-\frac{\hbar^2}{2m_e}\frac{d^2}{d\zeta^2} - \frac{\Lambda}{\zeta} + eE_\perp\zeta\right]\psi_n(\zeta) = E_n^\perp\psi_n(\zeta). \tag{6.4}$$

Thus, the electron occupies quantized image-potential states outside the liquid rather than being chemically bound to the helium.

For $E_\perp = 0$ and an infinitely high barrier, the vertical problem is equivalent to the radial Schrödinger equation for the hydrogenic s states. It is useful to introduce the effective Bohr radius and Rydberg energy

$$r_B = \frac{\hbar^2}{m_e\Lambda} = \frac{4a_0}{\alpha_{\mathrm{He}}}, \qquad R = \frac{m_e\Lambda^2}{2\hbar^2} = \frac{\hbar^2}{2m_e r_B^2}. \tag{6.5}$$

The vertical energy levels are then

$$E_n^\perp = -\frac{R}{n^2}, \qquad n = 1, 2, \ldots, \tag{6.6}$$

and the transition energy from the ground state is

$$\Delta_{1n} = E_n^\perp - E_1^\perp = R\left(1 - \frac{1}{n^2}\right). \tag{6.7}$$

For liquid ^{4}He, the hydrogenic approximation gives approximately

$$r_B \simeq 7.6\,\mathrm{nm}, \qquad \frac{R}{k_B} \simeq 7.6\,\mathrm{K}, \qquad \frac{R}{h} \simeq 158\,\mathrm{GHz}. \tag{6.8}$$

The mean height of an electron in the ground vertical state is therefore $\langle\zeta\rangle_1 \simeq 11.5\,\mathrm{nm}$. The first two vertical transition energies are approximately $\Delta_{12} \simeq 0.491\,\mathrm{meV} = k_B(5.7\,\mathrm{K}) = h(118\,\mathrm{GHz})$, and $\Delta_{13} \simeq 0.577\,\mathrm{meV} = k_B(6.7\,\mathrm{K}) = h(140\,\mathrm{GHz})$. Direct spectroscopy of electrons above liquid helium gave the zero-field transition energies $\Delta_{12}^{\mathrm{exp}} \simeq 0.521\,\mathrm{meV}$ and $\Delta_{13}^{\mathrm{exp}} \simeq 0.615\,\mathrm{meV}$. The difference between the simple hydrogenic estimates and the measured values reflects the finite helium barrier, the microscopic position of the effective image plane, and other short-distance corrections to the ideal $-\Lambda/\zeta$ potential [140, 141].

At the sub-kelvin temperatures relevant to Wigner crystallization, the vertical excited states are nearly empty. In thermal equilibrium, $P_n/P_1 \simeq \exp\left[-\frac{\Delta_{1n}}{k_B T}\right]$. For example, using $\Delta_{12}/k_B \simeq 6\,\mathrm{K}$,

$$\begin{aligned} \frac{P_2}{P_1} &\sim 2.5\times10^{-3} \qquad \text{at} \quad T = 1\,\mathrm{K}, \\ \frac{P_2}{P_1} &\sim 6\times10^{-6} \qquad \text{at} \quad T = 0.5\,\mathrm{K}. \end{aligned} \tag{6.9}$$

Thus, throughout the temperature range in which the electron solid is usually studied, the electron motion normal to the surface is frozen almost completely into the lowest image-potential subband.

A single-electron wave function and its corresponding energy can consequently be factorized as

$$\Psi_{\mathbf{p}}(\mathbf{r},\zeta) = \frac{1}{\sqrt{\mathcal{A}}} e^{i\mathbf{p}\cdot\mathbf{r}/\hbar}\psi_1(\zeta), \qquad E_{\mathbf{p}} = E_1^{\perp} + \frac{p^2}{2m_e}, \tag{6.10}$$

where $\mathbf{r} = (x, y)$ is the in-plane coordinate and $\mathcal{A}$ is the surface area. The electrons therefore form an effective two-dimensional system.

For N electrons, the projected in-plane Hamiltonian is

$$H_{\mathrm{2D}} = \sum_{j=1}^{N}\left[\frac{\mathbf{p}_j^2}{2m_e} + U_{\mathrm{conf}}(\mathbf{r}_j)\right] + \frac{1}{2}\sum_{i\neq j} V_{\mathrm{eff}}\left(|\mathbf{r}_i - \mathbf{r}_j|\right), \tag{6.11}$$

where U_{conf} is the electrostatic confinement produced by external electrodes. At distances much larger than the vertical extent of the wave function, the effective interaction is

$$V_{\mathrm{eff}}(r) \simeq \frac{e^2}{4\pi\epsilon_0\kappa r}, \qquad \kappa = \frac{1+\varepsilon_{\mathrm{He}}}{2} \simeq 1.03. \tag{6.12}$$

The interaction is therefore very close to the bare Coulomb interaction in vacuum.

The system is exceptionally clean as the electrons reside in vacuum rather than in a crystalline host. They are not exposed to substitutional impurities or an atomic-scale lattice potential, and their density and confinement are controlled electrostatically [138, 139, 142]. For the densities used in the original crystallization experiments, $3 \times 10^8\,\mathrm{cm}^{-2} \lesssim n_s \lesssim 9 \times 10^8\,\mathrm{cm}^{-2}$, the typical in-plane separation is several hundred nanometers, much larger than the vertical ground-state extent [143].

6.1.2 Classical Wigner crystallization

Wigner crystallization occurs when the Coulomb interaction dominates the motion that tends to delocalize the electrons [144]. For an areal density n_s, define the two-dimensional Wigner–Seitz radius $a_W = (\pi n_s)^{-1/2}$. The characteristic Coulomb energy is

$$E_C = \frac{e^2}{4\pi\epsilon_0\kappa a_W} = \frac{e^2}{4\pi\epsilon_0\kappa}\sqrt{\pi n_s}. \tag{6.13}$$

The conventional Wigner-crystal experiments on helium are in the non-degenerate regime. The Fermi temperature of a spin-unpolarized two-dimensional electron gas is

$$T_F = \frac{\pi\hbar^2 n_s}{m_e k_B}. \tag{6.14}$$

For the density range quoted above, $T_F \simeq 8$–$25\,\mathrm{mK}$, which is much smaller than the observed crystallization temperatures of several tenths of a kelvin. The relevant competition is therefore between the Coulomb energy and thermal motion rather than between the Coulomb energy and the zero-temperature Fermi energy. The classical coupling parameter is

$$\Gamma = \frac{E_C}{k_B T} = \frac{e^2\sqrt{\pi n_s}}{4\pi\epsilon_0\kappa k_B T}. \tag{6.15}$$

The system is a weakly correlated liquid for $\Gamma \ll 1$ and becomes strongly correlated as Γ increases. Classical Monte Carlo calculations give a melting coupling of approximately $\Gamma_m \simeq 125 \pm 15$, while the original experiment found $\Gamma_m^{\mathrm{exp}} = 137 \pm 15$ [143, 145]. The corresponding melting line is

$$T_m(n_s) = \frac{e^2\sqrt{\pi n_s}}{4\pi\epsilon_0\kappa k_B \Gamma_m}. \tag{6.16}$$

For the experimental density range, this gives $0.36\,\mathrm{K} \lesssim T_m \lesssim 0.63\,\mathrm{K}$, in close agreement with experiment.

For an isotropic repulsive interaction, the lowest-energy two-dimensional Bravais lattice is triangular. A convenient choice of primitive lattice vectors is

$$\mathbf{a}_1 = a(1,0), \qquad \mathbf{a}_2 = a\left(\frac{1}{2}, \frac{\sqrt{3}}{2}\right). \tag{6.17}$$

The area per electron is $n_s^{-1} = |\mathbf{a}_1 \times \mathbf{a}_2| = \sqrt{3}a^2/2$, and therefore the nearest-neighbor spacing is $a = \sqrt{\frac{2}{\sqrt{3}}} n_s^{-1/2}$. For the density range quoted above, $0.36\,\mu\mathrm{m} \lesssim a \lesssim 0.62\,\mu\mathrm{m}$. One possible choice of reciprocal-lattice vectors is

$$\mathbf{b}_1 = \frac{2\pi}{a}\left(1, -\frac{1}{\sqrt{3}}\right), \qquad \mathbf{b}_2 = \frac{2\pi}{a}\left(0, \frac{2}{\sqrt{3}}\right). \tag{6.18}$$

The six shortest nonzero reciprocal-lattice vectors have magnitude

$$G_1 = \frac{4\pi}{\sqrt{3}a} = \left(\frac{8\pi^2 n_s}{\sqrt{3}}\right)^{1/2}. \tag{6.19}$$

The crystalline order is characterized by the microscopic density amplitude and the static structure factor

$$\rho_{\mathbf{q}} = \sum_{j=1}^{N} e^{-i\mathbf{q}\cdot\mathbf{r}_j}, \qquad S(\mathbf{q}) = \frac{1}{N}\left\langle \rho_{\mathbf{q}} \rho_{-\mathbf{q}} \right\rangle. \tag{6.20}$$

In a liquid, $S(\mathbf{q})$ contains broad correlation peaks. In the ordered phase, it develops sharp features near reciprocal-lattice vectors $\mathbf{q} = \mathbf{G}$. These reciprocal-lattice components are the essential ingredient in Bragg–Cherenkov transport.

Strictly speaking, thermal displacement fluctuations in an infinite two-dimensional crystal reduce true long-range translational order to algebraically decaying quasi-long-range order [146, 147]. In the finite experimental systems considered here, the low-temperature phase nevertheless displays sharp Bragg coherence and is conventionally referred to as a Wigner crystal or Wigner solid.

6.1.3 Ripplons and the response of the helium surface

We now introduce the helium-surface excitations to which the electron system couples. Let $\xi(\mathbf{r}, t)$ denote the surface displacement, taken to be positive downward. We assume that the helium

is incompressible and that its flow is irrotational. The fluid velocity can then be expressed through a velocity potential,

$$\mathbf{u}_{\mathrm{He}} = \boldsymbol{\nabla}\Phi, \qquad \nabla^2\Phi = 0. \tag{6.21}$$

We use the Fourier convention

$$f(\mathbf{r},t) = \int_{\mathbf{q}} f_{\mathbf{q}}(t) e^{i\mathbf{q}\cdot\mathbf{r}}, \qquad \int_{\mathbf{q}} \equiv \int \frac{d^2q}{(2\pi)^2}. \tag{6.22}$$

Take the downward vertical coordinate inside the liquid to run from $z = 0$ at the equilibrium surface to $z = h$ at the bottom. The no-flow condition at the bottom and the linearized kinematic boundary condition at the surface are

$$\partial_z\Phi|_{z=h} = 0, \qquad \partial_z\Phi|_{z=0} = \dot{\xi}(\mathbf{r},t). \tag{6.23}$$

For a surface Fourier component of wave vector $\mathbf{q}$, the solution is

$$\Phi_{\mathbf{q}}(z,t) = -\frac{\dot{\xi}_{\mathbf{q}}(t)}{q\sinh(qh)}\cosh[q(h-z)]. \tag{6.24}$$

Substitution into the helium kinetic energy gives

$$T = \frac{1}{2}\int_{\mathbf{q}} M_q \left|\dot{\xi}_{\mathbf{q}}\right|^2, \qquad M_q = \frac{\rho_{\mathrm{He}}}{q\tanh(qh)}, \tag{6.25}$$

where ρ_{He} is the helium mass density. The effective inertia increases at long wavelength because a larger volume of liquid participates in the motion. For small surface slopes, gravity and surface tension give the quadratic restoring energy

$$U_0 = \frac{1}{2}\int_{\mathbf{q}} K_q \left|\xi_{\mathbf{q}}\right|^2, \qquad K_q = \rho_{\mathrm{He}} g + \sigma q^2, \tag{6.26}$$

where σ is the surface tension. If $p(\mathbf{r},t)$ is the downward pressure applied to the surface, the interaction energy is

$$H_p = -\int d^2r\, p(\mathbf{r},t)\xi(\mathbf{r},t). \tag{6.27}$$

Including a phenomenological amplitude-decay rate γ_q, the surface equation of motion is

$$\ddot{\xi}_{\mathbf{q}} + 2\gamma_q \dot{\xi}_{\mathbf{q}} + \omega_q^2 \xi_{\mathbf{q}} = \frac{q \tanh(qh)}{\rho_{\mathrm{He}}} p_{\mathbf{q}}(t), \qquad \omega_q^2 = \left(gq + \frac{\sigma}{\rho_{\mathrm{He}}} q^3 \right) \tanh(qh), \tag{6.28}$$

where ω_q is the gravity–capillary ripplon dispersion. The reciprocal-lattice wave vectors relevant to the Bragg–Cherenkov effect are ordinarily in the deep-water capillary regime, where

$$\omega_q \simeq \sqrt{\frac{\sigma}{\rho_{\mathrm{He}}}} q^{3/2}. \tag{6.29}$$

In frequency space, the surface response is $\xi_{\mathbf{q}}(\omega) = \chi^R(q, \omega) p_{\mathbf{q}}(\omega)$, with the retarded susceptibility

$$\chi^R(q, \omega) = \frac{q \tanh(qh)}{\rho_{\mathrm{He}}} \frac{1}{\omega_q^2 - \omega^2 - 2i\gamma_q \omega}. \tag{6.30}$$

Its imaginary part,

$$\chi''(q, \omega) = \frac{q \tanh(qh)}{\rho_{\mathrm{He}}} \frac{2\gamma_q \omega}{\left(\omega_q^2 - \omega^2\right)^2 + 4\gamma_q^2 \omega^2}, \tag{6.31}$$

describes the out-of-phase response responsible for irreversible energy and momentum transfer into the helium surface. A localized electron at in-plane position $\mathbf{R}$ exerts a downward normal force with Fourier components $\mathcal{F}_{\mathbf{q}}$. Its pressure can be written as

$$p_e(\mathbf{r} - \mathbf{R}) = \int_{\mathbf{q}} \mathcal{F}_{\mathbf{q}} e^{i\mathbf{q}\cdot(\mathbf{r}-\mathbf{R})}. \tag{6.32}$$

The force contains the contribution $eE_\perp$ from the pressing field and a polarization contribution associated with the image potential. For a static electron, the surface deformation is

$$\xi^{\mathrm{st}}(\mathbf{r}) = \int_{\mathbf{q}} \frac{\mathcal{F}_{\mathbf{q}}}{\rho_{\mathrm{He}} g + \sigma q^2} e^{i\mathbf{q}\cdot(\mathbf{r}-\mathbf{R})}. \tag{6.33}$$

This is the static dimple produced by the electron. A localized dimple is a superposition of many surface Fourier components rather than one ripplon mode. Once established, a static dimple is an equilibrium deformation and does not continuously radiate energy.

6.1.4 Experimental observation of the electron solid

Microwave spectroscopy first resolved the quantized vertical image-potential states [140, 141]. Measurements of collective in-plane oscillations subsequently verified the two-dimensional electron behavior and the coupling of the electron system to helium-surface excitations [148].

The electron liquid-to-solid transition was observed by Grimes and Adams in 1979. The electron density was varied from 3×10^8 to $9 \times 10^8\ \mathrm{cm}^{-2}$, while the transition temperature increased from approximately 0.35 to 0.65 K. The transition occurred at the approximately density-independent coupling $\Gamma_m = 137 \pm 15$. The observed resonances were associated with collective modes of the electron solid coupled to ripplons. Fisher, Halperin, and Platzman showed that the spectra could be understood as hybridized electron-phonon and helium-ripplon modes of a triangular electron lattice [143, 149].

Subsequent mobility and thermodynamic measurements provided complementary evidence for the crystalline phase [150, 151]. These experiments established electrons on helium as a tunable and nearly disorder-free realization of a classical two-dimensional Coulomb liquid and solid.

The coupling to ripplons also makes the transport of the crystal strongly nonlinear. Non-Ohmic transport and negative differential conductivity were observed in confined electron crystals [152]. Channel experiments identified sharp velocity jumps associated with the loss of a low-velocity, surface-coupled state [153], while time-resolved measurements observed repeated slipping and sticking of a Wigner crystal relative to the helium surface [154]. The physical origin of this nonlinear response is developed next.

6.2 Quasistatic Bragg–Cherenkov transport

The quasistatic Bragg–Cherenkov effect is the response of the helium surface to a spatially periodic pressure pattern translating with the Wigner crystal. Two ingredients are required. First, a source component of wave vector $\mathbf{q}$ moving at velocity $\mathbf{v}$ drives the surface at the Doppler frequency $\mathbf{q} \cdot \mathbf{v}$. Second, the crystalline density concentrates the pressure near reciprocal-lattice vectors $\mathbf{G}$.

The simultaneous conditions

$$\mathbf{q} = \mathbf{G}, \qquad \mathbf{G} \cdot \mathbf{v} = \omega_G \tag{6.34}$$

therefore select ripplons that are both coherently driven by the crystal and resonant with the free surface-wave dispersion.

6.2.1 Bragg coherence and resonant ripplon emission

For an ideal triangular lattice, the density is

$$\sum_j \delta^{(2)}\left(\mathbf{r} - \mathbf{R}_j\right) = n_s \sum_{\mathbf{G}} e^{i\mathbf{G}\cdot\mathbf{r}}. \tag{6.35}$$

If the crystal translates rigidly with velocity $\mathbf{v}$, its density becomes

$$n_e(\mathbf{r}, t) = n_s \sum_{\mathbf{G}} e^{i\mathbf{G}\cdot(\mathbf{r}-\mathbf{v}t)}. \tag{6.36}$$

The corresponding pressure on the helium surface is

$$p_{\mathrm{WC}}(\mathbf{r}, t) = n_s \sum_{\mathbf{G}} \mathcal{F}_{\mathbf{G}} D_{\mathbf{G}}^{1/2} e^{i\mathbf{G}\cdot(\mathbf{r}-\mathbf{v}t)}. \tag{6.37}$$

Here $D_{\mathbf{G}}^{1/2}$ is the amplitude Debye–Waller factor, which accounts for the reduction of the coherent reciprocal-lattice component caused by fluctuations of the electrons about their equilibrium lattice sites. If $\mathbf{u}_j$ denotes the displacement of the jth electron from its equilibrium position $\mathbf{R}_j$, and the displacements are approximately Gaussian and isotropic, with $\langle u^2 \rangle \equiv \langle |\mathbf{u}_j|^2 \rangle$, then $D_{\mathbf{G}}^{1/2} = e^{-G^2\langle u^2\rangle/4}$.

The origin of the coherent enhancement is seen directly from $\rho_{\mathbf{G}} = \sum_j e^{i\mathbf{G}\cdot\mathbf{R}_j}$. Since $e^{-i\mathbf{G}\cdot\mathbf{R}_j} = 1$ for every lattice site, we get $\rho_{\mathbf{G}} = N$. All electrons therefore drive the same spatial phase of the selected surface component. Using the susceptibility in Eq. (6.30), the surface deformation generated by the translating crystal is

$$\xi(\mathbf{r}, t) = n_s \sum_{\mathbf{G}} \mathcal{F}_{\mathbf{G}} D_{\mathbf{G}}^{1/2} \chi^R\left(G, \mathbf{G}\cdot\mathbf{v}\right) e^{i\mathbf{G}\cdot(\mathbf{r}-\mathbf{v}t)}. \tag{6.38}$$

The corresponding drag force per electron is

$$\mathbf{f}_{\mathrm{BC}}(\mathbf{v}) = -n_s \sum_{\mathbf{G}\neq 0} \mathbf{G}\, |\mathcal{F}_{\mathbf{G}}|^2\, D_{\mathbf{G}} \chi''\left(G, \mathbf{G}\cdot\mathbf{v}\right). \tag{6.39}$$

The force is largest when the pressure frequency lies on the ripplon dispersion, $\mathbf{G}\cdot\mathbf{v}=\omega_G$. This is the Bragg–Cherenkov condition. At resonance, the phase of the moving periodic pressure remains registered with the phase of the ripplon, so the electron lattice continually reinforces the same surface wave.

If $\theta_{\mathbf{G}}$ is the angle between $\mathbf{G}$ and $\mathbf{v}$, the resonant speed is $v_{\mathrm{BC}}(\mathbf{G})=\frac{\omega_G}{G\cos\theta_{\mathbf{G}}}$. For $\mathbf{G}\parallel\mathbf{v}$, it takes the form $v_{\mathrm{BC}}(G)=\omega_G/G$. In the capillary regime,

$$v_{\mathrm{BC}}(G)=\sqrt{\frac{\sigma G}{\rho_{\mathrm{He}}}}. \tag{6.40}$$

For the first reciprocal-lattice shell, $G_1\propto n_s^{1/2}$, and therefore $v_{\mathrm{BC}}(G_1)\propto n_s^{1/4}$. The resonance also depends on crystal orientation because it is controlled by the projection $\mathbf{G}\cdot\mathbf{v}$ rather than by G alone.

6.2.1.1 Microscopic quantum expression for the Bragg–Cherenkov force

The surface-susceptibility treatment above gives a classical description of the Bragg–Cherenkov force. A complementary microscopic description is obtained by quantizing the same ripplon modes and treating their coupling to the electron density perturbatively [155]. For a surface of area $\mathcal{A}$, the quantized displacement field can be written as

$$\hat{\xi}(\mathbf{r})=\sum_{\mathbf{q}}\xi_q^{(0)}\left(b_{\mathbf{q}}+b_{-\mathbf{q}}^{\dagger}\right)e^{i\mathbf{q}\cdot\mathbf{r}},\qquad \xi_q^{(0)}=\left[\frac{\hbar q\tanh(qh)}{2\rho_{\mathrm{He}}\mathcal{A}\omega_q}\right]^{1/2}, \tag{6.41}$$

where $b_{\mathbf{q}}^{\dagger}$ creates a ripplon of energy $\hbar\omega_q$ and in-plane momentum $\hbar\mathbf{q}$. The zero-point amplitude $\xi_q^{(0)}$ follows by quantizing the harmonic surface mode whose effective mass per unit area is given in Eq. (6.25). The coupling energy between the electron pressure and the surface displacement can then be written as

$$\hat{H}_{\mathrm{e-r}}=\sum_{\mathbf{q}}V_{\mathbf{q}}\hat{\rho}_{\mathbf{q}}\left(b_{\mathbf{q}}+b_{-\mathbf{q}}^{\dagger}\right),\qquad \hat{\rho}_{\mathbf{q}}=\sum_{j=1}^{N}e^{i\mathbf{q}\cdot\hat{\mathbf{r}}_j},\qquad V_{\mathbf{q}}=-\mathcal{F}_{\mathbf{q}}\left[\frac{\hbar q\tanh(qh)}{2\rho_{\mathrm{He}}\mathcal{A}\omega_q}\right]^{1/2}. \tag{6.42}$$

Now, let $\hat{\mathbf{P}}=\sum_{j=1}^{N}\hat{\mathbf{p}}_j$ be the total in-plane momentum of the electron system. The force per electron exerted by the surface is $\mathbf{f}(\mathbf{v})=\left\langle\partial_t\hat{\mathbf{P}}\right\rangle/N$. For a crystal translating uniformly with velocity $\mathbf{v}$, the center-of-mass motion supplies the Doppler frequency $\mathbf{q}\cdot\mathbf{v}$. To second order in $\hat{H}_{\mathrm{e-r}}$, Dykman

and Rubo obtained

$$\mathbf{f}(\mathbf{v}) = -\frac{1}{\hbar N}\sum_{\mathbf{q}} \mathbf{q}\left|V_{\mathbf{q}}\right|^2 \frac{\overline{n}(\omega_q)+1}{\overline{n}(\mathbf{q}\cdot\mathbf{v})+1}\int_{-\infty}^{\infty} dt\, e^{i[\mathbf{q}\cdot\mathbf{v}-\omega_q]t}\left\langle \hat{\rho}_{\mathbf{q}}(t)\hat{\rho}_{-\mathbf{q}}(0)\right\rangle_0, \tag{6.43}$$

where $\overline{n}(\omega) = \left(e^{\hbar\omega/k_BT}-1\right)^{-1}$ is the Bose occupation number. The average $\langle\cdots\rangle_0$ is evaluated for the electron system without the electron–ripplon coupling, in the frame translating with the crystal.

The physical content of Eq. (6.43) is made explicit by introducing the dynamical structure factor

$$\mathcal{S}(\mathbf{q},\omega) = \frac{1}{2\pi N}\int_{-\infty}^{\infty} dt\, e^{i\omega t}\left\langle \hat{\rho}_{\mathbf{q}}(t)\hat{\rho}_{-\mathbf{q}}(0)\right\rangle_0. \tag{6.44}$$

The force can then be written as

$$\mathbf{f}(\mathbf{v}) = -\frac{2\pi}{\hbar}\sum_{\mathbf{q}} \mathbf{q}\left|V_{\mathbf{q}}\right|^2 \frac{\overline{n}(\omega_q)+1}{\overline{n}(\mathbf{q}\cdot\mathbf{v})+1}\mathcal{S}\left(\mathbf{q},\mathbf{q}\cdot\mathbf{v}-\omega_q\right). \tag{6.45}$$

Thus, the force is determined jointly by the ripplon spectrum and the dynamical density correlations of the electron system. The factor $\mathbf{q}$ reflects the momentum $\hbar\mathbf{q}$ transferred in an emission or absorption event, $|V_{\mathbf{q}}|^2$ gives the coupling strength, and the dynamical structure factor determines whether the electron system can accommodate the associated energy and momentum transfer.

For a perfectly ordered crystal at zero temperature, the density correlator contains an elastic Bragg contribution and the force gives

$$\mathbf{f}_{\mathrm{BC}}^{T=0} = -\frac{2\pi N}{\hbar}\sum_{\mathbf{G}} \mathbf{G}\left|V_{\mathbf{G}}\right|^2 D_{\mathbf{G}}\,\delta\left(\mathbf{G}\cdot\mathbf{v}-\omega_G\right). \tag{6.46}$$

This expression displays both defining ingredients of Bragg–Cherenkov scattering. The momentum is restricted to a reciprocal-lattice vector by the elastic Bragg peak, while energy conservation imposes the Cherenkov condition $\mathbf{G}\cdot\mathbf{v} = \omega_G$. The factor N in the force per electron is the coherent many-electron enhancement: the ripplon emission amplitudes add before their absolute square is taken.

The delta function in Eq. (6.46) describes an ideal infinite crystal coupled to an undamped ripplon. Introducing a finite ripplon linewidth amounts, near resonance, to the replacement

$$\delta(x) \longrightarrow \frac{1}{\pi}\frac{\gamma_G}{x^2+\gamma_G^2}. \tag{6.47}$$

Using Eq. (6.42) and $N/\mathcal{A} = n_s$, the resonant contribution then becomes

$$\mathbf{f}_{\mathbf{G}}(\mathbf{v}) \simeq -n_s \mathbf{G} \left|\mathcal{F}_{\mathbf{G}}\right|^2 D_{\mathbf{G}} \frac{G \tanh(Gh)}{\rho_{\mathrm{He}} \omega_G} \frac{\gamma_G}{\left(\mathbf{G}\cdot\mathbf{v} - \omega_G\right)^2 + \gamma_G^2}. \tag{6.48}$$

This is the near-resonant limit of the classical force obtained from the imaginary part of the surface susceptibility in Eqs. (6.39) and (6.50). The quantum and classical descriptions therefore represent the same physical process in two complementary languages: coherent ripplon emission in the microscopic formulation and dissipative response of a driven surface mode in the susceptibility formulation.

At finite temperature, the density correlator also contains the dynamics of the Wigner-crystal phonons. Ripplon emission can then be accompanied by the creation or annihilation of phonons of the electron solid. These inelastic processes broaden the elastic Bragg resonance and generate sidebands. In an ideal two-dimensional crystal, the algebraic translational correlations can also produce a non-Lorentzian low-velocity tail of the form

$$f_{\mathbf{G}} \propto \left|\mathbf{G}\cdot\mathbf{v} - \omega_G\right|^{-1+\alpha(\mathbf{G})}, \qquad \alpha(\mathbf{G}) = \frac{k_B T G^2}{4\pi m_e n_s c_T^2}, \tag{6.49}$$

under the assumptions of the perturbative finite-temperature theory [155]. The phenomenological linewidth used below is a simpler representation of the regularized resonance, whereas Eq. (6.43) shows more generally that its line shape is controlled by the full dynamical structure factor.

An important point for the high-frequency problem considered later is that the microscopic force contains a sum over all wave vectors. In a crystal, the dominant elastic terms occur near all reciprocal-lattice vectors for which the coupling matrix element and Bragg weight remain appreciable; the first reciprocal-lattice shell is not selected by the formalism itself. Higher-order reciprocal vectors are suppressed by their electron–ripplon matrix elements and Debye–Waller factors, but they can provide additional resonant channels when the imposed motion contains sufficiently high frequencies.

6.2.2 Resonant drag and nonlinear conductivity

Consider a pair of reciprocal vectors $\pm\mathbf{G}$ parallel to the motion. Substitution of Eq. (6.31) into Eq. (6.39) gives the drag magnitude

$$f_G(v) = \frac{4n_s D_G |\mathcal{F}_G|^2 \gamma_G G^3 v \tanh(Gh)}{\rho_{\mathrm{He}} \left\{ \left[\omega_G^2 - (Gv)^2\right]^2 + 4\gamma_G^2 (Gv)^2 \right\}}. \tag{6.50}$$

For weak damping, this force has a narrow maximum near $v = \omega_G/G$. At resonance,

$$f_G^{\max} = \frac{n_s D_G |\mathcal{F}_G|^2 G^2 \tanh(Gh)}{\rho_{\mathrm{He}} \gamma_G \omega_G}. \tag{6.51}$$

Thus, a weakly damped ripplon produces a narrow but large drag force. The nonlinear conductivity follows from force balance. Let $f_{\mathrm{bg}}(v)$ denote all nonresonant drag mechanisms. The equation of motion per electron is

$$m_{\mathrm{eff}} \dot{v} = eE_{\parallel} - f_{\mathrm{tot}}(v), \qquad f_{\mathrm{tot}}(v) = f_{\mathrm{bg}}(v) + f_{\mathrm{BC}}(v). \tag{6.52}$$

A steady state satisfies $eE_{\parallel} = f_{\mathrm{tot}}(v)$. On the low-velocity side of the Bragg–Cherenkov resonance, $f_{\mathrm{BC}}(v)$ rises rapidly as the velocity approaches v_{BC}. An increase in the driving field is then balanced primarily by an increase in ripplon drag rather than by an increase in electron velocity. The crystal velocity consequently remains close to v_{BC}, producing a velocity plateau and strongly nonlinear current–voltage characteristics.

If the stable low-velocity solution ceases to exist, the system can undergo a sharp velocity jump. The microscopic nature of the high-conductivity state reached after this instability has been the subject of a long-standing debate. One interpretation is that the strong drive dynamically melts the Wigner crystal by generating defects and destroying its reciprocal-lattice coherence [156–158]. An alternative interpretation is that the electron lattice remains ordered but dynamically decouples from its self-generated surface deformation, after which it may slide rapidly, become re-dressed by ripplons, or undergo repeated stick–slip motion [153, 159–161]. The scalar force-balance model establishes only that the low-velocity branch loses stability; by itself, it cannot determine whether the state reached after the jump remains crystalline.

For the high-frequency measurements presented later in this chapter, we regard nonequilibrium melting as the more plausible interpretation. First, the dimple lattice is generated dynamically by the electron density and should not be viewed as a rigid external potential [155]. At 150 MHz, the estimated electron displacement is approximately 30 nm, which is four to seven times smaller than the electron-lattice spacing. This does not rule out dynamical decoupling in general, but it makes the simplest geometric picture in which an intact crystal translates from one set of dimple minima to the next less natural. Second, if the electron lattice remained ordered after the jump, its structure factor would retain Bragg peaks at reciprocal-lattice vectors. Since several higher-order reciprocal-lattice channels are kinematically available in the high-frequency regime, an intact crystal could continue to experience Bragg-selected drag and might display re-entrant locking or additional velocity-saturation features as spectral weight is redistributed among these channels. No clear sequence of such secondary pinned states is observed; instead, the response changes directly to a high-conductivity regime with much weaker evidence of coupling to the helium surface. Taken together, these observations favor a drive-induced loss of crystalline Bragg coherence over the depinning of an otherwise intact Wigner solid [66]. This identification remains an interpretation of the transport data rather than a direct structural measurement, and a momentum-resolved probe of the electron correlations would be required to establish melting unambiguously.

The nonlinear electronic response does not by itself require nonlinear helium hydrodynamics. At a fixed velocity, $\xi_{\mathbf{G}} = \chi^R(G, Gv)p_{\mathbf{G}}$ is linear in the applied pressure. The nonlinearity arises because changing v changes the frequency Gv at which the sharply resonant surface susceptibility is sampled: $f_{\mathrm{BC}}(v) \propto \chi''(G, Gv)$. The linear surface description remains geometrically valid when $G|\xi_G| \ll 1$.

Likewise, the common phrase "dynamically deepened dimple lattice" should be interpreted carefully. The resonantly enhanced quantity is a surface Fourier component. A single pair $\pm\mathbf{G}$ produces a sinusoidal corrugation,

$$\xi_G(\mathbf{r}, t) = 2|\xi_{\mathbf{G}}| \cos\left[\mathbf{G} \cdot (\mathbf{r} - \mathbf{v}t) + \phi_G\right], \tag{6.53}$$

rather than an array of isolated circular wells. A localized dimple lattice, on the other hand, requires

the superposition of several non-collinear reciprocal vectors. Near resonance, the phase lag also places the electrons near the slope of the dominant surface component, and this slope produces the horizontal reaction force. The rigid-lattice description captures the coherent surface corrugation, whereas a self-consistent treatment of its fluctuations and deformation requires including the Wigner-crystal phonons and their coupling to ripplons.

6.2.3 Meaning and limitation of the quasistatic approximation

The preceding formulas assume that the surface follows the electron motion as if the crystal had a constant instantaneous velocity. For an arbitrary electron trajectory $\mathbf{R}(t)$, however, the exact linear response is retarded:

$$\xi_{\mathbf{q}}(t) = \mathcal{F}_{\mathbf{q}} \int_{-\infty}^{t} dt' \, \chi^R(q, t-t') e^{-i\mathbf{q}\cdot\mathbf{R}(t')} = \mathcal{F}_{\mathbf{q}} \int_{0}^{\infty} d\tau \, \chi^R(q, \tau) e^{-i\mathbf{q}\cdot\mathbf{R}(t-\tau)}. \tag{6.54}$$

The present surface deformation therefore depends on the earlier electron trajectory over the memory time of the ripplon response.

If the velocity changes sufficiently slowly during this memory time, the trajectory can be approximated as $\mathbf{R}(t-\tau) \simeq \mathbf{R}(t) - \mathbf{v}(t)\tau$. Equation (6.54) then reduces to the instantaneous constant-velocity result,

$$\xi_{\mathbf{q}}(t) \simeq \mathcal{F}_{\mathbf{q}} \chi^R \left(q, \mathbf{q}\cdot\mathbf{v}(t)\right) e^{-i\mathbf{q}\cdot\mathbf{R}(t)}. \tag{6.55}$$

A sufficient condition for this approximation is $|\mathbf{q}\cdot\dot{\mathbf{v}}|\,\tau_{\mathrm{mem}}^2 \ll 1$, where

$$\tau_{\mathrm{mem}} \sim \left[\gamma_G^2 + (\omega_G - \mathbf{G}\cdot\mathbf{v})^2\right]^{-1/2}.$$

At exact resonance, it becomes $\tau_{\mathrm{mem}} \sim \gamma_G^{-1}$. For sinusoidal motion at frequency Ω_d, the near-resonance quasistatic condition is therefore

$$\Omega_d \ll \gamma_G, \tag{6.56}$$

rather than merely $\Omega_d \ll \omega_G$ [162]. A drive may be slow compared with the ripplon oscillation period while still being fast compared with the time required for the resonant surface deformation to build up.

Finite ripplon damping, finite crystal size, finite translational correlation length, density inhomogeneity, and the finite observation time all broaden the ideal Bragg–Cherenkov response. Inelastic processes involving Wigner-crystal phonons can also redistribute spectral weight away from the elastic Bragg condition [155]. These effects determine the detailed quasistatic line shape, but they do not remove the central mechanism: coherent reciprocal-lattice components of the electron density resonantly drive ripplons and generate a strongly velocity-dependent drag force.

When the drive frequency is no longer small compared with the ripplon relaxation rate, the helium surface retains memory of earlier parts of the electron trajectory, and the instantaneous force $f_{\mathrm{BC}}[v(t)]$ is no longer generally valid. This failure of the quasistatic approximation provides the starting point for the high-frequency nonlinear transport presented in the following section.

6.3 High-frequency nonlinear transport of a Wigner crystal

Transport measurements of electrons above liquid helium are commonly performed using an ac electric field and phase-sensitive detection. Conventional studies of nonlinear Wigner-crystal transport have used dc, smoothly increasing, or sufficiently low-frequency driving fields that the electron motion during each part of a cycle can be treated approximately as a quasistatic drift. The measurements discussed here instead span drive frequencies from 0.3 to 150 MHz [66].

The ripplon frequency associated with the first reciprocal-lattice shell is strongly density dependent. For the electron densities at which the saturated high-frequency response is observed, it lies in the approximate range

$$\frac{\omega_{G_1}}{2\pi} \simeq 55\text{–}110\,\mathrm{MHz}. \tag{6.57}$$

The upper part of the experimental drive frequency range is therefore comparable to, or larger than, the characteristic first-shell ripplon frequency. In this regime the motion cannot generally be treated as a sequence of constant-velocity states, and the conventional quasistatic Bragg–Cherenkov description is no longer sufficient.

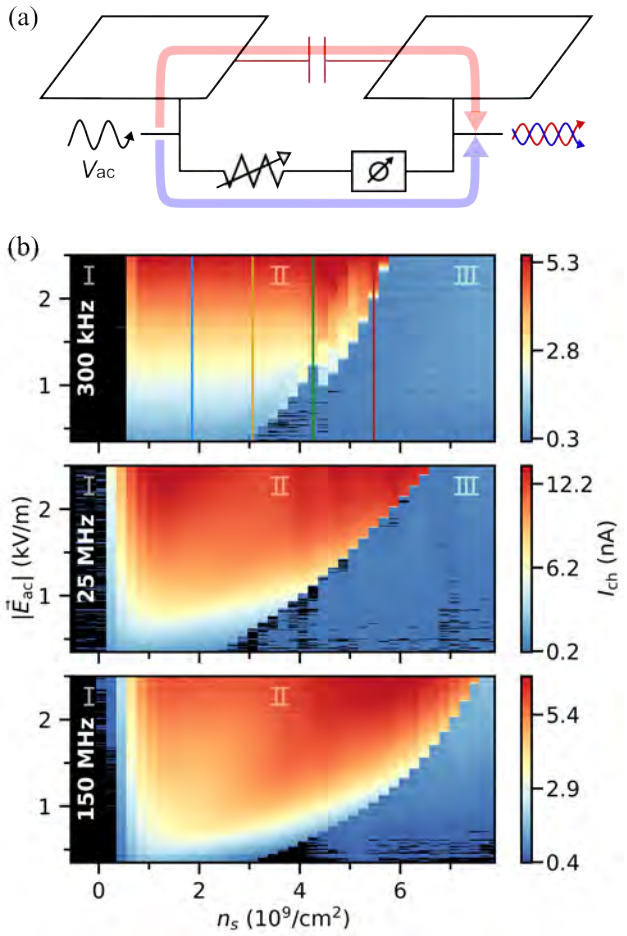


Figure 6.1 Representative high-frequency transport measurements of the microchannel-confined electron system. (a) Compensation-line scheme used to suppress the parasitic capacitive background. (b) Channel current I_{ch} as a function of the central-channel voltage V_{ch} and the amplitude of the ac driving field $\mathbf{E}_{ac}$ for drive frequencies 0.3, 25, and 150 MHz. The three transport regimes correspond to an empty channel, a high-conductivity electron state, and a low-conductivity Wigner-crystal state.

6.3.1 Experimental motivation

The electron system is confined in a central microchannel connecting two larger electron reservoirs. An ac voltage applied to one reservoir produces an in-plane driving field $\mathbf{E}_{ac}$ along the channel. The electron motion induces a voltage V_s on the opposite reservoir electrode, which is measured using a phase-sensitive lock-in technique. The electron density and spatial confinement in the central channel are controlled by the channel voltage V_{ch}. At high frequencies, capacitive cross-talk between the drive and detection electrodes is suppressed using a compensation line.

At 0.3 MHz, the transport displays the conventional low-frequency Bragg–Cherenkov response. In the crystalline regime, the channel current saturates as the driving field is increased because the

additional electric force is balanced predominantly by an increased ripplon drag. At this frequency, an electron moving at the saturated crystal velocity travels approximately 10 μm during one drive cycle, corresponding to motion over roughly one hundred lattice sites. The motion can therefore be treated quasistatically.

A saturated low-conductivity response remains visible at 25 and 150 MHz. At 150 MHz, however, the estimated electron displacement during one cycle is only approximately 30 nm, which is four to seven times smaller than the electron-lattice spacing. The electron solid is therefore far outside the conventional picture of a crystal drifting across many lattice periods during each cycle.

The velocity of the Wigner crystal is estimated from the channel current using

$$v_{\mathrm{WS}} = \frac{I_{\mathrm{ch}}}{e n_s w_{\mathrm{eff}}}, \tag{6.58}$$

where w_{eff} is the effective width of the electron system. The resulting velocities are of order 1–10 m/s, comparable to the phase velocities of helium-surface excitations. This supports the interpretation that the saturated high-frequency response continues to originate from electron–ripplon back-action.

Starting from the low-conductivity crystalline state, increasing the driving field at fixed density produces a sharp transition to a high-conductivity state. The high-frequency measurements now provide additional evidence relevant to the two interpretations discussed above. Although transport measurements alone cannot resolve it definitively, the high-frequency response is more consistent with nonequilibrium melting. At 150 MHz, the electron displacement is substantially smaller than the lattice spacing, making the simplest picture of an intact crystal slipping between neighboring dimple minima less natural. Moreover, as discussed below, ripplon coupling through higher-order reciprocal-lattice vectors remains kinematically allowed. If crystalline order survived the transition, the corresponding Bragg peaks could continue to support Bragg-selected friction. The abrupt change to a high-conductivity response therefore favors a drive-induced loss of crystalline Bragg coherence over the dynamical decoupling of an otherwise intact Wigner solid. This interpretation is not conclusive, and a direct structural, time-resolved, or hysteresis measurement would be required to distinguish the two scenarios definitively.

6.3.2 Electron–ripplon coupling under a periodic drive

Although additional high-frequency experiments are required to establish a complete microscopic model of the saturated response and its breakdown, we introduce a theoretical framework by extending the microscopic Bragg–Cherenkov formulation of Sec. 6.2.1.1 to a periodically driven Wigner crystal. We take the in-plane electric field to be

$$\mathbf{E}(t) = \mathbf{E}_0 \sin(\omega_d t), \tag{6.59}$$

and choose the vector potential

$$\mathbf{A}(t) = \frac{\mathbf{E}_0}{\omega_d} \cos(\omega_d t), \qquad \mathbf{E}(t) = -\partial_t \mathbf{A}(t). \tag{6.60}$$

For an electron of charge $-e$, minimal coupling gives $\mathbf{p}_j \longrightarrow \mathbf{p}_j + e\mathbf{A}$. The driven Hamiltonian can therefore be written as

$$\hat{H}(t) = \hat{H}_e^{(0)} + \hat{H}_r + \hat{H}_A(t) + \hat{H}_{\mathrm{e-r}}, \qquad \hat{H}_A(t) = \frac{e}{m_e}\mathbf{A}(t) \cdot \hat{\mathbf{P}}, \tag{6.61}$$

where $\hat{\mathbf{P}} = \sum_{j=1}^{N} \hat{\mathbf{p}}_j$ is the total momentum operator of the electrons. The term proportional to $A^2(t)$ has been omitted because it is a time-dependent scalar and does not affect the force. The electron and ripplon Hamiltonians are

$$\hat{H}_e^{(0)} = \sum_n \frac{\mathbf{p}_n^2}{2m_e} + \frac{1}{2}\sum_{n\neq m} \frac{e^2}{4\pi\varepsilon_0\kappa|\mathbf{r}_n - \mathbf{r}_m|}, \qquad \hat{H}_r = \sum_{\mathbf{q}} \hbar\omega_q b_{\mathbf{q}}^\dagger b_{\mathbf{q}}, \tag{6.62}$$

and the electron–ripplon interaction $\hat{H}_{\mathrm{e-r}}$ is given in Eq. (6.42).

For a translationally invariant electron Hamiltonian, $\left[\hat{H}_e^{(0)}, \hat{\mathbf{P}}\right] = 0$. The coupling to the uniform electric field can consequently be included exactly in the interaction-picture transformation. Integrating the drive Hamiltonian gives

$$\int_0^t dt'\, \hat{H}_A(t') = \mathbf{a} \cdot \hat{\mathbf{P}} \sin(\omega_d t), \tag{6.63}$$

where $\mathbf{a} = \frac{e\mathbf{E}_0}{m_e\omega_d^2}$ is the free-electron oscillation amplitude. The corresponding unitary operator translates every electron by $\mathbf{a}\sin(\omega_d t)$. Using the density convention in Eq. (6.42), the driven interaction-picture density operator transforms as

$$\tilde{\rho}_{\mathbf{q}}(t) = e^{i\alpha_{\mathbf{q}}\sin(\omega_d t)}\rho_{\mathbf{q}}(t), \qquad \rho_{\mathbf{q}}(t) = e^{i\hat{H}_e^{(0)}t/\hbar}\rho_{\mathbf{q}}e^{-i\hat{H}_e^{(0)}t/\hbar}. \tag{6.64}$$

where $\alpha_{\mathbf{q}} = \mathbf{q} \cdot \mathbf{a}$. The electron–ripplon interaction in this frame is therefore

$$\widetilde{H}_{\mathrm{e-r}}(t) = \sum_{\mathbf{q}} V_{\mathbf{q}} e^{i\alpha_{\mathbf{q}} \sin(\omega_d t)} \rho_{\mathbf{q}}(t) \left[b_{\mathbf{q}} e^{-i\omega_q t} + b^{\dagger}_{-\mathbf{q}} e^{i\omega_q t} \right]. \tag{6.65}$$

The periodic translation is expanded using the Jacobi–Anger identity,

$$e^{i\alpha \sin(\omega_d t)} = \sum_{m=-\infty}^{\infty} J_m(\alpha) e^{im\omega_d t}. \tag{6.66}$$

The integer m labels the sidebands generated by the periodic electron motion. A process in the mth sideband can exchange the energy $m\hbar\omega_d$ with the drive.

6.3.3 First-harmonic friction force

The force per electron exerted by the helium surface is

$$\mathbf{f}(t) = \frac{1}{N} \frac{d}{dt} \left\langle \hat{\mathbf{P}} \right\rangle = -\frac{i}{\hbar N} \left\langle \left[\hat{\mathbf{P}}, \hat{H}_{\mathrm{e-r}} \right] \right\rangle. \tag{6.67}$$

The force operator is linear in the electron–ripplon interaction. Its first nonzero average is therefore second order in $V_{\mathbf{q}}$:

$$\mathbf{f}(t) = \frac{1}{\hbar^2 N} \int_{-\infty}^{t} dt' \, \left\langle \left[\widetilde{H}_{\mathrm{e-r}}(t'), \left[\hat{\mathbf{P}}, \widetilde{H}_{\mathrm{e-r}}(t) \right] \right] \right\rangle_0. \tag{6.68}$$

Here $\langle \cdots \rangle_0$ denotes an average over the uncoupled electron and ripplon systems. Equation (6.68) is perturbative in the electron–ripplon interaction but retains the ac displacement $\mathbf{a}$ to all orders through the Bessel functions in Eq. (6.66).

After tracing over the ripplons, performing the Bessel expansion, and retaining the component of the force oscillating at the drive frequency, the low-temperature single-ripplon result is

$$\mathbf{f}^{(1)}(t) = -\frac{2\pi \cos(\omega_d t)}{\hbar} \sum_{\mathbf{q}} \sum_{m=1}^{\infty} \frac{m\mathbf{q}}{\alpha_{\mathbf{q}}} \left| V_{\mathbf{q}} \right|^2 J_m^2 \left(\alpha_{\mathbf{q}} \right) \frac{\overline{n}(\omega_q) + 1}{\overline{n}(m\omega_d) + 1} \mathcal{S} \left(\mathbf{q}, m\omega_d - \omega_q \right), \tag{6.69}$$

where $\mathcal{S}(\mathbf{q}, \omega)$ is the dynamical structure factor in Eq. (6.44), and $\overline{n}(\omega) = (e^{\hbar\omega/k_B T} - 1)^{-1}$.

Equation (6.69) contains the central physics of the high-frequency response. The dynamic structure factor selects wave vectors and frequencies supported by the electron system, while the ripplon frequency enters through the energy mismatch $m\omega_d - \omega_q$. The Bessel factor $J_m^2(\alpha_{\mathbf{q}})$ gives

the weight of the mth drive-induced sideband. In the elastic crystalline contribution, $\mathcal{S}(\mathbf{q},\Omega)$ is sharply concentrated near $\mathbf{q} = \mathbf{G}$ and $\Omega = 0$. The corresponding ac resonance conditions are therefore

$$\mathbf{q} = \mathbf{G}, \qquad m\omega_d = \omega_G. \tag{6.70}$$

Unlike the quasistatic condition $\mathbf{G}\cdot\mathbf{v} = \omega_G$, the high-frequency resonance is set by the imposed drive frequency and its harmonics.

6.3.4 Weak-excursion limit

For $|\alpha_{\mathbf{G}}| = |\mathbf{G}\cdot\mathbf{a}| \ll 1$, the Bessel functions satisfy

$$\begin{aligned} J_1(\alpha_{\mathbf{G}}) &\simeq \frac{\alpha_{\mathbf{G}}}{2}, \\ J_m(\alpha_{\mathbf{G}}) &= O\left(\alpha_{\mathbf{G}}^m\right), \qquad m > 1. \end{aligned} \tag{6.71}$$

The first sideband consequently dominates. For a perfectly ordered crystal at zero temperature, the elastic part of the density correlator restricts the momentum to reciprocal-lattice vectors. With the momentum normalization used here, the force reduces to

$$\mathbf{f}^{(1)}_{T=0}(t) \simeq -\frac{N\cos(\omega_d t)}{8\pi\hbar}\sum_{\mathbf{G}} \alpha_{\mathbf{G}}\mathbf{G}\left|\widetilde{V}_G\right|^2 \delta\left(\omega_d - \omega_G\right), \tag{6.72}$$

where $\widetilde{V}_G = V_G e^{-G^2\lambda^2/4}$ contains the Debye–Waller factor due to the zero-point mean-square displacement λ^2 of an electron about its lattice site.

Equation (6.72) is the ac analogue of the elastic Bragg–Cherenkov force. The reciprocal-lattice condition expresses coherent emission by the crystal, while $\omega_d = \omega_G$ expresses resonance between the first harmonic of the electron motion and a ripplon. It should not be identified with the constant-drift result by replacing ω_d with an instantaneous Doppler frequency.

The zero-temperature expression is used only to expose the selection rule. At finite temperature and in a finite crystal, the full dynamic structure factor in Eq. (6.69) must be retained. Thermal fluctuations, Wigner-crystal phonons, finite crystalline correlation length, and finite ripplon linewidth broaden the ideal delta-function resonance.

6.3.5 Higher-order reciprocal-lattice channels

The ripplon frequency associated with the first reciprocal-lattice shell depends on the electron density. For the densities corresponding to the saturated high-frequency response, the estimated range is $\frac{\omega_{G_1}}{2\pi} \simeq 55$–$110\,\mathrm{MHz}$. The response at the largest drive frequencies can therefore exceed the first-shell ripplon frequency, so additional reciprocal-lattice channels must be considered.

For a triangular Wigner crystal, the reciprocal-lattice vectors may be written as

$$\mathbf{G}_{hk} = h\mathbf{b}_1 + k\mathbf{b}_2, \qquad h, k \in \mathbb{Z}, \tag{6.73}$$

where the reciprocal-lattice basis vectors were defined in Eq. (6.18). The corresponding magnitudes are $G_{hk} = \gamma_{hk} G_1$, where $\gamma_{hk} = \sqrt{h^2 - hk + k^2}$. In the capillary regime, $\omega_G \propto G^{3/2}$, and therefore

$$\omega_{hk} = \omega_{G_1} \gamma_{hk}^{3/2} = \omega_{G_1} \left(h^2 - hk + k^2\right)^{3/4}. \tag{6.74}$$

The first shell has $\gamma_{hk}^2 = 1$. The next allowed shell of the triangular reciprocal lattice has $\gamma_{hk}^2 = 3$, and therefore $\omega_{hk} \simeq 2.28\,\omega_{G_1}$. Across the first-shell range in Eq. (6.57), this second-shell frequency lies approximately between

$$125\,\mathrm{MHz} \lesssim \frac{\omega_{hk}}{2\pi} \lesssim 251\,\mathrm{MHz}. \tag{6.75}$$

For example, at an electron density near $4.5 \times 10^9\,\mathrm{cm}^{-2}$, the estimated first-shell frequency is approximately 75 MHz, while the $\gamma_{hk}^2 = 3$ shell lies near 171 MHz. Higher-order reciprocal-lattice vectors therefore provide a natural kinematic route for coupling the driven Wigner crystal to ripplons in the hundreds-of-megahertz range.

This argument identifies the channels that satisfy the elastic Bragg and ripplon-frequency conditions; it does not imply that all such channels carry comparable spectral weight. Higher reciprocal-lattice vectors are generally suppressed by the electron–ripplon matrix element and the Debye–Waller factor. Inelastic components of the Wigner-crystal structure factor, Wigner-crystal phonons, finite crystalline correlation length, and dynamical pinning can broaden the resonances and redistribute spectral weight among the kinematically available channels.

6.3.6 Interpretation and limitations

The calculation shows that periodic motion modifies the Bragg–Cherenkov process in two essential ways. First, the density operator acquires Bessel-weighted sidebands at integer multiples of the drive frequency. Second, crystalline order selects reciprocal-lattice wave vectors from the continuum of possible ripplon momenta. The combination produces the resonance condition $m\omega_d = \omega_G$ and allows higher-order Bragg vectors to generate a frictional back-action at frequencies comparable to or above the conventional first-shell ripplon frequency.

The resulting force provides a mechanism for the observed high-frequency dynamical pinning. It does not, by itself, constitute a complete self-consistent theory of the measured current–voltage characteristics. The calculation is performed to the lowest nonvanishing order in the electron–ripplon coupling, assumes a prescribed sinusoidal center-of-mass displacement, and uses the dynamic structure factor of the undriven Wigner crystal. It does not determine self-consistently the electron heating, the drive-induced modification of crystalline correlations, or the transition into the high-conductivity state.

Within these limitations, the observed saturated response at drive frequencies comparable to or exceeding the first-shell ripplon frequency is consistent with a frictional back-action arising from coherent ripplon emission at higher-order reciprocal-lattice vectors.

CHAPTER 7

CONCLUSIONS AND OUTLOOK

This dissertation studied how nonequilibrium dynamics makes the internal structure of mesoscopic systems visible through experimentally accessible observables. We considered a parametrically driven spin chain, coupled vibrational modes in doped semiconductor resonators, and a Wigner crystal of electrons above liquid helium. These systems differ in their microscopic degrees of freedom and in the roles of coherence and dissipation. In each case, however, the central problem is to understand how the couplings, the preparation, and the available dynamical channels determine a measured response.

The results establish several connections between microscopic structure and collective dynamics. In the spin chain, resonant pair excitation converts properties of an effective topological Hamiltonian into magnetization and spin correlations. In semiconductor resonators, the redistribution of valence-band holes under strain produces a strong and tunable interaction between mechanical modes. For electrons on helium, crystalline density correlations select surface-wave channels that can generate a substantial frictional back-action even under rapid oscillatory motion. Relatively weak microscopic couplings can therefore have qualitative consequences when they act coherently or resonantly across a mesoscopic system.

7.1 Principal results and their physical implications

7.1.1 Topology and preparation in the driven spin chain

Part I considered a spin-$1/2$ chain in a strong static magnetic field, with a transverse exchange component modulated near twice the single-spin Larmor frequency. Within the rotating-wave approximation, the Jordan–Wigner transformation maps the spin dynamics onto the Kitaev chain. The static exchange provides fermion hopping, the modulation provides pairing, and the frequency detuning acts as an effective chemical potential. Switching on the modulation therefore both creates excitations and changes the topology of the effective excitation spectrum.

For a periodic chain initially in the polarized state, we obtained the continuous time-averaged

magnetization change following a sudden turn-on. In the topological interval,

$$\overline{\Delta m^z} = \frac{|F|}{|J| + |F|}, \qquad |\mu| < 2|J|. \tag{7.1}$$

The response is independent of detuning throughout this interval. Its height depends continuously on the ratio of pairing to hopping. The topological significance lies in the relation between this frequency-independent response, the winding of the Bogoliubov eigenstates, and the gap closings that delimit the interval.

The weak-drive limit makes this relation particularly transparent. Pair excitations are concentrated near the two momenta at which the unmodulated particle and hole branches cross. The winding-number density becomes concentrated near the same momenta. Changing the detuning moves these regions through the Brillouin zone while leaving their leading integrated weights unchanged. The exact finite-drive calculation extends the magnetization plateau beyond this narrow-resonance picture. It relates the response to the same complex-momentum structure that determines the winding number.

The spin correlations provide complementary information about the prepared state. In the thermodynamic periodic-chain calculation, the longitudinal correlations following a sudden turn-on vanish throughout the topological interval, whereas the transverse correlations vary with detuning. Thus, the absence of longitudinal correlations accompanies a state with nontrivial pair coherence and a finite excitation density. The combination of polarization and correlations gives a more informative diagnostic than either quantity alone.

A slow turn-on preserves a frequency-independent magnetization plateau but prepares different mode occupations and correlations. The distinction originates at the beginning of the ramp, where the pairing amplitude vanishes and the initial spectrum is gapless at selected momenta. Adiabaticity consequently fails in a momentum region that shrinks as the ramp becomes slower. For a linear ramp, the characteristic width scales with the square root of the ramp rate away from the transition and with its cube root at the critical detuning. The exact mode equations, their asymptotic solutions, and the parabolic-cylinder solution explain how this region connects to the adiabatic evolution of the remaining modes.

Preparation memory becomes explicit when amplitude ramps are compared with frequency sweeps. Two protocols can reach the same final Hamiltonian while retaining different quasiparticle occupations and spin correlations. The resulting hysteresis records the path through parameter space. The final excitation spectrum therefore supplies only part of the information needed to predict the response; the preparation determines how that spectrum is populated.

The laboratory-frame calculations confirm that the principal magnetization and correlation features persist when the counter-rotating terms are retained. This agreement supports the use of the effective Kitaev Hamiltonian to explain the anomalous response for the parameters studied.

7.1.2 Boundaries as a source of bulk dynamical sensitivity

Opening the chain introduces a separate spectral problem. The real-space Bogoliubov–de Gennes equations impose four boundary conditions, which generally cannot be satisfied by replacing traveling waves with a single standing wave. In the single-channel region, the mode contains a propagating component together with evanescent components required near the ends. In the two-channel region, the boundaries mix two distinct propagating momenta at the same quasienergy. The resulting quantization conditions account for the crossings, avoided crossings, and changing channel composition of the finite-chain spectrum.

The same characteristic roots also describe localized edge solutions. Their contribution must be distinguished from the modification of extended states. A nearest-neighbor topological chain supports two boundary Majorana components, which generally combine into a fermionic mode with an exponentially small finite-size splitting. Boundary channel mixing instead affects an extensive set of bulk modes. Although each extended mode has a small local weight, their combined contribution can appreciably modify an observable far from either end.

This sensitivity develops dynamically. Immediately after the quench, coherent addition of the mode contributions reproduces the initially polarized state. The interior subsequently follows the bulk dynamics until boundary-dependent propagation becomes appreciable. The relevant scale is set by the distance from the boundary and the bulk group velocities. The numerical results show that this propagation rule applies in both channel regimes. Their distinction concerns the weight of

the observable response: for the parameters studied, the early single-channel transients weaken with increasing length, while the two-channel response remains appreciable through the largest evaluated size, $N = 4096$.

The finite-window calculations further demonstrate convergence to the time averages of the individual finite chains. The observed separation from the bulk reference is much larger than the remaining averaging error at the longest evaluated durations. Exactly zero detuning provides an additional analytical example, where sublattice symmetry changes the degeneracy structure and makes the strict central-site result sensitive to size parity.

These results give boundaries an additional dynamical role. Besides supporting localized excitations, an end of the chain determines how extended propagation channels combine. A measurement in the interior can consequently contain information about boundary scattering after the corresponding propagation time has elapsed. Spatial resolution and control of the observation window are therefore essential when using a local response to infer bulk properties.

7.1.3 Carrier-mediated nonlinear coupling in mechanical resonators

Chapter 5 considered a different manifestation of collective response. In a doped semiconductor resonator, mechanical strain changes the valence-band energies and redistributes the holes. The strain-dependent carrier free energy then contributes to the elastic coefficients of the crystal. We extended this mechanism from the self-nonlinearity of one mode to the dispersive coupling between different vibrational modes.

The hole-induced quartic elastic response can greatly exceed the intrinsic lattice contribution in the relevant parameter range. Its dependence on density is nonmonotonic: increasing the number of carriers initially strengthens the response, while the increasing kinetic energy of a sufficiently degenerate hole gas suppresses its sensitivity to strain. The temperature dependence can also become nonmonotonic. The resulting coupling is therefore controlled jointly by carrier density, temperature, and crystal orientation.

For the Lamé and torsional modes of a thin silicon plate, the same nonlinear elasticity combination controls both dispersive shifts. Their fractional frequency shifts nevertheless differ substantially

because of their mode geometry and stiffness. Crystal orientation changes these sensitivities in opposite ways for the two modes. This provides a means of choosing which mode is more strongly affected by the vibration amplitude of the other.

The results have direct implications for precision frequency references. Compensation of the linear temperature dependence of a clock mode does not eliminate its sensitivity to the amplitude of an auxiliary mode. The thermometer must be driven strongly enough to be measured accurately, while its dispersive back-action remains within the desired clock stability. The calculated coupling coefficients make this tradeoff quantitative. Thermal occupation fluctuations of other modes provide a related source of frequency noise and phase diffusion, whose importance increases as the resonator becomes smaller.

7.1.4 Bragg-selected transport of electrons on helium

Chapter 6 studied the nonlinear transport of a Wigner crystal above liquid helium. The electron lattice couples coherently to surface waves near its reciprocal-lattice vectors. For steady drift, this produces the Bragg–Cherenkov condition: the Doppler frequency of a translating density component matches the corresponding ripplon frequency. The resonantly enhanced back-action can then limit the crystal velocity.

Rapid oscillatory motion changes the structure of this coupling. The periodic displacement generates sidebands of the electron density, while crystalline correlations continue to select reciprocal-lattice wave vectors. The corresponding elastic resonance condition is

$$m\omega_d = \omega_{\mathbf{G}}. \tag{7.2}$$

Higher-order reciprocal-lattice vectors give access to higher-frequency ripplons. This provides a mechanism for substantial surface back-action at drive frequencies comparable to or exceeding the first-shell ripplon frequency, including motion whose displacement is smaller than the electron-lattice spacing.

The theory identifies how a weak electron–ripplon interaction can produce a pronounced transport response through crystalline coherence and resonance. Its application to the measured conductivity also requires the spectral weights and linewidths of the available channels. Determining

the eventual breakdown of the low-conductivity state requires a further description of the driven crystal, including heating, internal excitations, and changes of positional order.

7.2 Experimental tests of the spin-chain response

The spin-chain predictions suggest a concrete experimental program. The required effective Hamiltonian can be written as

$$\hat{H}_{\text{target}} = \frac{\mu}{2} \sum_n \sigma_n^z - \frac{1}{2} \sum_n \left[(J+F)\sigma_n^x \sigma_{n+1}^x + (J-F)\sigma_n^y \sigma_{n+1}^y \right]. \tag{7.3}$$

The main requirements are independent control of the two transverse couplings, a tunable longitudinal field, preparation of a polarized state, and measurements over a resolved evolution interval.

7.2.1 Superconducting-qubit arrays

Superconducting transmon arrays provide a direct implementation route. Recent work demonstrated simultaneous hopping and pairing interactions in a chain of six transmons with tunable couplers [37]. Coupler modulation near the difference of neighboring qubit frequencies activates exchange, while modulation near their sum activates pair creation and annihilation. The amplitudes and phases of the two sidebands control the corresponding interaction coefficients.

For the present problem, the hopping drive can remain fixed while the pairing envelope is switched on suddenly or ramped slowly. Appropriate sideband detunings supply the effective μ, and their variation implements the frequency-sweep protocol. Bond calibration should establish the actual hopping and pairing amplitudes and compensate drive-induced frequency shifts. Residual longitudinal interactions and leakage outside the two-level subspace can then be included as measured corrections to the target model.

The first comparison should use the exact dynamics of the available finite array. Increasing its length subsequently increases the interval over which central sites can follow the bulk response. A controllable closing link would additionally permit a direct comparison of open and ring geometries at fixed size and coupling parameters.

7.2.2 Trapped-ion chains

Trapped ions offer complementary control of interaction geometry. Independent XX and YY interactions have been demonstrated with two $^{171}Yb^{+}$ spins using parallel spin-dependent optical forces [163]. The two forces have different spin phases and sufficiently separated frequencies to suppress unwanted cross terms. Their independently controlled strengths determine the sum and difference of the transverse couplings in Eq. (7.3). A separately controlled effective longitudinal field supplies the detuning.

Extending this approach to a chain would allow amplitude ramps to vary the coupling difference while maintaining the required hopping strength. Optical pumping and coherent rotations prepare the polarized state, and fluorescence detection provides spin readout. Spatially resolved correlation dynamics have already been measured in ion chains [164], making the propagation of the boundary response a natural observable.

The interaction matrix requires particular attention. Phonon-mediated ion couplings generally extend beyond nearest neighbors. Laser-field design provides routes to tailoring the coupling graph [165], but the remaining couplings must be calibrated and included in the comparison. A bare longer-range spin exchange introduces Jordan–Wigner strings and generally changes the interacting character of the fermionic problem. It therefore cannot automatically be treated as a small extension of the nearest-neighbor free-fermion dispersion.

7.2.3 Measurements and observation windows

A first test would prepare the polarized chain, activate the pairing interaction, and measure the magnetization as a function of detuning at fixed F/J. Repeating this measurement for several amplitudes would test both the location of the plateau and its predicted height. Measurements at selected evolution times, followed by averaging over repeated preparations, give a specified finite-window observable that can be compared directly with theory.

Joint spin readout gives longitudinal spin probabilities, while analysis rotations before readout give the transverse correlations. Repeating the preparation with different ramp rates and with the two paths through parameter space tests the predicted preparation memory. The measured correlations

must be compared with the theoretical quantity formed using the same averaging prescription.

The observation window must resolve the coherent dynamics while remaining within the experimentally established coherence time. For an initial bulk comparison in an open chain, it should also end before an appreciable boundary response reaches the observation site. To measure the boundary effect, the opposite timing requirement applies: the distance-over-velocity scale must fit within the coherence window. Varying the observation site and chain length then distinguishes propagation from a spatially uniform loss of contrast.

The most informative experimental signature is the combined dependence on detuning, pairing strength, preparation, geometry, and time. A magnetization plateau accompanied by the predicted correlation changes and preparation memory would test considerably more of the underlying mechanism than a flat polarization trace alone. These measurements would also provide a sensitive benchmark of the engineered interaction strengths and unwanted processes.

7.3 Future directions

7.3.1 Higher winding numbers and multiband systems

An immediate theoretical direction is to determine how much topological information the response can contain beyond the nearest-neighbor model. Extended quadratic fermion chains can support higher winding numbers. Their driven response would test whether magnetization and correlations distinguish only trivial and nontrivial sectors or can resolve different values of an integer invariant.

Multiple resonant momentum regions need not contribute equally, and additional bands introduce overlapping resonances and interband coherence. The useful question is therefore which combinations of observables retain information about the invariant and under what preparation conditions. Bogoliubov methods and controlled ramp calculations provide starting points for these extensions, while exact diagonalization and tensor-network dynamics allow their robustness to be tested. Spin implementations must preserve the distinction between deliberately engineered quadratic fermion terms and longer-range exchanges that also introduce interactions.

7.3.2 Interactions, memory, and relaxation

The next decisive question is how interactions change the response once different quasiparticle sectors cease to evolve independently. Interactions can renormalize the effective spectrum and produce scattering that redistributes occupations. Establishing the relative importance of these processes would determine the lifetime of the plateau, correlation structure, and preparation memory.

Time-dependent mean-field calculations provide a baseline for reversible quasiparticle renormalization. Comparison with matrix-product-state evolution and exact diagonalization can identify the additional effects of correlations and collisions. Weak-coupling perturbation theory can help determine which decay channels are available, while operator autocorrelations provide a direct measure of the persistence of dynamical memory.

Spectral diagnostics should be connected to these measured quantities. Level statistics and eigenstate-thermalization diagnostics, evaluated within the appropriate symmetry sectors, can be compared with the relaxation of magnetization and correlations. Entanglement growth supplies complementary information about the spreading of quantum correlations. The aim is to distinguish persistent response, a long-lived prethermal regime, and memory sustained by finite size. The dependence of the corresponding lifetime on interaction strength, length, and preparation would establish the experimentally useful domain of the noninteracting predictions.

7.3.3 Disorder and coupling to the environment

Disorder tests how strongly the response relies on translation symmetry. Random fields and couplings broaden resonances, alter mode profiles, and can change the relation between excitation and topology. Real-space Bogoliubov and covariance calculations provide scalable noninteracting benchmarks, while disorder averaging and size dependence can separate broadening from a qualitative change of the dynamics.

Environmental coupling introduces a related question about coherence. The open-chain results make controlled dissipation near the ends especially informative. Varying boundary loss or dephasing would test whether reduced reflection coherence weakens the channel-mixing contribution or produces a distinct driven open-system response. Such measurements could connect spatial

propagation, boundary scattering, and relaxation within the same device. General spin dissipation and dephasing dynamics can be studied using Lindblad exact diagonalization, quantum trajectories, and tensor-network methods. These comparisons would determine which imperfections primarily reduce visibility, which alter the prepared state, and which remove the response on experimentally accessible time scales.

7.3.4 From spin-$1/2$ dynamics to magnonics and higher dimensions

A complementary direction is to establish the crossover from spin-$1/2$ to larger spin. The local occupation constraint is central to the present fermionic description. With increasing S, a weak-drive, low-excitation regime becomes accessible to a Holstein–Primakoff expansion and spin-wave theory. Comparing these limits would determine which aspects of the anomaly require hard-core quantum dynamics and which follow more generally from resonant excitation and band geometry.

This comparison has a concrete experimental setting in parametric magnon pumping. Parallel pumping of yttrium iron garnet waveguides has generated propagating spin waves whose modes are resolved using Brillouin light scattering [166]. Pump-frequency and magnetic-field scans can therefore examine how the selected modes contribute to the response. Bosonic amplification, damping, and saturation must be incorporated before comparing these measurements with the bounded pair production of the spin-$1/2$ chain. At stronger excitation, $1/S$ corrections or semiclassical dynamics can describe frequency shifts, scattering, and mode competition.

Dimensionality provides an independent test. Driven Kitaev-honeycomb models offer controlled two-dimensional benchmarks when the protocol preserves a tractable Majorana description within a flux sector [167]. More general two-dimensional spin models can be approached with exact diagonalization and tensor networks on cylinders. The objective is to identify separately the roles of topology, hard-core constraints, dimensionality, and coherent preparation, and to determine whether a comparably simple bulk diagnostic survives beyond one-dimensional kinematics.

7.3.5 The breakdown of high-frequency Wigner-crystal pinning

For electrons on helium, the main unresolved problem is the transition out of the low-conductivity state. The present theory identifies resonant surface-wave channels for a prescribed oscillatory

motion. A fuller description should incorporate Wigner-crystal phonons, finite positional correlation length, electron heating, and the retarded helium-surface response. These ingredients can help distinguish rapid motion of an ordered solid from defect proliferation and dynamical melting. The broader objective is to determine what structural information a nonlinear transport measurement contains. A sharp conductivity change must be connected to the microscopic state through its dynamics, fluctuations, and coupling to the substrate.

7.4 Final perspective

The three projects developed here establish different forms of the connection between internal structure and nonequilibrium response. Topological winding influences the density and correlations generated by resonant pair excitation. Carrier redistribution controls nonlinear mechanical coupling and frequency stability. Crystalline coherence selects the surface excitations responsible for electronic drag. In each case, the observable becomes interpretable through a calculation of the processes that populate, mix, or relax the relevant modes.

The resulting analytical limits and numerical benchmarks provide a basis for studying more general systems in which interactions, disorder, and environmental coupling compete with coherent dynamics. They also identify measurements that can distinguish changes of the Hamiltonian from changes of the prepared state and its lifetime. This distinction is important both for interpreting experiments and for using programmable systems to investigate many-body physics.

A central opportunity is therefore to develop dynamical measurements that reveal increasingly detailed information while remaining experimentally simple. Magnetization, correlations, frequency shifts, and transport can carry information about topology and collective order when their dependence on preparation, geometry, and time is understood. Extending these connections beyond the controlled models studied here offers a path toward a more general theory of how nonequilibrium mesoscopic matter can be prepared, characterized, and tested through its response.

APPENDIX A

MATRIX PRODUCT STATE SIMULATIONS

To validate the analytical predictions derived in the thermodynamic limit ($N \to \infty$), we performed finite-size numerical simulations using the Matrix Product State (MPS) formalism. This approach is exceptionally well-suited for one-dimensional quantum systems with local interactions, such as the spin chain considered here.

A.0.1 The Matrix Product State Method

The Hilbert space of a chain of N spins has a dimension that grows exponentially as 2^N, making exact simulations intractable for even modest system sizes. The MPS method resolves this dimensionality problem by efficiently representing a specific class of quantum states that occupy a small corner of the total Hilbert space. These states are characterized by having a limited amount of entanglement, a feature common to the ground states of gapped, local Hamiltonians, as described by the area law of entanglement entropy.

A generic quantum state of the chain can be written as:

$$|\Psi\rangle = \sum_{s_1,\ldots,s_N} C_{s_1 s_2 \ldots s_N} \, |s_1 s_2 \ldots s_N\rangle \tag{A.1}$$

where $s_n \in \{\uparrow, \downarrow\}$ is the state of the spin at site n, and $C_{s_1 s_2 \ldots s_N}$ is an element of a rank-N tensor with 2^N elements. The core idea of MPS is to decompose this large tensor into a product of smaller, rank-3 tensors, one for each site:

$$C_{s_1 s_2 \ldots s_N} \approx A^{s_1}_{\alpha_0 \alpha_1} A^{s_2}_{\alpha_1 \alpha_2} \ldots A^{s_N}_{\alpha_{N-1} \alpha_N} \tag{A.2}$$

where the physical indices s_n range from 1 to 2, and the auxiliary indices α_n range from 1 to a maximum value χ, known as the *bond dimension*. In practical simulations, χ is a crucial parameter that balances computational cost with accuracy, typically chosen to be on the order of 10^2 to 10^3. While this value is truncated for efficiency, it's important to note that the MPS representation in (A.2) is mathematically exact for any arbitrary state in the limit that $\chi \to 2^{\lfloor N/2 \rfloor}$. The bond dimension determines the maximum amount of entanglement the MPS can represent across any bond of the

chain and thus controls the accuracy of the approximation. A state with no entanglement (a simple product state) can be represented with $\chi = 1$, while states with more complex correlation structures require a larger χ. The efficiency of MPS stems from the fact that many physically relevant states can be approximated with high fidelity using a bond dimension χ that is significantly smaller than what would be required to represent an arbitrary state in the Hilbert space.

Time evolution of an MPS is commonly performed using the *Time-Evolving Block Decimation (TEBD)* algorithm. This algorithm relies on a Trotter-Suzuki decomposition to approximate the time-evolution operator $U(t) = e^{-i\hat{H}t}$ as a sequence of local two-site gates $\hat{h}_{j,j+1}$. For a nearest-neighbor Hamiltonian, we can write $\hat{H} = \hat{H}_{\text{even}} + \hat{H}_{\text{odd}}$, where $\hat{H}_{\text{even/odd}} = \sum_{j\in\text{even/odd}} \hat{h}_{j,j+1}$ where $\hat{h}_{j,j+1}$. A second-order Trotter decomposition is then:

$$e^{-i\hat{H}\delta t} \approx e^{-i\hat{H}_{\text{odd}}\delta t/2} e^{-i\hat{H}_{\text{even}}\delta t} e^{-i\hat{H}_{\text{odd}}\delta t/2} + O(\delta t^3)$$

Applying each two-site gate increases the entanglement across the corresponding bond, which would lead to a growth in the required bond dimension. To keep the computation feasible, a truncation step is performed via a Singular Value Decomposition (SVD) across the bond, keeping only the χ largest singular values. This step controllably projects the state back into the manifold of states with a manageable bond dimension based on the desired accuracy.

A.0.2 Computational Scaling and Simulation Parameters

The computational cost of the MPS-based simulations scales with several key parameters:

- **System Size (N):** For a fixed bond dimension, the cost of a single TEBD step scales linearly with the system size, $O(N)$. This is the primary advantage over exact methods.

- **Bond Dimension (χ):** The computational cost is dominated by the SVD truncation step, scaling polynomially with the bond dimension as $O(\chi^3)$.

- **Entanglement Growth:** After a quantum quench (sudden change in Hamiltonian parameters), entanglement typically grows linearly in time. To maintain accuracy, the bond dimension must grow exponentially with time, which limits the maximum achievable simulation time. For

adiabatic evolution, the entanglement growth is much slower, allowing for longer simulation times and larger system sizes.

Our simulations were implemented using the ITensor library [168, 169] with a TEBD time-step of $\delta t = 0.1J^{-1}$ and with $J = 1$ as the unit of energy. Reflecting the difference in entanglement growth, we used a chain of $N = 40$ spins for the adiabatic protocols and a smaller chain of $N = 20$ for the sudden quench protocol, where entanglement grows more rapidly.

A.0.3 Sudden Quench Simulations

For the sudden quench, the system was initialized in the product state $|\Psi_0\rangle$ (all spins up) and then evolved under a time-independent Hamiltonian with a drive amplitude of $F = 0.5$. The total evolution was carried out to a final time of $t_f = 50$. To compare with the analytical predictions for the steady state, the expectation values of observables were averaged over the time interval from $t = 20$ to $t = 50$.

As discussed in the main text, the analytical results are derived in the thermodynamic limit, whereas our simulations are for finite N. We observe finite-size corrections in our results. Figure A.1 illustrates the deviation of the numerically computed correlator $Q^z(1)$ from the analytical solution. To quantify this deviation, we define an integrated error $E_N[Q^z(1)] = \int_0^5 d\mu |Q^Z(1)_{\text{analytical}} - Q^Z(1)_N|$, where $Q^Z(1)_N$ is the simulation result for N sites. As shown in Fig. A.2, this error scales as N^{-1}, confirming that our numerical results correctly converge to the analytical predictions as the system size increases.

A.0.4 Adiabatic Evolution and Hysteresis

The adiabatic switching protocol was simulated by linearly ramping the drive amplitude as $F(t) = F_f(t/\tau_{sl})$ from $t = 0$ to a ramp time of $t_f = \tau_{sl} = 10^3$, reaching a final amplitude of $F_f = 0.5$. After the ramp, the system was evolved with the constant final Hamiltonian for an additional time interval $\Delta t = 30$, over which the time-averaging of observables was performed.

To demonstrate the hysteresis effect, the detuning μ was varied after an initial adiabatic ramp-up of $F(t)$ at a fixed $\mu = 5$ (in the trivial phase). Subsequently, μ was slowly varied as $\mu(t) = 5 - \alpha t$ with a slow rate of $\alpha = 10^{-3}$. To obtain the time-averaged observables for each point on the hysteresis

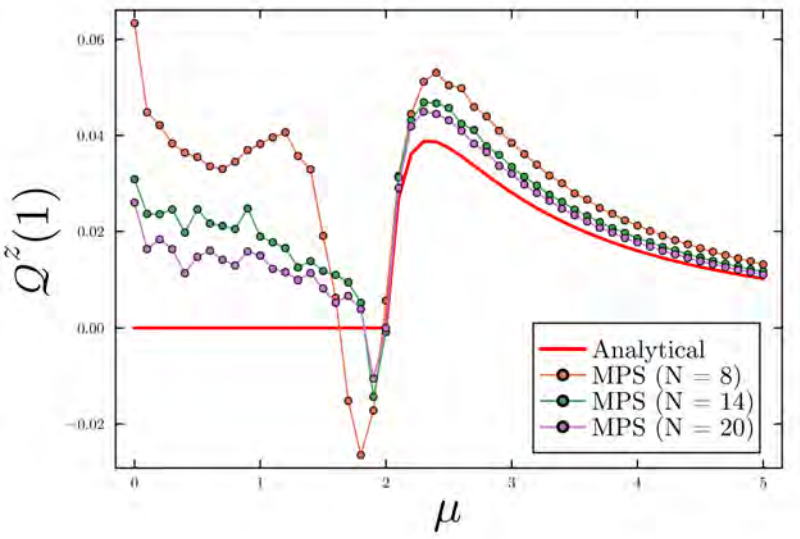


Figure A.1 The time-averaged correlator $Q^z(1)$ for a sudden turn-on of parametric modulation as a function of the scaled frequency detuning μ/J. The final modulation amplitude is $F/J = 0.5$. The analytical result (thermodynamic limit) is compared with MPS simulation results for a finite chain of $N = 20$.

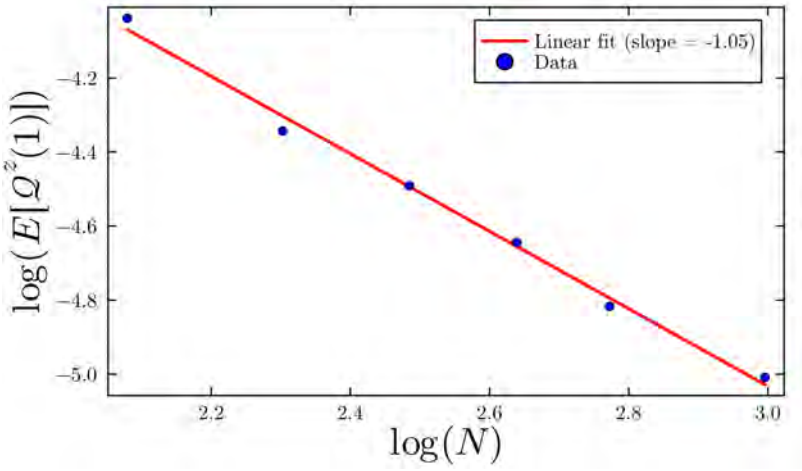


Figure A.2 A log-log plot of the integrated error $E_N[Q^z(1)]$ versus the number of sites N. The linear fit (dashed line) has a slope of approximately -1, confirming that the finite-size corrections to the correlator scale as N^{-1}.

loop, a copy of the wavefunction was made at the corresponding value of $\mu(t)$; this copy was then evolved independently under a constant Hamiltonian for an interval $\Delta t = 30$ for time-averaging. This procedure ensures that the averaging process does not interfere with the primary adiabatic evolution of $\mu(t)$. The resulting memory effect for $1 - \langle\sigma_z\rangle$ and $Q^z(1)$, which was not shown in the main text, is presented in Fig. A.3.

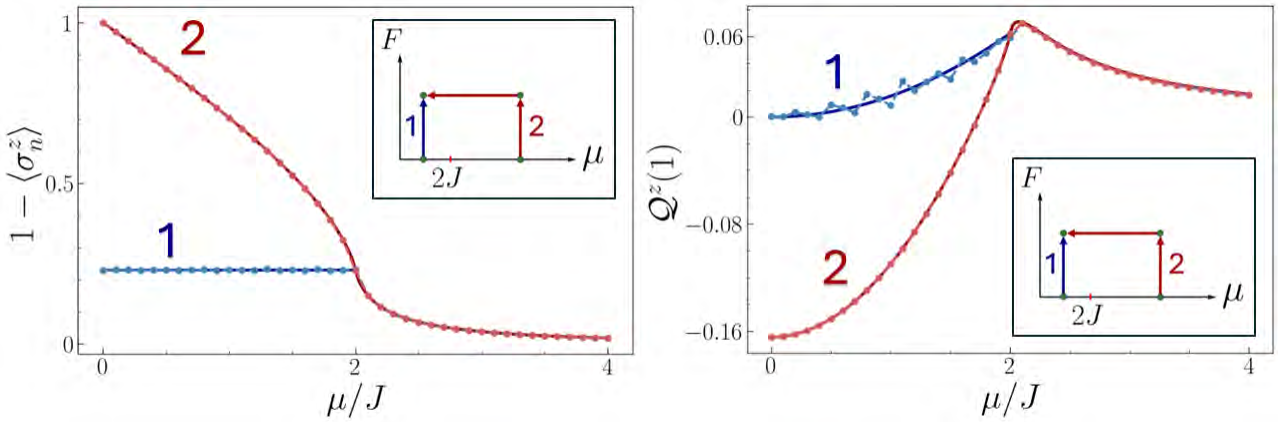


Figure A.3 The time-averaged correlators $1-\langle\sigma_z\rangle$ and $Q^z(1)$ obtained by slowly increasing the drive to $F(t_f)/J = 0.5$ for a fixed μ (line and circles 1) and by slowly turning on the drive to the same F/J in the trivial regime and then slowly changing the modulation frequency to arrive at the same μ (line and circles 2). The simulations refer to $N = 40$ and $F(t) = F(t_f)t/\tau_{\rm sl}$ with $\tau_{\rm sl} = 10^3/J$.

BIBLIOGRAPHY

[1] M. Z. Hasan and C. L. Kane, Reviews of Modern Physics **82**, 3045 (2010).

[2] X.-L. Qi and S.-C. Zhang, Reviews of Modern Physics **83**, 1057 (2011).

[3] C.-K. Chiu, J. C. Y. Teo, A. P. Schnyder, and S. Ryu, Reviews of Modern Physics **88**, 035005 (2016).

[4] M. Bukov, L. D'Alessio, and A. Polkovnikov, Advances in Physics **64**, 139 (2015).

[5] A. Polkovnikov, K. Sengupta, A. Silva, and M. Vengalattore, Reviews of Modern Physics **83**, 863 (2011).

[6] A. Mitra, Annual Review of Condensed Matter Physics **9**, 245 (2018).

[7] F. Bloch, Zeitschrift für Physik **61**, 206 (1930).

[8] T. Moriya, Physical Review **120**, 91 (1960).

[9] H. Katsura, N. Nagaosa, and P. A. Lee, Physical Review Letters **104**, 066403 (2010).

[10] R. Shindou, R. Matsumoto, S. Murakami, and J.-i. Ohe, Physical Review B **87**, 174427 (2013).

[11] L. Zhang, J. Ren, J.-S. Wang, and B. Li, Physical Review B **87**, 144101 (2013).

[12] A. E. Fahmy, A. J. Williams, Y. Li, T. T. Mai, K. F. Garrity, M. B. Stone, M. J. Karaki, S. Haravifard, A. R. H. Walker, R. V. Aguilar, *et al.*, arXiv preprint arXiv:2512.18534 (2025).

[13] P. A. McClarty, Annual Review of Condensed Matter Physics **13**, 171 (2022).

[14] R. Matsumoto and S. Murakami, Physical Review B **84**, 184406 (2011).

[15] Y. Onose, T. Ideue, H. Katsura, Y. Shiomi, N. Nagaosa, and Y. Tokura, Science **329**, 297 (2010).

[16] M. Nawwar, R. R. Neumann, J. Wen, I. Mertig, A. Mook, and J. P. Heremans, Reports on Progress in Physics **88**, 080503 (2025).

[17] M. J. Karaki, A. E. Fahmy, A. J. Williams, S. Haravifard, J. E. Goldberger, and Y.-M. Lu, npj Computational Materials **11**, 216 (2025).

[18] R. Chisnell, J. S. Helton, D. E. Freedman, D. K. Singh, R. I. Bewley, D. G. Nocera, and Y. S. Lee, Physical Review Letters **115**, 147201 (2015).

[19] J. Romhányi, K. Penc, and R. Ganesh, Nature Communications **6**, 6805 (2015).

[20] A. Y. Kitaev, Physics-Uspekhi **44**, 131 (2001).

[21] M. I. Dykman, Physical Review A **100**, 042101 (2019).

[22] M. T. Elewa and M. Dykman, Physical Review B **113**, L201407 (2026).

[23] T. Holstein and H. Primakoff, Physical Review **58**, 1098 (1940).

[24] F. J. Dyson, Physical Review **102**, 1217 (1956).

[25] J. H. P. Colpa, Physica A: Statistical Mechanics and its Applications **93**, 327 (1978).

[26] I. Dzyaloshinsky, Journal of Physics and Chemistry of Solids **4**, 241 (1958).

[27] F. D. M. Haldane, Physical Review Letters **61**, 2015 (1988).

[28] M. E. Zhitomirsky and A. L. Chernyshev, Reviews of Modern Physics **85**, 219 (2013).

[29] A. L. Chernyshev and P. A. Maksimov, Physical Review Letters **117**, 187203 (2016).

[30] T. Matsubara and H. Matsuda, Progress of Theoretical Physics **16**, 569 (1956).

[31] H. Suhl, Journal of Physics and Chemistry of Solids **1**, 209 (1957).

[32] T. Brächer, P. Pirro, and B. Hillebrands, Physics Reports **699**, 1 (2017).

[33] D. Malz, J. Knolle, and A. Nunnenkamp, Nature Communications **10**, 3937 (2019).

[34] P. Jordan and E. Wigner, Zeitschrift für Physik **47**, 631 (1928).

[35] E. Lieb, T. Schultz, and D. Mattis, Annals of Physics **16**, 407 (1961).

[36] P. Pfeuty, Annals of Physics **57**, 79 (1970).

[37] Y. Liang, W. Huang, L. Zhang, Z. Tao, K. Tang, J. Chu, J. Qiu, X. Sun, Y. Zhou, J. Zhang, *et al.*, arXiv preprint arXiv:2410.10208 (2024).

[38] E. Noether, Nachrichten von der Gesellschaft der Wissenschaften zu Göttingen, Mathematisch-Physikalische Klasse **1918**, 235 (1918).

[39] F. Bloch, Zeitschrift für Physik **52**, 555 (1929).

[40] J. H. Shirley, Physical Review **138**, B979 (1965).

[41] H. Sambe, Physical Review A **7**, 2203 (1973).

[42] A. Eckardt, Reviews of Modern Physics **89**, 011004 (2017).

[43] M. S. Rudner and N. H. Lindner, Nature Reviews Physics **2**, 229 (2020).

[44] N. Goldman and J. Dalibard, Physical Review X **4**, 031027 (2014).

[45] A. Eckardt and E. Anisimovas, New Journal of Physics **17**, 093039 (2015).

[46] W. Magnus, Communications on Pure and Applied Mathematics **7**, 649 (1954).

[47] F. Bloch and A. Siegert, Physical Review **57**, 522 (1940).

[48] D. V. Else, B. Bauer, and C. Nayak, Physical Review Letters **117**, 090402 (2016).

[49] V. Khemani, A. Lazarides, R. Moessner, and S. L. Sondhi, Physical Review Letters **116**, 250401 (2016).

[50] C. W. von Keyserlingk, V. Khemani, and S. L. Sondhi, Physical Review B **94**, 085112 (2016).

[51] M. Rigol, V. Dunjko, V. Yurovsky, and M. Olshanii, Physical Review Letters **98**, 050405 (2007).

[52] P. Calabrese, F. H. L. Essler, and M. Fagotti, Journal of Statistical Mechanics: Theory and Experiment **2012**, P07016 (2012).

[53] P. Calabrese, F. H. L. Essler, and M. Fagotti, Journal of Statistical Mechanics: Theory and Experiment **2012**, P07022 (2012).

[54] J. Alicea, Reports on Progress in Physics **75**, 076501 (2012).

[55] C. W. J. Beenakker, Annual Review of Condensed Matter Physics **4**, 113 (2013).

[56] A. P. Schnyder, S. Ryu, A. Furusaki, and A. W. W. Ludwig, Physical Review B **78**, 195125 (2008).

[57] S. Ryu, A. P. Schnyder, A. Furusaki, and A. W. W. Ludwig, New Journal of Physics **12**, 065010 (2010).

[58] S. Tewari and J. D. Sau, Physical Review Letters **109**, 150408 (2012).

[59] A. Alecce and L. Dell'Anna, Physical Review B **95**, 195160 (2017).

[60] P. Fendley, Journal of Physics A: Mathematical and Theoretical **49**, 30LT01 (2016).

[61] J. Kemp, N. Y. Yao, C. R. Laumann, and P. Fendley, Journal of Statistical Mechanics: Theory and Experiment **2017**, 063105 (2017).

[62] X. Mi *et al.*, Science **378**, 785 (2022).

[63] M. Tarnowski, F. N. Ünal, N. Fläschner, B. S. Rem, A. Eckardt, K. Sengstock, and C. Weitenberg, Nature Communications **10**, 1728 (2019).

[64] C.-R. Yi, L. Zhang, L. Zhang, R.-H. Jiao, X.-C. Cheng, Z.-Y. Wang, X.-T. Xu, W. Sun, X.-J. Liu, S. Chen, and J.-W. Pan, Physical Review Letters **123**, 190603 (2019).

[65] A. Liu, M. T. Elewa, and M. I. Dykman, Dispersive mode coupling in p-doped semiconductor nanomechanical resonators (2026), arXiv:2606.17392 [cond-mat.mes-hall] .

[66] A. J. Schleusner, M. T. Elewa, N. R. Beysengulov, C. A. Mikolas, and J. Pollanen, High-frequency nonlinear conductivity of a Wigner crystal (2026), arXiv:2607.06846 [cond-mat.mes-hall] .

[67] M. Ali, N. A. Kamar, A. Seif, and M. Maghrebi, Physical Review Letters **136**, 060404 (2026).

[68] I. S. Gradshteyn and I. M. Ryzhik, *Table of integrals, series, and products* (Academic press, 2014).

[69] F. W. Olver, *NIST handbook of mathematical functions hardback and CD-ROM* (Cambridge university press, 2010).

[70] J. Dziarmaga, Physical Review Letters **95**, 245701 (2005).

[71] J. Dziarmaga, Advances in Physics **59**, 1063 (2010).

[72] A. Blais, A. L. Grimsmo, S. M. Girvin, and A. Wallraff, Reviews of Modern Physics **93**, 025005 (2021).

[73] C. P. Slichter, *Principles of Magnetic Resonance*, 3rd ed. (Springer, Berlin, 1990).

[74] N. Leumer, M. Marganska, B. Muralidharan, and M. Grifoni, Journal of Physics: Condensed Matter **32**, 445502 (2020).

[75] A. N. Cleland and M. L. Roukes, Applied Physics Letters **69**, 2653 (1996).

[76] J. T. M. van Beek and R. Puers, Journal of Micromechanics and Microengineering **22**, 013001 (2012).

[77] O. Brand, I. Dufour, S. M. Heinrich, and F. Josse, eds., *Resonant MEMS: Fundamentals, Implementation, and Application* (Wiley-VCH, Singapore, 2015).

[78] H. Yamaguchi, Semicond. Sci. Techn. **32**, 103003 (2017).

[79] J. M. L. Miller, A. Ansari, D. B. Heinz, Y. Chen, I. B. Flader, D. D. Shin, L. G. Villanueva, and T. W. Kenny, Applied Physics Reviews **5**, 041307 (2018).

[80] A. Bachtold, J. Moser, and M. I. Dykman, Reviews of Modern Physics **94**, 045005 (2022).

[81] E. J. Ng, H. K. Lee, C. H. Ahn, R. Melamud, and T. W. Kenny, IEEE Sensors Journal **13**, 987 (2013).

[82] L. Comenencia Ortiz, H.-K. Kwon, J. Rodriguez, Y. Chen, G. D. Vukasin, D. B. Heinz, D. D. Shin, and T. W. Kenny, Journal of Microelectromechanical Systems **29**, 190 (2020).

[83] H.-K. Kwon, G. D. Vukasin, N. E. Bousse, and T. W. Kenny, Journal of Microelectromechanical Systems **29**, 1130 (2020).

[84] W. Jia, W. Chen, Y. Xiao, Z. Wu, and G. Wu, IEEE Transactions on Electron Devices **69**, 2597 (2022).

[85] Y. Xiao, J. Han, K. Zhu, and G. Wu, IEEE Electron Device Letters **44**, 1340 (2023).

[86] J. Yang, S. Verma, M. Gomi, J. Kim, J. Yan, J. Jing, G. Vukasin, R. Kwon, G. Bahl, and T. W. Kenny, in *2025 23rd International Conference on Solid-State Sensors, Actuators and Microsystems (Transducers)* (2025) pp. 184–187.

[87] J. Yan, J. Kim, R. Islam, J. Yang, K. Elmeligy, A. Bozkurt, T. W. Kenny, P. K. Hanumolu, and G. Bahl, arXiv:2605.08118 (2026).

[88] M. Born, J. Chem. Phys. **7**, 591 (1939).

[89] E. A. Stern, Phys. Rev. **111**, 786 (1958).

[90] I. Mahboob, N. Perrissin, K. Nishiguchi, D. Hatanaka, Y. Okazaki, A. Fujiwara, and H. Yamaguchi, Nano letters **15**, 2312 (2015).

[91] K. Asadi, J. Yu, and H. Cho, Philosophical Transactions of the Royal Society A: Mathematical, Physical and Engineering Sciences **376**, 20170141 (2018).

[92] P. Arrangoiz-Arriola, E. A. Wollack, Z. Wang, M. Pechal, W. Jiang, T. P. McKenna, J. D. Witmer, R. Van Laer, and A. H. Safavi-Naeini, Nature **571**, 537 (2019).

[93] A. A. Shevyrin, A. G. Pogosov, A. K. Bakarov, A. A. Shklyaev, and A. Naik, Phys. Rev. Appl. **22**, L061003 (2024).

[94] D. Allemeier, I. I. Kaya, M. S. Hanay, and K. L. Ekinci, Phys. Rev. A **112**, 023505 (2025).

[95] C. F. D. Wattjes, Z. Li, M. Xu, R. A. Norte, P. G. Steeneken, and F. Alijani, arXiv:2604.13920 (2026).

[96] W. J. Venstra, R. van Leeuwen, and H. S. J. van der Zant, Applied Physics Letters **101**, 243111 (2012).

[97] M. H. Matheny, L. G. Villanueva, R. B. Karabalin, J. E. Sader, and M. L. Roukes, Nano Letters **13**, 1622 (2013).

[98] K. Gajo, G. Rastelli, and E. M. Weig, Physical Review B **101**, 075420 (2020).

[99] M. Aspelmeyer, T. J. Kippenberg, and F. Marquardt, Reviews of Modern Physics **86**, 1391 (2014).

[100] N. R. Lee, Y. Guo, A. Y. Cleland, E. A. Wollack, R. G. Gruenke, T. Makihara, Z. Wang, T. Rajabzadeh, W. Jiang, F. M. Mayor, *et al.*, PRX Quantum **4**, 040342 (2023).

[101] R. W. Keyes, IBM Journal of Research and Development **5**, 266 (1961).

[102] R. W. Keyes, in *Solid State Physics*, Vol. 20, edited by F. Seitz, D. Turnbull, and H. Ehrenreich (Academic Press, 1968) pp. 37–90.

[103] G. L. Bir and A. Tursunov, Sov. Phys. Solid State **4**, 1925 (1963).

[104] J. J. Hall, Phys. Rev. **161**, 756 (1967).

[105] F. Cerdeira and M. Cardona, Phys. Rev. B **5**, 1440 (1972).

[106] C. K. Kim, M. Cardona, and S. Rodriguez, Phys. Rev. B **13**, 5429 (1976).

[107] N. S. Averkiev, Yu. V. Ilisavskiy, and V. M. Sternin, Solid State Communications **52**, 17 (1984).

[108] F. S. Khan and P. B. Allen, Phys. Status Solidi B **128**, 31 (1985).

[109] N. S. Averkiev, Yu. V. Ilisavskiy, and V. M. Sternin, Sov. Phys. Solid State **28**, 829 (1987).

[110] K. Moskovtsev and M. I. Dykman, Physical Review B **95**, 085426 (2017).

[111] A. Liu and M. Dykman, Physical Review B **111**, 235410 (2025).

[112] A. K. Samarao and F. Ayazi, IEEE Trans. Electron. Devices **59**, 87 (2012).

[113] A. Hajjam, A. Logan, and S. Pourkamali, Journal of Microelectromechanical Systems **21**, 681 (2012).

[114] E. J. Ng, V. A. Hong, Y. Yang, C. H. Ahn, C. L. M. Everhart, and T. W. Kenny, Journal of Microelectromechanical Systems **24**, 730 (2015).

[115] H. Majjad, J.-R. Coudevylle, S. Basrour, and M. de Labachelerie, in *Transducers' 01 Eurosensors XV: The 11th International Conference on Solid-State Sensors and Actuators June 10–14, 2001 Munich, Germany* (Springer, 2001) pp. 300–303.

[116] L. Khine and M. Palaniapan, Journal of Micromechanics and Microengineering **19**, 015017 (2009).

[117] O. Holmgren, K. Kokkonen, T. Veijola, T. Mattila, V. Kaajakari, A. Oja, J. V. Knuuttila, and M. Kaivola, Journal of Micromechanics and Microengineering **19**, 015028 (2009).

[118] H. Zhu, C. Tu, G. Shan, and J. E.-Y. Lee, Sensors and Actuators A: Physical **215**, 189 (2014).

[119] J. E.-Y. Lee, in *Encyclopedia of Nanotechnology*, edited by B. Bhushan (Springer, Dordrecht, 2016) pp. 1–9.

[120] A. Daruwalla, H. Wen, C.-S. Liu, and F. Ayazi, Microsystems & Nanoengineering **6**, 53 (2020).

[121] L. Landau and E. Lifshitz, *Theory of Elasticity*, 3rd ed. (Butterworth-Heinemann Ltd., Oxford, 1986).

[122] J. M. Luttinger and W. Kohn, Physical Review **97**, 869 (1955).

[123] G. L. Bir and G. E. Pikus, *Symmetry and Strain-Induced Effects in Semiconductors* (Wiley, New York, 1974).

[124] R. Winkler, *Spin-Orbit Coupling Effects in Two-Dimensional Electron and Hole Systems* (Springer, Berlin, 2003).

[125] S. M. Girvin and K. Yang, *Modern Condensed Matter Physics* (Cambridge University Press, 2019).

[126] V. L. Gurevich, *Transport in Phonon Systems* (Elsevier Science Ltd, 1988).

[127] A. Pandit and A. Bongiorno, Computer Physics Communications **288**, 108751 (2023).

[128] J. A. Garber and A. V. Granato, Phys. Rev. B **11**, 3990 (1975).

[129] C. Malica and A. D. Corso, Journal of Physics: Condensed Matter **32**, 315902 (2020).

[130] H. J. McSkimin, Journal of Applied Physics **24**, 988 (1953).

[131] Y. P. Varshni, Phys. Rev. B **2**, 3952 (1970).

[132] Y. A. Burenkov and S. P. Nikaronov, Sov. Phys. Solid State **16**, 963 (1974).

[133] M. Dykman and M. Krivoglaz, Zhurnal Eksperimental'noi i Teoreticheskoi Fiziki **64**, 993 (1973).

[134] R. E. Peierls, *Quantum Theory of Solids* (Clarendon Press, 1955).

[135] M. I. Dykman and M. A. Krivoglaz, Phys. Stat. Sol. B **48**, 497 (1971).

[136] K. F. Graff, *Wave Motion in Elastic Solids* (Dover, New York, 1991).

[137] A. W. Leissa, *Vibration of Plates* (U.S. Government Printing Office, Washington, D.C., 1969).

[138] M. W. Cole and M. H. Cohen, Physical Review Letters **23**, 1238 (1969).

[139] M. W. Cole, Reviews of Modern Physics **46**, 451 (1974).

[140] C. C. Grimes, T. R. Brown, M. L. Burns, and C. L. Zipfel, Physical Review B **13**, 140 (1976).

[141] C. C. Grimes and T. R. Brown, Physical Review Letters **32**, 280 (1974).

[142] Y. P. Monarkha and K. Kono, *Two-Dimensional Coulomb Liquids and Solids*, Springer Series in Solid-State Sciences, Vol. 142 (Springer, Berlin, 2004).

[143] C. C. Grimes and G. Adams, Physical Review Letters **42**, 795 (1979).

[144] E. Wigner, Physical Review **46**, 1002 (1934).

[145] R. C. Gann, S. Chakravarty, and G. V. Chester, Physical Review B **20**, 326 (1979).

[146] B. I. Halperin and D. R. Nelson, Physical Review Letters **41**, 121 (1978).

[147] A. P. Young, Physical Review B **19**, 1855 (1979).

[148] C. C. Grimes and G. Adams, Physical Review Letters **36**, 145 (1976).

[149] D. S. Fisher, B. I. Halperin, and P. M. Platzman, Physical Review Letters **42**, 798 (1979).

[150] R. Mehrotra, B. M. Guenin, and A. J. Dahm, Physical Review Letters **48**, 641 (1982).

[151] D. C. Glattli, E. Y. Andrei, and F. I. B. Williams, Physical Review Letters **60**, 420 (1988).

[152] P. Glasson, V. Dotsenko, P. Fozooni, M. Lea, W. Bailey, G. Papageorgiou, S. Andresen, and

A. Kristensen, Physical Review Letters **87**, 176802 (2001).

[153] H. Ikegami, H. Akimoto, and K. Kono, Physical Review Letters **102**, 046807 (2009).

[154] S. Zou, D. Konstantinov, and D. G. Rees, Physical Review B **104**, 045427 (2021).

[155] M. I. Dykman and Y. G. Rubo, Physical Review Letters **78**, 4813 (1997).

[156] R. Giannetta and L. Wilen, Solid State Communications **78**, 199 (1991).

[157] V. E. Syvokon, K. A. Nasyedkin, and A. S. Neoneta, Low Temperature Physics **34**, 600 (2008).

[158] V. E. Syvokon, K. A. Nasyedkin, and I. V. Sharapova, Low Temperature Physics **40**, 953 (2014).

[159] K. Shirahama and K. Kono, Physical Review Letters **74**, 781 (1995).

[160] W. F. Vinen, Journal of Physics: Condensed Matter **11**, 9709 (1999).

[161] D. G. Rees, N. R. Beysengulov, J.-J. Lin, and K. Kono, Physical Review Letters **116**, 206801 (2016).

[162] Y. P. Monarkha and K. Kono, Journal of Low Temperature Physics **156**, 95 (2009).

[163] N. Kotibhaskar, C.-Y. Shih, S. Motlakunta, A. Vogliano, L. Hahn, Y.-T. Chen, and R. Islam, Physical Review Research **6**, 033038 (2024).

[164] P. Richerme, Z.-X. Gong, A. Lee, C. Senko, J. Smith, M. Foss-Feig, S. Michalakis, A. V. Gorshkov, and C. Monroe, Nature **511**, 198 (2014).

[165] S. Korenblit, D. Kafri, W. C. Campbell, R. Islam, E. E. Edwards, Z.-X. Gong, G.-D. Lin, L. Duan, J. Kim, K. Kim, and C. Monroe, New Journal of Physics **14**, 095024 (2012).

[166] M. Mohseni, M. Kewenig, R. Verba, Q. Wang, M. Schneider, B. Heinz, F. Kohl, C. Dubs, B. Lägel, A. A. Serga, B. Hillebrands, A. V. Chumak, and P. Pirro, Physica Status Solidi RRL **14**, 2000011 (2020).

[167] A. Kitaev, Annals of Physics **321**, 2 (2006).

[168] M. T. Fishman, S. R. White, and E. M. Stoudenmire, SciPost Physics Codebases , 4 (2022).

[169] M. T. Fishman, E. M. Stoudenmire, *et al.*, Itensors.jl (2020).